
Numerical Simulation of Ice Accretion on Coated Wind Turbine Blades

Khaled Yassin



Von der Fakultät für Mathematik und Naturwissenschaften
der Carl von Ossietzky Universität Oldenburg
zur Erlangung des Grades und Titels eines

DOKTORS DER INGENIEURWISSENSCHAFTEN
DR.-ING.

angenommene Dissertation

von Herrn Khaled Yassin
geboren am 16.06.1988 in Bangor (Vereinigtes Königreich)

Gutachter: Prof. Dr. rer. nat. Joachim Peinke

Zweitgutachter: Prof. Dr. Taeseong Kim

Tag der Abgabe: 18.03.2022

Tag der Disputation: 01.07.2022

Contents

1	Introduction	1
1.1	Motivation	1
1.2	Wind energy in cold climates and hazards	2
1.3	Anti-icing and deicing systems of wind turbine blades	2
1.3.1	Active ADIS	3
1.3.2	Passive ADIS	4
1.4	Hydrophobic and ice-phobic coatings	5
1.4.1	Surface tension and contact angle	5
1.4.2	Effects of surface roughness	6
1.4.3	Effects of surface roughness on impinging water droplets	7
1.5	Scope of thesis	8
1.6	Thesis outline	8
2	Literature Review	11
2.1	Introduction	11
2.2	Simulation of flow over iced surfaces	11
2.2.1	Fully Resolved Roughness	12
2.2.2	Rough Wall Functions (rwf)	12
2.3	Water Particle Tracking	14
2.3.1	Lagrangian Particle Tracking (LPT)	15
2.3.2	Eulerian Particle Tracking (EPT)	15
2.4	Thermodynamic models of Ice Accretion	17
2.4.1	Messinger's model and its modifications	18
2.4.2	Shallow Water Icing Model (SWIM)	18
2.4.3	Makonnen's model	20
2.5	Wind tunnel ice accretion simulations	21
2.6	Ice-phobic coatings applications	21
2.6.1	Freezing delay effect	22
2.6.2	Water film slip	22
2.6.3	Droplet splashing	23
2.6.4	Wind tunnel experiments	24
2.7	Overview and general critic	25

3	Theoretical Background	27
3.1	Introduction	27
3.2	Overall Simulation Procedure	27
3.3	Background Flow Simulation	28
3.3.1	Governing Equations of Compressible Flow	28
3.3.2	Reynolds-Averaged Navier-Stokes (RANS) Method	29
3.3.3	Multi Reference Frame (MRF) Model:	30
3.3.4	Simulation of Rough Surfaces	30
3.4	Water Particle Tracking	32
3.4.1	Lagrangian Particle Tracking	33
3.4.2	Eulerian Flow Simulation	33
3.4.3	Drag force models	34
3.4.4	Droplet Size Distribution	35
3.4.5	Collection efficiency	36
3.5	Ice Accretion Thermodynamic Model	36
3.5.1	Liquid Film Solution	37
3.5.2	Shallow Water Icing Model (SWIM)	42
3.6	Mesh generation and Re-generation	43
3.7	Effects of blade design and materials	44
3.7.1	Anti-icing with heating	46
3.7.2	Effects of ice-phobic coatings	46
3.7.3	Surface roughness analysis	47
3.8	Local icing conditions calculation	48
3.9	Description of the new OpenFOAM codes	52
3.10	Conclusions and remarks	53
4	Flow field simulation over rough ice surfaces	55
4.1	Introduction	55
4.2	Rough wall functions (rwf)	55
4.2.1	Validation of the rough wall functions	56
4.2.2	Simulation of iced airfoils	56
4.3	Discussion and conclusions:	70
4.3.1	General remarks and discussion	70
4.3.2	Conclusions and remarks	72
5	Ice accretion on 2D airfoil profiles	75
5.1	Introduction	75
5.2	Simulation of collection efficiency	75
5.2.1	Comparison of mono- vs polydispersed particles	76
5.2.2	Comparison of different MVD values	76
5.2.3	Comparison of splashing droplets	79
5.2.4	Effect of airfoil geometry on collection efficiency	79
5.3	Simulation of ice accretion profiles	81
5.3.1	Validation with icing wind tunnel results	81
5.4	Simulation of ice accretion on coated airfoils	83

5.5	Conclusions and remarks	85
6	Ice accretion on wind turbine blades	89
6.1	Introduction	89
6.2	Simulation of icing using Quasi-3D particle ice accretion	89
6.2.1	Validation of airflow field	90
6.2.2	Validation of ice accretion	90
6.3	Simulation of NREL 5MW wind turbine blade	92
6.3.1	Validation of air flow field	95
6.3.2	Simulation of collection efficiency	95
6.3.3	Simulation of ice profiles	95
6.3.4	Simulation of anti-icing heat	97
6.4	Conclusions and remarks	102
7	Intermittent wind fields simulations	103
7.1	Introduction	103
8	Conclusions and Outlook	135
8.1	Conclusions	135
8.2	Outlook	136
	References	139
	List of Publications	151
	Acknowledgement	153
	Curriculum Vitae	155
	Erklärung	157

List of Figures

1.1	Comparison between a)Cassie-Baxter and b)Wenzel contact angles	6
1.2	Roughness element geometrical parameters	7
3.1	Flowchart of ice accretion simulation process	28
3.2	Roughness element geometrical parameters	31
3.3	Different phase-coupling ranges with diffrent disperced phase volume fraction α_d and the ratio between particle response time τ_p and Kolmogorov time scale τ_K (adapted from Elghobashi [1])	33
3.4	SWIM model source terms in (a) mass and (b)energy conservation equations . .	41
3.5	Evolution of mesh around iced NACA0012 airfoil using GMSH for case 30 [2] at the start of (a) step 1, (b) step 2, and (c) step 3	45
3.6	Slip phenomenon in hydrophobic surfaces(adapted from Choi and Kim [3] and Ybert et al. [4])	48
3.7	Abbott-Firestone diagram to calculate R_{sm} and R_{pk} (regenerated from Ref. [5])	49
3.8	a) Raw roughness heights, b) De-trended roughness heights, and c) Abbott-Firestone diagram of Layer 1 (taken from NEWA [6])	50
3.9	Minimum air temperature at 100m height above see level over Germany	51
3.10	a) Histogram and b) Cumulative Histogram of ambient air temperature over the year 2017 at at 53.15336°N, 8.16353°E extracted from the NEWA [6]	51
4.1	Pressure coefficient C_p distribution over rough cylinders using implemented wall functions at $Re = 4 \times 10^6$ and: (a) $K_s = 75 \times 10^{-5}$ m, (b) $K_s = 3 \times 10^{-3}$ m, (c) $K_s = 9 \times 10^{-3}$ m where $\theta = 0^\circ$ at stagnation point and increases downstream.	57
4.2	The wind tunnel setup of testing profile 1 in open section wind tunnel at the German-Dutch wind tunnels	58
4.3	Ice profiles 1 and 2 accumulated on airfoil's leading edge	59
4.4	Mesh of a)rough and b)smoothened ice profile 1	60
4.5	Mesh of a)rough and b)smoothened ice profile 2	60
4.6	Rough vs smoothened ice profiles 1 and 2	61
4.7	Case 1: (a) lift C_l and (b) drag C_d coefficients vs AoA for different wall functions	62
4.8	Case 1: pressure coefficient C_p distribution for AoA = (a) 0° , (b) 4° , (c) 8° , and (d) 12°	63
4.9	Case 2: (a) lift C_l and (b) drag C_d coefficients vs AoA for different wall functions	65
4.10	Case 2: pressure coefficient C_p distribution for AoA = (a) 0° , (b) 4° , (c) 8° , and (d) 12°	66

4.11	Case 3: (a) lift C_l and (b) drag C_d coefficients vs AoA for different wall functions	68
4.12	Case 3: C_p distribution for AoA = (a) 0° , (b) 4° , (c) 8° , and (d) 12°	69
4.13	Average error between experimental and simulation results of C_p distribution (a) case 1, (b) case 2, and (c) case 3	71
4.14	Line Integral Convolution (LIC) of flow in (a) case 2 at AoA = 0° (b) case 3 at AoA = 0°	73
5.1	Particle diameter of the a) mono vs b) poly-dispersed particle distributions sim- ulations	77
5.2	β distribution at AoA = (a) 0° and (b) 8°	78
5.3	β distribution for different MVD values at AoA = (a) 0° and (b) 8°	78
5.4	β distribution for non-splashing vs splashing droplets at AoA = (a) 0° and (b) 8°	79
5.5	Comparison between the leading edge profile of airfoils (left) and β distribution (right) with t/c = a) 18% b) 21% c) 25%	80
5.6	Ice accretion simulation of Case 27 for different number of icing loops	83
5.7	Ice accretion simulation of Case 30 for different number of icing loops	84
5.8	Ice accretion simulation of Case 31 for one time step	84
5.9	Ice accretion on coated 2D airfoils with a) Layer 1 and b) Layer 2	86
6.1	Comparison of C_p distribution of quasi-3D, full 3D CFD simulations using OpenFOAM and experimental results [7] of NREL PhaseVI blade sections for r/R = a) 0.467, b) 0.633, c) 0.8	91
6.2	Comparison of rime ice profiles of simulations of NREL PhaseVI blade of present work, Son and Kim [8], and FENSAP-ICE [9] sections for r/R = a) 0.467, b) 0.633, c) 0.8	93
6.3	Comparison of glaze ice profiles of simulations of NREL PhaseVI blade of present work, Son and Kim [8], and FENSAP-ICE [9] sections for r/R = a) 0.467, b) 0.633, c) 0.8	94
6.4	C_p distribution of 2D vs 3D CFD simulations of NREL 5MW blade sections for r/R = a) 0.4, b) 0.5, c) 0.6, d) 0.7, e) 0.8, and f) 0.95	96
6.5	Collection efficiency distribution with the surface distance from the leading edge on different NREL 5MW blade sections	97
6.6	Rime ice profiles for NREL 5MW blade sections using quasi-3D approach for r/R = a) 0.4, b) 0.5, c) 0.6, d) 0.7, e) 0.8, and f) 0.95	98
6.7	Glaze ice profiles for NREL 5MW blade sections using quasi-3D approach for r/R = a) 0.4, b) 0.5, c) 0.6, d) 0.7, e) 0.8, and f) 0.95	99
6.8	a) Accumulated liquid water film mass and b) the resulting anti-icing heat per meter span of the section at different radial positions for NREL 5MW wind turbine blade	101
6.9	Anti-icing heat distribution over blade section at r/R = 0.99 for ordinary and ice-phobic coating	102

Abstract

As the demand for renewable energies, especially wind energy, increases worldwide, wind farm developers try to invest all available areas with suitable wind resources to build wind turbines. Since wind speeds generally increase with the increase of altitude, many wind farms nowadays are located at high altitude areas to benefit from these high wind speeds. Also, some sites with high wind resources are located in cold areas like North Europe and North America. However, turbines located in such cold areas suffer from ice accretion. Ice accretion causes many problems like increasing the weight of the rotor, excessive vibrations due to unbalanced ice masses, decreased turbine performance, or ice through. These problems can lead to the complete shut down of the turbines and losing energy. Therefore, many manufacturers use heating-based anti-icing techniques to avoid ice accretion. However, such systems consume a significant amount of energy.

This thesis aims to develop new codes within the open-source CFD software to simulate the ice accretion phenomenon that occurs during the operation of wind turbines in cold climates. These developed tools should be able to simulate the rough ice profile formed on the blade, the airflow around these profiles, and how much energy needed for the anti-icing system. Also, the new coded enables the simulation of the effects of special ice-phobic coatings when they are applied on the surface of the blade and their effect on the overall anti-icing heat required.

To simulate such a phenomenon, the solver should be able to simulate the airflow around the blade to enable water particle tracking. To avoid any excessive computation costs of resolving complex profiles of ice, wall boundary conditions or rough wall functions can be used to model the effects of roughness on the airflow without completely resolving the flow field. This is done by the compressible flow simulation around the blade sections to enable the calculation of the temperature field that plays a very important role in the thermodynamic process of ice accretion. After that, water particles carried by air are tracked using Lagrangian particle tracking to calculate the exact location and velocity of particles impingement on the solid surface. After this impingement, a mathematical model is applied to calculate determine the behavior of these particles whether they are pinned to the surface or bouncing again to the airflow. Form this step, the amount and water mass on the surface can be determined and the thermodynamic model of icing can be applied to determine the final ice profile on the surface.

By applying this procedure on 2D airfoil profiles, the results from the new OpenFOAM code show good agreement with different experiments from published literature and from project partners. After proving its ability to simulate the ice accretion on 2D airfoils, the same solver is used in simulating the 3D rotating wind turbine blade using the quasi-3D technique. This technique is then compared with other CFD codes to validate it and then used to simulate the ice accretion on NREL 5MW wind turbine blade as an example of a multi-megawatt wind turbine. Also, a comparison between the expected minimum anti-icing heat in case ordinary and ice-phobic surfaces is held to study the feasibility of using such coatings in wind turbine applications. The results show how much the ice accretion can result in a rough and non-aerodynamic profile, which gives an idea about the harsh effects of ice accretion on the performance of wind turbines. Also, the results show that ice-phobic coatings can be feasible if they are applied on the leading edge of the blade in the middle and tip sections. These

areas are the most affected by ice accretion and require the highest heating energy. This topic still needs a lot of enhancement of the used models and more analysis of the effect of the ice profiles on the overall performance, the generated power, and the overall loads of the turbine.

Zusammenfassung

Da die Nachfrage nach erneuerbaren Energien, insbesondere nach Windenergie, weltweit steigt, versuchen Windparkentwickler, alle verfügbaren Gebiete mit geeigneten Windressourcen zu erschließen, um dort Windturbinen zu bauen. Da die Windgeschwindigkeiten im Allgemeinen mit zunehmender Höhe zunehmen, befinden sich viele Windparks heutzutage in hoch gelegenen Gebieten, um von diesen hohen Windgeschwindigkeiten zu profitieren. Außerdem befinden sich einige Standorte mit hohen Windressourcen in kalten Gebieten wie z.B. Nordeuropa und Nordamerika. Turbinen, die in solch kalten Gebieten stehen, leiden jedoch unter der Eisbildung an ihren Flügeln. Der Eisansatz an diesen Standorten verursacht viele Probleme, wie z. B. eine Gewichtszunahme des Rotors, übermäßige Vibrationen aufgrund von unausgewogenen Eismassen oder eine geringere Leistung der Turbine oder Eisdurchbruch. Diese Probleme können zur vollständigen Abschaltung der Turbinen und zu Energieverlusten führen. Daher setzen viele Hersteller heizungsbasierte Vereisungsschutztechniken ein, um Eisansatz zu vermeiden. Solche Systeme verbrauchen jedoch eine beträchtliche Menge an Energie.

Ziel dieser Doktorarbeit ist die Entwicklung neuer Codes innerhalb der Open-Source-CFD-Software zur Simulation des Phänomens der Eisbildung, das beim Betrieb von Windkraftanlagen in kalten Klimazonen auftritt. Diese entwickelten Tools sind in der Lage, das auf dem Rotorblatt gebildete grobe Eisprofil zu simulieren und die Luftströmung um diese Profile herum sowie den Energiebedarf für das Anti-Eis-System zu berechnen. Außerdem ermöglicht der neue Code die Simulation der Auswirkungen spezieller eisabweisender Beschichtungen, wenn diese auf der Schaufeloberfläche aufgebracht werden, und deren Auswirkung auf die insgesamt benötigte Anti-Icing-Wärme.

Um ein solches Phänomen zu simulieren, sollte der Solver in der Lage sein, die Luftströmung um den Blatt zu simulieren, um die Verfolgung der Wasserpartikel zu ermöglichen. Um übermäßige Berechnungskosten für die Auflösung komplexer Eisprofile zu vermeiden, können Wand-Randbedingungen oder raue Wandfunktionen verwendet werden, um die Auswirkungen der Rauheit auf die Luftströmung zu modellieren, ohne das Strömungsfeld vollständig aufzulösen. Dies geschieht durch die kompressible Strömungssimulation um die Blattabschnitte, um die Berechnung des Temperaturfeldes zu ermöglichen, das eine sehr wichtige Rolle im thermodynamischen Prozess der Eisakkretion spielt. Anschließend werden die von der Luft mitgeführten Wasserpartikel mit Hilfe der Lagrangeschen Partikelverfolgung gerechnet, um den genauen Ort und die Geschwindigkeit des Auftreffens der Partikel auf der festen Oberfläche zu berechnen. Nach diesem Aufprall wird ein mathematisches Modell angewandt, um das Verhalten dieser Partikel zu berechnen, ob sie an der Oberfläche anhaften bleiben oder wieder in den Luftstrom zurückprallen. Aus diesem Schritt können die Menge und die Wassermasse auf der Oberfläche bestimmt werden, und das thermodynamische Modell der Vereisung kann angewandt werden, um das endgültige Eisprofil auf der Oberfläche zu ermitteln.

Bei Anwendung dieses Verfahrens auf 2D-Profilen von Tragflächen zeigen die Ergebnisse des neuen OpenFOAM-Codes eine gute Übereinstimmung mit verschiedenen Experimenten aus der veröffentlichten Literatur und von Projektpartnern. Nach dem Nachweis seiner Fähigkeit,

die Eisbildung auf 2D-Schaufeln zu simulieren, wird derselbe Solver bei der Simulation eines rotierenden 3D-Windturbinenblattes unter Verwendung der Quasi-3D-Technik eingesetzt. Diese Technik wird dann mit anderen CFD-Codes verglichen, um sie zu validieren, und dann zur Simulation der Eisakkumulation an einem NREL 5MW-Windturbinenblatt als Beispiel für eine Multimegawatt-Windturbine verwendet. Außerdem wird ein Vergleich zwischen der erwarteten minimalen Anti-Icing-Wärme bei normalen und eisabweisenden Oberflächen durchgeführt, um die Machbarkeit der Verwendung solcher Beschichtungen in Windkraftanlagen zu untersuchen.

Die Ergebnisse zeigen, wie sehr der Eisansatz zu einem rauhen und nicht aerodynamischen Profil führen kann, was einen Eindruck von den harten Auswirkungen des Eisansatzes auf die Leistung von Windturbinen vermittelt. Die Ergebnisse zeigen auch, dass eisabweisende Beschichtungen machbar sind, wenn sie an der Vorderkante des Blattes in der Mitte und an der Spitze angebracht werden. Diese Bereiche sind am stärksten von der Eisbildung betroffen und erfordern die höchste Heizungsenergie. Zu diesem Thema müssen die verwendeten Modelle noch erheblich verbessert und die Auswirkungen der Eisprofile auf die Gesamtleistung, die erzeugte Leistung und die Gesamtlasten der Turbine genauer analysiert werden.

Nomenclature

Latin symbols

A	Area normal to the flow velocity
A_{cs}	Area of control surface
A_p	Projected area of roughness element
A_s	Area of roughness element projected in flow direction,
A_{wall}	Wall area
b_{eff}	Effective slip length
C_D	Drag coefficient of the particle
C_l	Lift coefficient
$C_{l,max}$	Max lift coefficient
C_p	Pressure coefficient
C_w	Specific heat of water
D_{AB}	Diffusion of material A in material B
e_{avg}	Average error
f	Area fraction of the solid interface
h	Convective heat transfer coefficient
H	Contact angle hysteresis
h_{conv}	Convective heat transfer coefficient
h_{ice}	Ice layer thickness
h_{mass}	Mass transfer coefficient
k_{rough}	Roughness
K_s	Equivalent sand roughness height
k_w	Turbulent kinetic energy at the wall
K_{avg}	Average roughness height
K_s	Equivalent sand roughness height
L	Surface roughness periodicity
L_{evap}	Latent heat of evaporation
L_F	Latent heat of fusion
L_{fusion}	Latent heat of fusion
M	Formed ice mass
m_{evap}	Evaporated mass
m_{imp}	impinging mass on the surface
m_{sep}	Separated mass
m_{splash}	Splashed mass

n_{cl}	Normal direction to liquid surface
Nu	Nusselt number
p_{evap}	Vapor recoil effect
p_{imp}	Pressure on the surface due to impinging mass
P_{sat}	Saturation pressure
p_{splash}	Pressure on the surface due to splashed mass
$P(d)$	Probability of particles with diameter d
Pr	Prandtl number
q	Specific internal energy
$Q_{anti-ice}$	Anti-icing heat
Q_{conv}	Energy transfer due to convection
$Q_{conv,low}$	Energy transfer due to convection with the lower film surface
$Q_{conv,up}$	Energy transfer due to convection with the upper film surface
Q_{evap}	Energy loss due to evaporated mass
Q_{ice}	Energy stored in ice mass
Q_{imp}	Energy of impinging droplets
Q_k	Kinetic heat of droplets
Q_{latent}	Latent heat gain due to fusion
Q_{rad}	Energy transfer due to radiation
Q_{sep}	Energy loss due to separated mass
Q_{splash}	Energy loss due to splashed mass
r	Radial location of a blade section
R	Total radius of the turbine
R_{pk}	Reduced peak height
R_{sm}	Profile element width
Re	Reynolds number
Re_L	Reynolds number with respect to surface distance
Re_p	Reynolds number relative to particle
Rnd	Random number
S	Energy source term
S_{energy}	The sum of energy source terms
S_{imp}	Momentum source due to impinging mass
S_{mass}	The sum of mass source terms
$S_{momentum}$	The sum of momentum source terms
$S_{splashing}$	Momentum source due to splashing mass
Sc	Schmidt number
Sh	Sherwood number

T_a	Air temperature
T_{air}	Air temperature
T_d	Droplet temperature
T_{film}	Film temperature
T_∞	Ambient temperature
T_w	Wall temperature
\tilde{T}	Difference between Ambient and surface temperatures
Δu	Velocity shift due to roughness
u_∞	Far-field air velocity
u_{evap}	evaporation velocity
u_f	Fluid velocity
u_p	Particle velocity
u_r	Relative air velocity
u_τ	Friction velocity
$v_{incident}$	Droplet incident velocity
v_∞	Far-field air velocity
$v_{rebound}$	Droplet rebound velocity
W	Specific humidity
w	Mass concentration
We	Weber number
$We_{average}$	Average Weber number
We_c	Critical Weber number
y^+	dimensionless wall distance

Greek symbols

α_{wall}	Water volume fraction at the wall
α_d	Dispersed phase volume fraction
α_i	Volumetric ration of species I
β	Collection efficiency
δ	Film thickness/Slip length
Δ_{cell}	Cell width
ε	Emissivity
Γ	Gamma function
γ_{LV}	Interfacial tension force for liquid-vapor interface
γ_{Sl}	Interfacial tension force for solid-liquid interface
γ_{SV}	Interfacial tension force for solid-vapor interface
λ	distribution slope parameter
μ_a	Dynamic viscosity of air
μ_l	Dynamic viscosity of liquid
ν	Kinematic viscosity
ν_t	Turbulent kinematic viscosity
$\tilde{\nu}$	Kinematic eddy viscosity
Ω	Rotational speed
ω_w	Turbulence specific rate of dissipation at the wall
ρ_i	Density of species i
ρ_p	Density of particles
σ	Volumetric ration of species I
σ_{rad}	Stefan-Boltzmann constant
τ_{air}	Shear stress exerted by air
τ_{cap}	Thermo-capillary force
τ_{wall}	Shear stress on the wall
τ_K	Kolmogorov time scale
τ_p	Particle response time
Θ_{adv}	Advancing contact angle
Θ_{CB}	Cassie-Baxter contact angle
Θ_{eff}	Effective contact angle
Θ_{eq}	Equivalent contact angle
Θ_{max}	Maximum contact angle
Θ_{rec}	Recessing contact angle

-
- Θ_o Contact angle on ordinary surface
 Θ_w Wenzel contact angle

Abbreviations

<i>ADIS</i>	Anti-icing and deicing systems
<i>AEP</i>	Annual Energy Production
<i>AoA</i>	Angle of attack
<i>BEM</i>	Blade element momentum
<i>CFD</i>	Computational fluid dynamics
<i>CSD</i>	Computational structural dynamics
<i>DRA</i>	Defense Research Agency
<i>EPT</i>	Eulerian particle tracking
<i>FSSP</i>	Forward Scattering Spectrometer Probe
<i>GRP</i>	Glass-fiber reinforced plastics
<i>GWEC</i>	The Global Wind Energy Council
<i>IPCC</i>	Intergovernmental Panel on Climate Change
<i>LBM</i>	Lattice-Boltzmann method
<i>LPT</i>	Lagrangian particle tracking
<i>LWC</i>	Liquid water content
<i>MRF</i>	Multiple reference frame
<i>MVD</i>	Median volumetric diameter
<i>NASA</i>	National Aeronautics and Space Administration
<i>NREL</i>	National renewable energy lab
<i>OAP</i>	Optical Array Probe
<i>ONERA</i>	The French Aerospace Lab
<i>PDE</i>	Partial differential equation
<i>PIV</i>	Particle Image Velocimetry
<i>PV</i>	Photo-voltaic
<i>RANS</i>	Reynold-averaged Navier-Stokes
<i>ROM</i>	Reduced order modeling
<i>SA</i>	Spalart-Almaras turbulence model
<i>SHS</i>	Superhydrophobic substrate
<i>SLD</i>	Supercooled large droplets
<i>SST</i>	Shear stress transport
<i>SWIM</i>	Shallow water icing model

Chapter 1

Introduction

1.1 Motivation

Over the last few decades, the world has witnessed accelerating changes in the global climate. The increasing temperatures of the atmosphere are thought to be the reason behind the increasing number of natural catastrophes the world witnessing these days. Many reports, like the Intergovernmental Panel on Climate Change (IPCC) report for 2021 [10], have linked the increasing wildfires, desertification, droughts, and even floods to the increase of the temperatures of our atmosphere. This global warming is caused by the increase of the percentage of the greenhouse that prevents the earth from releasing part of the thermal energy it receives from the sun. As a result, the governments have started to plan and apply swift actions and strategies to cut the use of fossil fuels that are responsible for most of the greenhouse gases that are emitted daily into our atmosphere. To cut the production and the consumption of fossil fuels, the world faced a global challenge, which is changing the sources of energy that we have been using in our daily life since the Industrial Revolution in the 18th century till now. This process is called the Energy Transition. This global Energy Transition necessitates using energy sources that involve less Carbon Dioxide emissions to slow down the increase of the global temperatures and to limit it to 1.5°C by 2050.

One of the cornerstones of this Energy Transition is the increase in using wind energy in supplying the world with its needs of electricity. Therefore, the global demand for wind energy witnessed a huge increase during the last two decades. In 2020, the global year-over-year growth of the installed wind power was estimated by 93 GW which represents 53% of the former year's installed power [11]. The Global Wind Energy Council (GWEC) expects this rate of increase in the newly installed capacity to, in the worst case, stay constant over the following five years. This increasing demand for wind energy resources motivates the governments and wind energy site developers to push the utilized wind energy resources to their limits. Therefore, wind sites in cold climate areas have gained more importance over the last few years because of their high wind potential and low population. It was estimated that wind sites in cold climates contributed with 127 GW in the global wind market in 2015, and this contribution is expected to grow [12].

1.2 Wind energy in cold climates and hazards

To benefit from all available wind resources, governments and wind developers tend to use all wind sites that have high power density. Some of the wind sites that have high power density are located in cold climate areas, where wind turbines are exposed to icing atmospheric conditions. For instance, some wind sites are located at high altitudes to benefit from the fact that wind speeds increase by 0.1% per 100m of altitude for the first kilometer from sea level [13]. These icing atmospheric conditions happen when the wind turbines are exposed to airflow with water particles at temperatures below 0°C. This means, when the water particles hit the surface, they will be frozen into solid ice which changes the aerodynamic profile of the blade. Ice formation (or sometimes called ice accretion) causes different problems for wind turbines and their operation including [14]:

- **Power loss:** this problem happens due to the change in the aerodynamic profile of the blade. At severe icing conditions, airfoil sections can suffer from ice accretion that takes different shapes like horn ice. This leads to an increase in drag force and a decrease in lift force. This power loss can reach up to 30% of the annual energy production (AEP) [12, 15]. This power loss will be studied in Sec. 6.3
- **Overproduction:** in the contrast to the aforementioned problem, the higher air density and the new ice profile can sometimes lead to an increase in the wind turbine power production [16].
- **Mechanical failure:** ice masses added to the turbine components can lead to mechanical failure of blades and tower. Also, like any other rotating machine, the turbine rotor can show unbalance due to uneven ice formation. This unbalance can lead to excessive vibrations and decrease the turbine lifetime due to higher fatigue loads [17].
- **Safety hazards:** the accreted ice masses on the wind turbine blades can separate from the blade during its rotation. This makes forms a hazard for all personnel and properties within the range of 1.5 times the combined hub height and the rotor diameter [18]. Accordingly, large wind turbines in this case cannot be located near housing areas, motorways, train lines, or even in wild areas.

All these problems necessitate tripping the turbine until it is assured that the blade surface is free from ice to resume the operation again. This can cause huge losses for the operator of the farm. To avoid all these problems, turbine manufacturers equip the blades with different equipment to prevent ice formation or at least to melt down the ice rapidly after its accretion on the blade surface to reduce the tripping time. This kind of equipment is called Anti-icing and deicing systems.

1.3 Anti-icing and deicing systems of wind turbine blades

Inspired from the aircraft wings and engine inlets, the wind turbine blades designed for operation in cold climates are equipped with anti-icing and deicing systems (ADIS). These two kinds of systems are used in wind turbine blades to mitigate the problems resulting from ice accretion

on the wind turbine blades. The Anti-icing system aims to prevent ice from the formation on the blade. This ensures continuous operation of the turbine and avoids the necessity of tripping the turbine to remove the ice. However, this usually requires a large amount of energy and very accurate sensors and controllers to predict ice formation. On the other hand, deicing systems are used to melt down the ice and remove off the blade surface. In some cases, such a system works after the tripping of the turbine. However, it needs less accuracy in prediction and usually less energy to operate. Both anti-icing and deicing systems can be divided into two categories: active and passive [14].

1.3.1 Active ADIS

This type of ADIS uses external energy to prevent or remove ice masses of the blade. Active ADIS has different techniques that are used or proposed to be used in the future for wind turbine blades. The main advantage of using such systems is their effectiveness. Using heat energy or any other technique with adequate rates can completely prevent the formation of ice on the blade or remove it rapidly. However, a major disadvantage of using such systems is that their energy consumption is very high compared to a ratio of annual energy production (AEP). Another disadvantage is the additional maintenance work that is necessary for these systems [19] and the complexity added to the design of the wind turbine parts. These techniques include:

Embedded electric heaters

This ADIS depends on applying an electric heating layer within the composite layers of the blade. After that, once these electric heaters are operated, a thin film of liquid water between the blade surface and the ice mass will form. This liquid film works on breaking the adhesion between ice mass and blade surface, which will lead to the detachment of the ice mass [20]. Despite the complexity of wiring and its maintenance, this system shows some good features that make it attractive for wind turbine manufacturers.

One advantage of using such an ADIS is that the electric heater layers can be located to cover certain areas of the blade, the leading edge, for example, to concentrate heating on the areas with the most ice formation. Another advantage is the simplicity of the idea that does not require any complicated systems for operation. On the other hand, there are quite a lot of disadvantages of using this system. One disadvantage is that if a heater in one location fails, this will cause an unbalanced ice formation on the rotor and hence sever vibrations during operation [21]. Another disadvantage of concentrating the heaters near the leading edge using the electric heaters is that the run-back water film freezes again once it touches the cold surface. This causes an interruption of the airflow downstream from the leading edge causing come aerodynamic penalties [22]. Also, this system requires some advanced lightning protection to avoid lightning attraction to the blade [23].

Warm air heating

This system is used to warm the surface of the blade by circulating hot air through the hollow parts. This hot air is generated by blowing the air using a blower through a heating radiator usually operated by an electric current. To increase the heating efficiency, the air flows through

the blade in a closed-circuit flow. This means that the air should be blown from one half of the blade and returned to the radiator again through the other half of the blade.

The main advantage of such a system is that the heating equipment is located at the blade root, which makes its maintenance easier compared to electric heaters ADIS mentioned earlier. Also, it consumes relatively lower energy [24] especially when it is used for de-icing [20]. This system also overcomes the problem of run-back water refreeze because the hot air flows through the whole blade and heats it entirely. However, using this ADIS has many drawbacks. One of them is the fact that the composite materials of which the blade is manufactured, Glass-fiber reinforced plastics (GRP) for instance, are good thermal insulators [14]. This means that the thermal energy is not well transferred to the surface of the blade. This also means that this system should operate early enough before the ice formation to prevent it. This needs very accurate sensors and advanced ice prediction techniques. Also, the source of heat in this system is located at the blade root while most of the anti-icing or deicing heat is required at the blade tips where [14]. This poor distribution of the thermal energy makes the efficiency of the system very low compared to the electric heaters ADIS.

Other active ADIS

Other than the aforementioned two techniques, many other active ADIS systems could be used in wind turbine blades to prevent ice formation or remove ice masses. One of these techniques is using microwaves to heat the blade surface and meltdown the ice [25]. Another technique is to use vibration pulses of the structure to crack the ice and shed it off the structure [26]. Both of these two techniques are not yet tested on large-scale wind turbines and still no reports on their advantages and disadvantages.

1.3.2 Passive ADIS

Unlike the active ADIS techniques, passive ADIS does not consume any external energy to prevent ice formation. However, these systems use the physical properties of the blade surface to slow down the ice formation and accelerate the deicing process. In general, this kind of ADIS is slower in its operation and sometimes not effective enough. However, the fact that they do not consume energy makes it attractive for many manufacturers[14]. That is why many researchers are considering passive ADIS in combination with one of the active thermal ADIS to provide a hybrid ADIS with low energy consumption.

Ice-phobic coatings

This type of coatings has many applications to prevent ice formation on different structures in cold climates like satellite dishes, PV cells, house roofs ... etc. This ice prevention happens due to the microscopic structures of such coatings that repel water droplets upon impingement on the surface and decrease the adhesion forces between the solid surface and the ice mass. The details about the physical phenomena behind the operation of these coatings will be discussed in Sec. 1.4. Currently, many researchers are trying to find adequate ice-phobic coatings to be applied on wind turbine blades to slowdown the icing process and help to reduce the anti-icing or deicing energy when it is used in a hybrid ADIS.

Like any other passive ADIS, ice-phobic coatings require no energy to reduce ice formation and less maintenance if the proper coating is used. However, once the coating is covered with ice, it becomes not effective since the micro-structured surface is covered with ice in this case and its effects cannot reach the impinging water droplets anymore [27]. Also, since this type of coating is micro-structured, it becomes sensitive to the different types of erosions like rain, hail, and sand erosions and also other particles like bugs and dirt. Once the coating is eroded or covered by other deposits, it becomes unable to repel water and ice particles anymore [18]. This means that the applied coating should be hard enough to withstand the presence of other particles in the atmosphere.

Black paints

By using black paints to cover the blade surface, the surface can absorb more solar radiation and accordingly increase temperature. The simplicity of the idea and the low cost of maintenance of this paint forms a major advantage. However, this technique will not properly function if there is not enough solar radiation or if the blade is fully covered with ice [19]. Accordingly, this technique is only suitable for cold climate areas with high solar intensities.

Chemicals

Chemicals can be applied to prevent icing on the surface by lowering the freezing point of liquid water. Despite this technique being widely used in airports to prevent icing on aircraft bodies before the take-off, this technique is a pollutant and requires a continuous supply of the anti-freeze liquid fed to the turbine [28].

1.4 Hydrophobic and ice-phobic coatings

Hydrophobic surfaces are one of the modern surface technologies that have an increasing interest due to their several applications. This kind of surface is characterized by its capability to repel water droplets and prevent them from pinning to it. The effect of promoting water droplets rolling is called the Lotus effect. This name comes from the observation of the Lotus leaves that roll small water droplets on its surface as a self-cleaning mechanism to clean the surface from small particles like dust. This phenomenon is now used in many metallic or textile surfaces to provide a non-wetting or self-cleaning surface in many applications like raincoats, PV cells, car surfaces...etc.

1.4.1 Surface tension and contact angle

To understand this phenomenon, one must first understand why do water droplets take a spherical shape in the air and why do they take a spherical sector shape when it touches a solid surface. All these phenomena can be understood through the understanding of adhesion and cohesion forces of liquid droplets. Cohesion forces are the intermolecular forces that bond liquid droplets together. These forces are the reason behind surface tension where liquid molecules on the free surface tend to attract the surrounding molecules. This surface tension phenomenon explains

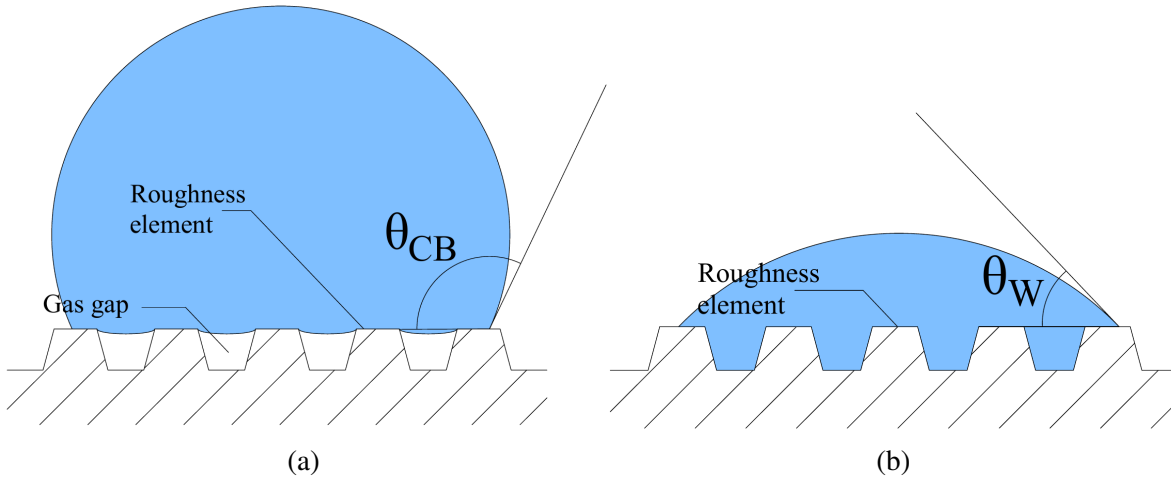


Figure 1.1: Comparison between a) Cassie-Baxter and b) Wenzel contact angles

why a liquid droplet takes a spherical shape when it is not affected by any surrounding forces. This spherical shape happens when each molecule in the liquid droplet is pulled equally from all directions to result in a net-zero force [29].

When a liquid droplet comes in contact with a solid surface, another force affects the droplet called the adhesion force. Adhesion force is the attraction force between liquid and solid surface molecules which makes the liquid stick to the solid surface. As mentioned earlier, the balance between adhesion and cohesion forces is responsible for the shape of the liquid droplet once it is pinned to the surface. Accordingly, the angle between the liquid droplet and the solid surface (called the equivalent contact angle θ_{eq}) can be calculated through the force balance between the molecules of the three substances namely: liquid droplet, solid surface, and the surrounding gas. Young [30] has calculated θ_{eq} using the equation:

$$\cos \theta_{eq} = \frac{\gamma_{sv} - \gamma_{sl}}{\gamma_{lv}} \quad (1.1)$$

where γ_{sv} , γ_{sl} , and γ_{lv} are the interfacial tension forces for solid-vapor, solid-liquid, and liquid-vapor interfaces. Additionally, if the liquid droplet is moving on the surface, two different contact angles appear in the droplet, namely advancing θ_{adv} and recessing θ_{rec} contact angles [31]. The difference between the two contact angles is called contact angle hysteresis (H).

1.4.2 Effects of surface roughness

The contact angle between a liquid droplet and solid surface does not depend only on the type of the liquid and the solid, it also depends on the surface roughness. According to this roughness, the liquid droplet can have one of two different wetting states: Cassie-Baxter state or Wenzel state. In Cassie-Baxter's case, the roughness elements height and the distances between roughness elements lead to partial contact between the liquid and the solid surface. This partial wetting leads to a higher contact angle due to the lower adhesion force between the liquid and the solid. In this case, the contact angle is calculated by [32]:

$$\cos \theta_{CB} = f \cos \theta_{eq} - (1 - f) \quad (1.2)$$

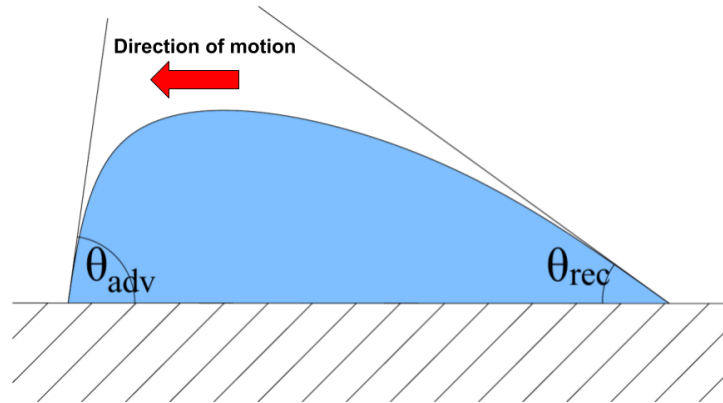


Figure 1.2: Roughness element geometrical parameters

where f is the area fraction of the solid surface with which the liquid is in contact. The value of f must be less than unity to achieve lower adhesion force and accordingly higher contact angle. On the other hand, when the roughness height is not high enough to carry the liquid away from the solid surface or the distances between roughness elements are too wide that the liquid surface is in contact with the solid, the Wenzel state happens. In this case, the contact angle is calculated using the relation [33]:

$$\cos \theta_w = r \cos \theta_{eq} \quad (1.3)$$

where r is the ratio between the total area of contact between liquid and solid and the flat area of the solid surface. The value of r must be higher than unity to achieve a higher adhesion force between the liquid and the solid surface.

1.4.3 Effects of surface roughness on impinging water droplets

In the case of impinging water droplets on a surface, the previously explained states become more complicated since new factors come into effect, which is the dynamic effects. To understand these dynamic effects, The mechanism of liquid droplet impingements should be clear in mind. When a liquid droplet hits a solid surface, the liquid is spread over the solid surface under the effect of its kinetic energy which is dissipated by the presence of adhesion force between liquid and solid and the cohesion force which tends to keep the liquid droplet in its spherical shape. This spread can also result in smaller water droplets splashing off the surface. Once the kinetic energy is dissipated, the cohesion forces tend to retract the droplet again towards the original point of impingement which generates kinetic energy again in the liquid. If the kinetic energy in the liquid is large enough to overcome the adhesion force completely, the water droplet will completely or partially bounce off the solid surface. On the other hand, If the adhesion force is high enough that it dissipates the kinetic energy in the spreading and retraction phase, the liquid will not have enough kinetic energy to jump off the surface again [34].

From the above brief introduction, it can be concluded that to ensure the minimum adhesion forces between liquid droplets and solid, the surface roughness of the solid should be designed

to have relatively high and narrow roughness elements. In the case of sub-cooled water droplets impingement and the presence of surface roughness that enables hydrophobicity, Liquid water droplets should, partially or completely, bounce off the surface. Another effect of this hydrophobicity is that it enables faster water runback on the surface [27], which means less anti-icing heat. Also, hydrophobic surfaces work on extending the freezing delay time[35], lowering heat transfer between the cold solid surface and the water film, decreasing adhesion force between solid ice and the blade surface[36].

1.5 Scope of thesis

From the previous overview on ice accretion on a wind turbine blade, it becomes necessary to simulate this process to help both industrial and academic research and development anticipate ice accretion and mitigate its negative consequences. Also, performing such simulations in an open-source simulation tool can have an advantage for this field of research since all researchers with different research interests can collaborate to an advanced, high fidelity, multi-physics simulation toolbox within the reach of most of the researchers all over the world.

This thesis discusses the development of ice accretion simulation modules within the OpenFOAM [37] framework to simulate the ice accretion process with its different aspects that include:

1. Simulation of flow field over iced, rough surfaces. This kind of simulation aims to understand the behavior of the airflow field when it passes over ice accretion and to simulate the aerodynamic penalties due to such roughnesses.
2. Simulation of water particles' transport with airflow over 2D airfoils and wind turbine blades to calculate the collected mass by the solid surface. This step is crucial to calculate the ice mass distribution over the surface, and hence the new ice profile.
3. Simulation of the thermodynamic process of ice formation on aerodynamic geometries like 2D airfoils or wind turbine blades after collecting the water mass. This involves different heat transfer modes between water film from one side and solid surface and ambient air from the other side.
4. Simulating the effects of using ice-phobic coatings on airfoils and blade surface.

1.6 Thesis outline

In chapter 2 in this thesis, a review of state-of-the-art research work is shown and a general conclusion and criticism are provided. Chapter 3 shows the scientific background on which this work was based and shows how the different equations are combined in the OpenFOAM framework to simulate the flow field around the rough ice surface and the ice accretion process. Chapter 4 compares different rough wall functions used in simulating the aerodynamic performance of rough, iced airfoils using experimental results and site collected ice profiles. After that, chapters 5 and 6 validate and analyze the simulation codes implemented in OpenFOAM

with experimental data and other high fidelity simulation results in 2D airfoil cases and 3D turbine blades respectively. Conclusions from the analysis of the different ice accretion methods and the resulting profiles are shown in chapter 7. Also in chapter 7, an outlook for some interesting points that were not discussed in this thesis is provided as possible research topics for other researchers.

Chapter 2

Literature Review

2.1 Introduction

In the early 1950's, the interest in studying the ice accretion on structures exposed to icing conditions has grown rapidly. This growth was due to a number of aircraft accidents that happened because of ice formation on either aircraft wings or engine parts. Since then, the investigation of ice formation phenomenon and its aerodynamic and thermodynamic aspects have been investigated. As the importance of wind energy has grown in the last decades, the ice accretion models are being adapted to wind turbines and its special operation characteristics. The following sections tries to investigate the state-of-the-art research work in this area. First, the numerical models dedicated to simulate rough ice surfaces are presented. This includes fully resolved and modeled roughness simulations with its consequences. After that, previous work on different water particle tracking techniques are introduced to find the advantages and disadvantages of each technique. The different thermodynamic models simulating the water film freezing process are shown with their results. Then, the research work involving the effects of using ice-phobic coatings and the behavior of water droplets and water film is shown. In the end, a general conclusion and critic to this previous work is presented trying to find the research gap in this topic as a starting point for the research work shown in this thesis.

2.2 Simulation of flow over iced surfaces

One of the most challenging type of problems in the field of CFD of the simulation of rough surfaces. This challenge comes from the fact that there is no computational turbulence model, until now, able to accurately predicts the behavior of the flow during detachment and reattachment. During the flow of any fluid over a rough surface, the flow suffers from multiple detachment and reattachment points. Accordingly, it is very hard to accurately simulate such cases. However, a lot of work was done to simulate rough surface cases, especially with ice accumulation. The literature in this area are divided into two methods: either to fully resolve roughness elements, even if it was very fine, or to use a coarse computational grid and model the effect of roughness on boundary layer.

2.2.1 Fully Resolved Roughness

From computational point of view, it is known that to correctly model the viscous sub-layer in CFD methods, the height of the grid's first cell should fulfill the dimensionless first cell height criteria of $y^+ \leq 1$. Additionally, to avoid high aspect ratio cells, large number of cells over the surface should be generated. Accordingly, one method to simulate rough surfaces is to generate a fine grid that fits the rough surface.

Shih [38] used over-set grids to generate the computational grid technique to generate grid for the complex ice shapes near the leading edge. Zhu et al. [39] studied the convergence rates of CFD simulations of the iced NLF0414 airfoil and compared the convergence of single-block vs multi-block structured grid. In both cases, a rough ice profile with two horns on its leading edge was simulated using $k-\omega$ SST turbulence model. They have concluded that both techniques shown the same convergence time. Also the same research group numerically simulated NLF-0414 with both rime and glaze (horn) ice profiles [40, 41]. In these two papers, Spalart-Allmaras (SA), the standard $k-\epsilon$, and v^2-f turbulence models with fine computational grid were compared to conclude that Spalart-Allmaras turbulence model provided the best results in both cases. Chi et al. [42, 43] also analyzed the flow field for iced GLC-305 airfoil and Q3D wing in both rime and glaze ice cases using fine meshes in FLUENT-UNS CFD solver. They have found that using such an approach resulted in satisfactory results in both 2D and 3D cases.

Li et al. [44] simulated the flow over iced GLC-305 airfoil using Lattice-Boltzman Method (LBM) with replacing the molecular relaxation time scale with a different effective relaxation time derived from systematic renormalization group. They have found that using such an approach led to good agreement for surface pressure coefficient and accordingly for the airfoil's lift and drag coefficients. Cao et al. [45] used hybrid multi-block grid technique to generate computational mesh over complex ice profile while Shim et al. [46] studied the usage of over-set grid. Marongiu et al. [47] Applied CFD techniques with fine computational grid to be used with Reynolds averaged Navier-Stokes (RANS) $k-\omega$ SST model using an in-house code to analyze the NLF-0414 iced airfoil. Jun et al. [48] compared experimental and computational results of lift and pressure coefficients of ice profiles over NACA23012 airfoil using fine mesh. The presented technique showed good agreement between the two types of results at low AoA. Pendenza et al. [49] aimed to provide a robust approach to provide mesh deformation to be applied to icing simulations to decrease the need for re-meshing.

It can be concluded from the previously mentioned work that very fine computational grids and complex meshing techniques, over-set grid for instance, must be used to fit the irregular shape of ice with the adequate grid. This resulted in the requirement of high computational cost to simulate the flow, due to fine grids, or special solvers to cope with the special computation grid, like what happens in case of using over-set grids.

2.2.2 Rough Wall Functions (rwf)

The other approach to simulate the effect of roughness was to model what happens near the wall due to roughness. Since the 1930s, several experiments were conducted to investigate the effect of roughness on flow-field over rough surfaces. Nikuradse [50] investigated turbulent flow in rough pipes with different relative roughness values in pipes with Reynolds numbers between 10^4 to 10^6 . He concluded that the boundary layer follows the log-law as in the case

of smooth surface. However, in case of rough surface, there is a clear velocity shift (Δu). A few years later, Schlichting [51] studied the internal flow of a square-section channel with one rough wall with spherical segments, cones and angular shaped roughness elements. He found that the velocity shift depends on four different geometrical parameters of roughness elements, namely: element's height, the area projected on the surface, area projected in flow direction and the average distance between elements. Accordingly, he derived an equation to calculate the friction coefficient on the plate surface.

Chen and Patel [52] introduced a new two-layer model and a wall function in the k- ϵ model to simulate rough surfaces. Hellsten and Laine [53] provided a new extension for the k- ω -SST turbulence model to simulate the flow field, Wilcox [54] provided a correction model for ω value near the wall such that:

$$\omega_w = \frac{u_\tau^2 S_R}{\nu} \quad (2.1)$$

$$\Delta S_R = \begin{cases} \left(\frac{50}{k_s^+}\right)^2 & : K_s^+ \leq 25 \\ \frac{100}{k_s^+} & : 25 < K_s^+ \leq 2000 \end{cases} \quad (2.2)$$

Also, George et al. [55] modeled the roughness effects on turbulent boundary layer using the elliptic relaxation method to modify the $\tilde{\nu}^2$ - f turbulence model. The results of the simulations were compared to Laser-Dopler Velocimetry (LDV) for various roughnesses. Aupoix and Spalart [56] compared two different extension to the Spalart-Allmaras turbulence model to adapt to the presence of roughness. The first extension, that was named Boing extension [57], provided a link between turbulent eddy viscosity ν_t and the transported variable $\tilde{\nu}$ by the equation:

$$\nu_t = f_{v1} \tilde{\nu} \quad (2.3)$$

$$f_{v1} = \frac{\chi^3}{\chi^3 + c_{v1}^3} \quad (2.4)$$

$$\chi = \frac{\tilde{\nu}}{\nu} + c_{R1} \frac{k_s}{d_o} \quad (2.5)$$

where $d_o \approx 0.03k_s$ and $c_{R1} = 0.5$.

The second extension is ONERA extension. It provides a wall value of $\tilde{\nu}$ as:

$$\begin{aligned} \tilde{\nu}_w^+ = & (0.377 \ln k_s^+ - 0.447) \exp\left(\frac{-k_s^+}{70}\right) + 1.257 \times 10^{-2} k_s^+ [1 - \exp\left(\frac{-k_s^+}{70}\right)] \\ & + \max\left(0, \frac{k_s^+}{10}\right) \min\left(1, 1.36 \exp\left(\frac{-k_s^+}{250}\right), 25 \exp\left(\frac{-k_s^+}{100}\right)\right) \end{aligned} \quad (2.6)$$

Then, the authors compared the results of the two models with the experimental results of Blanchard [58], Acharaya et al. [59], and Hosni et al. [60, 61]. Both extensions showed good agreement with most of the experimental results.

To take the effect of velocity shift into consideration, the turbulence models or the wall boundary conditions models should be modified in a way that the behavior of flow over rough surfaces is grasped without the need for a fine grid. The challenge in this approach lies in modeling such phenomena in the proper mathematical model. Most of the researchers built their mathematical

models on the results of the aforementioned experiments. Knopp et al. [62] followed the ideas of Aupoix and Spalart in adding the velocity shift effect to the wall function. However, instead of applying the shift on turbulent viscosity as in [56], they used their procedure to adapt k and ω turbulence parameters. The new k and ω rwf states that

$$\omega|_w = \min\left(\frac{u_\tau}{\beta_k^{0.5} \kappa \tilde{d}_o}, \frac{6\nu}{\beta_{\omega y}(1)^2}\right) \quad (2.7)$$

$$\tilde{d}_o = 0.033 \phi_{r_2} k_s \quad (2.8)$$

$$\phi_{r_2} = \min\left(1, \frac{k_s^{+2/3}}{30}\right) \min\left(1, \frac{k_s^{+1/4}}{45}\right) \min\left(1, \frac{k_s^{+1/4}}{60}\right) \quad (2.9)$$

$$k|_w = \phi_{r_2} k_{rough} \quad (2.10)$$

$$k_{rough} = \frac{u_\tau}{\beta_k^{0.5}}, \phi_{r_2} = \min\left(1, \frac{k_s^+}{90}\right) \quad (2.11)$$

Where $\beta_k = 0.09, \kappa = 0.41, \beta_w = 0.075$. This rwf deals with modifying k and ω values near the wall. Hence, this rwf is used with k - ω SST turbulence model. The new rwf showed good agreement with validation case of Ligrani and Moffat [63], Nikuradse [50], and Hosni et al. However, this extension showed fair agreement with rough NACA 65₂215 airfoil done by Abbott and von Doenhoff [64] and Ljungström [65]. Later, Lee [66] modified the $\omega|_w$ in this model to be:

$$\omega|_w = \min\left(\frac{u_\tau \ln\left[\frac{n_p + \tilde{d}_o}{\tilde{d}_o}\right]}{\beta_k^{0.5} \kappa \tilde{d}_o}, \frac{6\nu}{\beta_{\omega y}(1)^2}\right) \quad (2.12)$$

He proved that this modification improved the prediction of open channel flow simulations. Chedevergne and Aupoix [67] applied the approach used by Suga et al. [68] in adapting k and ω turbulence parameters to rough surfaces and fitted the resulting formula to Colebrook's experimental data. This resulted in:

$$\omega|_w = \left(\frac{300}{k_s^+} \left(\tanh \frac{15}{4k_s^+}\right)^{-1} + \frac{191}{k_s^+} \left[1 - \exp\left(-\frac{k_s^+}{250}\right)\right]\right) \quad (2.13)$$

$$k|_w = \max\left(0, \frac{1}{\sqrt{\beta^*}} \tanh\left[\left(\frac{\ln \frac{k_s^+}{90}}{\ln 10} + 1 - \tanh \frac{k_s^+}{125}\right) \tanh \frac{k_s^+}{125}\right]\right) \quad (2.14)$$

This rwf is also used with k - ω SST turbulence model.

Recently, da Silva et al. [69] applied a new v_t wall function base on the work of Suga et al. [68]. This wall function will be provided in details in Section 3.3.4

2.3 Water Particle Tracking

After simulating the flow field over rough surfaces, comes the next step towards simulating the ice accretion. This step aims to track water particles from the far field region until hitting the surface of the body. To reach this aim, there are two approaches used, either Lagrangian or Eulerian Particle tracking.

2.3.1 Lagrangian Particle Tracking (LPT)

One of the first and most reputable software in using LPT in the simulation of ice accretion is NASA LEWICE. LEWICE [70] and its newer version [71] are aerodynamic icing software that are based on Messinger's model, will be explained later in Section 2.4.1, by using Lagrangian particle tracking to calculate the impinging mass. Also the same cases were simulated using numerical simulations. Bragg et al. [72] tested ice accretion on NACA23012 airfoil at different Temperatures, LWC, and AoA in order to classify the ice accretion shapes into four different categories: roughness, horn, streamwise and spanwise ridge. They also simulated the same profile at the same conditions using both LEWICE software and CFD techniques. However, this research was dedicated to 2D airfoil and it did not take into consideration the 3D effects and the consequences of using LPT with large number of droplets.

For 3D simulations, Fujiwara and Bragg [73] simulated CRM65 aircraft [74] and compared their results with experimental results at different wing section obtained by Fujiwara et al. [75] at NASA Glenn icing wind tunnel. Also, the authors compared the simulation results with results from LEWICE3D software. Recently, Fujiwara et al. [76] has compared the 3D ice simulation results from LEWICE3D software with experimental results of CRM65 swept-wing model. They have found that the numerical simulations were only capable of generating smooth 2D ice profiles with fair agreement with experimental results.

Besides LEWICE and FENSAP-ICE, many other research institutes have created their in-house ice accretion simulation codes that use LPT like ICECREMO code [77] and the code developed by Özgen and Cambek [78, 79].

Yirtici et al. [79] coupled the Blade Element Momentum Theory (BEMT) with ice accretion simulations to calculate the turbine performance under ice accretion conditions and accordingly calculated the Annual Energy Production (AEP) the Aeolos 30 kW wind turbine. They have concluded that ice accretion can cause 24% drop in power generation. Since they have used BEMT to simulate the iced rotor, the effect of centrifugal force on the profile of ice accretion was not taken into consideration. This approximation leads to underestimation of ice masses near the tip of the blade.

Yirtici et al. [80] has simulated the power production drop due to ice formation also on Aeolos-H 30kW wind turbine blade using a combination of BEM and airfoil simulation codes like XFOIL and SU2. In this work, it was found that the overall performance losses due to ice accretion of about 20% when compared to experimental results which was within the expected range. Despite providing a computationally efficient approach to simulate such cases, the effects of the centrifugal force due to blade rotation was not included in the simulations despite having significant effects in this case as shown in Wang and Zhu [81] that will be discussed in the next section.

2.3.2 Eulerian Particle Tracking (EPT)

The other alternative to the Lagrangian approach to track particles is the Eulerian approach where the volume fraction is simulated as a continuous field. More details on this approach is provided in Sec. 3.4.2. Sznajder [82] presented numerical simulation of determination of collection efficiency on NACA23012 airfoil using Eulerian approach. Also, the effect of AoA of the airfoil was studied by simulation of the same airfoil at different AoA's ranging between

2.5°-11°. In this paper, water droplets are only influenced by drag, gravity and buoyancy forces as momentum sources. In this work, two simulation cases were conducted: the first with $LWC = 1.89 \text{ g/m}^3$ and $MVD = 236 \text{ }\mu\text{m}$ and the second one with $LWC = 0.19 \text{ g/m}^3$ and $MVD = 20 \text{ }\mu\text{m}$. Both cases at $AoA = 2.5^\circ$. The results of the simulations were compared to experimental results. Presented simulations showed good agreement with experimental results for the second case. However, an interesting conclusion was highlighted in this paper that for the first case, with relatively high MVD and LWC value, the collection efficiency was overestimated due to not including the effect of water droplets splash on the surface which is expected to make the results more accurate. Despite studying the effect of the droplet size and AoA on the collection efficiency, the study should have been exceeded to include more droplet sizes and flow velocities.

Hospers and Hoeijmakers [83] studied the collection efficiency of the same two cases presented in [82]. However, in this work, the authors took into consideration the splashing effect by dividing the impinging mass to different droplet sizes by dividing the droplet sizes into 10 bins for the first case and 27 bins for the second case. Then, the authors used the calculated collection efficiency to simulate ice accretion on single element airfoil at $T = 268.15^\circ\text{K}$. They also reached the same conclusion that for high MVD values, the collection efficiency is over predicted. However, after accounting for splashing effect, the results were improved but still not agreeing very well with experiments.

Kim et al. [84] used an in-house CFD and Eulerian droplet solver to simulate collection efficiencies for NACA0012 airfoil, MS317 airfoil, and oscillating SC2110 airfoil. After that they compared their results with the results from the Lagrangian solver and the standard industry analysis software LEWICE. The solver presented resulted in good agreement with the Lagrangian solver and LEWICE software. Despite providing better results than Hospers and Hoeijmakers [83], this work simulated NACA0012 airfoil which is a relatively simple, 2D geometry. Accordingly, the study did not provide any details about such an approach for complicated geometry.

Also, Bilodeau et al. [85] simulated collection efficiency of water supercooled large droplets (SLD) and the accompanying phenomena splash and bouncing on NACA23012 and MS(1)-0317 airfoils using the Eulerian approach. In this work, the simulation of the effect of water droplets' splashing and bouncing was simulated by adding the re-injection of the reflected water mass back to the air flow field to undergo further tracking. The authors found that the splash effect on simple geometries is not negligible and can increase the local collection efficiency up to 50%. They have also concluded that the accumulation of such reflected droplets downstream of the airfoil can form a threat to aircrafts since it can freeze downstream and add more penalties to the aerodynamic performance of the airfoil.

To illustrate the differences between the two approaches, LPT and EPT, to be used, da Silveira et al. [86] provided a comparison between Eulerian and Lagrangian approaches in determination of collection efficiency. Both particle tracking approaches were used to simulate collection efficiency on NACA0012 airfoil at $LWC = 0.78 \text{ gm/m}^3$ and a cylinder at $LWC = 0.55 \text{ gm/m}^3$ for comparison. It was shown that the Lagrangian approach is more suitable to simulate simple 2D cases, 2D single-element airfoils for instance. However, The Eulerian approach showed better effectiveness in case of complex 3D geometries.

Chang et al. [87] provided rime and glaze ice accretion analysis GLC-305 wing using Eulerian approach for particle tracking, classical Messenger icing model and k- ϵ turbulence model simulated in ANSYS Fluent commercial software. The simulations provided relatively good

agreement with experiments and LEWICE software but they did not provide any details about the computational time needed for this case.

Fu and Farzaneh [88] used the Eulerian approach to simulate rime ice accretion on NREL phase VI wind turbine blades at different air wind and rotational speeds. In this work, The NREL VI wind turbine rotor was simulated at wind speeds of 7, 10, and 13 m/s at 5, 7.5 and 10 rad/s rotational speeds under $LWC = 1 \text{ g/m}^3$, $MVD = 20 \text{ }\mu\text{m}$, and $T_\infty = 10^\circ \text{ C}$. From these simulations, the authors concluded that the rotational speed of the rotor has the biggest impact on ice accretion. Accordingly, the highest ration of ice accumulation occurs near the tip of the blade due to high linear speed and due to centrifugal force and Coriolis forces that drives the liquid water film towards the tip. Also the have found some formed ice near the trailing edge of the blade due to separation bubbles that carries out some water droplets and trough it back again near the trailing edge. This study did not provide a validation of CFD results with any wind tunnel experiments.

Hu et al. [89] presented simulation results of rime ice accretion on the NREL Phase VI blade at only one ambient condition. In this work, the authors validated the results of their simulations with the results of Eulerian ice simulations of the S809 airfoil done by Kim et al. [84]. After that, ANSYS Fluent was used to simulate ice accretion. The authors concluded that ice mainly forms on the blade leading edge and increase in thickness with the increase of radius. Accordingly, power mainly degenerates at the outer blade. Despite providing a valuable 3D simulations of wind turbine blades, the 3D results were not compared with any other results.

Recently, Son and Kim [8] developed a 3D icing simulation code within OpenFOAM framework to simulate icing on wind turbine blades. The authors performed simulations of the NREL Phase VI wind turbine under different wind velocities, rotation velocities, and temperatures using their code. The results of this code were compared to other results published by Hu et al. [89] and Reid et al. [9] using FENSAP-ICE. From the comparison, They have found that the new code tends to underestimate the ice mass on the pressure side in case of glaze ice. Despite providing good results in case of rime ice, the computational cost of using LPT in simulating the whole rotor of the NREL Phase VI wind turbine is not indicated in this paper. The computational cost is expected to be very high in this case. Despite providing good concepts of simulation using OpenFOAM, the computational power used in this case was not mentioned in the published work to be compared with other methods. Also, this article assumes that the effect of the centrifugal force is negligible which contradicts with what shown by Hu et al. [89]. Which indicates that this point need more investigation.

From the research work introduced in this, it can be seen that main purpose of using the Eulerian approach to simulate ice accretion is to simulate large structures. Regardless the icing model used to simulate the thermodynamic process of ice formation, the Eulerian approach managed to simulate the ice formation using less computational effort that the Lagrangian approach. However, it should be expected that this will provide less accurate results.

2.4 Thermodynamic models of Ice Accretion

The calculation of the new iced profile results from the calculation of how much of the impinging mass is converted into ice. This frozen fraction is calculated using different thermodynamic models which are trying to simulate mass, momentum and energy conservation during the icing

process.

2.4.1 Messinger's model and its modifications

Messinger [90] published one of the first icing simulation models after the repeating flight accidents due to ice formation on aircraft's body and wings. In this model, convective, evaporative, latent heat and friction heat transfer to the water film were investigated under two different conditions, namely $T = 273.15^\circ$ and $T < 273.15^\circ$. Then, these energy values were applied to energy conservation equation to calculate the frozen fraction in the form. This resulted in relatively accurate simulations of ice shapes.

$$\dot{Q}_c + \dot{Q}_e + \dot{Q}_d = \dot{Q}_k + \dot{Q}_l \quad (2.15)$$

where convective heat transfer $\dot{Q}_{conv} = h(T_w - T_a)$, evaporative heat transfer $\dot{Q}_{evap} = W(P_{sat@T_w} - P_{sat@T_a})$, heat from impinging mass $\dot{Q}_{imp} = \beta \cdot LWC \cdot v_\infty \cdot C_w(T_w - T_d)$, kinetic energy of droplets $\dot{Q}_k = \beta \cdot LWC \cdot v_\infty \cdot (v_d^2/2)$, and the latent heat $\dot{Q}_{latent} = \rho \cdot L_F(\partial h_{ice}/\partial t)$.

However, there were some assumptions that were modified in the Extended Messinger Model proposed by Meyers [91–93] to improve the model and the temperature profile through the formed ice using ordinary differential equation. Accordingly, a more accurate simulation of ice and water film thickness were simulated, especially in glaze ice case. Ozgen [78] applied this extension to simulate ice accretion on multi-element airfoils using multi-step approach. In this study, the authors concluded that a multi-step approach yields more accurate result than a single-step one.

For wind turbine blades, Ali and Lakshimi [94] used the extended Messinger model to simulate the ice accretion on NREL Phase VI wind turbine blade at different pitch angles. The authors has used BEMT to find that AoA's and relative velocities of each blade section, then the collection efficiency was calculated using the flow-field resulting from a panel-method code. After that, the authors used extended Messinger model on each of the blade sections to calculate the ice shapes and to find the change in lift and drag coefficients. Then, BEMT was used once again to find the performance loss due to ice formation. The authors concluded that the biggest ice accretion mass, and hence the biggest drop in turbine performance, was found to occur on the top sections. Also, they have found that the loss of power generation ranges from 10% to 50% and it was increasing with the increase of pitch angle. This work has provided a computationally efficient approach to simulate the wind turbine performance. However, the centrifugal force affecting of the water film was not taken into consideration in this case.

2.4.2 Shallow Water Icing Model (SWIM)

Bourgault et al. [95] introduced a thermodynamic ice accretion model based in the shallow water assumptions and solves PDE's of water film to predict ice profile. This model is explained in details in Section 3.5.2. Lavoie et al. [96] provided a comprehensive comparison between Messinger's model and its derivatives and SWIM model. In this paper, the authors showed the main differences between the four models and applied the models on two different icing cases on NACA0012 airfoil for both glaze and rime ice conditions. The simulations concluded to that the four applied models where close in results. However, more addition of physical phenomena, such as gravity, water shedding and surface tension models, should be taken into consideration.

Pourbagian and Habashi [97] used SWIM model to optimize Electro-thermal ice protection cycles of NACA-0012 airfoil using reduced-order modeling (ROM) to avoid high computational cost in this simulation case. Also, the used geometry was simple and it would have been more interesting if a more complex geometry, aircraft wing for instance, was studied.

Kelly et al. [98] used the same method to simulate icing effect on Helicopter rotor by applying heat transfer and film motion due to centrifugal force. The final results were compared with experimental results. The authors noticed fair agreement between simulations and experiments in hover and forward flight cases. Also, the simulations under-predicted the performance degradation of the rotor after ice formation, especially in thrust degradation in forward flight.

Switchenko et al. [99] Used the SWIM model along with Eulerian solver to simulate ice accretion on WindPACT 1.5MW wind turbine using weather event from collected data at a wind farm in Québec, Canada. In this work, the authors compared the results from both 2D and 3D solvers of ice accretion. Then, they have applied the 17-hour data collected from site in the form of 30-minute time steps. Each time step had a certain wind velocity, ambient temperature and LWC. After that, the icing event time was simulated and the generated power from the turbine was plotted vs time. They conclude that the aforementioned approach provided a generated power from simulation comparable to what was measured from site. However, they have tried many different MVD values since there was no measurements for these values on site. Despite applying a very interesting approach, the authors did not provide a real solution for the problem of using different MVD values. This problem could be avoided by using some meteorological models that can give a rough estimate of the droplets' sizes.

Also, Yassin et al. [100] coupled CFD solver using SWIM model with CSD solver to simulate the torque degradation on helicopter rotor. The simulation results were compared with experimental ones. The study offers a simulation method for performance degradation due to icing using a loosely coupled CFD-CSD method to be used in early design stages of the rotors. However a more advance method should be used to fully understand the effects of icing.

Wang and Zhu [81] applied Eulerian particle tracking to simulate ice accretion on NREL Phase VI wind turbine blade using ANSYS Fluent and ice accretion model applied as user defined function. In this work, only one blade was included in this simulation process and the effect of rotation was taken into consideration using multiple reference frame (MRF) model. In the beginning, the solver was validated with experimental ice profile of a rotating cylinder. After showing good agreement with validation case, the solver was used to simulate the NREL Phase VI turbine. They concluded that the centrifugal force plays a very important role in accurate simulation of ice on any rotating structure, wind turbine rotor for instance. Also, they concluded that the most affected area with ice formation is the leading edge and the stagnation point. The provided approach to simulate the effect of centrifugal force is not clear and can only be applied in simple calculation methods, like Messinger's model. However, a more suitable form of centrifugal force should be applied, if transient ice accretion shall be used in simulations. On the other hand, the centrifugal force effect in this paper was only shown at 190 rpm, which is not realistic for wind turbine blades.

2.4.3 Makonnen's model

Makkonen [101] presented a numerical model to calculate the icing rates on structures. This model reads as:

$$\frac{dM}{dt} = \alpha_1 \alpha_2 \alpha_3 w v A \quad (2.16)$$

where w is the mass concentration, v is flow velocity, A is area normal to the flow velocity. Also, α_1 , α_2 , and α_3 represents collision, sticking and accretion efficiencies respectively. The aforementioned model was applied in TURBICE ice accretion simulation software and Marjaniemi et al. [102].

Hudecz et al. [103] simulated ice accretion on NACA64-618 airfoil at AoA = 7° experimentally in icing wind tunnel and numerically using TURBICE software. In this work, three different ice cases were simulated: glaze ice at T = -3° C, mixed ice at T = -5° C and rime ice at T = -8° C. All three cases were simulated at AoA = 7°, MVD = 25 μm, and LWC = 0.7 g/m³. The authors concluded that mixed ice case caused the maximum lift force deterioration between the three cases. Also, they noticed the rime ice case produced a streamlined ice accretion profile. The ice profiles resulting from TURBICE showed fair agreement with experimental results.

Makkonen et al. [22] presented also a specific numerical model to simulate ice accretion on wind turbine blades. Also, they have presented a numerical model to simulate anti-icing heating system.

Homola [104] provided a numerical study of flow-field at 85% of 5MW wind turbine blade section taking the profile of NACA64618 airfoil using TURBICE software. They have found that glaze ice case results in the biggest drop in lift force due to its non-streamlined ice profile. Also, Virk et al. [105] studied the effect of ice accretion on different airfoils of four different wind turbine sizes, namely: 450kW, 600kW, 1MW, and 2MW. The effect of ice formation on velocity field, turbulence intensity near the leading edge of the airfoil, and coefficients of lift, drag, and moment was studied in this work. The authors concluded that the rime ice has more effect on larger wind turbines than on smaller ones due to higher effect of ice on coefficient of moment on larger airfoils.

Virk et al. [106] has simulated the icing process of NREL 5MW wind turbine blade at different atmospheric temperatures ranging between -15° and -2.5°. From this study, they managed to analyze the ice accretion profiles and thicknesses on five different sections at radial positions ranging between 20% and 100% of the total blade length. By studying each of the five sections using 2D CFD techniques to calculate the collection efficiencies and ice profiles on these sections. The authors concluded that tip sections has showed higher thicknesses of ice relative to its chord lengths due to its high speed, and higher collection efficiencies as a result, and also due to its smaller chord lengths. Accordingly, the authors concluded that the geometrical parameters of the blade, like chord lengths and thicknesses, has a major effect on the ice profile and thickness. This work provided a good analysis of the resulting final ice profile. However, it did not show any of the important 3D effects, centrifugal forces for instance, on the ice profile. These results contradicts with what mentioned in the conclusion that the work was done using 3D CFD based numerical simulations.

Li and Jiang [107] studied the change of collection efficiency, and accordingly the ice profile, on a 300kW wind turbine blade at different inlet velocities, MVD, and LWC values. They have noticed that with the increase of wind velocity, LWC, and MVD to a certain limit, the ice thickness is directly proportional to these values. Also, they have found that LWC value had

the biggest influence among the three parameters. This paper did not present the effect of the aforementioned parameters on the whole blade.

2.5 Wind tunnel ice accretion simulations

To validate any ice accretion software, it should be validated with wind tunnel experiments that were conducted for this reason. Fortunately, there are plenty of such wind tunnel experiments published from different sources. Wright et al. [2] collected different ice profiles resulting from the collaboration project between NASA, ONERA, and DRA and compared the results with three different numerical software of the three parties. In this report, 14 different ice shapes resulting from different wind tunnel simulations at different flow velocity, temperature, AoA, LWC, and MVD values were reported. This Work is considered the main source of wind tunnel results for the validation of most ice simulation software. Addy et al. [108] studied the change in lift, drag and moment coefficients due to ice accretion by testing GLC-305 airfoil with molded ice shapes on the leading edge. The ice formation conditions applied in this work were for $LWC = 0.4 \text{ g/m}^3$ and 0.54 g/m^3 at $AoA = 4^\circ$ and 6° . The wind tunnel tests of molded ice shapes were conducted at $Re = 3 \times 10^6$ and 10.5×10^6 . The experiment concluded that a two-minute glaze ice accretion resulted in reducing the maximum lift coefficient $C_{l,max}$ by 22% while the 22.5-minute glaze ice accretion led to 48% of $C_{l,max}$. Also, Krogenes et al. [109] applied wind tunnel measurements of NREL S826 with different molded ice shapes representing rime, glaze and mixed ice. They concluded that for rime and glaze ice shapes, the lift was reduced by 10% while drag increased by 80%. However, in case of mixed ice, the lift was reduced by 30%, drag increased by 340% and stall AoA was reached at 5° due to the presence of two horns of ice on the leading edge.

Han et al. [110] presented ice accretion test of a test rig that is similar to NREL Phase VI wind turbine rotor. The experimentally obtained ice shapes at different LWC and AoA values are compared to results from LEWICE software. For rime ice cases, the authors have found that LEWICE managed to simulate the rime ice cases with good agreement to the experimental results. They also noticed that the effect of the AoA was low between $AoA = 2^\circ - 4^\circ$ and high for operating AoA's which ranges between $4^\circ - 8^\circ$. For glaze ice cases, they have found that the most effective parameters were ambient temperature and LWC.

Gao et al. [111] experimentally studied the performance degradation of wind turbine model blade in research wind tunnel. In this work, they have found using PIV measurements that the flow-field over the airfoil was heavily disturbed due to the presence of ice. Accordingly, they have found that after 600 seconds of the experiment of the airfoil at $AoA = 5^\circ$, the lift force becomes 12% of its original value while the drag force becomes 450% of its original value.

2.6 Ice-phobic coatings applications

After the huge development in manufacturing of coatings, like nano-structured coatings for instance, a lot of effort was focused in using their properties in the field of aerodynamics in general. In this part, a brief overview of the efforts of scientist to apply these properties to mitigate ice formation is shown.

First, to understand the effects of ice-phobic coatings on water particles and film formation, Huang et al. [112] surveyed different state-of-art ice-phobic coatings, their properties, and how they are manufactured. However, the most important part for this work is their explanation of how the ice-phobic coating can lead to the decrease of anti-icing heat. The authors mentioned that the use of ice-phobic coatings leads to: Splashing of water droplets on the surface before freezing, delay of crystallization of water droplets on the substrate by decreasing heat transfer between water drops and the surface, and reducing the ice adhesion to the surface. Antonini et al. [27] showed the results of the experimental testing of NACA0021 airfoil with different coatings and studied the required heating power for each case to prevent ice formation. They have concluded that using super-hydrophobic substrates (SHS) has significantly decreased the anti-icing heat by enhancing water droplets' rebound and water shedding due to faster water runback.

2.6.1 Freezing delay effect

For the freezing delay phenomenon, Alizadeh et al. [35] proved using infrared thermometry and high-speed photography that SHS not only delay the ice accretion by reducing the heterogeneous nucleation of ice embryos in water droplet, but also decreases the heat transfer between the substrate and the water droplet. Also, Tropea et al. [113] provided a detailed study of the physics of solidification of supercooled large drops (SLD) on a cold surface. In this research, the authors first introduced the concept of nucleation, its types, and the concept of nucleation delay. They have also covered the different researches regarding the freezing delay and how it can be described. Also, The authors described the experimental approach to calculate the rate of spread of a thin ice layer and the rate of freezing of the bulk of the water drop using the two-phase Stephan problem solution. In the end, they have posed several open questions regarding future work that should be done in order to successfully simulate the complete process of SLD solidification on surfaces like knowing exactly the shear stress exerted by the external airflow and the convective heat transfer process.

2.6.2 Water film slip

To study the second effect of ice-phobic coatings on ice formation, namely enhancing liquid water film slip, Barrat and Bocquet [114] used extensive molecular dynamics simulations to show that when the contact angle is higher than a certain value, the boundary conditions cannot be considered a non-slip condition anymore. This study was conducted on mercury droplet on glass that resulted in a contact angle of 140° . Also, Choi and Kim [3] measured the slip effect of water-glycerin solution on a solid surface with nanoposts using a cone-and-plate rheometer system. The authors of this work proved that the slip effect happens if both conditions are fulfilled:

$$b > \frac{1 - \sin(\theta_A - \alpha)}{\sqrt{2} |\cos(\theta_A - \alpha)|} \quad (2.17)$$

$$d < 2\sqrt{2}\sigma \frac{|\cos(\theta_A - \alpha)|}{\Delta P} \quad (2.18)$$

where b is the height of the nanopost, θ_A is the contact angle, α is the post angle, σ is liquid surface tension, and ΔP is 0.1 MPa. In this case, the slip length $\delta = b(\mu_l/\mu_a - 1)$.

Ybert et al. [4] showed a more generalized formulation to calculate the slip length of a film over a hydrophobic surface. In their work, the authors suggested that effective slip length

$$b_{eff} = \frac{-L}{\pi} \log \left[\cos \left(\frac{\pi}{2} (1 - \phi_s) \right) \right] \quad (2.19)$$

where L is the surface roughness periodicity and ϕ_s is the ratio between width of the post (a) and L . Also, they have provided another slip length formula in terms of contact angle θ_{eff} as follows:

$$b_{eff} \simeq \alpha L \sqrt{\frac{\cos \theta_o + 1}{\cos \theta_{eff} + 1}} - \beta \quad (2.20)$$

where $\alpha=0.325$, $\beta = 0.44$, and θ_o is the contact angle on ordinary surface.

2.6.3 Droplet splashing

Splashing of water droplets on ice-phobic surfaces is considered the most important effect that influences the ice formation on surfaces. However, there is no common model in the literature describing the water splashing capabilities of certain surface based on its properties. Douezan and Brochard-Wyart [115] studied the dependence of bounce threshold velocity on surface tension and viscosity. They have found that this threshold is highly dependent on the wettability of the surface. McCarthy et al. [116] fabricated a super-hydrophobic hierarchical surface to mimic biological surfaces and studied the bouncing of 10 μm water droplet. They have found that each length scale of the hierarchical structure has an effect on the bouncing of water droplets.

Aboud and Kietzig [117] derived a model to predict the overall restitution coefficient of rebounding droplets. Also, they have concluded that regardless the impact angle, both normal and tangential components of the restitution coefficient ε (which equals $v_{rebound}/v_{incident}$) are function of normal Weber number. Also, Wang et al. [118] presented a simple analysis to model the impact of water droplets on inclined SHS. They have noticed that the contact time is reduced due to the asymmetric drop spreading and retraction. Almohammadi and Amirfazli [119] studied the effect of wettability and viscosity on splashing. They have found that the wettability only affects the splashing threshold at extreme contact angles but it has less effect on spreading. Also they have found that increasing viscosity can promote splashing.

After the huge development in numerical simulation software, a lot of research effort was done to use such advanced techniques to predict splashing of water droplets on SHS. For example, Moqaddam et al. [120] studied the effect of impacting droplets on complex surface using numerical simulations. They have also analyzed the effects of Weber number, texture density and tilting angle of the surface using entropic lattice Boltzmann method (LBM). Also, the authors introduced an energy analysis technique to analyze the exchange between surface and kinetic energy. The simulation process showed good agreement with the experiments.

Yin et al. [121] performed a 3-D simulation of droplets impacting SHS using different impact angles and velocities using LBM. They have concluded that the increase in normal Weber number leads to an increase in incomplete retracting-bouncing. Also, the impact dynamics are found to be highly affected by viscous forces. Delele et al. [122] compared experimental and numerical

data of impacting water droplets on different plant surfaces. The numerical simulation used volume of fluid (VoF) approach to simulate the droplets' behavior for different values of Weber and Reynolds numbers. The numerical simulations provided good agreement with experimental results.

Roisman et al. [123] studied the prompt splash of different liquids on rough and porous surfaces with different Reduced peak heights (R_{pk}) and profile element widths (R_{sm}). From the results of their experiments, the authors concluded that the average deposition/splashing threshold Weber number on rough and porous surfaces can be found using the relation:

$$We_{average} = 10.2 \left(\frac{R_{pk}}{R_{sm}} \right)^{-0.83} \quad (2.21)$$

For porous surfaces, they have introduced a modified Reynolds number (called χ) which has a better description for droplet impact on porous surfaces.

$$\chi = \frac{\rho R_{pk} U_p}{\mu} \Phi \quad (2.22)$$

where Φ is the surface porosity percentage.

Another work was done by Quetzeri-Santiago et al. [124] provided a more enhanced model for critical impact velocity using the splashing ratio (β) [125] where

$$\beta \approx \frac{2.2}{\tan \alpha} \frac{\mu_g^{1/2} (\rho D U_p^5)^{1/6}}{\sigma^{2/3}} \quad (2.23)$$

where $\alpha = 60^\circ$ and μ_g is the viscosity of the gas surrounding the process. In their model, the authors of this work have also taken into consideration the effect of dynamic contact angle (θ_{max}) and their experiments resulted into the following threshold of β :

$$\beta \approx \frac{2.2}{\tan \alpha} \left(0.191 - 0.0654 \left(1 - \frac{R_{pk}}{R_{sm}} \right) (1 - \cos \theta_{max}) \right) \quad (2.24)$$

In addition to the above mentioned researches, there are different review articles were issued in this topic to combine the different empirical models in this area like in [126–129].

2.6.4 Wind tunnel experiments

To combine all the above effects, many research papers were published showing wind tunnel simulation of the icing process of coated airfoils. De Pauw and Dolatabadi [130] simulated the ice accretion on coated NACA0012 airfoil at air temperatures ranging between 0° - $-15^\circ C$, LWC between $1-4.8 \text{ g/m}^3$, and MVD between $25-60 \text{ }\mu\text{m}$. After the simulation of ordinary aluminum surface and super-hydrophobic surface, the authors found that no frozen water rivulet are present in the surface of the airfoil. Also, they have found that the SHS managed to resist the ice formation at air temperature as low as $-10^\circ C$. For anti-icing and deicing heat, the anti-icing heat in case of SHS coated airfoil is 50% less than the corresponding power in case of aluminum surface to ensure completely ice-free surface. Also, two deicing cases were studied for ice accreted. They found that the deicing time was decreased by 75% in case of using SHS.

This paper provided a foundation for future experiments studying the effect of SHS on ice accretion. However, the authors did not provide any physical explanation of the results.

Gao et al. [131] simulated the ice accretion on coated and uncoated DU91-W2-250 (which was originally dedicated to wind turbines) under both rime and ice glaze conditions. For both icing conditions, the anti-icing and deicing of the airfoils was studied in both coated and uncoated surfaces. Also, the distribution of heating power over the surface was studied to optimize the heating process of the airfoil. The authors found that using SHS resulted in decreasing the anti-icing heat up to 90% in case of glaze ice and 94% in case of rime ice by using heating element that extends to 5% and 10% of the chord length respectively. The authors in this article provided an extensive discussion on the mechanism with which the SHS contributed in achieving such savings in heat. However, they did not quantify the contribution of each physical effect.

Morita et al. [132] also studied the same idea of using SHS to reduce the anti-icing. This research focused on simulating NACA0012 exposed to in-flight icing conditions. The experiments resulted in more than 70% decrease in anti-icing heat. Also, they optimized the heating element to 15% of the chord length. This research also proved the concept of using SHS to reduce anti-icing heat. But the study included only NACA0012 thin airfoil which is not suitable for wind turbine cases.

2.7 Overview and general critic

Next, an overall critic of the state-of-the-art research work explained above is provided. Despite the sections of this chapter might seem diverse, the aim of this section is to find a gap in the previous work to fill.

The main goal of this work is to simulate the effect of using ice-phobic coatings on the surface of wind turbine blades in order to mitigate the operational problem resulting from ice accretion. The effects of applying such coatings on ice profiles, overall performance losses, and decreasing the anti-icing heat will be studied. To achieve this goal, the knowledge gained from previous work should be carefully analyzed.

From Section 2.2 we can conclude that using the fully resolved as explained in Section 2.2.1 required high computational power and special meshing techniques. From our previous experience at ForWind - University of Oldenburg, mesh generation of wind turbine blades is not an easy task, even for smooth surfaced wind turbine blade. So, one can imagine how such a task will be hard for a near-wall grid for iced airfoil blade. That is why, the rwf approach explained in Section 2.2.2 is preferred to achieve the goal of this research.

Also, from Section 2.3, it can be concluded that using LPT is accurate to predict ice profiles. However, using such an approach to simulate 2D blade sections (like the work of Yirtici et al. [79, 80]) can be reasonable in computational power. Another approach to simulate ice accretion on blades is to use EPT approach (like the work shown in Sec. 2.3.2) and sacrifice some accuracy to carry out such a simulation using reasonable computation resources.

After that, one should still decide, which thermodynamic model would fit to the studied case while taking into consideration all involving parameters. In this chapter, it was shown that the SWIM model proposed by Bourgault et al. [95] was derived directly from conservation equations of fluid film using minimum assumptions. It was shown also that this model was widely tested and validated for different applications ranging from 2D airfoils to rotating helicopter

rotors. Another advantage is that the equations of this model is very close to what is applied in OpenFOAM to simulate liquid film flow, which makes the implementation much easier. From Section 2.6, we can see that all proviosly done work in the field of the effect of using SHS and ice-phobic coatings on ice accretion were experiments work for stationary, 2D airfoils. That means that a numerical simulation technique is still needed and could be a good research point. The work of Huang et al. [112] and Antonini et al. [27] presented an explanation of the effects of ice-phobic coatings on ice formation.

It can be noticed also that most of the research work shown in this chapter was done on commercial or closed-source CFD codes. This limits the reach of other researchers to such advances. This raised the need for an ice accretion code within an open-source framework, like OpenFOAM. The presented work in this chapter shows that the present tools can simulate ice formation on 2D airfoils efficiently and accurately. However, the 3D simulation tools are still not well validated and are under development. Since ice formation of large structures, wind turbines, for instance, is a critical issue as shown in Ch.1, a more validated method should be employed to simulate ice accretion on such large structures. Also, all thermodynamic models ignore the properties of the surface on which the ice forms and grows. This ignores all development in surface technology and how they can help in solving this problem.

This work aims to create an ice accretion simulation code that works within the open-source OpenFOAM framework to be able to simulate ice accretion on wind turbine blades using well-validated ice accretion methods, which are LPT with SWIM model. Also, this code should be able to consider the surface properties of spacial coatings while simulating such a phenomenon. This thesis provides the details of the models used in this code, its validation 2D and 3D cases, and a test case of ice accretion on a multi-megawatt wind turbine blade. The next chapter explains in detail the equations of numerical models used to achieve the goal of numerically simulating the ice accretion on coated wind turbine blades.

Chapter 3

Theoretical Background

3.1 Introduction

As it can be concluded from the literature review shown in the previous chapter, the ice accretion phenomenon is a complicated multi-physics problem. This means that to simulate such a phenomenon, different kinds of simulation models should be integrated to calculate the final ice shape and its impact on the final aerodynamic performance of the blade.

In this chapter, a detailed description of the different physical phenomena affecting ice accretion will be discussed and explained. First, an overall look at the main steps of ice accretion simulations will be explained. The first step is the simulation of the airflow that carries the water particles from the atmosphere to the solid surface. Then comes the mathematical models used in tracking water particles until they hit the solid surface to determine the location of the impinging location of each group of particles. After that, the thermodynamic models were used to simulate the ice formation process to determine ice thickness and calculate a new profile. Finally, the mesh modification to fit the new profile is used. Each of the aforementioned steps is explained in detail both physically and mathematically.

3.2 Overall Simulation Procedure

To simulate the ice formation process over structures, the overall icing simulation time is divided into several time steps that each time step is assumed to be a steady-state ice accretion process. For each time step, the exact location of water particles hitting the surface of the structure should be calculated. Since the water particles are carried by airflow around the structures due to the drag force exerted by airflow on the spherical water particles, simulating the airflow, or in general can be called background flow, is necessary to track the water particles and find the exact location and velocity of water particles impinging on the surface.

After calculating the water particles' impinging locations and velocities, mass flow rate and kinetic energy of water impingement could be calculated. After that, ice thickness, and accordingly the new ice profile, can be calculated using the icing thermodynamic model. After this step, there are two possibilities: either to finish the simulation processor to continue with another time step. In case the simulation is required to be continued, the computational grid should be modified to the new iced profile to simulate the flow field over it exactly the first flow

filed simulation in the preceding step. The aforementioned proceedings are represented in Fig. 3.1

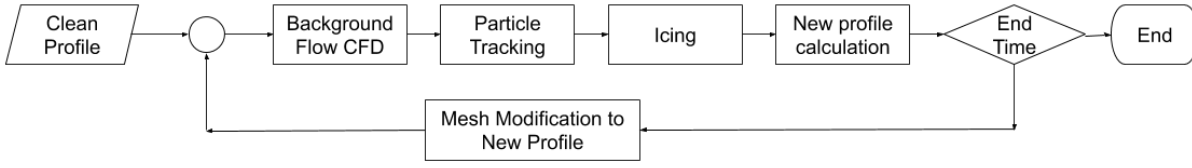


Figure 3.1: Flowchart of ice accretion simulation process

3.3 Background Flow Simulation

As explained in the previous section, a calculated background flow should be calculated to be able to calculate the drag forces on water particles carried by air. Since the drag force affecting particles is the most important and most influential in the particle tracking process, it is very important to be able to simulate the airflow as accurate as possible to ensure the accuracy of particle tracking. After this simulation process, the background flow is assumed to be frozen. This means that background flow is simulated only once before the particle tracking and assumed not to change anymore and all the effects of particles on the airflow are neglected. This method is called on-way coupling between air and droplets. The benefit of using this approach is to reduce the computational cost of the simulations since taking the effect of particles on airflow will significantly increase the number of calculated equations per time step. This section illustrates fundamental governing equations of fluid flow and the different turbulence models used in this research to simulate the airflow field.

3.3.1 Governing Equations of Compressible Flow

The basic three equations that governs all kinds of fluid flows are: mass momentum and energy conservation equations. From the fundamental forms of these three equations, the governing equations of fluid flow can be written as:

$$\frac{\partial \rho}{\partial t} + \nabla \cdot (\rho u) = 0 \quad (3.1)$$

$$\frac{\partial \rho u}{\partial t} + \nabla \cdot (\rho u u) = -\nabla p + \mu \nabla^2 u + \rho g \quad (3.2)$$

$$\frac{\partial (\rho E)}{\partial t} + \nabla \cdot (\rho E u) = -\nabla \cdot (p u) - \nabla \cdot (\tau_{ij} \cdot u) - \nabla \cdot q + \rho S \quad (3.3)$$

In this work, flow is considered compressible for many reasons:

1. To complete the icing simulations, airflow temperatures around the simulated body should be simulated to give a correct simulation of the heat transfer process between the background flow and the surface, and accordingly to the water film on the surface, to be included in the thermodynamic simulation.

2. In some cases, especially in modern, high diameter wind turbines, the compressibility effects can be seen at the tip of blades where Mach number Ma can reach the value of 0.3.

3.3.2 Reynolds-Averaged Navier-Stokes (RANS) Method

Since the start of using CFD in simulating turbulent flow, many turbulence models were introduced. From this large number of models, only two turbulence models will be discussed in this section, namely, Spalart-Allmaras and $k-\omega$ SST turbulence models.

Spalart-Allmaras Turbulence Model (SA)

Spalart-Allmaras Turbulence Model is a one-equation model that solves the viscosity-like variable ($\tilde{\nu}$) using the following equation [133]:

$$\frac{\partial \tilde{\nu}}{\partial t} + u_j \frac{\partial \tilde{\nu}}{\partial x_j} = C_{b1}(1 - f_{t2})\tilde{S}\tilde{\nu} - [C_{w1}f_w - \frac{C_{b1}}{\kappa^2}f_{t2}](\frac{\tilde{\nu}}{d})^2 + \frac{1}{\sigma}[\frac{\partial}{\partial x_j}((\mathbf{v} + \tilde{\nu})\frac{\partial \tilde{\nu}}{\partial x_j}) + C_{b2}\frac{\partial \tilde{\nu}}{\partial x_i}\frac{\partial \tilde{\nu}}{\partial x_i}] \quad (3.4)$$

$$\mu_t = \rho \tilde{\nu} f_{v1},$$

$$f_{v1} = \frac{\chi^3}{\chi^3 - C_{v1}^3}$$

$$\chi = \frac{\tilde{\nu}}{\nu}$$

$$\tilde{S} = \Omega + \frac{\tilde{\nu}}{\kappa^2 d^2} f_{v2}$$

where the magnitude of the vorticity:

$$\Omega = \sqrt{2W_{ij}W_{ij}}$$

$$W_{ij} = 0.5\left(\frac{\partial u_i}{\partial x_j} - \frac{\partial u_j}{\partial x_i}\right)$$

and the following constants:

$$c_{b1} = 0.1355, \sigma = 2/3, c_{b2} = 0.622, \kappa = 0.41, c_{w2} = 0.3, c_{w3} = 2, c_{v1} = 7.1, c_{t3} = 1.2, c_{t4} = 0.5$$

$$c_{w1} = \frac{c_{b1}}{\kappa^2} + \frac{1 + c_{b2}}{\sigma}$$

$k-\omega$ SST Turbulence Model

$k-\omega$ SST Turbulence Model is a two-equation model that can calculate both turbulence kinetic energy (k) and turbulent frequency (ω) using the equations [134]:

$$\frac{\partial \rho k}{\partial t} + \frac{\partial \rho u_j k}{\partial x_j} = P - \beta^* \rho \omega k + \frac{\partial}{\partial x_j}[(\mu + \sigma_k \mu_t) \frac{\partial k}{\partial x_j}]$$

$$\frac{\partial \rho \omega}{\partial t} + \frac{\partial \rho u_j \omega}{\partial x_j} = \frac{\gamma}{\nu_t} P - \beta \rho \omega^2 + \frac{\partial}{\partial x_j} [(\mu + \sigma_\omega \mu_t) \frac{\partial \omega}{\partial x_j}] + 2(1 - F_1) \frac{\rho \sigma_{\omega 2}}{\omega} \frac{\partial k}{\partial x_j} \frac{\partial \omega}{\partial x_j}$$

where

$$P = \tau_{ij} \frac{\partial u_i}{\partial x_j}$$

$$\tau_{ij} = \mu_t (2S_{ij} - \frac{2}{3} \frac{\partial u_k}{\partial x_k} \delta_{ij}) - \frac{2}{3} \rho k \delta_{ij}$$

$$S_{ij} = \frac{1}{2} (\frac{\partial u_i}{\partial x_j} + \frac{\partial u_j}{\partial x_i})$$

$$\mu_t = \frac{\rho a_1 k}{\max(a_1 \omega, \Omega F_2)}$$

and the above-mentioned constants have values of:

$$\gamma_1 = \frac{\beta_1}{\beta^*} - \frac{\sigma_{\omega 1} \kappa^2}{\sqrt{\beta^*}}, \gamma_2 = \frac{\beta_2}{\beta^*} - \frac{\sigma_{\omega 2} \kappa^2}{\sqrt{\beta^*}}, \sigma_{k1} = 0.85, \sigma_{\omega 1} = 0.5, \beta_1 = 0.075, \sigma_{k2} = 1.0$$

$$\sigma_{\omega 2} = 0.856, \beta_2 = 0.0828, \beta^* = 0.09, \kappa = 0.41, a_1 = 0.31$$

3.3.3 Multi Reference Frame (MRF) Model:

Instead of applying mesh rotation techniques, an alternative to simulate rotating machines, including wind turbine rotors, is to use MRF model. MRF model adds new momentum sources to simulate both centrifugal and Coriolis forces and replaces absolute velocity with angular velocity in all Navier-Stokes equations. In this case, Navier-Stokes equations become

$$\frac{\partial \rho}{\partial t} + \frac{\partial (\rho u_r)}{\partial x_i} = 0 \quad (3.5)$$

$$\frac{\partial}{\partial t} (\rho u_r) + \nabla \cdot (\rho u_r u_r) + 2\rho \Omega \times u_r + \rho \Omega \times (\Omega \times r) = -\nabla p + \rho \nu \nabla \cdot \nabla (u_r) \quad (3.6)$$

where $u_r = u - \Omega \times r$

3.3.4 Simulation of Rough Surfaces

To avoid high computation costs resulting from using fully resolved rough walls, rough wall functions will be used in this work to simulate the flow field over rough walls. As explained in Section 2.2, it was found that the boundary layer behaves in the same manner inflow over both rough and smooth surfaces. The only exception is that the whole velocity profile is shifted away from the wall by a certain parameter called the velocity shift (Δu). The value of Δu depends on the roughness height as will be indicated in this section.

Roughness Parameters calculations

The difference between most of the proposed RWFs in different works of literature is how to calculate this shift. After Schlichting [51] found the parameters on which the velocity shift depends, the four parameters (as shown in Fig. 3.2) are used together to calculate one parameter called equivalent sand roughness height (K_s) that can be calculated by the equations

$$\frac{K_s}{K_{avg}} = \begin{cases} 0.0164 \times \Lambda^{3.78} & \text{for } \Lambda < 4.93 \\ 139.0 \times \Lambda^{-1.90} & \text{for } \Lambda > 4.93 \end{cases} \quad (3.7)$$

$$\Lambda = \frac{L_{avg}}{K_{avg}} \left(\frac{A_p}{A_s} \right)^{-4/3} \quad (3.8)$$

where K_{avg} is the average roughness element height, A_p is projected area of roughness element

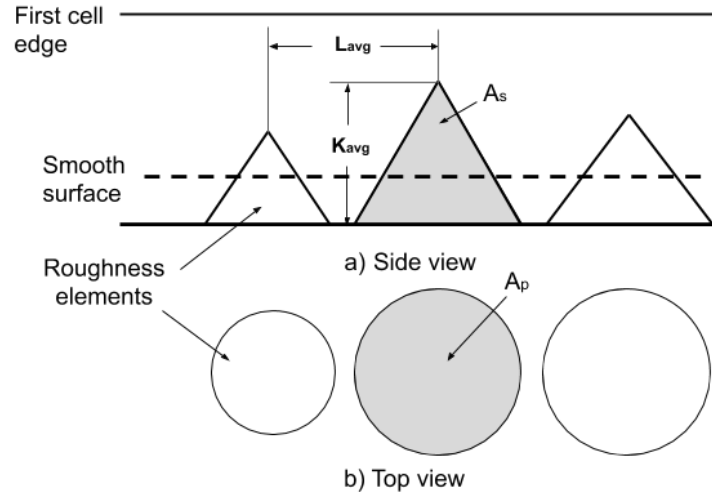


Figure 3.2: Roughness element geometrical parameters

on the smooth surface, A_s is area of roughness element projected in flow direction, L_{avg} is the average distance between roughness elements' peaks and D_{avg} is the average diameter of roughness elements as mentioned in [135]. By calculating K_{avg} , L_{avg} , and D_{avg} and assuming roughness elements take conical shapes for approximation, A_p and A_s can be calculated. For conical roughness elements, $A_p/A_s = \pi D_{avg}/2K_{avg}$. The final value of the velocity shift in all RWFs used in this work depends on the calculated value of K_s from Equ. 3.7.

Momentum Rough Wall Function

Da Silva et al. [69] applied the velocity shift to the well-known log-low equation by introducing a new term, namely ΔB , that represents this velocity shift as a function of K_s according to Cebeci [136] ideas in the equations

$$u^+ = \frac{1}{\kappa} \ln(Ey^+ - \Delta B) \quad (3.9)$$

$$\Delta B = \begin{cases} 0 & : K_s^+ \leq 2.5 \\ \frac{1}{\kappa} \ln \left[K_s^+ - \frac{2.25}{87.75} + C_s K_s^+ \right] \sin[0.4258(\ln K_s^+ - 0.811)] & : 2.5 < K_s^+ < 90 \\ \frac{1}{\kappa} \ln(1 + C_s K_s^+) & : K_s^+ \geq 90 \end{cases} \quad (3.10)$$

Where $y^+ = y(1)u_\tau/\nu$, $K_s^+ = u_\tau K_s/\nu$, $E = 9.8$, $\kappa = 0.41$ and

$$C_s = \frac{E}{32.6} - \frac{1}{K_s^+} \quad (3.11)$$

Finally, turbulent viscosity can be calculated by:

$$\nu_t|_w = \nu \left(\frac{y^+ \kappa}{\ln(Ey^+/e^{\kappa\Delta B})} \right) \quad (3.12)$$

Since this wall RWF deals mainly with ν_t , it is used with the Spalart-Allmaras turbulence model to simulate rough surface.

3.4 Water Particle Tracking

To understand particle tracking in general, it should be clear in mind how the particles interact with the surrounding fluid. In this sense, Elghobashi [1] provided an extensive discussion of the different phase-coupling modes that happen between fluid and particles as shown in Fig. 3.3. This figure divides the interaction between dispersed and main phases into three regions according to the value of the dispersed phase volume fraction (α_d) and the ratio between particle response time (τ_p) and Kolmogorov time scale (τ_K). These three regions are:

1. One-way coupling: in this mode, the particles (or dispersed phase) volume fraction is below 10^{-6} . This α_d value is very low that the existence of particles has a negligible effect on the flow field of the main fluid. In this case, a contentious background flow can be assumed.
2. Two-way coupling: for $10^{-6} \leq \alpha_d \leq 10^{-3}$, the effect of the particles starts to influence the flow around them. for lower τ_p values (which means smaller particle diameters) at the same α_d , the sum of the surface areas of the particles increases. This leads to higher dissipation of turbulent kinetic energy. On the other hand, increasing τ_p values increase vortex shedding around the particles. This means higher production of turbulent kinetic energy.
3. Finally, for $\alpha_d \geq 10^{-3}$, the whole flow behavior becomes more like granular flow and the effect of the surrounding fluid starts to fade out. Also, the particles become more affected by inter-particle collisions.

Since most of the simulation cases in this work have an LWC $\approx 10^{-3} \text{ kg/m}^3$ which corresponds to $\alpha_d \approx 10^{-3}$, On-way coupling can be assumed and frozen background flow is valid.

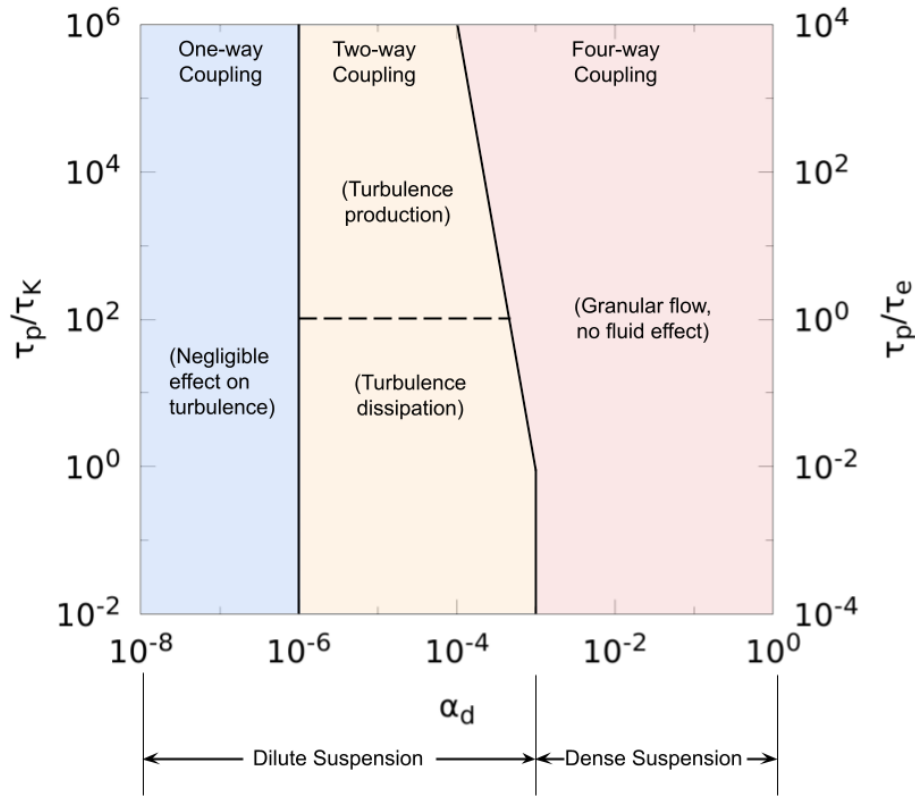


Figure 3.3: Different phase-coupling ranges with different dispersed phase volume fraction α_d and the ratio between particle response time τ_p and Kolmogorov time scale τ_K (adapted from Elghobashi [1])

3.4.1 Lagrangian Particle Tracking

To calculate the amount of impinging water \dot{m}_{imp} , impingement locations and its kinetic energy, Lagrangian particle tracking is used. The trajectory of each droplet is calculated using Newton's second law which takes the form:

$$m_p \frac{du_p}{dt} = -\frac{1}{2} |u_p - u_f| (u_p - u_f) \frac{\pi d^2}{4} C_D + F \quad (3.13)$$

where F represents any other forces that affect the droplet and C_D is the coefficient of drag of the droplet. In OpenFOAM, modules for Lagrangian particle tracking and film calculation have already existed. The additional modules that should be implemented in OpenFOAM are \dot{m}_{ice} and \dot{Q}_{ice} that is applied as a phase change model and solved along with other film conservation equations.

3.4.2 Eulerian Flow Simulation

Eulerian approach is usually used to simulate multiphase flow since it depends on assuming that both phases, water and air in this case, are inter-penetrating continua and the flow field of

each phase is solved using separate conservation of mass, momentum and energy equations as indicated in Equ. 3.14 and 3.15 using the volume fraction (α). Assuming water particles and air are homogeneously mixed, we can use this approach in order to simulate the transport of water particles to blade surface and hence simulate ice formation. In this case, the conservation equations reads

$$\frac{\partial}{\partial t} \alpha_i \rho_i + \nabla \cdot (\alpha_i \rho_i \mathbf{u}_{r,i}) = 0 \quad (3.14)$$

$$\alpha_d \rho_d \left(\frac{\partial}{\partial t} (\mathbf{u}_{r,d} + \nabla \cdot (\alpha_d \rho_d \mathbf{u}_{r,d} \mathbf{u}_{r,d})) \right) = -\frac{\alpha_d}{\rho_d} \nabla p + \nabla \rho_d \alpha_d \mathbf{v} \nabla \cdot \nabla (\mathbf{u}_r) + I \quad (3.15)$$

where α_d is the volume fraction of dispersed phase and ρ_d is the density of the respective fluid. The sum of all volume fraction of the different phases should always be unity. It denotes the momentum transfer between the phases, which may include drag forces, gravitational force, etc.

In this work, it is assumed that the only force affecting water particles is the drag force and there is no pressure gradient affecting the field. To simplify the equations, the term $\alpha_i \rho_i$ for the water droplets field will be replaced by $\bar{\rho}_p$ which is the mass of water particles in the unit volume of air. The Eulerian particle tracking equations becomes [8]:

$$\frac{\partial \bar{\rho}_d}{\partial t} + \nabla \cdot (\bar{\rho}_d \mathbf{u}_{r,d}) = 0 \quad (3.16)$$

$$\frac{\partial \bar{\rho}_d}{\partial t} (\mathbf{u}_{r,d} + \nabla \cdot (\bar{\rho}_d \mathbf{u}_{r,d} \mathbf{u}_{r,d})) = \frac{3}{4} \frac{\bar{\rho}_d \mu_{air} C_D Re_d}{\rho_{water} D_d^2} (\vec{u}_{r,a} - \vec{u}_{r,d}) \quad (3.17)$$

where C_D is the drag coefficient, Re_d is the droplet Reynolds number, This new equation is solved by adapting the rhoPimpleFoam solver in OpenFOAM to include a new source term that represents drag force.

3.4.3 Drag force models

Since the drag force is the main force affecting particles while being carried by the airflow, it is very important to calculate this force accurately. However, the drag force of water droplets cannot be considered an ordinary sphere due to the following reasons:

- Since the water droplet is very small (droplet diameter in the order of magnitude of 10^{-5} m), the no-slip condition cannot be applied between the droplet surface and air molecules.
- It is not necessary that water droplets keep their spherical shapes during their travel through the air. Due to this deformation, the frontal area of the droplet is increased, and accordingly the drag force.

In OpenFOAM there are two common equation to calculate C_D : sphereDrag which is based on the work of Putnam [137] and the SchillerNaumannDrag model which is based on the work of Naumann and Schiller [138].

In sphereDrag model, C_D can be calculated using the equation:

$$C_D = \begin{cases} \frac{24}{Re_d} (1 + \frac{1}{6} Re_d^{2/3}) & : Re_d \leq 1000 \\ 0.44 & : Re_d > 1000 \end{cases} \quad (3.18)$$

On the other hand, SchillerNaumannDrag can be calculated by:

$$C_D = \begin{cases} \frac{24}{Re_d}(1 + 0.15Re_d^{0.687}) & : Re_d \leq 1000 \\ 0.424 & : Re_d > 1000 \end{cases} \quad (3.19)$$

where Re_p is droplet Reynolds number. In most lagrangian OpenFOAM cases, sphereDrag model is used.

3.4.4 Droplet Size Distribution

In reality, water droplets in the atmosphere do not have a single size. Therefore, many pieces of research were dedicated to finding the closest distribution to reality. The first idea that should come to one's mind is that water the diameter of water droplets follow the Gaussian distribution:

$$P(d) = \frac{1}{\sigma\sqrt{2\pi}} \exp\left(-\frac{1}{2}\left(\frac{d-\mu}{\sigma}\right)^2\right) \quad (3.20)$$

where μ is the mean droplet diameter and σ is the standard deviation.

Another more realistic distribution was created by Langmuir and Blodgett [139] to find different distribution models that can fit to different particle types. These distributions are named Langmuir's B, C, D, and E. The LWC percentage of each size is shown in Tab. 3.1 [139, 140]. An-

Table 3.1: Percentage of each droplet size for Langmuir B, C, D, and E distributions

Bin No.	m_{bin}/m_{total} [%]	d/MVD			
		B	C	D	E
1	5	0.56	0.42	0.31	0.23
2	10	0.72	0.61	0.52	0.44
3	20	0.84	0.77	0.71	0.65
4	30	1.00	1.00	1.00	1.00
5	20	1.17	1.26	1.37	1.48
6	10	1.32	1.51	1.74	2.00
7	5	1.49	1.81	2.22	2.71

other distribution that is very common in the field of liquid atomization is Rosin-Rammler distribution. This distribution follows the Gamma distribution function and takes the form [140]:

$$f(d) = \frac{n}{c} \left(\frac{d}{c}\right)^{n-1} \exp\left[-\left(\frac{d}{c}\right)^n\right] \quad (3.21)$$

$$c = \frac{v_m}{\Gamma(1+1/k)} \quad (3.22)$$

where n is the shape factor and Γ is the Gamma function. Riley and Jeck [140] compared Langmuir's distributions of types B and C, Normal (Gaussian) distribution, and Gamma distribution with measurements of water droplets' sizes responsible for ice formation. They have found that Gamma distribution provides the best prediction of particle sizes.

In OpenFOAM, the user can select between table, uniform, exponential, and normal distribution. Additionally, OpenFOAM includes Gamma distribution (named `massRosinRammler` and `RosinRammler` distribution) based on the work of Yoon et al [141]. In both distributions, a random number is generated and used to find the value of the droplet diameter in case it lays between `minValue` and `maxValue`. In this thesis, the Gamma distribution is used in all simulations as the particle size distribution.

3.4.5 Collection efficiency

The key parameter to calculate the mass on surfaces and to compare their values between different airfoils is the collection efficiency (β). Collection efficiency is a dimensionless number that represents the ratio between the water mass impinging the surface per unit area of the surface to the water mass carried by the airflow upstream of the airfoil per unit area upstream. Or in other words, it represents how much water carried out by the air is collected by the surface of the airfoil. This value can be calculated using the equations:

$$\beta = \frac{\dot{m}_{wall}/A_{wall}}{\dot{m}_{upstream}/A_{upstream}} \quad (3.23)$$

since $\dot{m}_{upstream} = u_{\infty} \cdot LWC \cdot A_{upstream}$, the above equation can be rewritten as:

$$\beta = \frac{\dot{m}_{wall}/A_{wall}}{u_{\infty} \cdot LWC} \quad (3.24)$$

In OpenFOAM, if A_{wall} is taken to be the area of the control surface on the wall and \dot{m}_{wall} is the mass of water sticking to the surface per second, β can be calculated.

For Eulerian particle tracking, it becomes useful to rewrite the last equation in another form [84]:

$$\beta = \frac{\alpha_{wall}(\vec{u}_{inf} \cdot \vec{A}_{wall})}{\alpha_{\infty}|\vec{u}_{\infty}|} \quad (3.25)$$

where α_{wall} and α_{∞} are water volume fractions on the wall and upstream respectively. Also, as aforementioned in Sec. 3.4.2, $\alpha_{water}\rho_{water} = \bar{\rho}_p$ or in this case, $\alpha_{water} = \rho_{water}/\bar{\rho}_p$. Also, $\bar{\rho}_{p,\infty} = LWC_{\infty}$. Accordingly, β can be calculated from the equation:

$$\beta = \begin{cases} \frac{-\bar{\rho}_p(\vec{u}_{\infty} \cdot \vec{A}_{wall})}{LWC_{\infty}|\vec{u}_{\infty}|} & : \vec{u}_{\infty} \cdot \vec{A}_{wall} \leq 0 \\ 0 & : \vec{u}_{\infty} \cdot \vec{A}_{wall} > 0 \end{cases} \quad (3.26)$$

3.5 Ice Accretion Thermodynamic Model

After the simulation of the mass and locations of impinging water droplets on the surface, a thermodynamic icing model should be applied to calculate the mass of frozen water and

accordingly calculate the new iced profile. Since the 1950s, many thermodynamic models were applied to model ice accretion as illustrated in Sec. 2.4. This section explains in detail how the liquid film model is simulated in OpenFOAM and the different physical phenomena are taken into consideration. Also, this section explains the Shallow Water Icing Model (SWIM) thermodynamic icing model and how it was applied in OpenFOAM.

3.5.1 Liquid Film Solution

Any ice accretion software must contain some models that can simulate water film motion on any surface. In OpenFOAM, different liquid film solvers solve such equations. In this section, a detailed explanation of each mass, momentum, pressure, and energy source term is provided. This is because of the complexity of the fluid and thermal phenomena that occurs during the ice formation process that entails a deep understanding of each phenomenon to be able to modify them according to our needs from the solver.

Meredith et al. [142] illustrated the complete film solution that is used in OpenFOAM in there work as follows:

$$\frac{\partial \rho \delta}{\partial t} + \nabla \cdot (\rho \delta \bar{u}) = S_{mass} \quad (3.27)$$

$$\frac{\partial \rho \delta \bar{u}}{\partial t} + \nabla (\rho \delta \bar{u} \bar{u}) = -\delta \nabla p + S_{momentum} \quad (3.28)$$

$$\frac{\partial \rho \delta h}{\partial t} + \nabla (\rho \delta \bar{u} h) = S_{energy} \quad (3.29)$$

where δ is the film height on the control surface. While S_{mass} , $S_{momentum}$, p , and S_{energy} are sources of mass, tangent momentum, normal momentum, and energy respectively. Equations 3.27 and 3.28, namely mass and momentum equations, are solved in OpenFOAM by calling `kinematicSingleLayer` class to be solved. This class is called through `thermoSingleLayer` that additionally solves the energy equation (Equ. 3.29) with the other two conservation equations.

Each of the three aforementioned source terms contains different sources (and sinks) of the three quantities as follows:

$$S_{mass} = \dot{m}_{imp,net} - \dot{m}_{evap} - \dot{m}_{sep} \quad (3.30)$$

$$S_{momentum} = S_{imp,net} - S_{sep} + F_{\theta} + \rho g_t \delta + \tau_{air} - \tau_w + \tau_{cap} \quad (3.31)$$

$$p = p_{imp,net} + p_{evap} + p_{\sigma} + \rho g_n \delta + p_g \quad (3.32)$$

$$S_{energy} = \dot{Q}_{imp,net} - \dot{Q}_{evap} - \dot{Q}_{sep} - \dot{Q}_{conv} + \dot{Q}_{rad} \quad (3.33)$$

Sources of mass, momentum, pressure and energy in equations 3.30 to 3.33 are illustrated in Fig. 3.4.

Impinging source terms

The impinging sources (namely $\dot{m}_{imp,net}$, $S_{imp,net}$, $p_{imp,net}$, $\dot{Q}_{imp,net}$) are the net mass, momentum and energy sources introduced to the film due to the net particle mass impinging the surface. This means that:

$$\dot{m}_{imp,net} = \dot{m}_{imp} + \dot{m}_{splash} \quad (3.34)$$

$$S_{imp,net} = S_{imp} + S_{splash} \quad (3.35)$$

$$P_{imp,net} = P_{imp} + P_{splash} \quad (3.36)$$

$$\dot{Q}_{imp,net} = \dot{Q}_{imp} + \dot{Q}_{splash} \quad (3.37)$$

The impingement sources in equations 3.34, 3.35, and 3.36 are solved by transferring the impinging mass from the air flow field to the surface film through `cloudMassTrans_` (that represents $\dot{m}_{imp,net}$) and `cloudDiameterTrans_` in `kinematicSingleLayer` class and accordingly in `thermoSingleLayer` class. After that, in `thermoSingleLayer` class, `cloudMassTrans_` is multiplied by the air flow field sensible enthalpy $h_$ to result in impinging energy $\dot{Q}_{imp,net}$ shown in Equ. 3.37.

Separation source terms

Separation source terms are mass and energy source terms due to the separation of mass from the surface at the corners. The separated mass and the energy contained in it are subtracted from mass and energy equations by using `primaryMassTrans_` in `kinematicSingleLayer` class and accordingly in `thermoSingleLayer` class. Also, in `thermoSingleLayer` class, `primaryMassTrans_` is multiplied by the airflow field sensible enthalpy $h_$ to result in separated energy \dot{Q}_{sep} shown in Equ. 3.33.

Convection source terms

This term represents mass and energy transfer by convection of the liquid film to the surrounding gas. As illustrated in Fig. 3.4-b, the convective heat transfer of the liquid film is divided into two types:

- Convective heat transfer through the upper film surface ($\dot{Q}_{conv,up}$): which happens between the liquid film and the ambient air,
- Convective heat transfer through the lower film surface ($\dot{Q}_{conv,low}$): which happens between the liquid film and the solid surface (solid wall or ice).

The total convective heat transfer \dot{Q}_{conv} is the sum of the two quantities. Following the equations explained by Bergman et al. [143], heat flux of vaporization can be calculated by:

$$Nu = \begin{cases} 0.664Re_L^{0.5}Pr^{0.334} & \text{for } Re_L < 5 \times 10^5, Pr > 0.6 \\ 0.037Re_L^{0.8}Pr^{0.334} & \text{for } 5 \times 10^5 < Re_L < 10^7, Pr > 0.6 \end{cases} \quad (3.38)$$

where Prandtl number $Pr = \nu/\alpha$. After that, convective heat transfer coefficient can be calculated by:

$$h_{conv} = \frac{Nu \cdot k}{L} \quad (3.39)$$

$$\dot{Q}_{conv} = \frac{h_{conv,up}\rho A(T_{film} - T_{air}) + h_{conv,low}\rho A(T_{film} - T_{wall})}{\Delta t} \quad (3.40)$$

Where k is the thermal conductivity of the liquid film.

Using Chilton-Colburn analogy, similar formula to Equ. 3.38 is used to calculate convective mass transfer. However, in the case of mass transfer, Pr is replaced with Schmidt number (Sc), and Nu is replaced with Sherwood number (Sh). Accordingly, Equ. 3.38 can be written for mass transfer as follows:

$$Sh = \begin{cases} 0.664Re_L^{0.5}Sc^{0.334} & \text{for } Re_L < 5 \times 10^5, Sc > 0.5 \\ 0.037Re_L^{0.8}Sc^{0.334} & \text{for } 5 \times 10^5 < Re_L < 10^7, Sc > 0.5 \end{cases} \quad (3.41)$$

where Schmidt's number (Sc) = ν/D_{AB} as D_{AB} is the diffusion of the film liquid in the air. In case of water in air, $D_{water,air} = 2.09 \times 10^{-5} \text{ m}^2/\text{s}$ at $P_{atm} = 10^5 \text{ Pa}$ and $T = 273^\circ\text{K}$. The convective mass transfer coefficient h_{mass} can be calculated using Sherwood's number (Sh) where:

$$h_{mass} = \frac{Sh \cdot D_{AB}}{L} \quad (3.42)$$

$$\dot{m}_{conv} = \frac{h_{mass}\rho_{air}A}{\Delta t} \left(\frac{Y_s - Y_\infty}{1 - Y_s} \right) \quad (3.43)$$

where Y_s and Y_∞ is the mass fraction of fluid on the surface of the liquid film and in the atmosphere respectively.

Because of this evaporation, vapor recoil effect (p_{evap}) occurs:

$$p_{evap} = \frac{\rho_v u_{evap}^2}{2} = \frac{(\dot{m}_{evap}'')^2}{2\rho_v} \quad (3.44)$$

The calculation of convective heat transfer coefficient between the film and airflow field through the upper surface of the film is calculated by using `mappedConvectiveHeatTransfer`. This is done by mapping the heat transfer coefficient of the airflow field on the solid surface of the wall. Also, for convective heat transfer coefficient between film and the solid wall through the lower surface of the film is newly implemented in OpenFOAM using the same equations. However, the fluid properties in these equations are liquid film properties.

For mass transfer by convection between the liquid film and the air is applied by selecting `standardPhaseChange` in `constant/surfaceFilmProperties` input file. This model uses equations 3.41 and 3.42 to calculate \dot{m}_{conv} .

Evaporation source terms

When liquid film evaporates by convection as calculated in Equ. 3.43, the latent heat of evaporation is absorbed from the rest of the liquid film to enable the liquid molecules to turn into vapor and mix with the air. The absorbed latent heat is calculated by:

$$\dot{Q}_{evap} = \dot{m}_{conv}L_{evap} \quad (3.45)$$

where L_{evap} is latent heat of evaporation. In case of water, $L_{evap} = 2500.9 \text{ kJ/kg}$. This energy source is applied in OpenFOAM also by using `standardPhaseChange` model.

Radiation source terms

Liquid films loses energy also to the surrounding air in case of the liquid film is warmer than it. This temperature difference leads to heat transfer by radiation:

$$\dot{Q}_{rad} = \varepsilon A \sigma_{rad} (T_{film}^4 - T_{air}^4) \quad (3.46)$$

The implementation of this model will be discussed in the implementation of `icingPhaseChange` after discussing the icing thermodynamic model in the next sections.

Gravitational source terms

The two momentum source terms, namely $\rho g_t \delta$ and $\rho g_n \delta$ occur due to gravity. The gravitational force is divided into normal force due to the gravitational acceleration component normal to the wall (g_n) and the gravitational acceleration component tangent to the wall (g_t). Gravitational forces are already applied as source terms during solving the momentum equation in `kinematicSingleLayer` class.

Free surface shear and wall shear source terms

These two momentum sources represent shear stress transported from ambient air to the water film (τ_{air}) and the opposite shear stress exerted by the wall on the liquid film (τ_{wall}) due to no-slip between them. Airflow shear is also applied as source terms during solving the momentum equation in `kinematicSingleLayer` class by mapping the airflow field velocity on the wall $U_{s_}$ and the velocity boundary condition on the wall $U_{w_}$. Both velocities are then averaged to find mean liquid velocity $U_$ which is used to solve the momentum and energy equations.

Source term due to liquid properties

These two momentum sources represents thermo-capillary forces (τ_{cap}) due to the existence of surface tension force. This term can be calculated by:

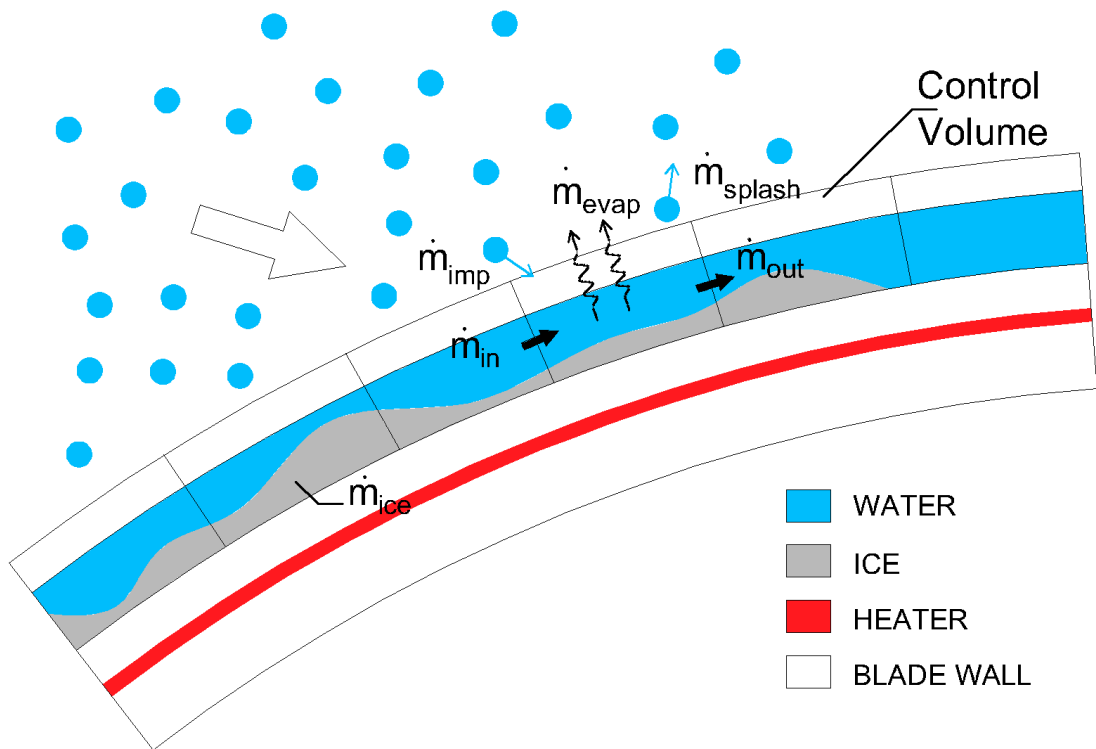
$$\tau_{cap} = -\nabla_s \sigma \quad (3.47)$$

Another source if the contact angle force (F_θ) exerted tangentially to the film surface and can be calculated using the formula:

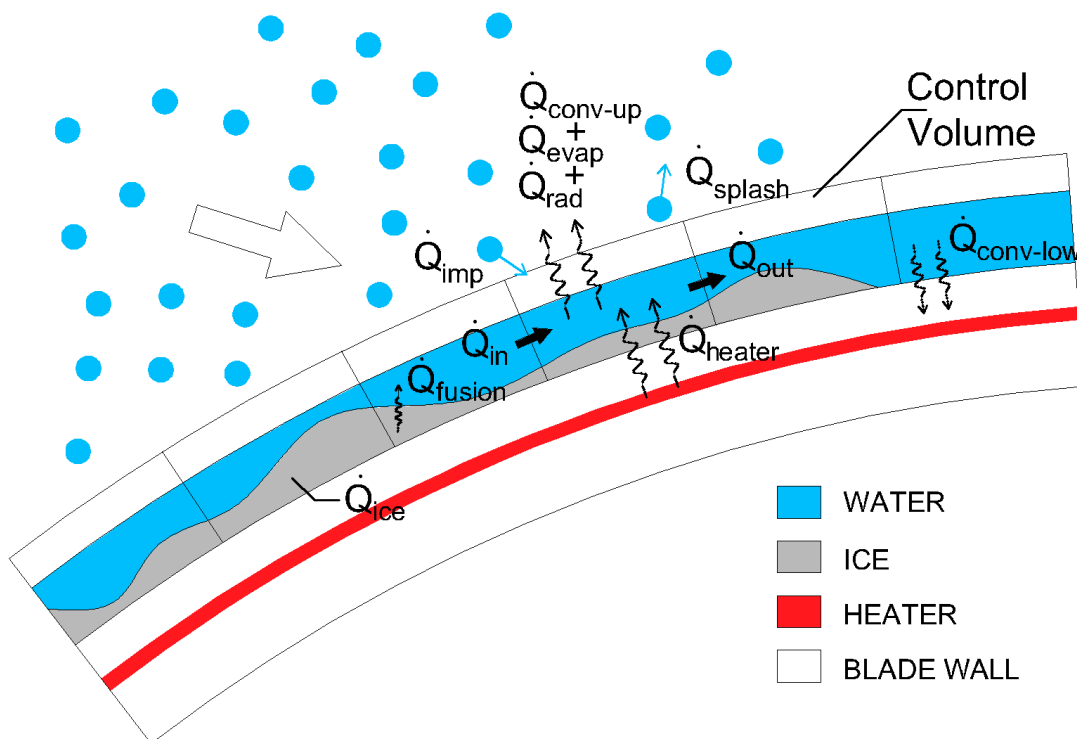
$$F_\theta = C_{cf} \frac{\sigma(1 - \cos \theta_c)}{\Delta_{cell}} n_{cl} \quad (3.48)$$

where C_{cf} is an empirical constant taken, θ_c is the contact angle between the surface and the liquid, Δ_{cell} is the cell width, and n_{cl} is the normal direction to the liquid surface.

In addition to the previously detailed sources, some additional sources that occurs only during ice formation process will be explained in the next section.



(a)



(b)

Figure 3.4: SWIM model source terms in (a) mass and (b) energy conservation equations

3.5.2 Shallow Water Icing Model (SWIM)

SWIM is a thermodynamic model that consists of conservation equations of the three thermodynamic quantities, namely: mass, momentum, and energy, of the liquid film on the blade surface in partial differential equations form. The main advantage of using this model is that it depends on using the partial differential equations derived from Navier-Stokes equations of liquid film flow over a surface. Therefore, this model fits with OpenFOAM liquid film solvers that also work with the same concept. The only change that shall be introduced to OpenFOAM to be able to apply this model was to add some source terms to mass, momentum, and energy conservation equations that represent specific phenomena that happen during the ice accretion process.

Governing Equations

Bourgault et al. [95] presented the SWIM model for the first time in their work in the year 2000. After that, this model gained so much trust in both research and industry to simulate ice accretion on aerodynamic bodies like aircraft, helicopters, wind turbines, etc. According to the article of Bourgault et al., SWIM model equations reads as follows:

$$\rho_w \left[\frac{\partial \delta}{\partial t} + \nabla(\bar{u}\delta) \right] = S_{mass} \quad (3.49)$$

$$\bar{u}(x) = \frac{1}{\delta} \int_0^\delta u(x,y) dy = \frac{\delta}{2\mu_w} \tau_{wall}(x) \quad (3.50)$$

$$\rho_w \left[\frac{\partial \delta C_w \tilde{T}}{\partial t} + \nabla(\bar{u} \delta C_w \tilde{T}) \right] = S_{energy} \quad (3.51)$$

Equations 3.49, 3.50, and 3.51 are mass, momentum and energy equations in SWIM model respectively. It can be noted that Equ. 3.50 is a very simplified form of momentum equation. However, in OpenFOAM, a more sophisticated form of momentum equation of water film is solved to ensure a more realistic film behavior. The form implemented in OpenFOAM (see equations 3.28, 3.32, and 3.31) is used in this work.

It also should be noted that in case of icing, few terms in mass and energy source term equations should be slightly modified to adapt to the ice formation process. In equations 3.30 and 3.33, $\dot{m}_{imp,net}$ can be calculated by:

$$\dot{m}_{imp,net} = u_\infty LWC \beta \quad (3.52)$$

accordingly, $\dot{Q}_{imp,net}$ becomes

$$\dot{Q}_{imp,net} = u_\infty LWC \beta \left[C_w \tilde{T}_{d,\infty} + \frac{|u_d|^2}{2} \right] \quad (3.53)$$

where $\tilde{T} = T_w - T_{ref}$, u_∞ is the upstream velocity, and β is collection efficiency of the surface. A detailed explanation of term β and how it can be calculated was presented in section 3.5.1.

The above explained conservation equations also need closure relations to be used to calculate ice profile. Accordingly, compatibility relations must be satisfied, which are:

$$\delta \geq 0 \quad (3.54)$$

$$\dot{m}_{ice} \geq 0 \quad (3.55)$$

$$\delta \tilde{T} \geq 0 \quad (3.56)$$

$$\dot{m}_{ice} \tilde{T} \leq 0 \quad (3.57)$$

From the SWIM model equations and the compatibility relations mentioned above, three different ice cases can be solved, namely, rime ice, glaze ice, and anti-ice cases.

Rime Ice

In this case (also called dry ice), all the impinging water droplets are frozen. Accordingly, δ , in this case, is set to be zero. Also, \dot{m}_{ice} for each time step in this case should equal $\dot{m}_{imp,net}$. This reflected on the comparability relations that the left-hand side of relations 3.54 and 3.56 will be zero while the other two relations will be satisfied.

Glaze Ice

The second ice case which is called glaze ice or wet ice, The impinging mass is partially frozen. The frozen mass \dot{m}_{ice} in this time step can be calculated by the equation:

$$\dot{m}_{ice} = \delta A_{cs} \rho_w \left(\frac{C_w \tilde{T}}{L_{fusion}} \right) \quad (3.58)$$

where A_{cs} is the area of the control surface and L_{fusion} is the latent heat of fusion from water to ice. In the SWIM model, the ice is then assumed to be at ambient temperature T_∞ and water film is assumed to be heated to the triple point of water i.e. $T_w = 273.15^\circ K$ (and consequently $\tilde{T} = 0$) by the latent heat of fusion emitted by ice due to change of state.

3.6 Mesh generation and Re-generation

One of the most challenging steps of the procedure illustrated in Fig. 3.1 is to generate the computational grid around the iced airfoils and to regenerate the grid for each new time step. Many literature [38–49] have used the over-set grid technique to account for the irregular profile shapes. This technique wasn't adopted in this work since it is still unreliable in the latest OpenFOAM versions.

One of the other solutions is using mesh deformation solvers, `moveDynamicMesh` mesh manipulation tool, for instance, to adapt the original mesh to the new profile. However, this technique is computationally expensive since it solves equations of motion for the mesh. Also, the results are not guaranteed since the deformation is large relative to the airfoil chord length.

For the above reasons, The most suitable technique is to simply regenerate the computational grid for each time step. the challenge in this solution is to find software that can generate the

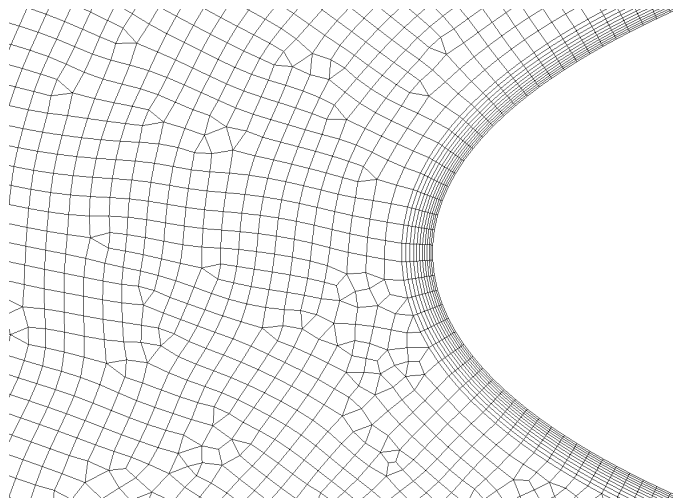
mesh using unstructured cells techniques with low computational cost. It was found that the most suitable mesh generator for this job is GMSH [144]. According to GMSH's main web page, it is an open-source 3D finite element grid generator with different 2D and 3D grid generation capabilities. Accordingly, GMSH was selected for the following reasons:

- GMSH uses a C++-based script to describe the mesh generation inputs. This makes it very easy to integrate with any programming language (like Python, which is used in this work),
- Mesh generation process can be carried out completely using Linux terminal, which enables the automation of the entire process without loading any graphical user interface (GUI),
- It has the capability of generating structured and unstructured grids. In this case, structured grids are used in the far-field to save computational time in both preprocessing and simulations. However, the area close to the airfoil is meshed using unstructured, quad-dominated grids to adapt to the new iced profile.
- Structured boundary layer cells can be easily generated using specific commands to define the boundary layers parameters (first cell height, number of cells in the layer, growth rate..etc.)
- OpenFOAM includes a converter called `gmshToFoam` that converts the output mesh file to OpenFOAM mesh format,
- It has the capability of assigning an internal surface to a `faceSet`. This makes it very easy to run the `createBaffles` utility in OpenFOAM to generate internal patches in the grid for better droplet injection,
- Ease of controlling the number of cells on the surface of the airfoil with simple inputs,
- The most important feature is that generating the grid in GMSH and converting it to OpenFOAM format is very computationally efficient. A typical airfoil icing case takes 46 s to prepare the mesh with 16 s in GMSH and the other 30 s in conversion and preparation of patches required to run the process. This computational time is calculated while using a single core of Intel Xeon CPU E5-2650 v4 12C with 2.2GHz and 256 GB main memory (RAM) available on HPC EDDY, University of Oldenburg.

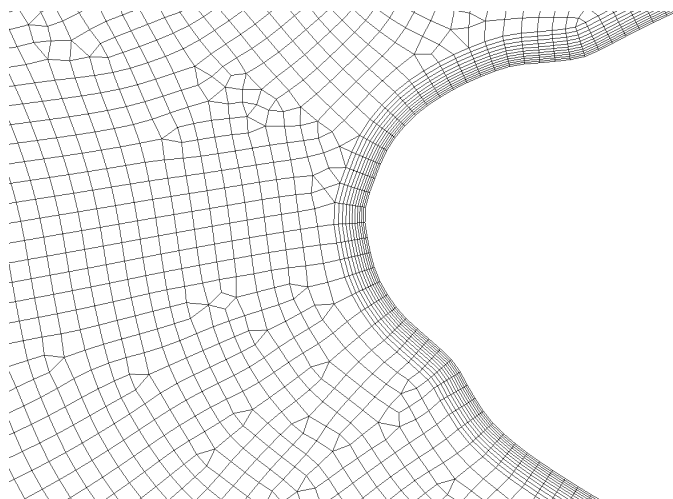
An example of the re-meshing progress for case 30, that will be explained in Ch. 5, is shown in Fig. 3.5. This example shows how fine can the mesh of each step can be in GMSH using quad-dominated unstructured grid algorithms to adapt to complex geometry of the ice.

3.7 Effects of blade design and materials

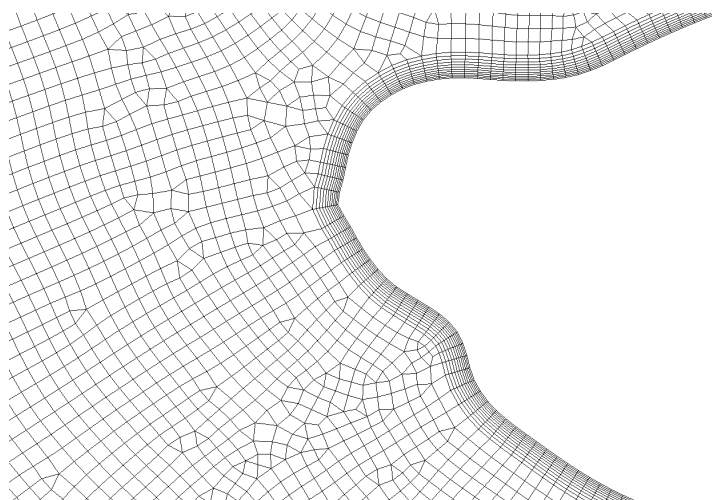
In case of cold climate, the blades should be designed to avoid ice accretion or to be able to melt down the ice after its formation on the surface. Therefore, the blades in this case are equipped with either active anti-icing system, passive ice-phobic coatings, or with both methods



(a)



(b)



(c)

Figure 3.5: Evolution of mesh around iced NACA0012 airfoil using GMSH for case 30 [2] at the start of (a) step 1, (b) step 2, and (c) step 3

to optimize the energy consumption of the anti-icing heat. To study these systems, each system should be numerically simulated within the ice accretion simulation codes. In this section, the models used to calculate the anti-icing heat and the effects coatings are introduced.

3.7.1 Anti-icing with heating

In this case, the minimum heating power required to be delivered to the water film to keep it in the liquid state to be calculated. By forcing $T_w = 273.15^\circ K$, which is the temperature lower threshold of liquid state of water at 1 bar, into the equations and also by setting $\dot{m}_{ice} = \dot{Q}_{ice} = 0$, anti-icing heating power \dot{Q}_{cond} can be calculated from the equation:

$$\dot{Q}_{anti-ice} = \delta A_{cs} \rho_w (C_w \tilde{T} + L_{fusion}) / \Delta t \quad (3.59)$$

It should be noted that this required heating power is the minimum heating power delivered to the water film. However, the actual required heating power from the anti-icing system is much higher than this value. This is because of the actual design of the anti-icing system.

In case of using hot air flow inside the blade, convective heat transfer between the hot air and the inner side of the blade and between the water film and the outer side of the blade along with the conductive heat transfer inside the blade material should be calculated. Using such a technique requires much higher heating power than the calculated because hot air provides heat to the whole blade surface while most of the required heating power is needed only near the leading edge.

In the case of using electrical heaters embedded between the blade composite layers, the heating power can be concentrated. However, heat will also diffuse within the solid blade walls.

In both cases, if it is required to calculate the exact heating power required for anti-icing, the simulation of conjugate heat transfer (CHT) process is to be done. This process is usually complicated and it is out of the scope of this thesis.

3.7.2 Effects of ice-phobic coatings

As mentioned in Sec. 1.4, using ice-phobic coatings is one of the modern, innovative ideas that have a growing interest in the industry because of its expected capabilities of decreasing the anti-icing heat required for icing prevention. To understand how this happens, the different effects of this type of coatings are explained in the following sections.

Droplet splash

Hydrophobic and ice-phobic coatings are characterized by increasing the contact angle between the substrate and the water droplet. As explained earlier, the increase of contact angle decreases the amount of energy lost during the droplet retraction in the form of adhesion force between the liquid and the solid substrate. Accordingly, the amount of splashed water droplets increases by decreasing the wettability of the surface. To express the equations in a more independent value, the droplet incidence conditions are expressed in terms of Weber number. Weber number represents the ratio between drag force on the droplet to cohesion force ($We = \frac{\rho D_d U_d^2}{\sigma}$).

The exact amount of the critical conditions of the droplet that leads to splashing is still under

research since it involves different physical phenomena. In ordinary, Bai and Gosman's model found in Bai et al. [145, 146] is implemented in OpenFOAM. However, in the case of hydrophobic surfaces, the model should be altered to consider the low wettability. In this work, the conclusions of the work of Roisman et al. [123] should be used (Eq. 2.21). This equation states that:

$$We_{average} = 10.2 \left(\frac{R_{pk}}{R_{sm}} \right)^{-0.83} \quad (2.21)$$

where $We_{average}$ is the average weber number at which the droplet exhibits prompt splashing. After that, the residual mass on the surface after splashing is calculated using Bai and Gosman's model [145] where:

$$\frac{m_{splash}}{m_{imp}} = 0.2 + 0.6Rnd \quad (3.60)$$

where Rnd is a random number. This new value of critical Weber number is much less than the critical value used in Bai and Gosman's model if the structured surface is well designed. In a typical case, the critical Weber number when using Bai and Gosman's model $We_{critical} \approx 800$ while in case of Roisman's model $We_{critical} \approx 10$. This means a much higher probability of the droplet exhibiting splashing behavior upon impinging the surface.

Convective heat transfer coefficient decrease

The basic idea that gives the hydrophobic coatings their ability to increase the contact angle between them and liquid droplets is by decreasing the contact area between the surface and liquid. However, this decrease should also lead to a decrease in convective heat transfer between the liquid and the solid substrate. This leads to a slower heat transfer between the cold solid substrate and relatively warmer liquid film and hence a slower rate of water fusion and conversion into ice.

Increasing water film slip

As explained in Sec. 2.6.2, Choi and Kim [3] has shown that the slip effect of a structured surface can occur when the roughness height and the distance between posts are within limits indicated in equations 2.17 and 2.18. Fig. 3.6 shows that this phenomenon happens when the roughness elements are close and high enough to prevent the water surface from completely touching the solid surface. In this case, the slip length δ can be calculated by:

$$\delta = b(\mu_l/\mu_a - 1) \quad (3.61)$$

where μ_l and μ_a are the viscosity of liquid (water in this case) and air respectively. For hydrophobic and ice-phobic coatings, such a microscopic structure should be present to achieve this phenomenon.

3.7.3 Surface roughness analysis

To apply Eq. 2.21, the structured surface should be analyzed to extract the value of R_{pk} and R_{sm} for the coating. The DIN-EN-ISO 4287 standard [147] details the different roughness pa-

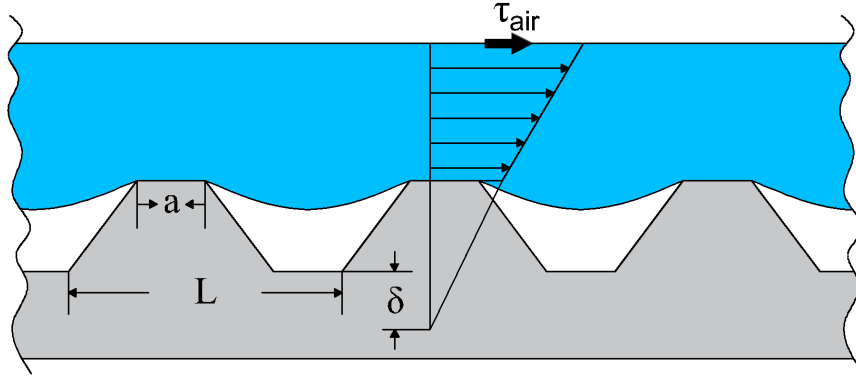


Figure 3.6: Slip phenomenon in hydrophobic surfaces(adapted from Choi and Kim [3] and Ybert et al. [4])

rameters including these two required parameters. The profile element widths (R_{sm}) can be found easily by averaging the distances between every two corresponding points of the roughness elements. In other words, the distance between the roughness points intersects with mean roughness height. To extract the Reduced peak height (R_{pk}), the following steps should be followed:

1. A proper sample of the layer should be scanned with one of the scanned techniques to extract the roughness heights as shown in Fig. 3.8a.
2. The raw data should be de-trended to get rid of any curvature in the surface. This de-trending process is done by finding a smooth trend line of the layer and subtracting the coordinate of this trend line from each measured point to calculate the absolute roughness height as shown in Fig. 3.8b.
3. Abbott-Firestone diagram should be plotted by plotting the cumulative probability of roughness presence higher than each roughness height and applying the procedure described in Salcedo et al. [148].

The R_{pk} and R_{sm} are then fed to the in-house code hydrophobicSplash in the cloud's surfaceFilmModel to simulate the splashing process as explained earlier.

3.8 Local icing conditions calculation

As explained earlier, wind speed, ambient temperature, liquid water content, and mean volumetric diameter is the main icing parameters that influence the icing process and the final ice profile on the structure. From the current work, it was concluded that getting these parameters

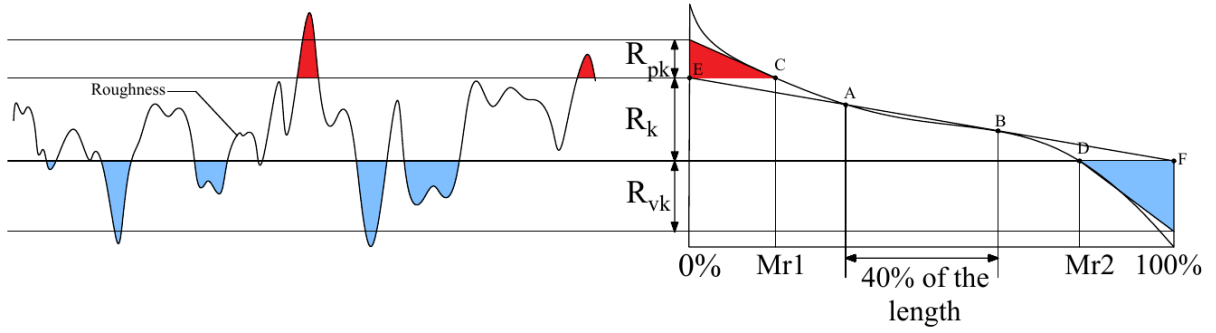


Figure 3.7: Abbott-Firestone diagram to calculate R_{sm} and R_{pk} (regenerated from Ref. [5])

for a certain wind site is not an easy task. Therefore, a detailed methodology of extracting such parameters from open-source wind data will be explained in detail.

First, the New European Wind Atlas (NEWA) [6] will be used in this work to get the icing parameters. From NEWA different wind conditions can be extracted like: wind speeds at different heights, air temperatures, air densities, specific humidity, and many other parameters. All these data are available for download from the NEWA website. For example, Fig. 3.9 shows the minimum air temperature at 100m height above sea level over Germany. The same data can be downloaded from the NEWA website and also analyzed for any required location. For example, ambient temperature histogram and cumulative histogram occurred at ForWind Lab - the University of Oldenburg (located at 53.15336°N , 8.16353°E) at 75m height along the year 2017 is shown in the figure.

An in-house Python code was made to analyze the data downloaded for any site conditions to plot the histogram of ambient temperature occurrence (shown in Fig. 3.10) and the corresponding specific humidity (W) and air density (ρ_{air}). By knowing these parameters, LWC can be assumed to be:

$$LWC = \frac{W}{\rho_{air}} \quad (3.62)$$

Nygaard et al. [149] have shown in their work that MVD can be calculated using the equations:

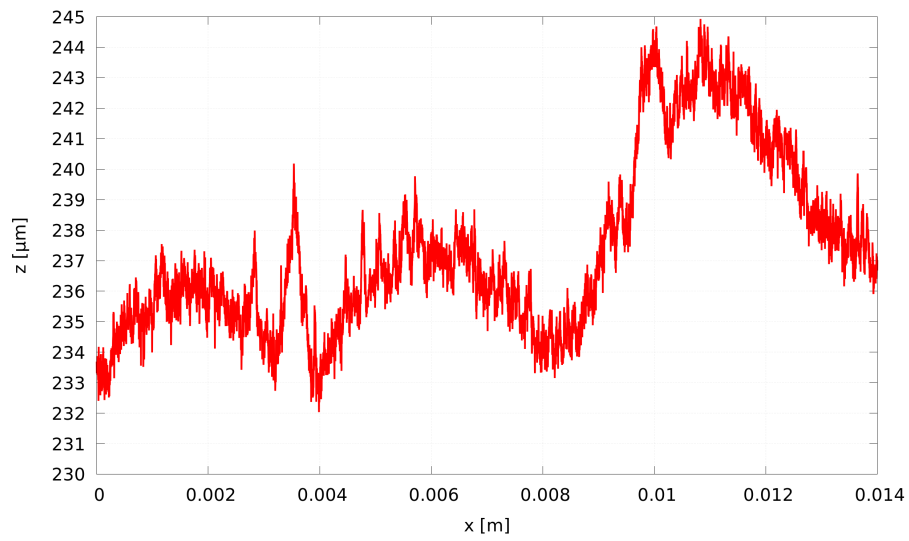
$$MVD = \frac{3.672 + \mu}{1000\lambda} \quad (3.63)$$

where μ is the droplet size distribution shape parameter and λ is the slope parameter. These two parameters can be calculated by using the equations:

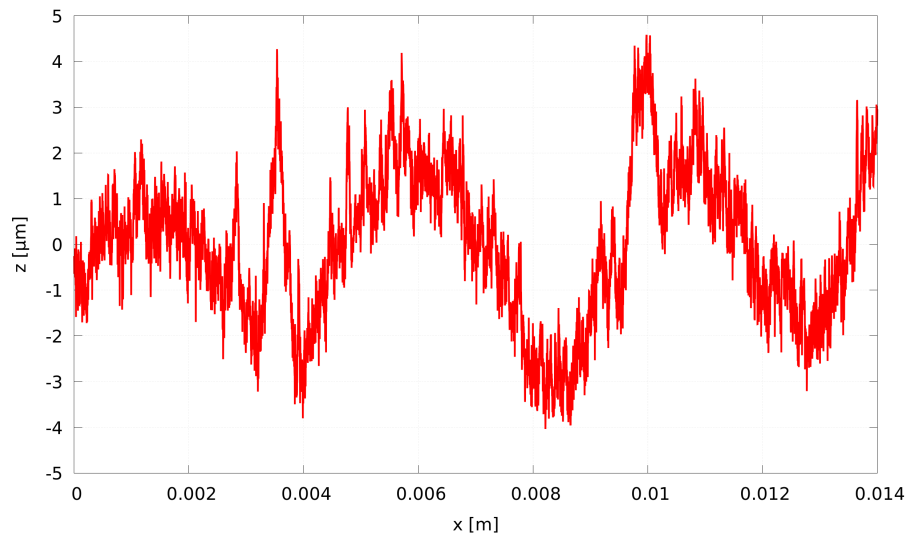
$$\mu = \min\left(15, \frac{1000}{N_c} + 2\right) \quad (3.64)$$

$$\lambda = \left[\frac{\pi \Gamma(4 + \mu)}{6 \Gamma(1 + \mu)} \frac{N_c}{LWC} \right] \quad (3.65)$$

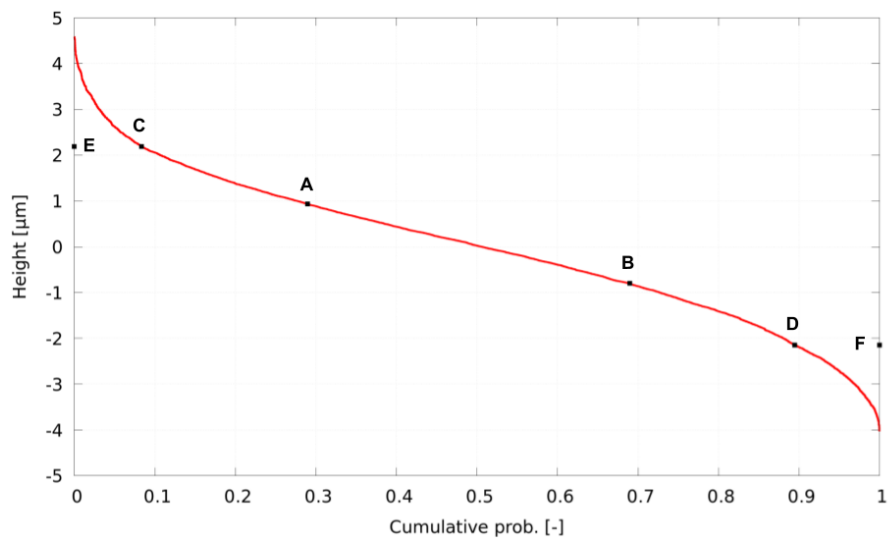
also, N_c is the droplet concentration per cubic centimeter. As explained by Nygaard et al. [149], N_c should equal 250 and LWC in gm/m^3 . These equations resulted in $LWC = 1.864 gm/m^3$ and $MVD = 29.46 \mu m$ at 270.15°K that occurs about 100 hr/yr at this location.



(a)



(b)



(c)

Figure 3.8: a) Raw roughness heights, b) De-trended roughness heights, and c) Abbott-Firestone diagram of Layer 1 (taken from NEWA [6])

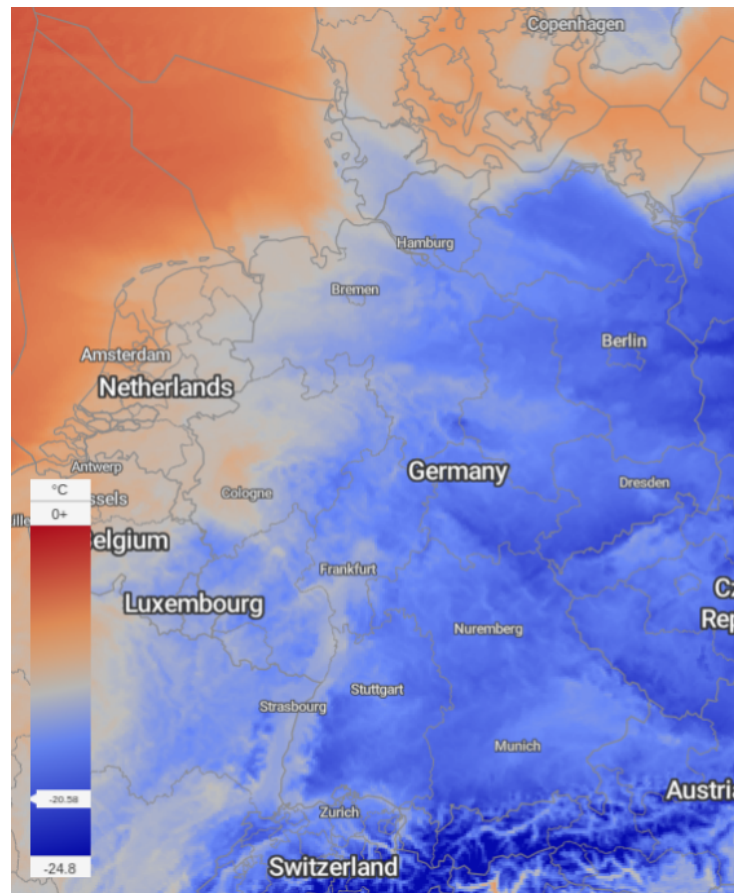


Figure 3.9: Minimum air temperature at 100m height above sea level over Germany

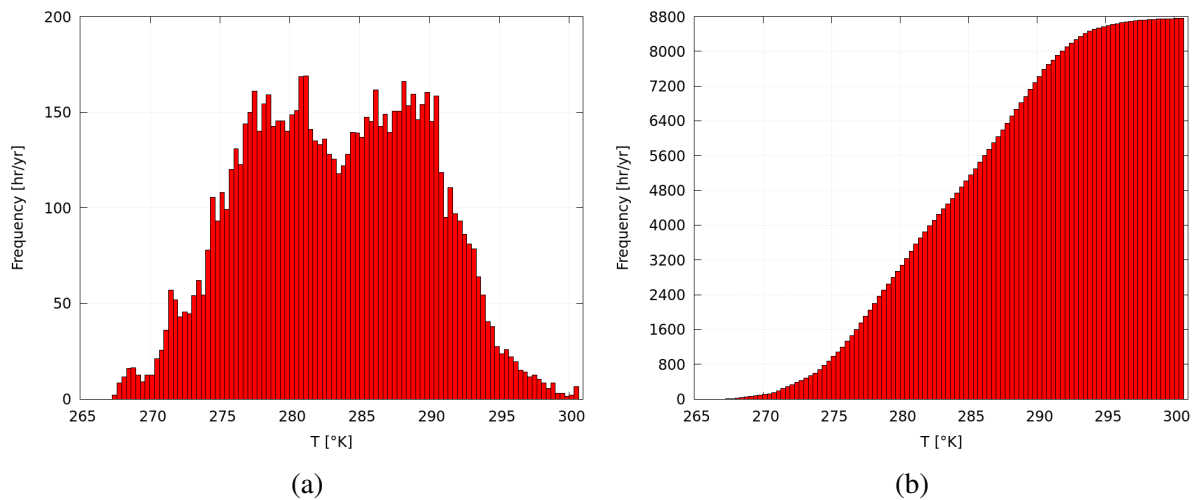


Figure 3.10: a) Histogram and b) Cumulative Histogram of ambient air temperature over the year 2017 at 53.15336°N, 8.16353°E extracted from the NEWA [6]

3.9 Description of the new OpenFOAM codes

After explaining the different mathematical models behind the simulation of ice accretion, all the aforementioned physical phenomena and numerical models should be simulated in a certain order to be able to simulate the process. The new OpenFOAM based framework used in this thesis to simulate ice accretion consists of:

1. Background airflow simulation: using `rhoSimpleFoam` to simulate velocity, pressure, and temperature of this flow field necessary for the next steps of ice accretion. Also, to simulate the airflow field over the rough surfaces resulting from ice correctly, rough wall functions (rwf's) should be used.
2. Lagrangian particle tracking (LPT) of water particles: This is done using `bouyantReactingFoam` and using the option of not solving the background flow (frozen background flow assumption). From this step, a new field is generated named `mImp` which is a surface scalar field with values representing the mass impinging on the surface per second for each control surface.
3. Ice formation and new profile calculation: This part uses also `bouyantReactingFoam` but with using the surface film solution only. To simulate the ice profile, a new liquid film phase change model named `icingPhaseChange` was implemented. This phase change model calculates ice mass, liquid water mass, and ice thickness for each control surface.
4. Calculation of the new ice profile: using a Python code to read the generated ice thickness field and offsetting the cell center of each control surface by a distance that equals the ice thickness.
5. Mesh modification: by using GMSH to generate the mesh of the new profile calculated from the previous step.
6. All the former steps are ordered and connected with a Python code that handles the different solvers and performs post-processing.

In these procedures, the following OpenFOAM modules were newly implemented:

1. The DLR and Colebrook's rough wall functions (named `dlrRoughWallFunction` and `colebrookRoughWallFunction` respectively)
2. A phase-change like module name `lagrangeImpingement` that stores the `mImp` field.
3. Ice phase change module named `icingPhaseChange` that simulated the ice formation using the SWIM model.
4. Post-processing function named `faceCenters` and `normalVector` to store the face center coordinates and the normal vector of each control surface of the wall.

3.10 Conclusions and remarks

From the above-explained methodology, it can be seen that the ice accretion phenomenon is a multi-physics phenomenon that requires the simultaneous numerical simulation of different physical problems. However, and for the sake of simplification and saving computational costs, each of the three steps of the ice accretion process, namely: background flow, particle tracking, and film and ice formation simulations, can be separated and performed one after the other. Despite that such an approach will lead to less accurate results, it is inevitable to carry out the simulations with this method to ensure an achievable computational cost.

Another important remark is that some models describing this complicated phenomenon are empirical models, splashing on ice-phobic coatings for instance. This implies that the results of these models are not necessarily accurate and need further improvement and validation.

Chapter 4

Flow field simulation over rough ice surfaces

4.1 Introduction

As explained in detail in the previous chapter, the first step towards simulating the ice accretion process is to simulate the background flow. This step should be carried out as accurately as possible to ensure an accurate tracking for water carried by the airflow field. However, this process can be very computationally expensive since it can involve the aerodynamic simulation of very complicated ice profiles.

In this chapter, one of the approaches explained in chapters 2 and 3 will be detailed, namely using boundary conditions and rough wall functions to model the changes in the velocity field around the solid surface without resolving the details of this rough surface. This chapter shows the implementation wall functions which were previously published. The accuracy of these wall functions will be compared by comparing their results when used to simulate airfoils with real ice profiles collected from wind sites.

4.2 Rough wall functions (rwf)

In this chapter, the focus will be on three rwf's: Momentum rwf published by da Silva et al. [69] and explained in detail in Sec. 3.3.4, DLR rwf published by Knopp et al. [62] and explained in equations 2.7, and $k-\omega$ wall function fitted to Colebrook experimental results explained by Chedevergne and Aupoix [67].

To apply the aforementioned rwf, equations DLR and Colebrook rwf's were implemented within the OpenFOAM framework. The Momentum rwf is already available in OpenFOAM (named `nutURoughWallFunction`). However, the other two wall functions, namely DLR and Colebrook rwf, are not available. However, before proceeding in the comparison between the three rwf, the results from each of them should be validated against experimental results.¹

¹The results in this chapter were published in: "Yassin, K., Kassem, H., Stoevesandt, B., Klemme, T., and Peinke, J.: Numerical Investigation of Aerodynamic Performance of Wind Turbine Airfoils with Ice Accretion, Wind Energ. Sci. Discuss. [preprint], <https://doi.org/10.5194/wes-2021-3>, in review, 2021."

4.2.1 Validation of the rough wall functions

The newly implemented rwf's within the OpenFOAM framework should be tested and validated before proceeding to the simulation cases with real ice profiles. This is done by comparing the simulation results using the rwf's against experimental results published by Achenbach [150]. In his paper, the author analyzed the flow field around a circular copper cylinder with paramedical roughness elements to study both fluid flow and heat transfer. This experiment was done on a 0.5 m length, 0.15 m diameter copper cylinder at different roughness heights and Reynolds numbers. It is known that RANS simulations of the flow field around a cylinder are already unstable and hard to predict, especially when it comes to the prediction of separation location. However, this case was selected to identify any false implementation of rwf's in OpenFOAM that may lead to unstable numerical solutions.

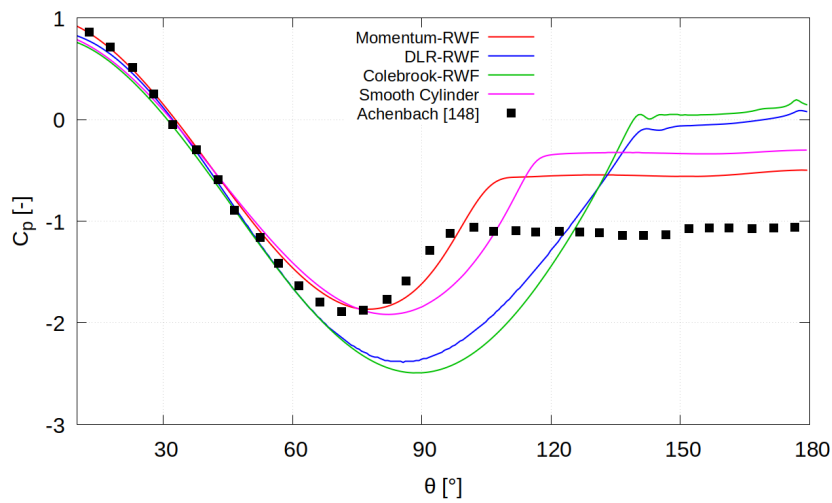
Fig. 4.1 shows the results of simulating circular cylinder at $Re = 4 \times 10^6$ and $K_s = 75 \times 10^{-5}$ m, 3×10^{-3} m, 9×10^{-3} m, and smooth cylinder surface respectively. Despite the experiments being carried out at different Re numbers, only the comparison with $Re = 4 \times 10^6$ is considered since this value is in the same order of magnitude of the wind tunnel results of iced airfoils that will be shown in the next sections. Also, this work did not take into consideration the heat transfer results of Achenbach. The main focus was the airflow only. As shown in Fig. 4.1, all of the three rwf's managed to predict C_p of this case correctly between 0° and 60° of the cylinder surface. For angles higher than 60° , each rwf had different behavior. For the Momentum rwf, a good agreement between numerical and experimental results can be predicted up to 100° where the model fails to correctly simulate the separation location. On the other hand, both DLR and Colebrook rwf's underestimate the value of C_p and overestimate the separation location over the cylinder.

Figures 4.1-a, b, and c also show the results of simulation of smooth, resolved cylinder simulation using Splart-Allmaras Turbulence Model. In comparison with Momentum rwf simulations, it can be noticed that the rwf caused earlier prediction of the location of separation. This matches with the fact that a rough surface prevents the transition from laminar to turbulent flow and initiates separation earlier.

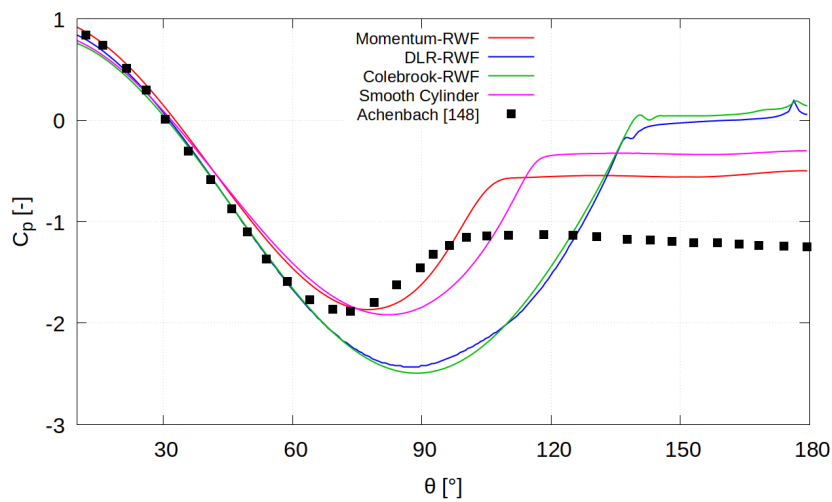
While analyzing the results of these validation cases, one must keep in mind that such a complicated simulation case of flow over a cylinder at a high Reynolds number using steady-state RANS simulation is difficult. Accordingly, one should not expect good agreement between numerical and experimental simulation on all locations over the cylinder. These low expectations come from the fact that all RANS models fail to accurately predict the flow separation location even for airfoils with relatively high AoA. For the cylinder case, the situation is even harder. Since the aim of this validation process is to make sure that the rwf's have been correctly implemented and are working properly and not to judge the mathematical behavior of these rwf's, it can be concluded that the rwf's follow the trend of C_p distribution over the cylinder.

4.2.2 Simulation of iced airfoils

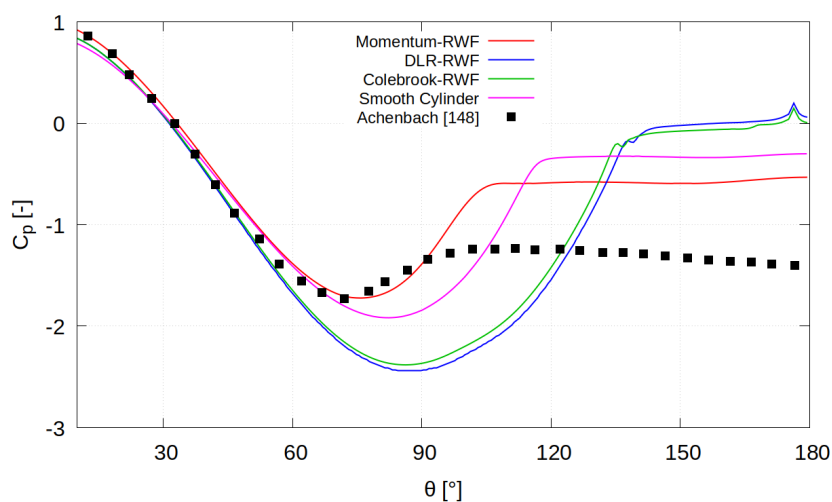
After the validation of the implemented rwf's, the same setup is used to simulate wind turbine airfoils with ice accretion profiles. The ice profiles were collected from the site by the turbine manufacturer and project partner SENVION. In this work, two ice profiles were tested: profile 1 and profiles 2 that are shown in Fig. 4.3.



(a)



(b)



(c)

Figure 4.1: Pressure coefficient C_p distribution over rough cylinders using implemented wall functions at $Re = 4 \times 10^6$ and: (a) $K_s = 75 \times 10^{-5}$ m, (b) $K_s = 3 \times 10^{-3}$ m, (c) $K_s = 9 \times 10^{-3}$ m where $\theta = 0^\circ$ at stagnation point and increases downstream.



Figure 4.2: The wind tunnel setup of testing profile 1 in open section wind tunnel at the German-Dutch wind tunnels

After that, the ice profiles were scanned and molded to airfoil leading edge and then tested in a wind tunnel by SENVION and the German-Dutch wind tunnels [151] as shown in Fig. 4.2.

Both ice profiles take the horn-ice form which usually occurs under severe icing conditions and also both of them extend to 7.5-10 % of chord length. However, it can be noticed that profile 1 is smoother than profile 2. Also, it can be noticed that profile 1 takes a more aerodynamic shape than profile 2 since profile 2 has two horns which form a stagnation area between them.

Mesh generation for the iced profiles:

To use rough wall functions, the height of the first cell center should be large enough to cover the roughness element. By converting the rough surface into a smoother one, the resulting grid is much coarser than the grid required by smooth wall functions which require $y^+(1) < 1$ to be able to correctly simulate the boundary layer. Accordingly, the studied approach in this work requires less computational resources. In the case of the two ice profiles studied in this work, to properly generate a grid that fulfills the condition of $y^+(1) < 1$, is found to require a number of cells $\approx 4 \times 10^5$ cells in 2D simulations. On the other hand, when using rough wall functions with the proper first cell height and roughness smoothing, it is found to require $\approx 1 \times 10^5$ cells in 2D simulations. A comparison between smooth and rough wall function grids is shown in Figures 4 and 5. Resulting from the numerical setup described above, the computational grids

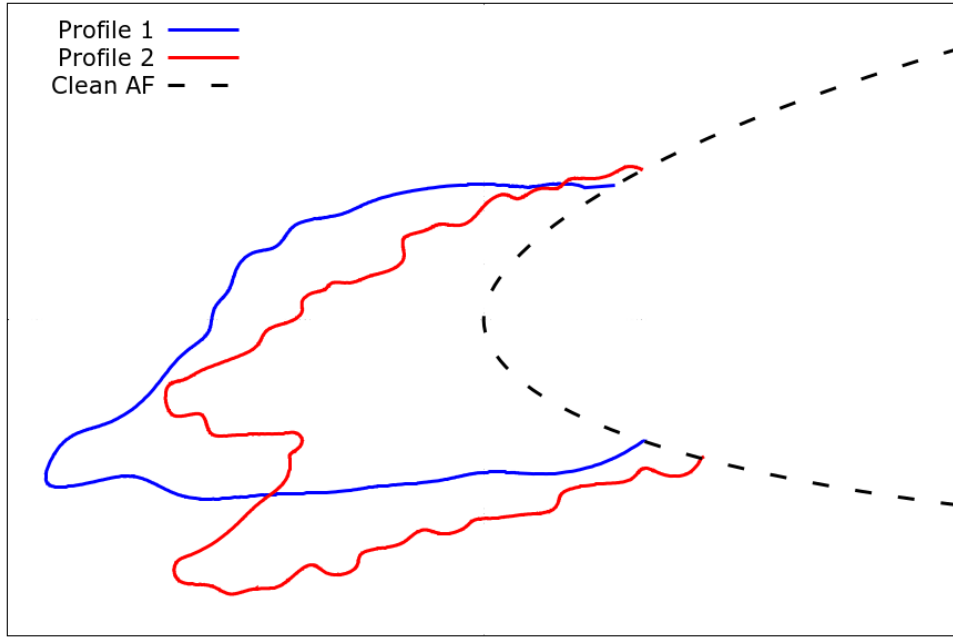


Figure 4.3: Ice profiles 1 and 2 accumulated on airfoil's leading edge

used in this work are given in Tab. 4.1.

Table 4.1: Simulation cases

Case No.	Profile	Re	y(1) [m]	AoA [$^{\circ}$]
1	profile 1	2.6×10^6	9×10^{-3}	-4° to 16°
2	profile 1	5.2×10^6	9×10^{-3}	0° to 16°
3	profile 2	3.1×10^6	10×10^{-3}	-4° to 16°

Roughness parameters calculation:

Since all rwf's treat, the rough wall as a smooth wall with a velocity shift as explained in 3.3.4, the actual rough surface of the ice profile is replaced with another equivalent smooth surface. The new smooth surface will be used to generate the computational grid around the profile and will be numerically treated as a rough surface, i.e. a velocity shift will be added to the smoothed surface. To calculate this new surface, the rough surface was smoothed with cubic splines as shown in Fig. 4.6. Knowing the distance between roughness elements and height of elements, average sand roughness height Fig. 3.2 can be calculated using Eq. (3.7) assuming roughness elements take conical shapes, then $A_p = \pi D_{avg}^2/4$ and $A_s = 0.5K_{avg}D_{avg}$. The above analysis gives results in $K_s = 1 \times 10^{-3}m$ and $1 \times 10^{-2}m$ for profiles 1 and 2 respectively.

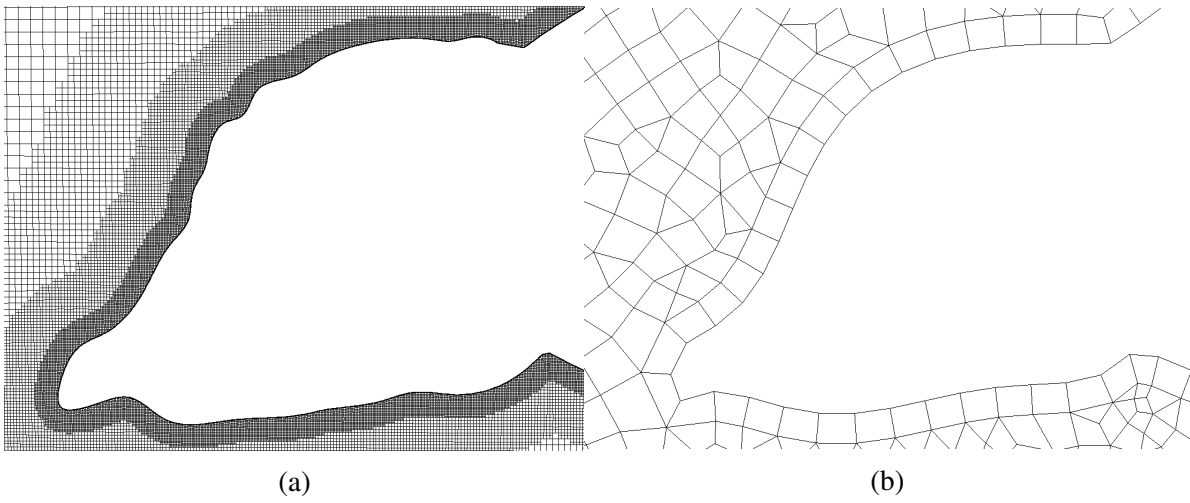


Figure 4.4: Mesh of a)rough and b)smoothened ice profile 1

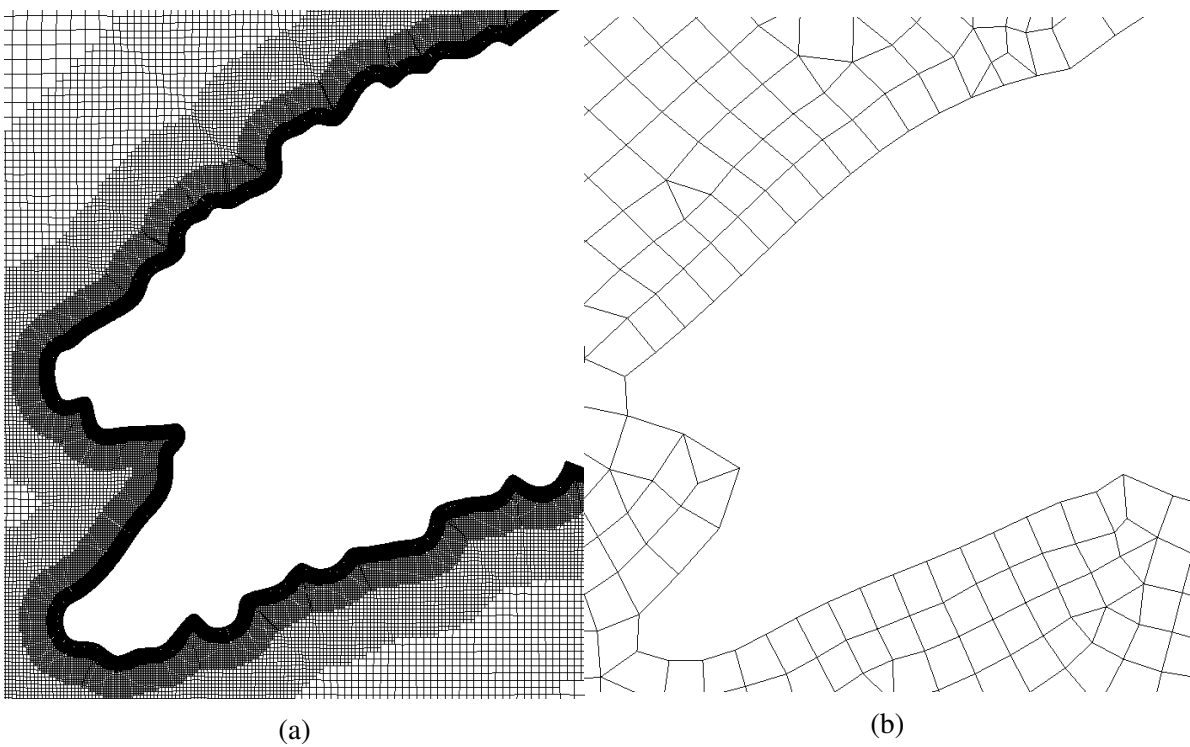


Figure 4.5: Mesh of a)rough and b)smoothened ice profile 2

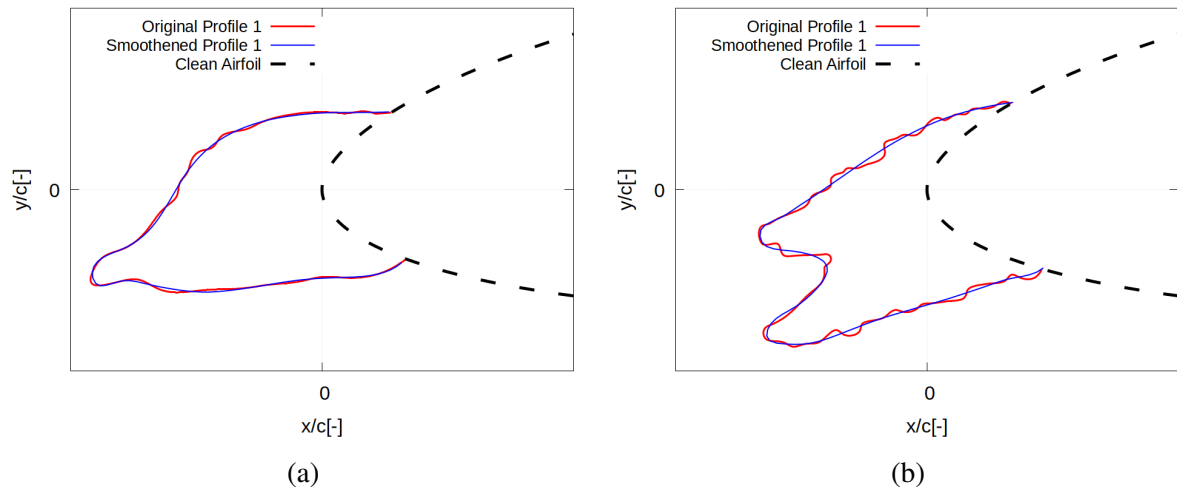
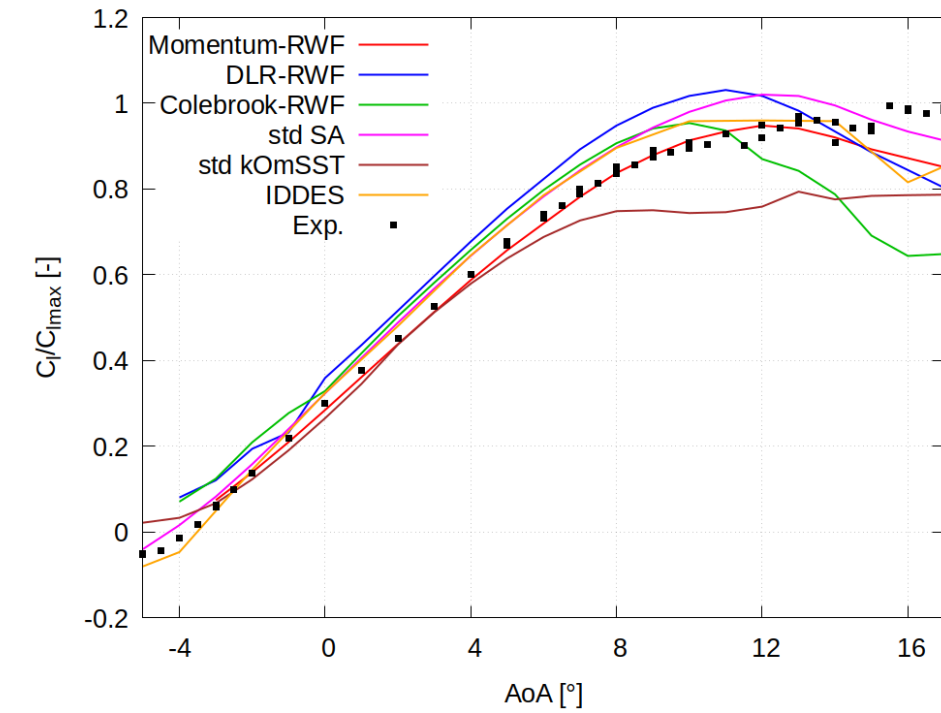


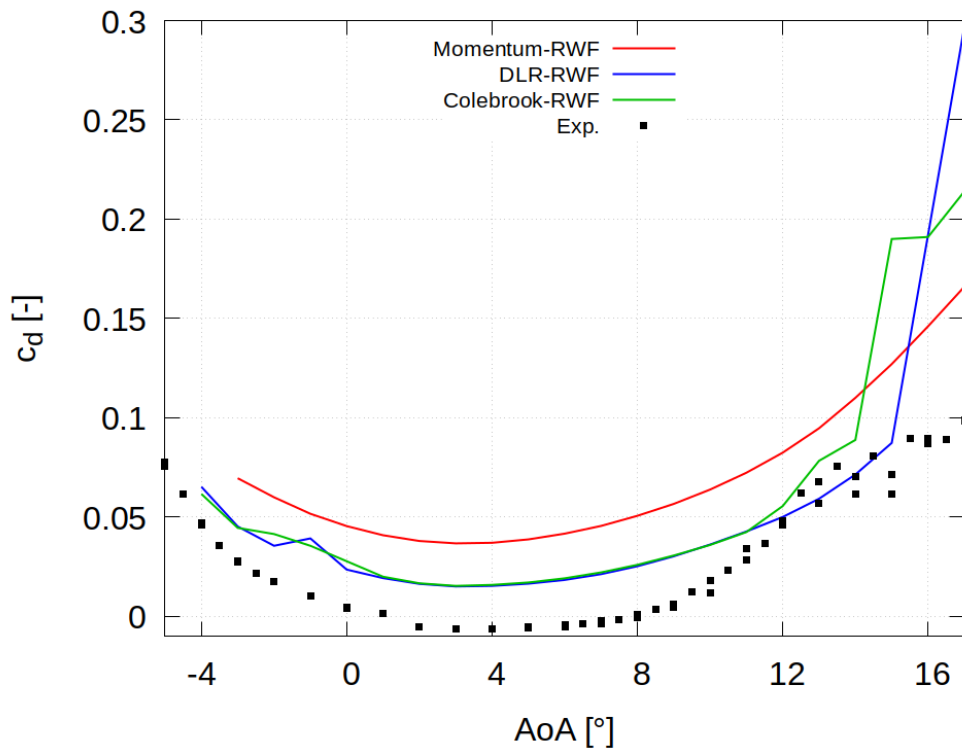
Figure 4.6: Rough vs smoothed ice profiles 1 and 2

Case 1: profile 1 at $Re = 2.6 \times 10^6$:

In this case, profile 1 was tested at $Re = 2.6 \times 10^6$, which is a relatively low Reynolds number compared to the other two cases. Fig. 4.7 shows the comparison between the predictions of each of the three rwf's with wind tunnel results. On the other hand, Fig. 4.8 gives a deeper look at the prediction of pressure distribution on the surface of the profile and compares the results with pressure-tap measurement values.

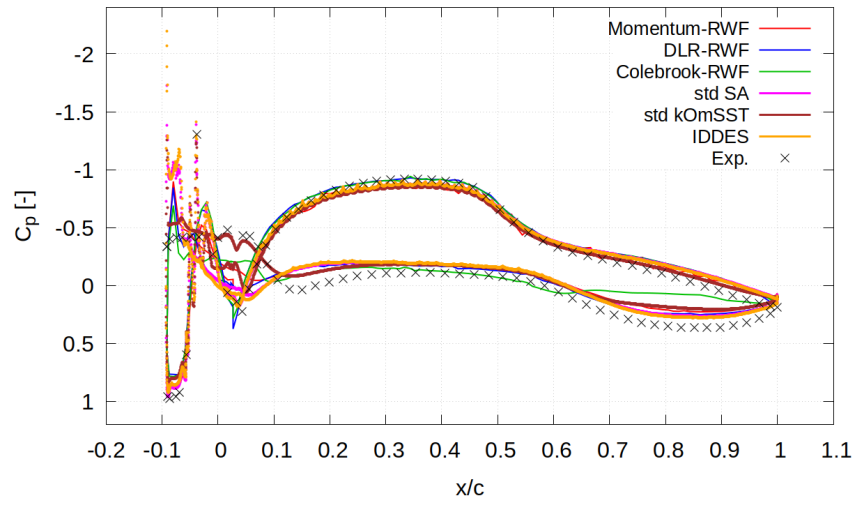


(a)

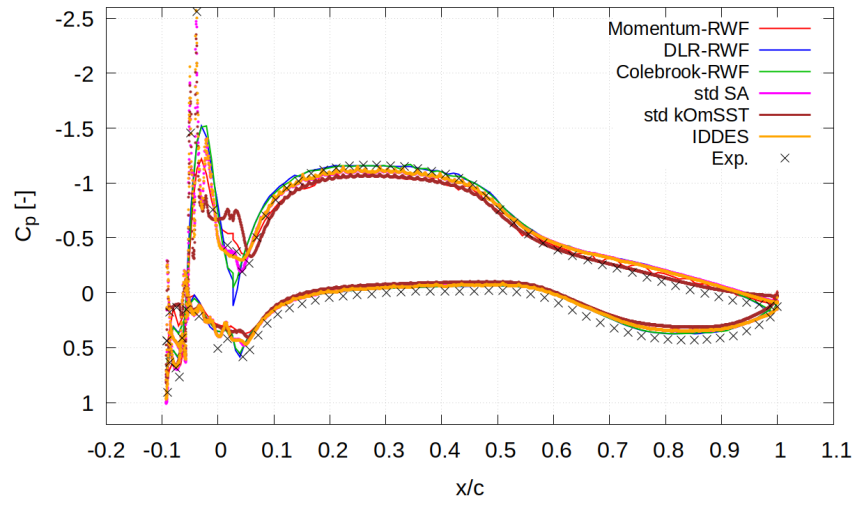


(b)

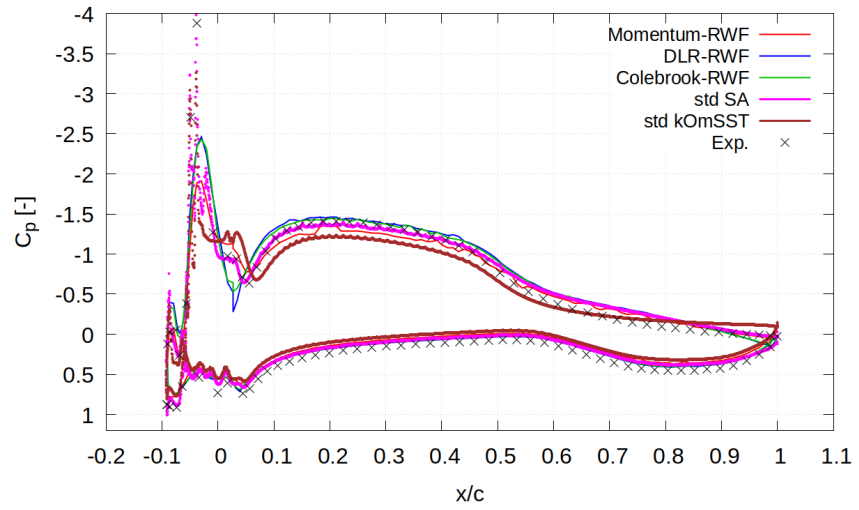
Figure 4.7: Case 1: (a) lift C_l and (b) drag C_d coefficients vs AoA for different wall functions



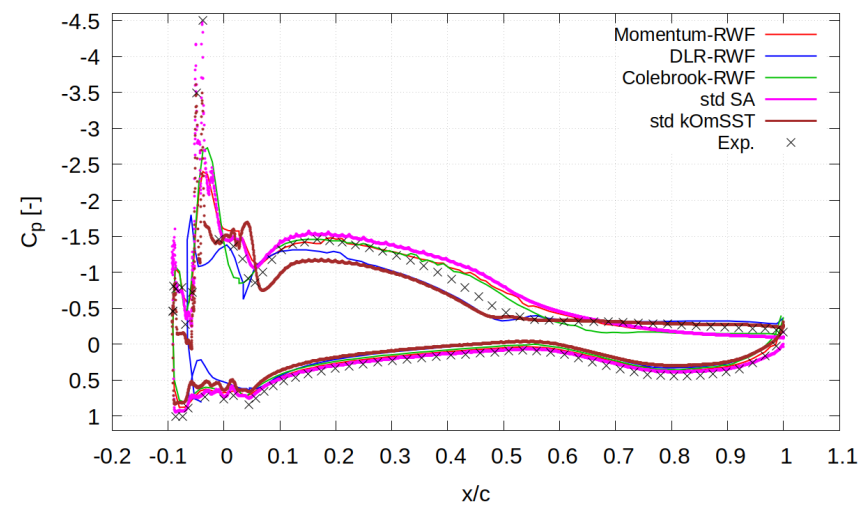
(a)



(b)



(c)



(d)

Figure 4.8: Case 1: pressure coefficient C_p distribution for AoA = (a) 0° , (b) 4° , (c) 8° , and (d) 12°

It can be noticed from Fig. 4.7, that each model has a different prediction for the maximum lift coefficient $C_{l_{max}}$ value or the angle of attack (AoA) at which this $C_{l_{max}}$ occurs. However, Momentum-rwf showed the best agreement with C_l values. On the other hand, the pressure coefficient (C_p) shows different behaviors depending on the angle of attack.

Fig. 4.8 show that the C_p distribution at AoA = 0° , 4° , 8° , and 12° respectively. At AoA = 0° , a good agreement between experimental and CFD results can be seen except for the lower surface region at $x/c \approx -0.05$ to 0.05 . At AoA's = 4° and 8° , good agreement was achieved over both smooth and rough surfaces of the airfoil. This agreement starts to suffer from some deviations at AoA = 12° . These deviations are expected due to relatively high AoA that is higher than the AoA of max C_l .

Case 2: profile 1 at $Re = 5.1 \times 10^6$:

This case is exactly like the previous case except for being tested at $Re = 5.1 \times 10^6$. This high Reynolds number is challenging for rwf's since it leads to more violent separation and hence is harder to be predicted.

This case shows good agreement (Fig. 4.9) especially in the linear region of AoA vs C_l relationship. However, over prediction of $C_{l_{max}}$ can be noticed in DLR and Colebrook rwf's results. The effect of the high Reynolds number can be seen in C_p distribution curves (Figures 4.10a-4.10d) where large differences between DLR rwf predictions and experimental results occurs for AoA = 0° and 4° . Also, Colebrook rwf shows an underestimation of pressure on the upper surface of the airfoil at AoA = 4° . While the Momentum rwf shows better agreement for all studied AoA's.

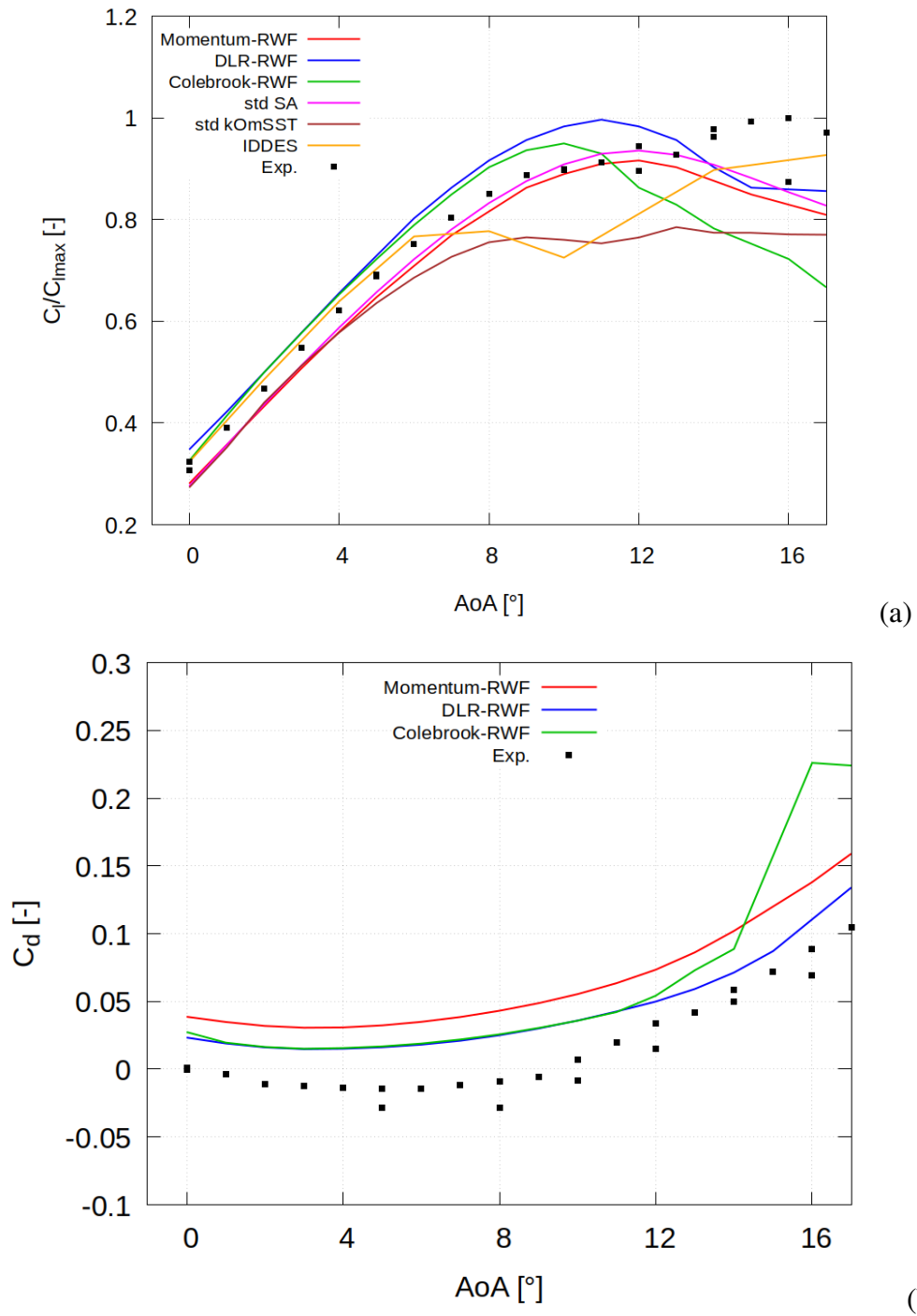


Figure 4.9: Case 2: (a) lift C_l and (b) drag C_d coefficients vs AoA for different wall functions

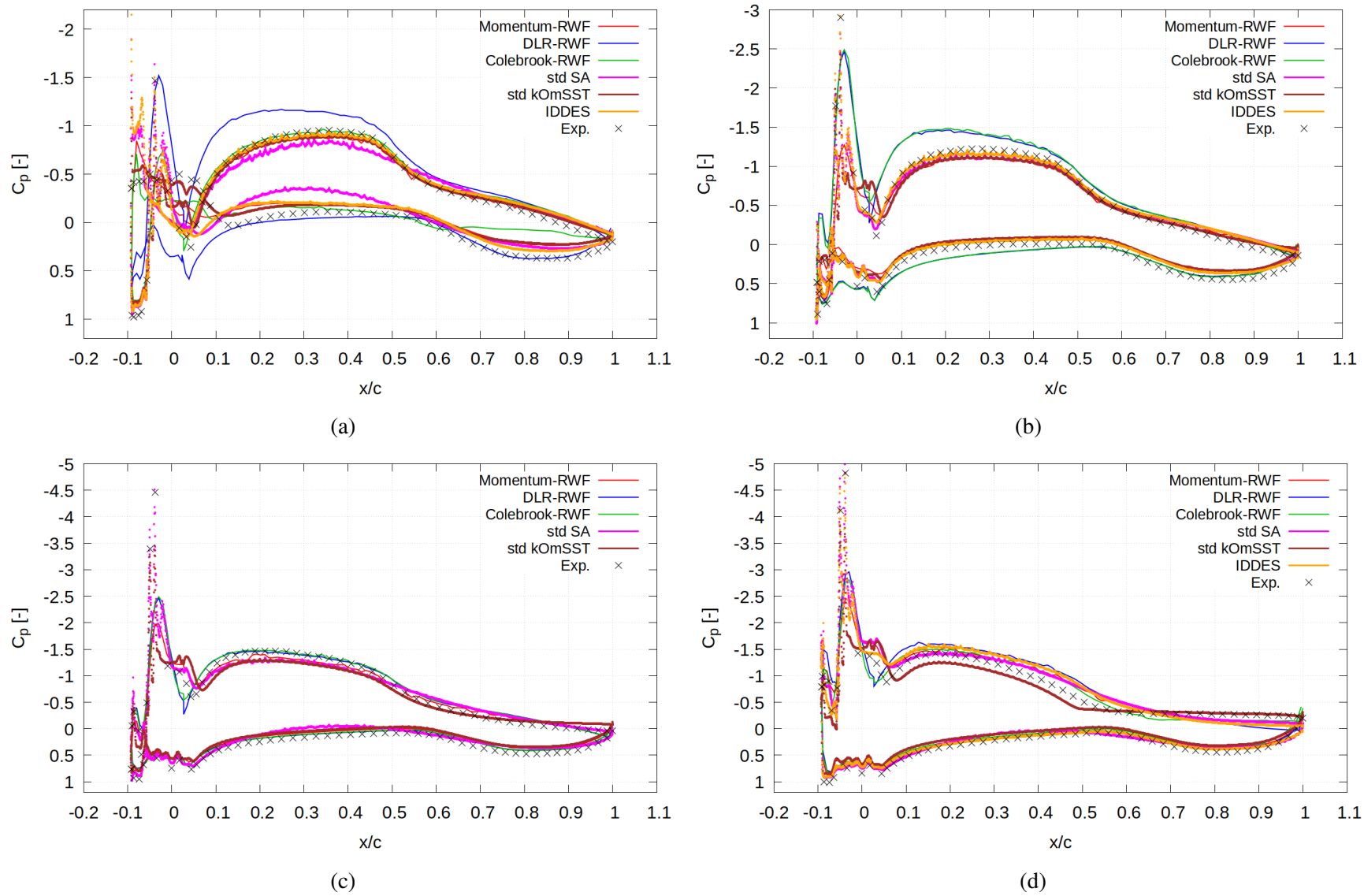


Figure 4.10: Case 2: pressure coefficient C_p distribution for AoA = (a) 0° , (b) 4° , (c) 8° , and (d) 12°

Case 3: profile 2 at $Re = 3.1 \times 10^6$:

In this case, the flow over profile 2 was simulated. It can be noticed from Fig. 4.3 that profile 2 has not only two ice horns, but also it has a rougher surface, i.e. has a higher K_s value. The effect of this complex shape can be seen Fig. 4.11. It can be noticed from this figure that the C_l curve does not show a clear stall AoA. Only the slope of the C_l curve decreases starting from AoA = 5° .

Fig. 4.11 also shows that all compared models had good agreement with experimental results for AoA's in a range between -1° and 5° . Out of this range, each model shows different behavior. For Colebrook and Momentum rwf's, the models show large deviations from experimental results for AoA's higher than 5° while DLR rwf shows better agreement in this range. For C_p distribution, Fig. 4.12a shows good agreement between experiment and all simulations at AoA = 0° on the upper surface of the airfoil while they have higher deviations from the experiment on the lower surface in the x/c range between -0.1 to 0.4. At AoA = 4° results shown in Fig. 4.12b, Colebrook and DLR rwf's show large deviations over the whole airfoil while Momentum rwf shows better agreement. In Figures 4.12c and 4.12d good agreement between all models and experimental results can be noticed.

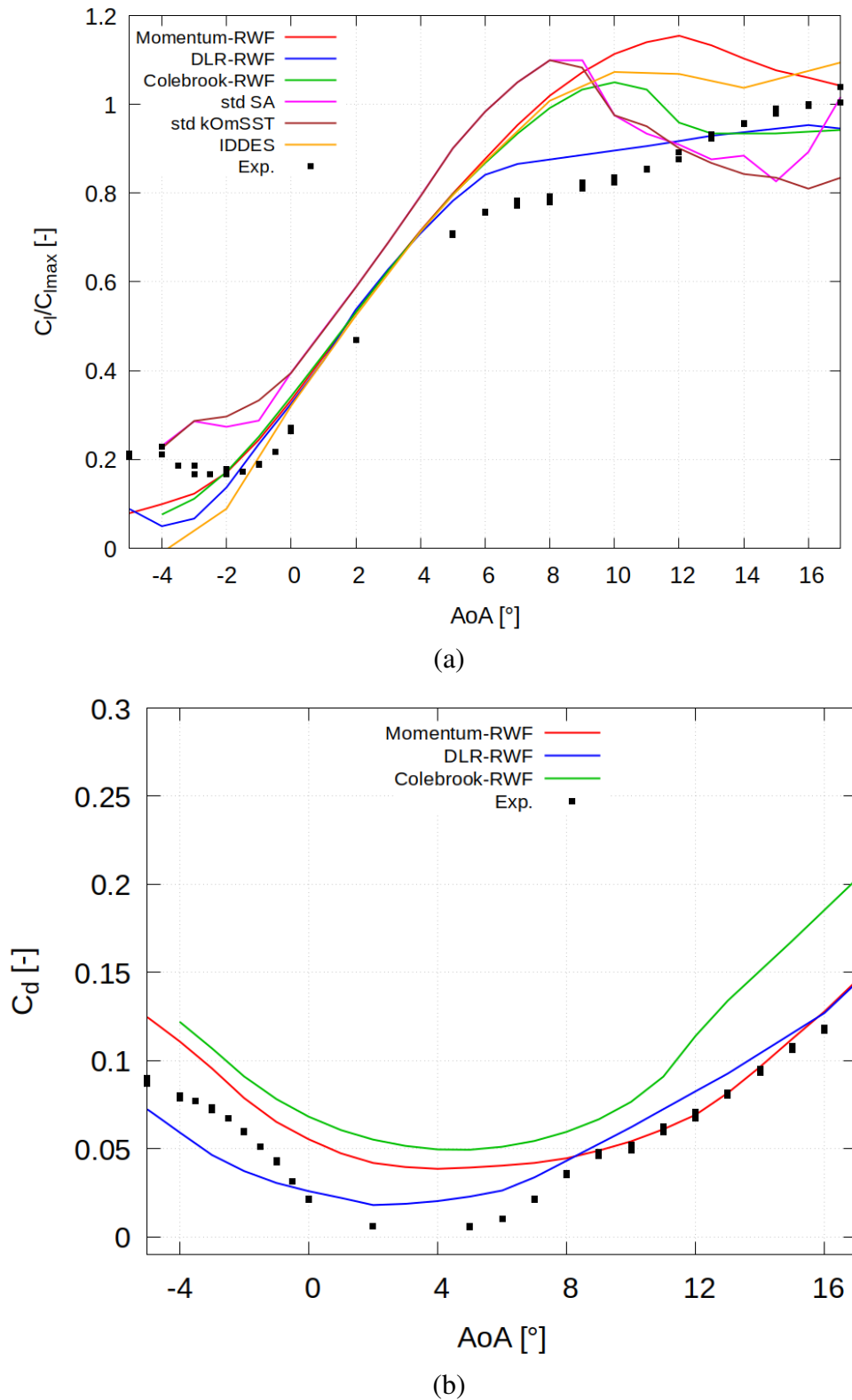


Figure 4.11: Case 3: (a) lift C_l and (b) drag C_d coefficients vs AoA for different wall functions

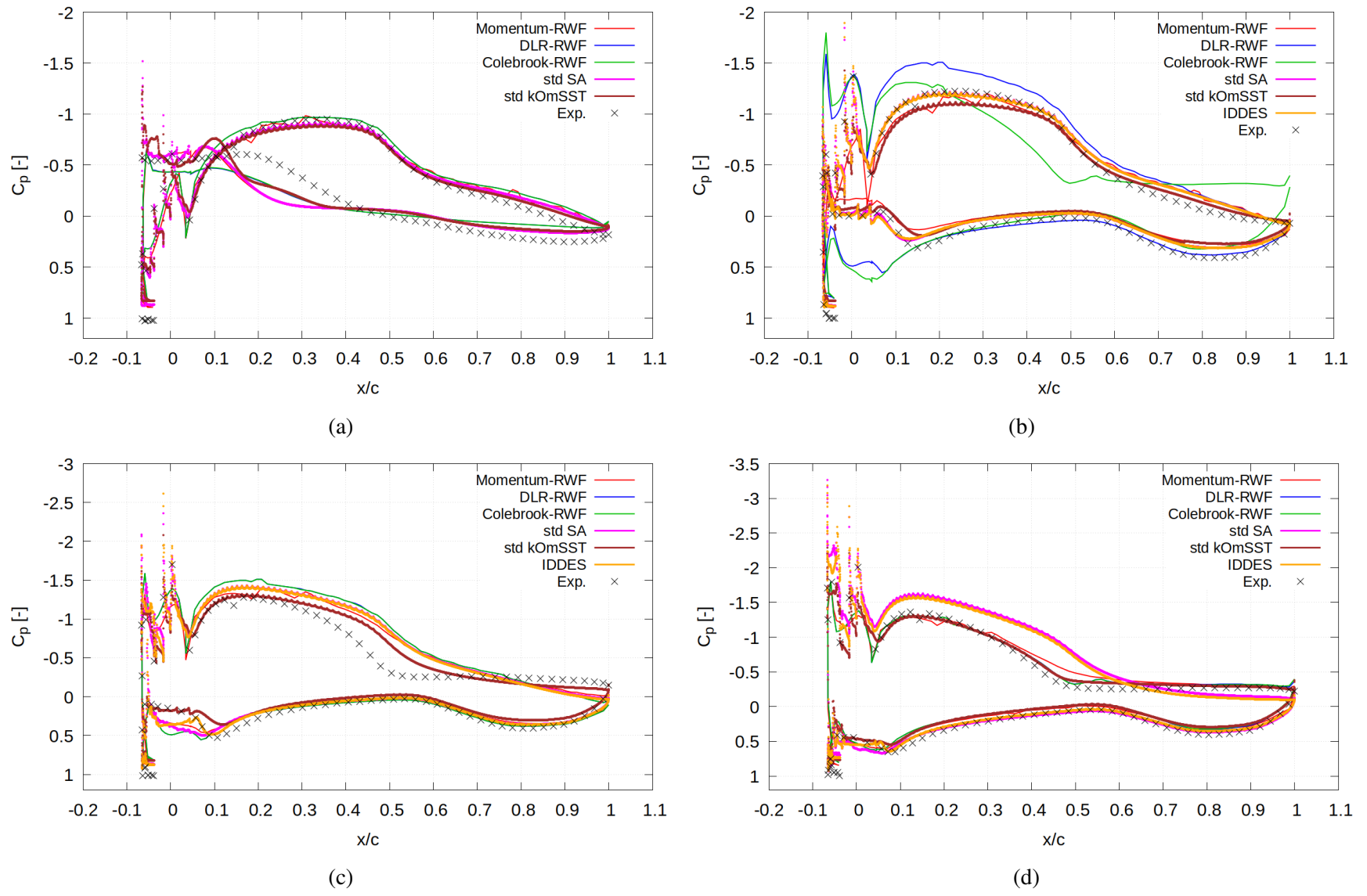


Figure 4.12: Case 3: C_p distribution for AoA = (a) 0° , (b) 4° , (c) 8° , and (d) 12°

Agreement analysis

The results in the last sections show that the flow field has different behaviors with using each rwf's. To find out which of the three rwf's resulted in the most accurate results, error analysis should be done to find out which rwf had less deviation from the experimental results. C_p distribution was chosen as the main criteria to compare since as explained earlier, the C_p distribution gives a better understanding of the shape of the flow field over the body which is very important to simulate ice accumulation. In this work, the average absolute error between C_p calculated from pressure measurements in the wind tunnel and the corresponding C_p calculated from simulations using the equation:

$$e_{avg} = \frac{1}{N} \sum_1^N |C_{p,exp} - C_{p,sim}| \quad (4.1)$$

where e_{avg} is the average error and $C_{p,exp}$ and $C_{p,sim}$ are coefficients of pressure of experiments and simulations respectively.

As shown in the figures 4.13-a and b, it can be noticed that the higher the AoA value, the more error between simulation and wind tunnel results. While in Fig. 4.13-c, we can see that the error values are not increasing with the increase of AoA at the same rates as shown in the previous two figures. These error results show that all rwf's has limited capabilities in simulating the detachment of the flow and accordingly give results deviated from actual results. Also, in case 3, where profile 2 was simulated, the detachment and reattachment of the flow were more violent at all tested AoA's that it caused close error values between all cases except for AoA = 12° that showed higher errors.

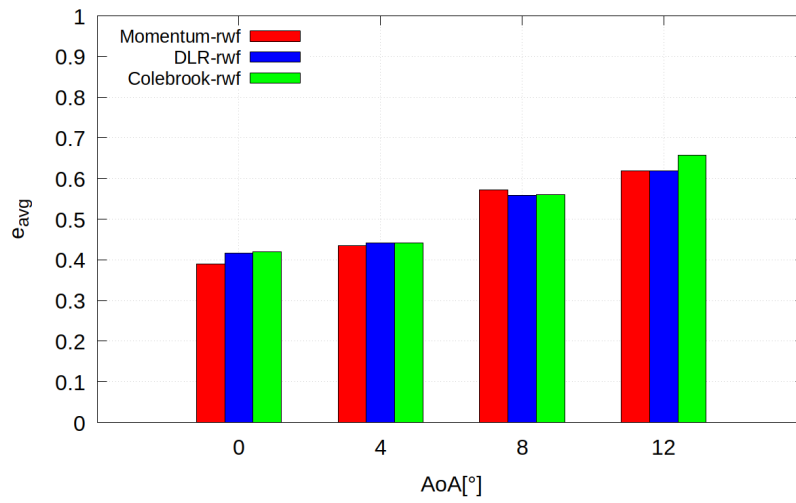
4.3 Discussion and conclusions:

In this work, three different rough wall functions were tested on iced wind turbine airfoils. This comparison aimed to find out which rwf will be the most suitable one to simulate ice accretion on wind turbine blades exposed to icing atmospheric conditions. To be able to apply these rwf's, DLR and Colebrook rwf's were implemented to OpenFOAM v6 CFD framework along with the existing Momentum rwf. After that, two ice profiles collected from the wind site, molded to the airfoil, and tested in the wind tunnel were smoothed by a cubic spline to find the equivalent smooth surface. Also, roughness parameters described in Section 4.2.2 were calculated and used to calculate the velocity shift value Δu .

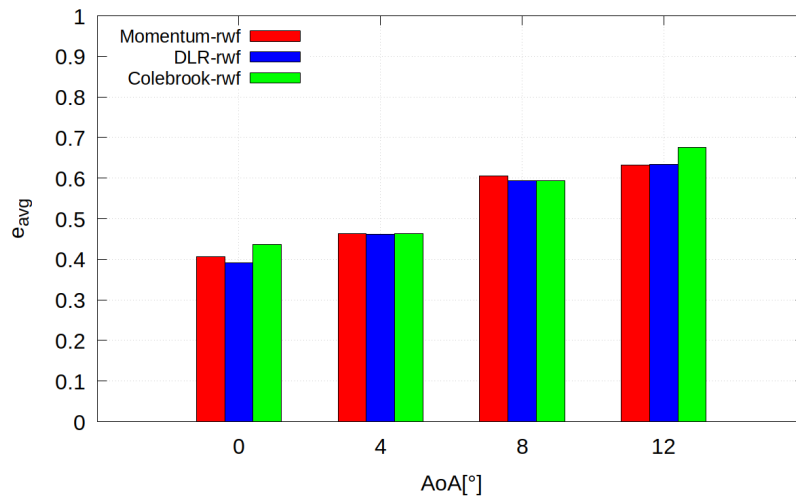
In this section, general remarks and discussions of the results are introduced. Then the conclusions from the outcomes of this work will be highlighted.

4.3.1 General remarks and discussion

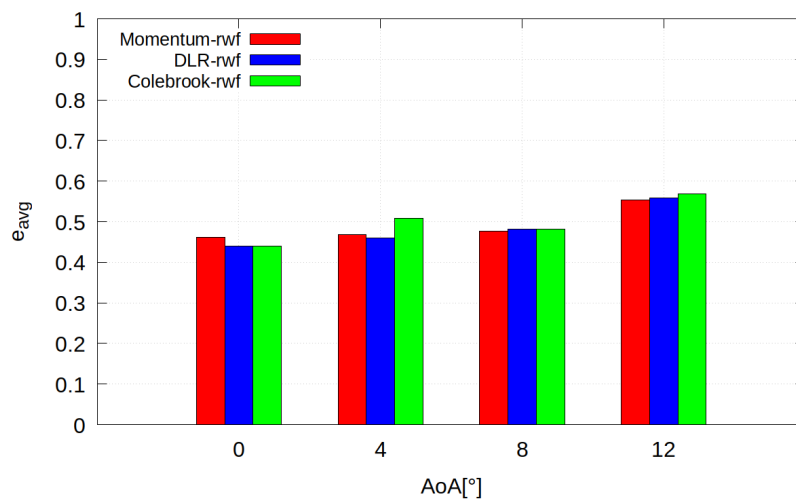
Regarding the rough ice surface shown in Fig. 4.3, one should keep in mind that the ice formation process (or roughness formation in general) is a stochastic phenomenon. This means, if the same airfoil is exposed to the same atmospheric conditions, the ice profile resulting will not be the same. So, to find the real smooth surface required for the simulations, a large number of ice profiles of the same atmospheric conditions should be studied and averaged to find the real



(a)



(b)



(c)

Figure 4.13: Average error between experimental and simulation results of C_p distribution (a) case 1, (b) case 2, and (c) case 3

average surface. Also, each rough surface will give different attachment and reattachment bubbles' locations, other than what is shown in Fig. 4.14, and might have different overall pressure distribution. However, the scope of this work is only to prove that the rwf approach results in good prediction of C_l and C_p compared to experiments for most of the range of AoA's in which the wind turbine blade section is operating.

From the geometry of the two ice profiles shown in Fig. 4.3, it can be noticed that both profiles are slightly inclined downwards. This inclination forms a relatively big separation bubble behind the profile on the lower surface as shown in Fig. 4.14. That is why we can see deviations between simulations and experimental results of C_p distribution in this region (i.e. the lower surface between $x/c = -0.1$ to 0.1) in most of the studied cases.

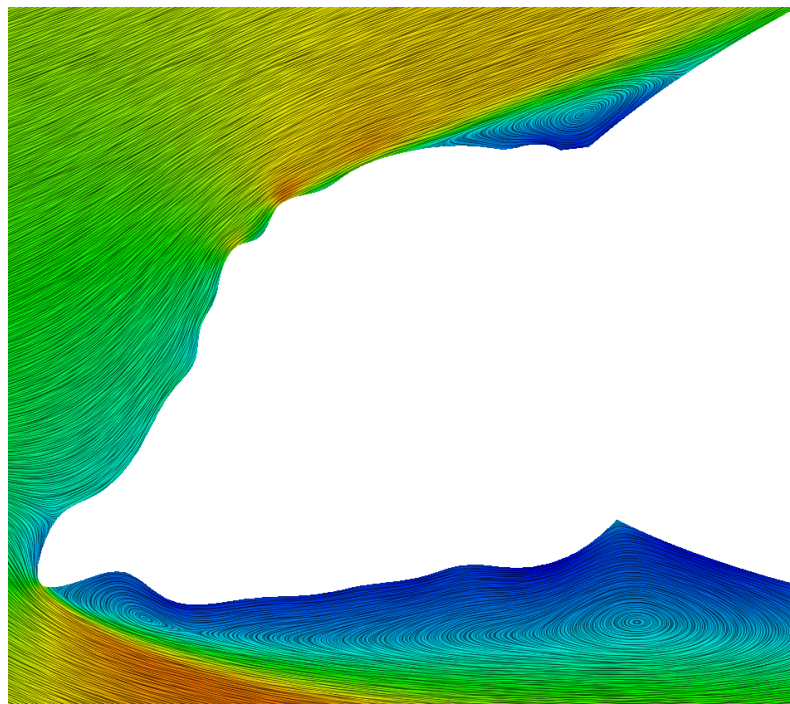
It can be noticed from the results that agreement of C_l curves between simulations and experimental results doesn't necessarily mean that the flow field was accurately simulated. For example, in case 3, DLR rwf shows better C_l agreement than other models at $\text{AoA} = 4^\circ$ while from C_p distribution, DLR rwf showed larger deviations from experimental results. The same happened with case 2 at $\text{AoA} = 0^\circ$ and 4° . The overall C_l at these AoA's, in the end, had good agreement because the deviations on the upper and lower surfaces compensate each other which can be misleading in this case. To accurately access the C_l , it should be studied together with the C_p distribution curves.

It is noteworthy that all the rwf's used are only algebraic equations that express the behavior of the flow near that wall. Accordingly, the three different implementations have the same computational cost and the overall computational cost depends only on the number of cells in the used computational grid.

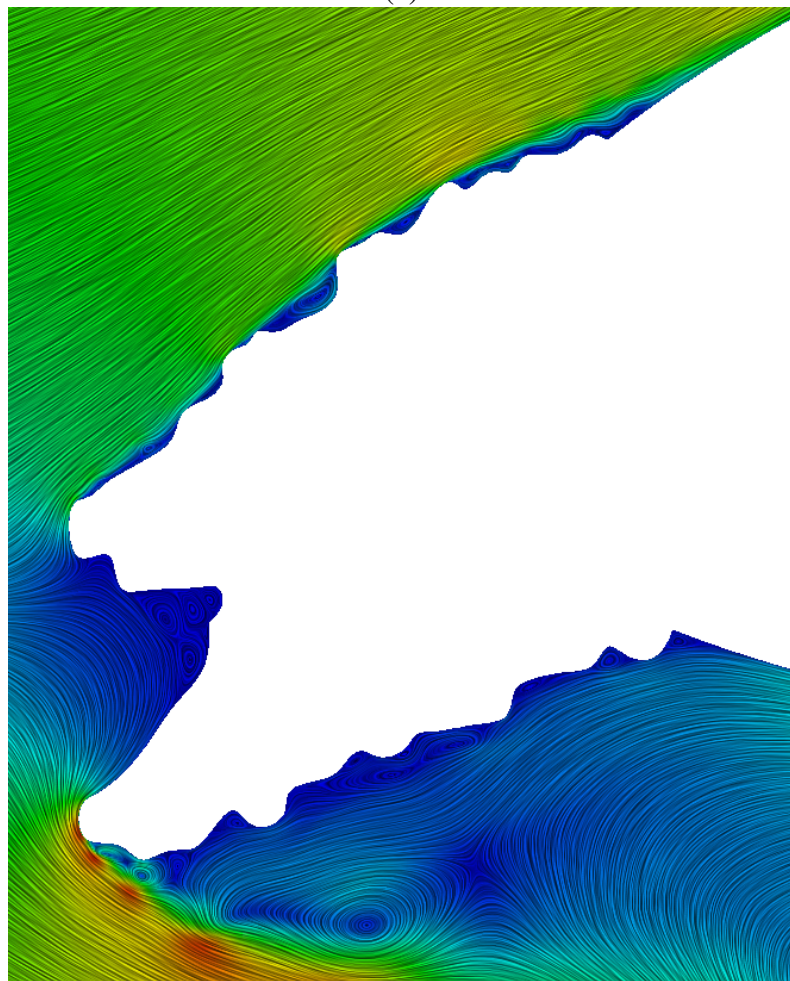
4.3.2 Conclusions and remarks

The simulation cases show that Momentum rwf provides the best agreement of simulations with experiments compared to the other models. However, in some cases, the simulations show fair agreement at locations that witness violent separation like concave areas between ice and airfoil. This fair agreement is expected due to using steady-state RANS simulations. Also, it can be concluded that the DLR rwf also gives good agreement in most of the cases and was close to results achieved by the Momentum rwf.

From this work, we can conclude that in simulations of rough, iced airfoil profiles, the Momentum rwf should be used to simulate the effect of the presence of roughness on the overall aerodynamic performance. This rough wall function should be used since it shows in most of the cases the minimum error for angles of attaching 0° and 4° which represent the operation range of AoA's for airfoils. Such a method should be beneficial for the simulation of the performance drop of wind turbine blades exposed to icing atmospheric conditions with minimum computational effort.



(a)



(b)

Figure 4.14: Line Integral Convolution (LIC) of flow in (a) case 2 at $AoA = 0^\circ$ (b) case 3 at $AoA = 0^\circ$

Chapter 5

Ice accretion on 2D airfoil profiles

5.1 Introduction

After successfully simulating the background flow field around airfoils, the water particles can now be tracked until it hits the surface and their transformation from liquid to solid ice can be simulated. Despite that the main goal of this thesis is to introduce a new OpenFOAM code to simulate the ice accretion on 3D, rotating wind turbine blades, it is important to validate this code on well-known airfoil ice accretion cases. If any code fails to simulate ice accretion on simplified cases like 2D airfoils, then it would be impossible to trust the simulation results of this code in any other 3D ice accretion simulations. Fortunately, there were numerous experimental works published by researchers since the 1950s.

In this chapter, validation of the new code will be presented. First, the accuracy of prediction of collection efficiency (β) will be validated against experimental results dedicated for this goal. After that, the new code will be tested by simulating the ice accretion on NACA0012 airfoil at different ambient conditions by comparing the resulting ice profiles. By gaining the confidence in the capability of the new solver to successfully simulate the ice accretion on ordinary surfaces, the application of the effects of ice-phobic coatings on the icing process will be also simulated to apply the same techniques to wind turbine blade simulations that will be shown in the next chapter.

5.2 Simulation of collection efficiency

By looking at the equations 3.52 and 3.53, it can be directly noticed that one of the most important parameters in the simulation process of the ice accretion is to correctly simulate β . This is because it is the main parameter in calculating mass and energy source terms in equations 3.49 - 3.51 representing mass and energy conservation in SWIM. Papadakis et al. [152] conducted a thorough experimental investigation of water droplet impingement on different 2D airfoil geometries and other 3D shapes to investigate the collection efficiency. Using the Forward Scattering Spectrometer Probe (FSSP) and the Optical Array Probe (OAP), the authors of this work managed to measure MVD and LWC of the different experimental cases. After that, the impinging mass was measured β was plotted for each case over the airfoil. The measurement techniques and instrumentation were explained in detail in Ref. [152]. In this work, the

distribution of β over the NACA 65₂ – 415 airfoil was studied at different MVD values (namely, 11.5, 21, and 92 μm). Each MVD was tested at two different AoA's (namely 0° and 8°).

5.2.1 Comparison of mono- vs polydispersed particles

To show the effect of the particle size distribution on β , Fig. 5.2 shows the simulated β distribution using mono- and polydispersed particle sizes according to Equ. 3.21 at $\text{MVD} = 21 \mu\text{m}$. It can be noticed that for $\text{AoA} = 0^\circ$ and due to the geometry of the NACA 65₂ – 415 airfoil which has a steeper leading edge on the upper surface, higher collection efficiency can be noticed on the upper surface. From the simulation results of this region, specifically between $s = 0.02\text{-}0.05\text{m}$, it can be noticed that the simulations overestimate the collection efficiency. This happens due to rapid change in flow velocity in this region and the simulations cannot accurately simulate the effect of such rapid changes on water droplets.

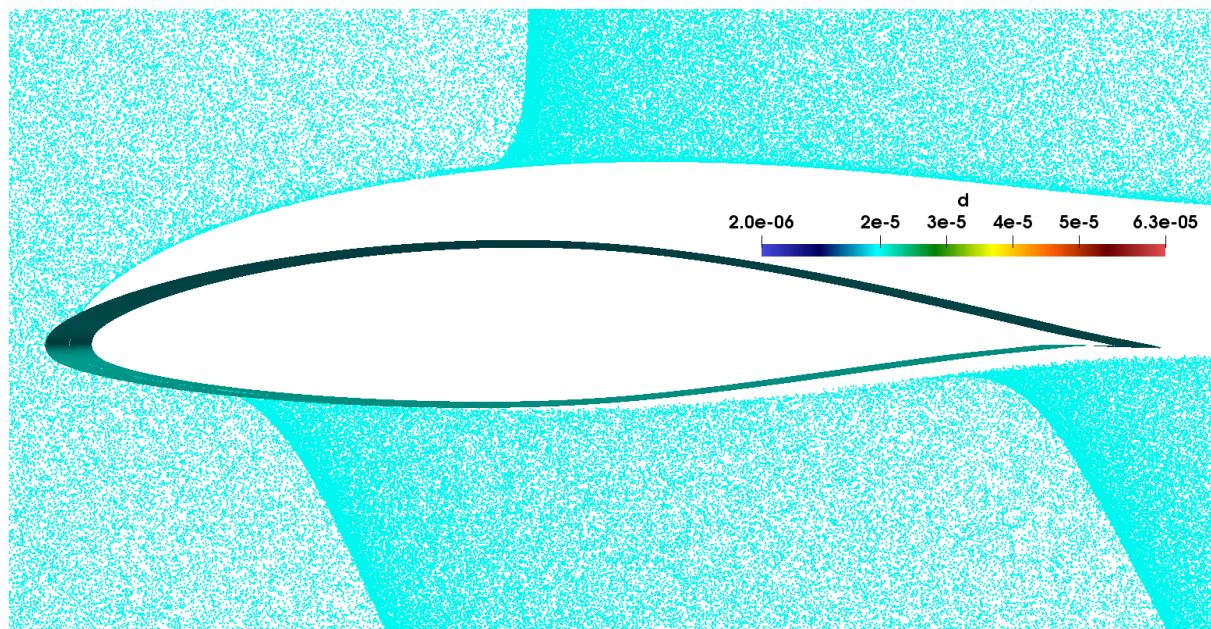
It can be seen that both mono- and poly-dispersed particle distributions show good agreement in both AoA's. However, mono-dispersed droplet distribution provided a slightly better agreement in the case of $\text{AoA} = 0^\circ$, especially at the point with maximum collection efficiency that corresponds to the stagnation point. On the other hand, poly-dispersed particle distribution provided good agreement with experimental results between $s = -0.03 - 0.02 \text{ m}$. For s values lower than -0.03 m , the gap between the simulation and experimental results becomes wider for both cases.

In general, we can conclude that simulations provided good agreements in the two tested cases. However, $\text{AoA} = 8^\circ$ had a better agreement, especially on the suction side of the airfoil. This gives some confidence in the collection efficiency simulation results for AoA's $\geq 0^\circ$, which happens in the case of wind turbine sections. Also, poly-dispersed particles at this AoA provided better agreement with experimental results. This agreement was expected since the experiment was carried out with poly-dispersed particles according to Papadakis et al. [152].

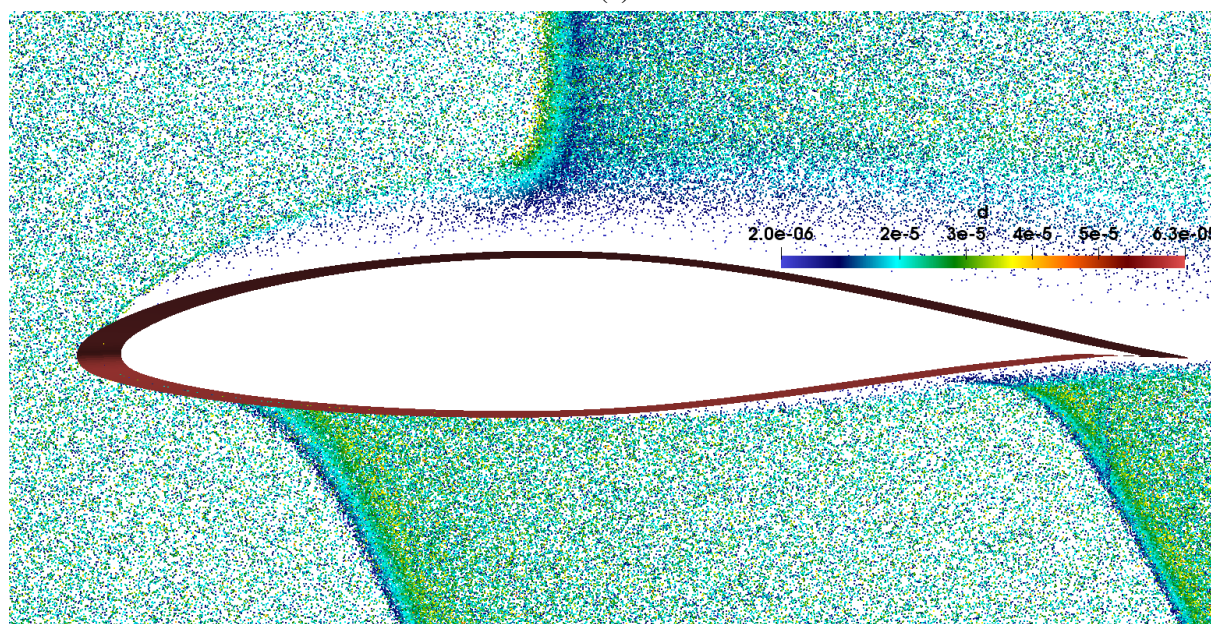
5.2.2 Comparison of different MVD values

Another factor that affects on β distribution is the median volumetric diameter (MVD) value. It is known that the higher the MVD, the higher the average particle and hence the harder the particles can change their trajectory with the change of flow velocity. This section investigates how accurate can the new codes simulate the collection efficiency for different particles' diameters.

Fig. 5.3 shows the distribution of β values over the airfoil for polydispersed cloud with $\text{MVD} = 11.5, 21, \text{ and } 92 \mu\text{m}$. From this figure we can see that the best agreement between simulation and experiment happens at $\text{MVD} = 21 \mu\text{m}$. As the MVD value deviates from $\text{MVD} = 21 \mu\text{m}$, the β value deviates away from the experimental results. A possible explanation behind this result is that the mathematical model used in OpenFOAM to calculate the C_D value of the droplet, which is a crucial value in particle tracking as explained in Sec. 3.4.1, is optimized for diameters close to $21 \mu\text{m}$. In case of particles with diameters far from this optimum value, the modeled C_D value can deviate from the actual C_D value. Additionally, using RANS turbulence models, in this case, can be not accurate because we assume turbulent flow, while the flow is not (yet) turbulent near the leading edge of the airfoil, especially at $\text{AoA} = 8^\circ$.



(a)



(b)

Figure 5.1: Particle diameter of the a) mono vs b) poly-dispersed particle distributions simulations

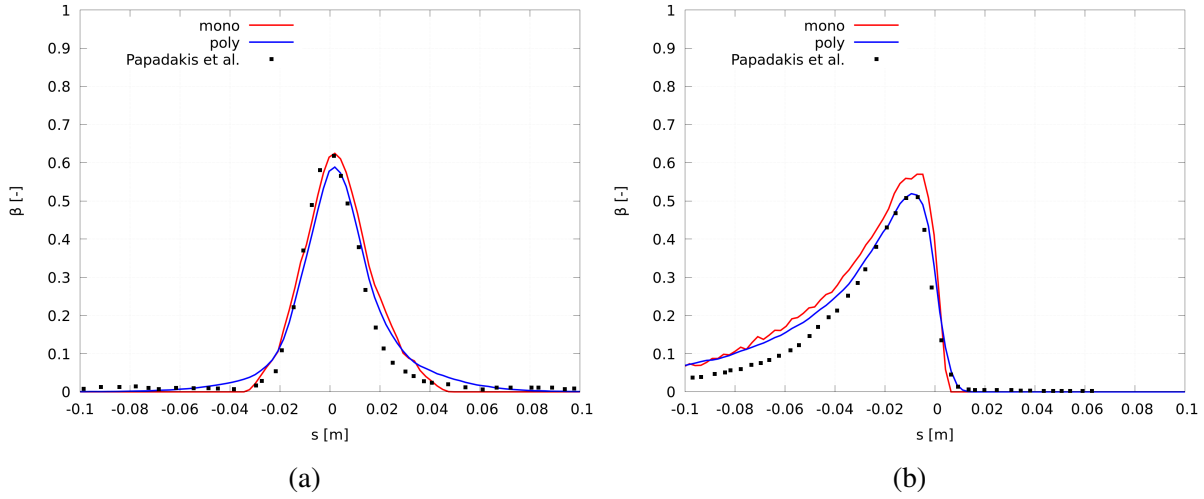


Figure 5.2: β distribution at AoA = (a) 0° and (b) 8°

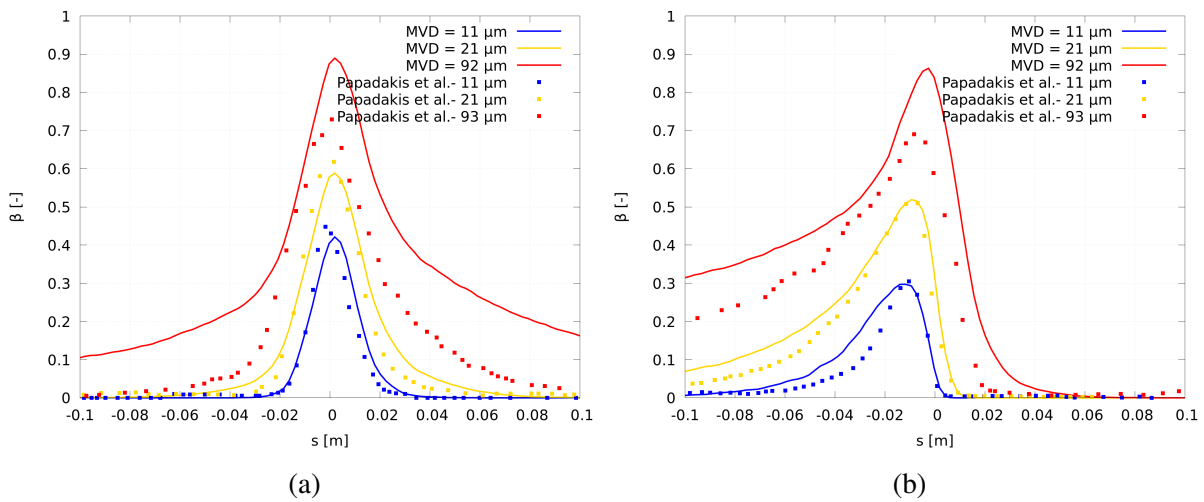


Figure 5.3: β distribution for different MVD values at AoA = (a) 0° and (b) 8°

5.2.3 Comparison of splashing droplets

To show the effect of the particle size distribution on β distribution, Fig. 5.2 shows the simulated β distribution using mono- and poly-dispersed particle sizes according to Equ. 3.21 at MVD = 21 μm . For both AoA's, the splashing model described in Bai et al. [145, 146] fails to correctly predict the splashing mass of droplets impinging on the airfoil, especially around the leading edge. As mentioned in the last section, it could be the deviation of C_D value from the actual value that leads to such a deviation, especially when studying such a high MVD value. Another explanation could be the deviations coming from Bai and Gosman's model itself. This model is still based on empirical data and must include some errors.

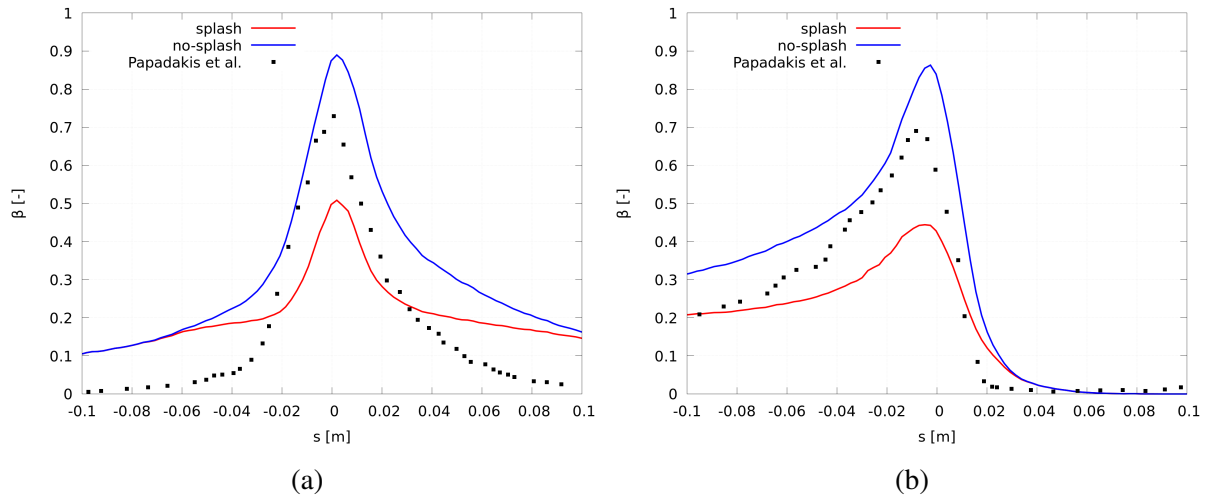


Figure 5.4: β distribution for non-splashing vs splashing droplets at AoA = (a) 0° and (b) 8°

5.2.4 Effect of airfoil geometry on collection efficiency

As explained earlier, collection efficiency β and ice accretion profile is affected by many parameters that control the impingement location on the solid surface. This section studies the effect of the airfoil nose shape on the collection efficiency and ice accretion profile.

To have a fair comparison between airfoils, six airfoil profiles with three different thickness-to-chord (t/c) ratios were selected for the comparison:

1. $t/c = 18\%$: DU 95-W-180 and NACA 64618 profiles
2. $t/c = 21\%$: DU 93-W-210 and S830 profiles
3. $t/c = 25\%$: DU 91-W2-250 and S815 profiles

All the profiles indicated above are simulated at MVD = 20 μm , LWC = $1 \times 10^{-3} \text{ kg/m}^3$, chord length = 1m, $T = 266.3^\circ\text{K}$, AoA = 4° , $U_\infty = 60 \text{ m/s}$, and total ice accretion time = 480 s.

Fig. 5.5 shows the leading edge and the distribution of β of the airfoil profiles with different t/c ratios. For the two airfoils with $t/c = 18\%$ in Fig. 5.5a, the nose of the DU 95-W-180 profile is sharper (i.e. has a smaller radius) than the nose of the NACA 64618 profile. Also, it can be

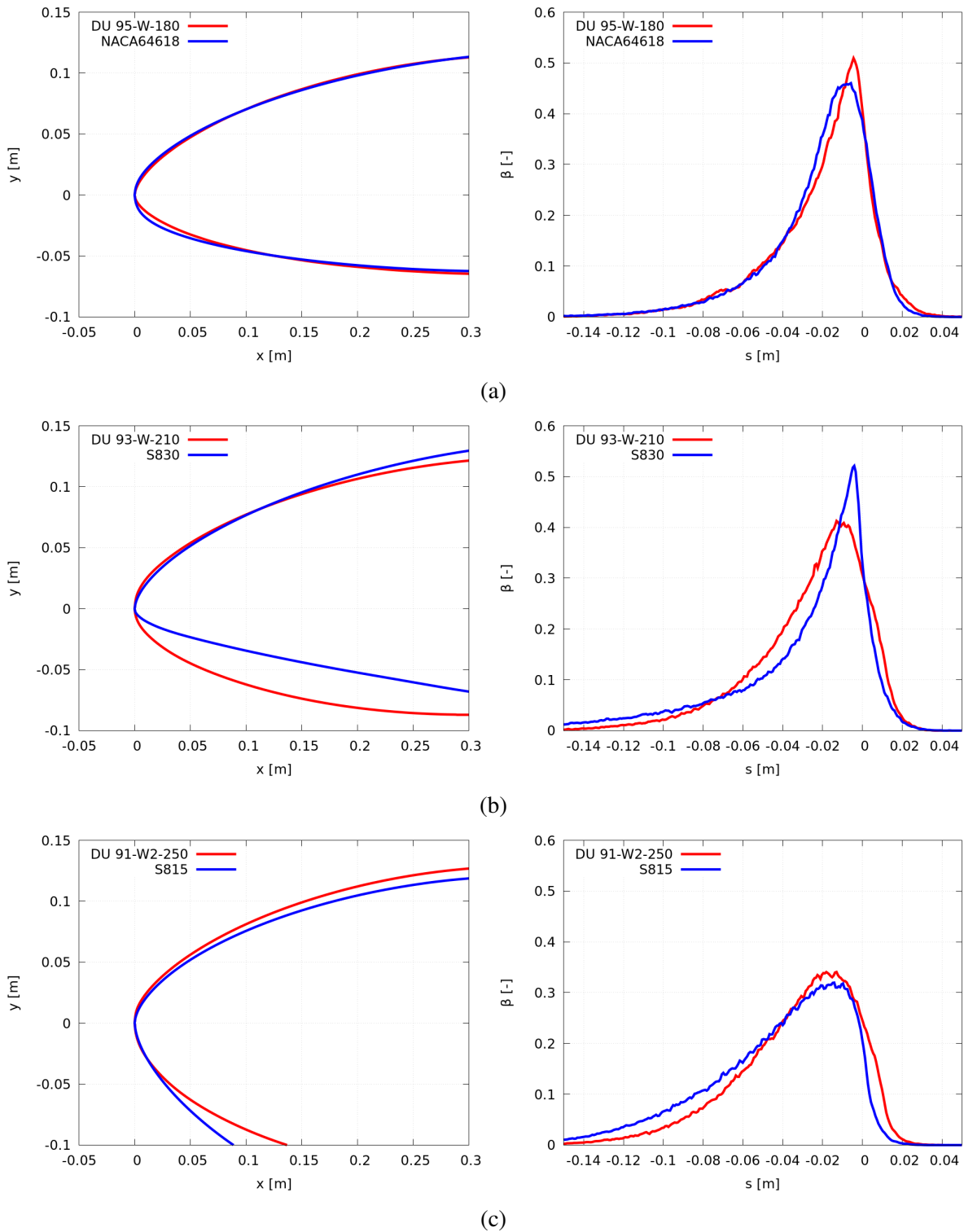


Figure 5.5: Comparison between the leading edge profile of airfoils (left) and β distribution (right) with $t/c =$ a) 18% b) 21% c) 25%

noticed that the lower surface of the DU 95-W-180 profile is higher than the corresponding area of the NACA 64618 profile. While the upper surface is almost the same for both airfoils. These differences in geometry affect the β distribution. The sharper nose of the DU 95-W-180 profile leads to a sharp increase of the maximum value of β compared to the NACA 64618 distribution. Also, the wider projected area of the lower surface of the NACA 64618 profile leads to higher values of β on it relative to β values for DU 95-W-180.

Clearer differences in β distribution is shown in Fig. 5.5b for airfoils with $t/c = 21\%$. In this figure, the nose of the S830 profile is much sharper than the nose of the DU 93-W-210 profile. Furthermore, the area of the lower surface of the DU 93-W-210 profile is much wider than the one for the S830 profile. This leads to a sharp increase in the maximum β value at the stagnation point and also higher values of β on the lower surface. The same behavior is noticed in Fig. 5.5c. Additionally, the upper surface of the DU 91-W2-250 and S815 profiles is different too. This leads to different β distributions over the whole leading edge.

These differences in β distributions happen since the two main forces affecting particles while flowing over the airfoils are drag and inertia forces. When the background airflow exhibits rapid changes in magnitude and direction of the velocity vector, the inertia force tends to keep the particles on the same trajectory. This means sharp noses and wide upper or lower surfaces lead to an increase in β . On the other hand, a wider nose and more stream-lined upper and lower surface lead to lower β values. From the shown study, it can be concluded that the leading edge geometry has a considerable effect on β distribution. This conclusion can be very useful while designing and optimizing airfoils not only for minimum ice accretion but also for minimum rain and sand erosion and dust and bugs accumulation on airfoils.

5.3 Simulation of ice accretion profiles

After comparing the behavior of water particles between CFD and experiments as shown in the previous section, the new thermodynamic icing code is validated with different benchmark cases of ice accretion on airfoils. This validation aims to make sure that the new OpenFOAM implementation can capture (most of) the physical phenomena described in Sec. 3.5. After that, a case study of the effect of airfoil nose shape is introduced.

5.3.1 Validation with icing wind tunnel results

The ice profiles resulting from the new OpenFOAM solver developed in this work is validated against the experimental results reported by Wright et al. [2]. These experimental ice accretion simulations were executed by the National Aeronautics and Space Administration (NASA) in the US, Defense Research Agency (DRA) in the UK, and The Office National d'Etudes et de Recherches Aérospatiales (ONERA) in France. The three agencies collaborated to provide benchmark cases for different conditions to be used as a reference for ice accretion numerical simulation codes. In this thesis, only three cases, shown in Tab. 5.1, from this report are used for comparison with numerical simulation results.

Table 5.1: 2D ice Accretion cases studied in this section

Parameter	Case 27	Case 30	Case 31
Profile	NACA0012	NACA0012	NACA0012
V_∞ [m/s]	58.1	58.1	58.1
Chord [m]	0.53	0.53	0.53
AoA [$^\circ$]	4	4	4
T_∞ [$^\circ K$]	245.2	266.3	269.1
Ice Type	Rime	Glaze	Glaze
LWC [g/m^3]	1.3	1.3	1.3
MVD [μm]	20	20	20
Exp. Time [s]	480	480	480

Rime Ice

Rime ice occurs in case 27 where all water particles are frozen once they touch the solid surface. 5.6 shows the results of ice accretion simulations for 1, 3, and 5 ice simulation loops compared with the experimental results. In the case of simulating the icing time, which extends to 480 s, on a single loop, an ice profile with a relatively flat front is formed. In other words, when comparing the experimental with the simulation results, we can notice the simulated ice thickness at the stagnation point of the flow is lower than the measured one. However, this lower thickness is compensated by relatively higher thicknesses downstream on the suction side of the airfoil. The ice thickness at the stagnation point is better estimated as the number of ice simulation loops is increased. This can be seen from the ice profiles at 3 and 5 icing loops. Also, the ice profile on the pressure side of the airfoil shows more roughness as the number of simulation loops increases too.

The change of the ice thickness at the stagnation point happens due to the change of the profile over which the airflow field is calculated. As the ice thickness at the stagnation point gets sharper, the flow fields change rapidly in a way that the water droplets cannot follow this change due to droplets' inertia. This results in a higher rate of impingement on the new stagnation point and hence a sharper ice profile. The same happens on the pressure side where feathers of ice are formed resulting in the same effect explained earlier. Rapid changes of the flow field near these feathers result in more impingement rates and hence sharper and higher ice feathers.

Glaze Ice

In cases 30 and 31, ambient temperature is not low enough to freeze the whole mass of water impinging on the surface. This means an influence of water film flow on the surface and its heat exchange with both ambient air and solid surface on the final ice profile. This is the reason behind being calculating the convective heat transfer coefficient accurately is crucial for this case. To see how the liquid water film motion affects the profile, Fig. 5.7 shows the ice profile

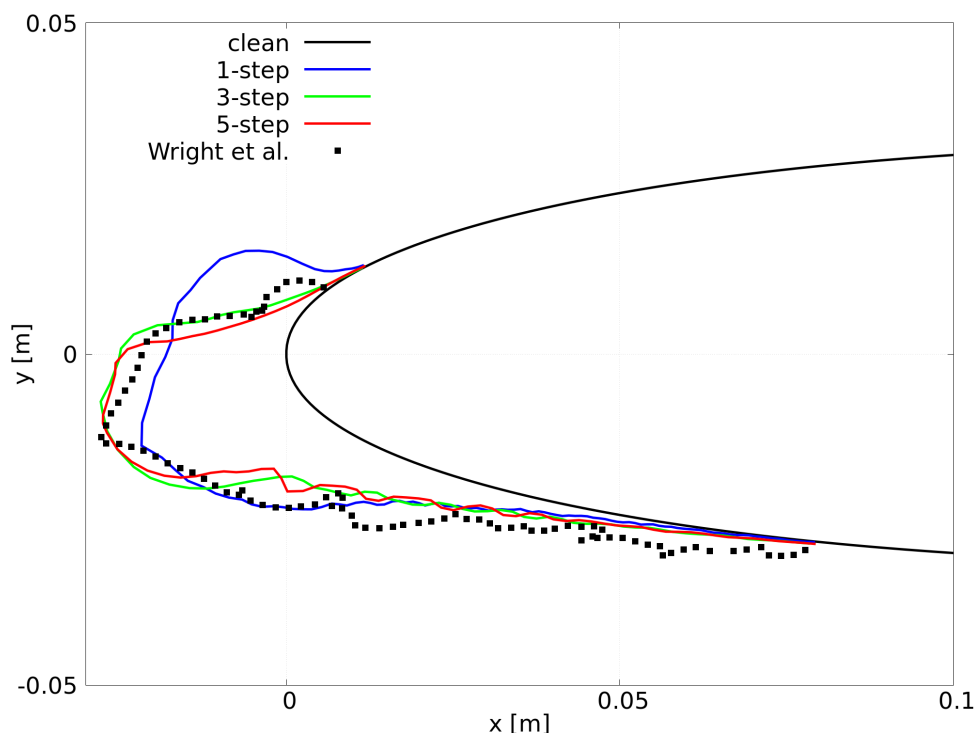


Figure 5.6: Ice accretion simulation of Case 27 for different number of icing loops

for case 30 after 1, 3, and 5 ice simulation loops after 480 s of exposure time. In this case, the temperature at the stagnation point is not low enough to freeze the complete water mass. This leads to a water film flow downstream the stagnation point. This water film is frozen later due to heat transfer by convection between water mass and the ambient air and the cold solid surface. The differences between the resulting profiles after running the ice accretion for 1, 3, and 5 steps are resulting from the change of the β distribution over the new profile after ice accretion. It is expected that the more loops are used to simulate ice accretion the more accurate the final profile will be. However, the new non-streamlined shape of the ice causes disturbance of the flow field behind this profile. Such disturbances are hard for steady-state aerodynamic CFD solvers to simulate and will result in inaccurate results.

Also, Fig. 5.8 shows the simulation results of case 3. In this case, ambient temperature is higher than the temperature simulated in case 2. Therefore, it can be noticed that the ice horn on the upper leading edge is smaller compared to the ice profile resulting from case 31.

5.4 Simulation of ice accretion on coated airfoils

In this section, airfoils with ice-phobic coatings are simulated using the newly implemented code in OpenFOAM that uses Eq. 2.21 to calculate the critical Weber number. The simulation results are then compared with experimental data carried out at TU-Braunschweig icing wind tunnel which were provided by the DLR-Institute of Composite Structures and Adaptive Systems.

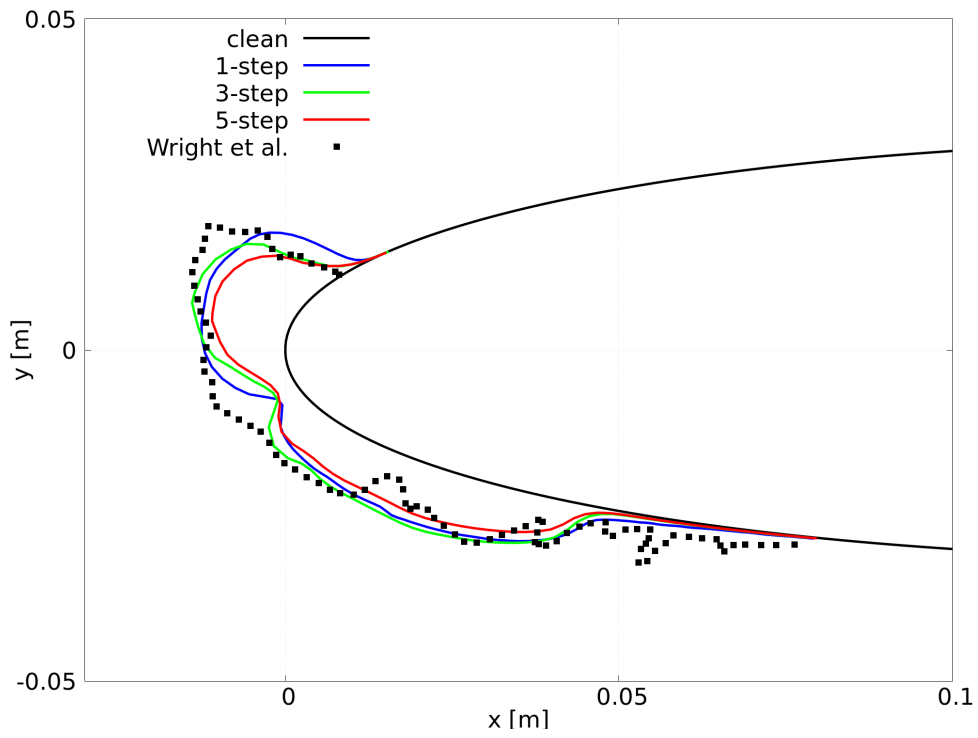


Figure 5.7: Ice accretion simulation of Case 30 for different number of icing loops

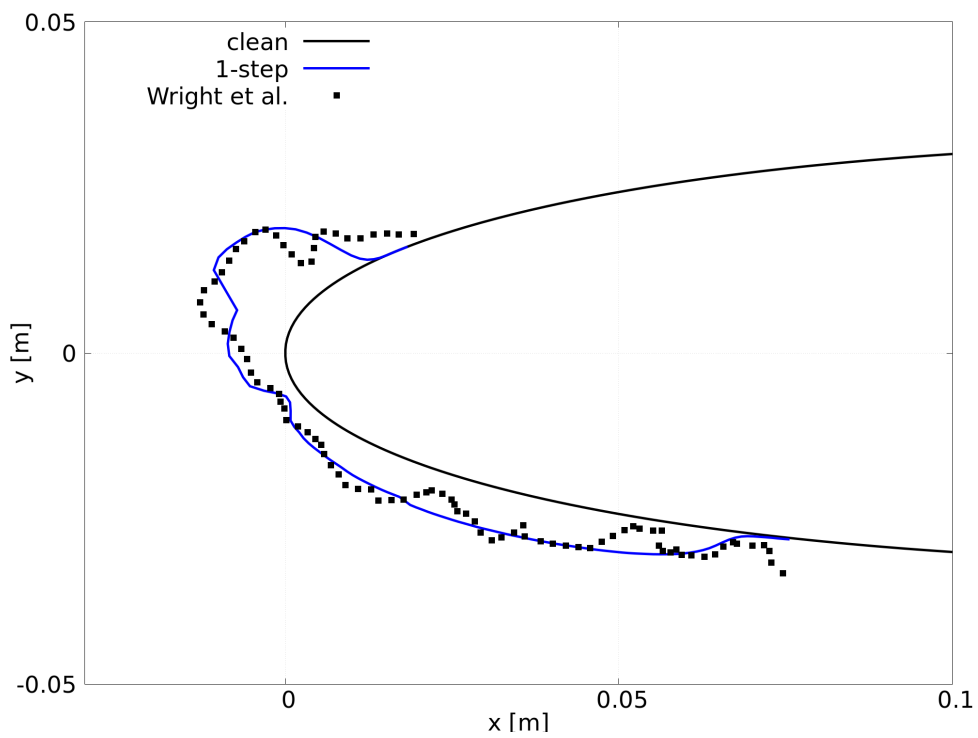


Figure 5.8: Ice accretion simulation of Case 31 for one time step

As explained in Sec. 3.7.2, the critical Weber number after which water droplets exhibits partial splashing off the surface is dependent on the two roughness parameters: Reduced peak heights (R_{pk}) and profile element widths (R_{sm}). Two different layers are studied: Layer 1 which has $R_{sm} = 1.174 \times 10^{-5}$ and $R_{pk} = 1.094 \times 10^{-5}$. While Layer 2 has $R_{sm} = 1.17 \times 10^{-5}$ and $R_{pk} = 1.2 \times 10^{-5}$. Both layers are applied to an airfoil sample approximated to NACA0027 chord length = 0.112 m and was tested at AoA = 0° , $U_\infty = 31$ m/s, and total ice accretion time = 60 s. For icing conditions, the tests were carried out at liquid water content (LWC) = 0.35 g/m³ and median median volumetric diameter (MVD) = 60 μ m, and T = 268.15° K.

In Fig. 5.9, each of the two-layer is simulated and compared with the case in which no splashing effect is taken into account (referred to as ordinary). In both figures, it can be noticed that the ice profiles in ice-phobic and ordinary cases are very close. This can be justified by the fact that ice-phobic coatings lose their water repulsion capabilities once they are covered with ice. The critical ice thickness that makes the layer loses its properties in these simulations should correspond to the ice thickness that fills the roughness valleys shown in Fig. 3.7. However, the applied value in the simulations was found by trial and error to be around 1×10^{-8} . This shows the need for more accurate experiments and models to have a better conclusion about such a value.

Also, in Fig. 5.9, the simulations of both layers show good agreement on the upper and lower airfoil surfaces starting at $x = 0.01$ m while the difference in agreement happens around the leading edge. The ice simulation for layer 2 in Fig. 5.9b shows better agreement with the experiments than the ice simulation for layer 1 in Fig. 5.9a. This could be happening due to taking the results of only one wind tunnel experiment in testing layer 1, while three different test cases were taken into consideration for layer 2 simulations.

From these plots, it can be concluded that the approach for simulating ice accretion on ice-phobic coatings is possible using the suggested approach and can lead to good agreement in case of having the correct critical ice thickness after which the ice-phobic coating is no longer effective. It can also be concluded that since ice-phobic coatings are practically effective only when they are ice-free, the analysis of their effects in this thesis will be considered only in the case of anti-icing. In this case, it is expected to give reasonable results.

5.5 Conclusions and remarks

In this chapter, the simulation results of different particle tracking and ice accretion validation cases were presented to validate the new solver. Also, the wind tunnel experiments of ice accretion on coated 2D airfoils carried out by the DLR were presented.

By comparing the collection efficiency of the experiment and numerical simulations, it can be found that the numerical simulations provide the most accurate results for droplet sizes around 20 μ m as shown in Fig. 5.3. If the particles' sizes deviate from this value, the numerical simulation starts to deviate from the experiment. This could be due to the C_D model that was fine-tuned for this range of droplet sizes. A further investigation for this issue could be done by implementing different droplet drag models in OpenFOAM and comparing the results of the different models with the experiments.

Also, this chapter Has shown that the current droplet splash models implemented in OpenFOAM, namely Bai and Gosman [145, 146], are not accurate for water droplet splash as can be

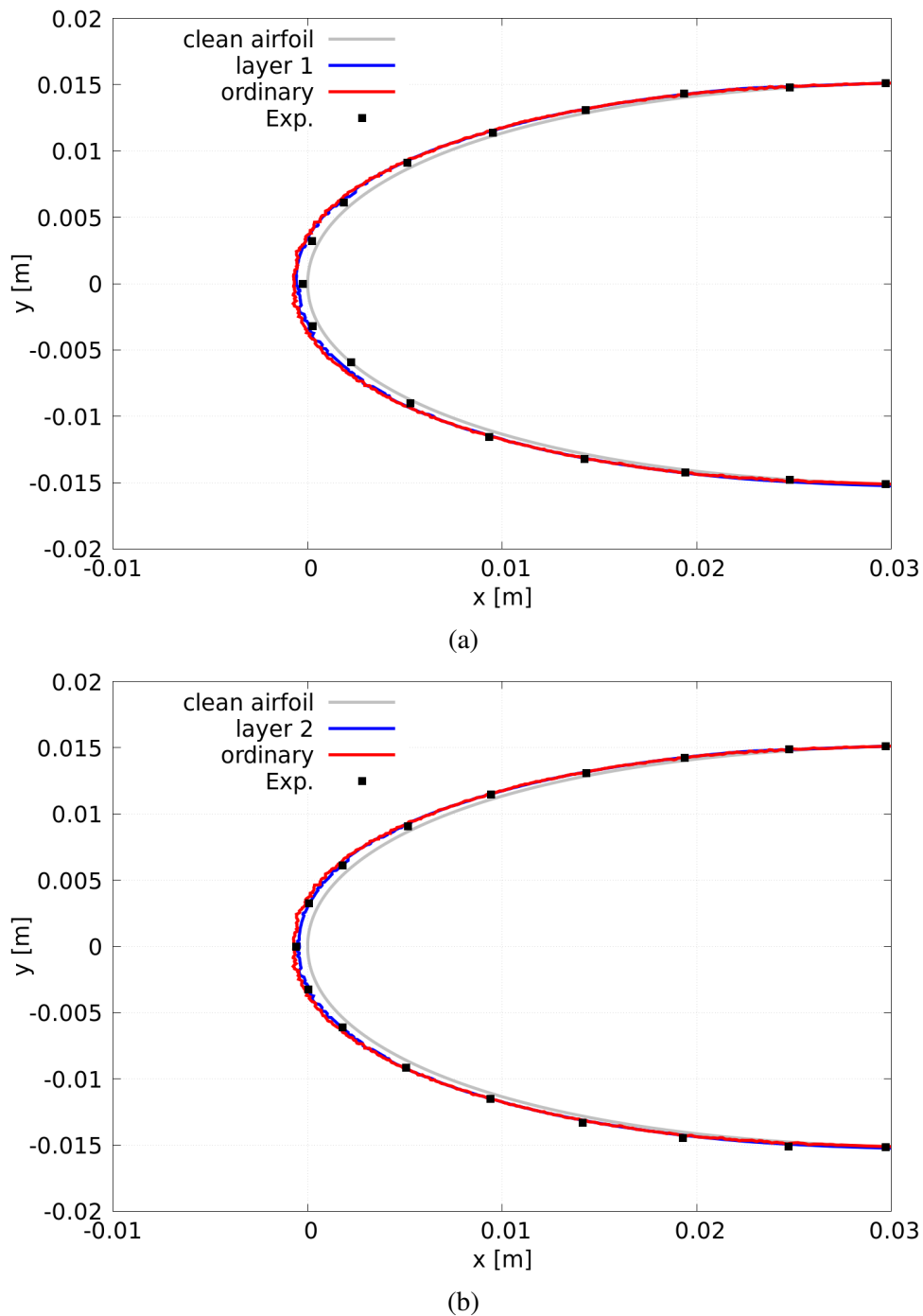


Figure 5.9: Ice accretion on coated 2D airfoils with a) Layer 1 and b) Layer 2

seen in Fig. 5.4. The current splashing models are currently used for the splash of diesel fuels on smooth surfaces, like engine combustion chambers. However, in this case, the water droplets are different in viscosity, density, and velocity. Accordingly, new splashing models should be investigated.

The study of the effect of airfoil geometry on the collection efficiency that was studied in Sec.

5.2.4 shows that leading-edge geometry of the airfoils has a significant effect on the collection efficiency. Fig. 5.5 shows that the sharper the leading edge, the higher the maximum collection efficiency on this nose. Also, the steeper the lower the airfoil surface, the lower the collection efficiency on this surface. This gives an idea of the effect of nose geometry on ice formation and also can lead to some ideas about the optimization of airfoils for minimum ice accretion.

For ice accretion simulations, the new OpenFOAM ice accretion solver provided good agreement with experiments done by Papadakis et al. [152] for collection efficiency and Wright et al. [2] for ice accretion profiles. However, the results from icing wind tunnel experiments done by the DLR for coated 2D airfoils are still questionable due to the less-controlled environment of the experiment. Also, the other published literature like Ma et al. [153] did not provide enough information about the coating to be considered during the CFD simulations.

Chapter 6

Ice accretion on wind turbine blades

6.1 Introduction

The previous chapter has shown the capabilities of the new OpenFOAM solver in simulating ice accretion on 2D airfoils. This chapter shows how this Lagrangian solver can be used to simulate ice accretion and predict anti-icing heat for 3D wind turbine blades. As discussed in Sec. 2.7, Lagrangian particle tracking is computationally too expensive to be used in simulating ice accretion on 3D blades. However, the following section is discussing the quasi-3D approach that can solve this issue.

First, the quasi-3D approach is introduced and its assumptions considered to simplify the 3D case are explained. After that, this approach is applied to the NREL PhaseVI wind turbine blade and the results are compared with other literature for validation. Then, this approach is applied to the NREL 5MW wind turbine blade to simulate ice accretion and anti-icing heat of a multi-megawatt wind turbine.

6.2 Simulation of icing using Quasi-3D particle ice accretion

Like the Blade Element Momentum (BEM) approach to simulate wind turbines, this approach depends on calculating the local AoA's and relative wind speeds of different blade sections over the blade while rotating using any method (in this work, steady-state 3D OpenFOAM blade simulations are used to get the AoA values). After knowing the AoA and the relative wind speed, each section should be simulated with a 2D section as explained in the previous chapter to get the ice accretion profile. Accordingly, this approach implies the following assumptions:

- No radial effects are considered: This is because each section is assumed to be a pure 2D section. Accordingly, no flow is simulated in the radial direction. This assumption could be reasonable only in the case of the turbine operation at the low wind and rotational speed up to rated conditions. In this case, the radial effects are minimum and the flow field around the leading edge of the blade sections can be approximated to a 2D case.
- Rapid changes in the flow field near the leading edge will not affect the droplet's trajectory. This is reasonable too due to the inertia of the droplet.

A detailed validation, analysis, and case study is shown in the following sections.

6.2.1 Validation of airflow field

As explained in chapters 3 and 5, the key to accurately simulating the impinging water mass on the surface is to accurately simulate the airflow field around the airfoil. Accordingly, to use the quasi-3D simulation approach in simulating ice formation on a 3D rotating blade, one must make sure that the flow field around every section of the blade is correctly simulated.

To validate this approach, the C_p distribution of clean blade sections should be compared between the quasi-3D and the 3D cases to make sure that the surrounding airflow field is accurately simulated. Also, one has to make sure that the radial effects along the blade span are minimum and hence will not have significant effects on the particles and their impinging locations. For the NREL PhaseVI wind turbine blade, the results of the C_p comparisons at 7 m/s wind velocity and a rotational speed of 72 rpm are shown in Fig. 6.1. To validate the simulation results, the experimental results from Sørensen et al. [7] were also included in this figure.

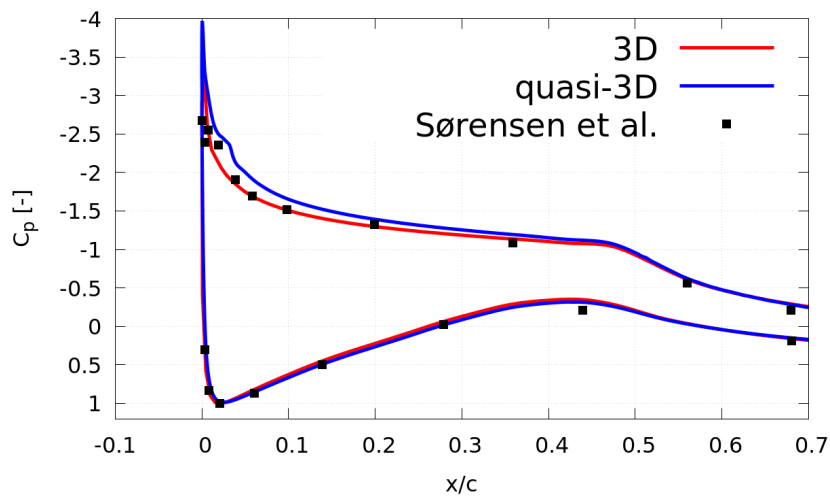
It can be noticed in Fig. 6.1 that the differences in C_p distribution between quasi-3d and full 3D are minimal on the lower surface of the three shown sections. However, some differences can be noticed on the upper surface of all sections starting between $s/c = 0 - 0.5$. These differences are at a maximum value at the leading edge of each section. Also, it can be noticed that the differences at the leading edge are increasing as the radial location of the section increases.

The differences between the two CFD methods happen due to the radial effects that cause air velocity components along the blade span. This radial velocity component is not taken into account in the quasi-3D approach since it assumes pure 2D flow over each section. On the other hand, the difference in pressure values on the leading edge is not expected to have a major effect on the velocity or location of the particle since it happens only on a small area of the section and the inertia of the particles will make the response to such a rapid change in velocity very low.

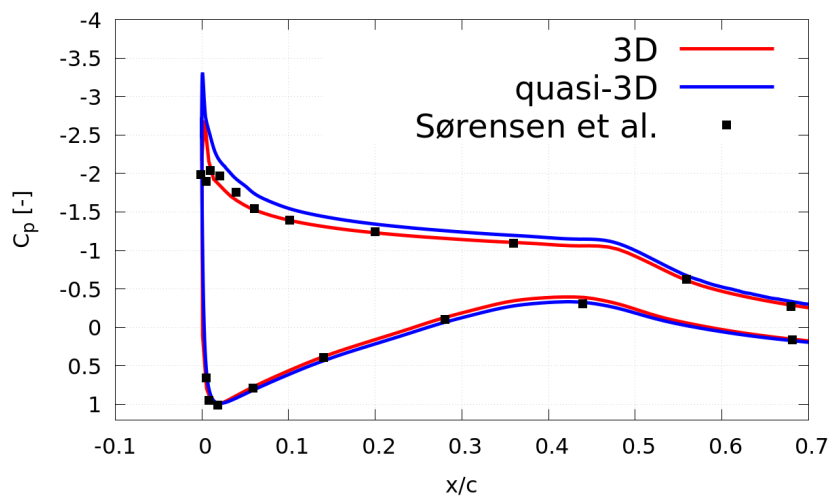
In this case, the deviations between the quasi-3D and the full 3D CFD simulations were minimal since the simulations were carried out at the rated wind and rotational speeds. This makes the aforementioned assumptions of the quasi-3D approach are valid and the approach can be used in ice accretion simulation. However, we can expect that at the higher wind and rotational speeds, the radial effects will have higher effects and the quasi-3D approach cannot be valid anymore.

6.2.2 Validation of ice accretion

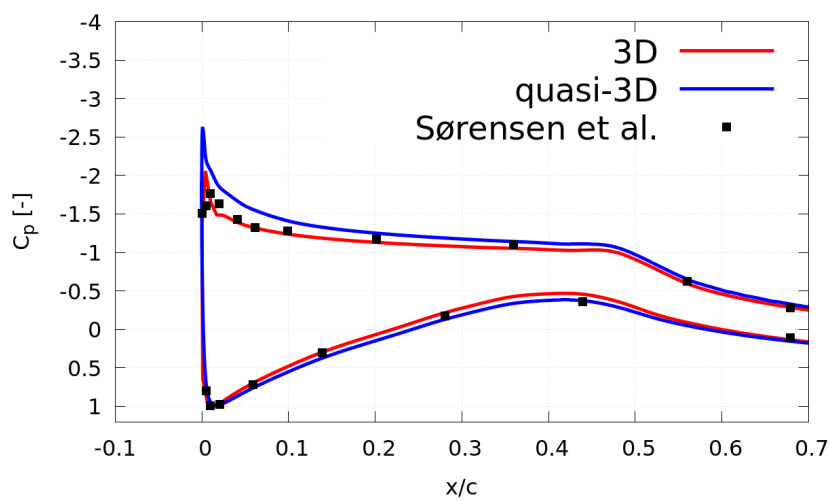
After the validation of the C_p distribution over the blade sections, ice accretion simulated using the quasi-3D method was compared with other simulation results from different works of literature. In this thesis, the simulation results from the new OpenFOAM code are compared with ice accretion results from Son and Kim [8] that were simulated using an Eulerian solver and the results from Reid et al. [9] using FENSAP-ICE software that also uses the Eulerian approach. The problem with this validation case is that three simulation cases are compared with no experimental results. The nature of ice accretion wind tunnel experiments makes it too expensive to be carried out on a large structure like wind turbines. Also, the rotating blades of the wind turbines need a lot of expensive precautions to avoid any damage to the wind tunnel because of ice separation from the blades due to centrifugal force. This causes a lack of experiments that can mimic the ice accretion on wind turbine blades.



(a)



(b)



(c)

Figure 6.1: Comparison of C_p distribution of quasi-3D, full 3D CFD simulations using OpenFOAM and experimental results [7] of NREL PhaseVI blade sections for $r/R =$ a) 0.467, b) 0.633, c) 0.8

Figures 6.2 and 6.3 shows the ice accretion simulations of rime and glaze ice accretion respectively on blade sections at $r/R = 0.467, 0.633, \text{ and } 0.8$. For these ice cases, the simulations were carried out at the rated wind and rotational speeds as in the C_p distribution comparison. Also, the ice accretion occurs at $LWC = 0.5 \text{ gm}/\text{m}^3$ and $MVD = 20 \text{ }\mu\text{m}$ for 60 minutes of accretion time. For these two cases, ambient temperature $T_\infty = 258^\circ\text{K}$ and 270.15°K for rime and glaze ice respectively.

In Fig. 6.2a and 6.2b, a good agreement between present work, Son and Kim, and FENSAP-ICE results can be noticed. However, in Fig. 6.2c, deviations from the other simulations can be noticed. The differences between the ice profiles from the different simulation cases can be seen in both the ice thickness at the stagnation point and the end of the ice profile on the lower surface of the airfoil. These differences could be due to the presence of radial effects near the tip region of the blade. Since the radial effects are ignored in the quasi-3D case, the differences between the results are increasing as the radial location of the section increases.

In Fig. 6.3 which shows the glaze ice case simulation, all simulation cases have the same range of total ice thickness on the leading edge. However, the quasi-3D approach manages to capture the horns of ice on the lower side of the leading edge while the other two methods couldn't capture this phenomenon. These differences can be justified by the difference in the calculation methods of the convective heat transfer coefficient's distribution over the sections. Also, the radial effects can play a bigger role in this case than the rime ice case due to the presence of a relatively thick liquid water film on the blade and some radial effects that can also change the convective heat transfer coefficient and the shear stress applied on the liquid film.

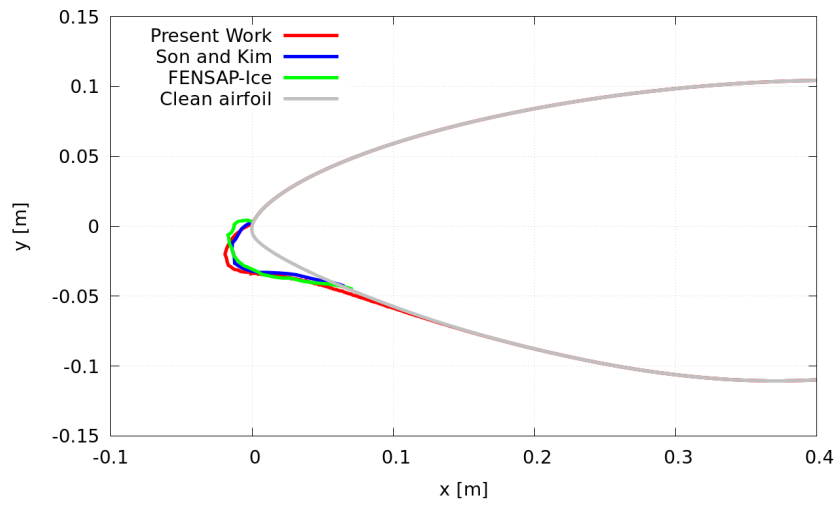
From the results shown in this section, it can be concluded that such a method should provide adequate results for the ice accretion as long as the operating conditions do not involve radial effects on the turbine blade. Despite showing some radial effects, especially at the leading edge of the blade tip region, this method can still be feasible to use to simulate ice formation because of its simplicity and low computational cost.

6.3 Simulation of NREL 5MW wind turbine blade

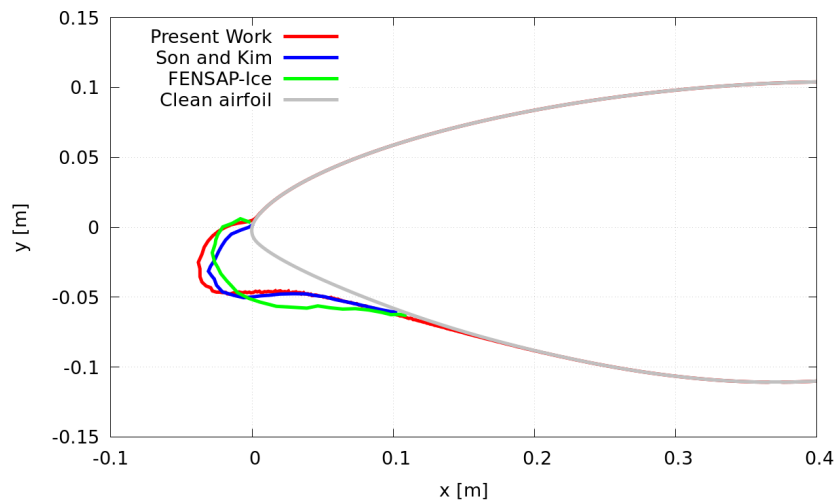
The NREL 5MW wind turbine blade was selected as a case study for ice accretion on the wind turbine blade. This blade was particularly selected as it represents a multi-megawatt blade that has enough information about the blade geometry to be used and replicated. The same procedure applied to the NREL PhaseVI wind turbine blade in the previous section is applied on the NREL 5MW blade to simulate ice formation and anti-icing heat. In this section, The NREL 5MW blade icing is simulated at the rated wind and rotational speeds for three different cases:

- Rime ice case: at $T_\infty = 245.2^\circ\text{K}$
- Glaze ice case: at $T_\infty = 270.15^\circ\text{K}$
- Anti-icing heat case: also at $T_\infty = 270.15^\circ\text{K}$

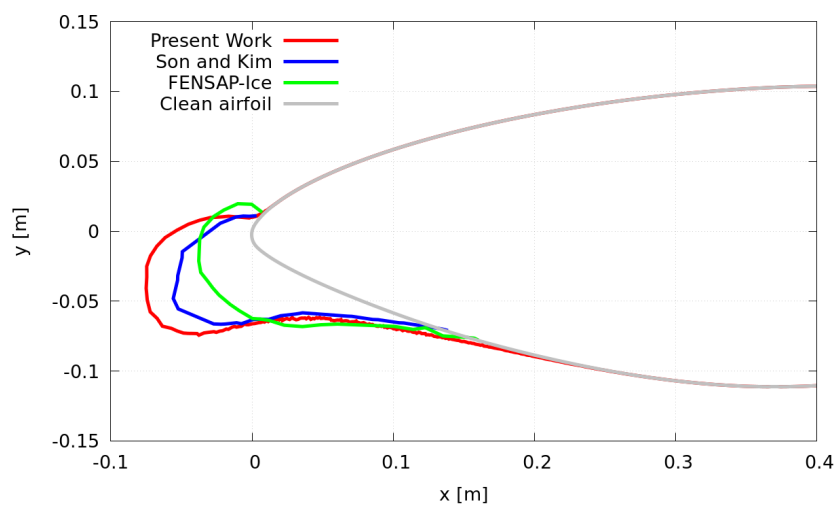
Instead of assuming a value for LWC, a calculated value could be obtained using the analysis of NEWA data. By selecting the location of ForWind lab - University of Oldenburg, the analysis of the atmospheric data results in a value for $LWC = 1.864 \text{ gm}/\text{m}^3$ which occurs at the chosen location for almost 100 hours every year.



(a)



(b)



(c)

Figure 6.2: Comparison of rime ice profiles of simulations of NREL PhaseVI blade of present work, Son and Kim [8], and FENSAP-ICE [9] sections for $r/R =$ a) 0.467, b) 0.633, c) 0.8

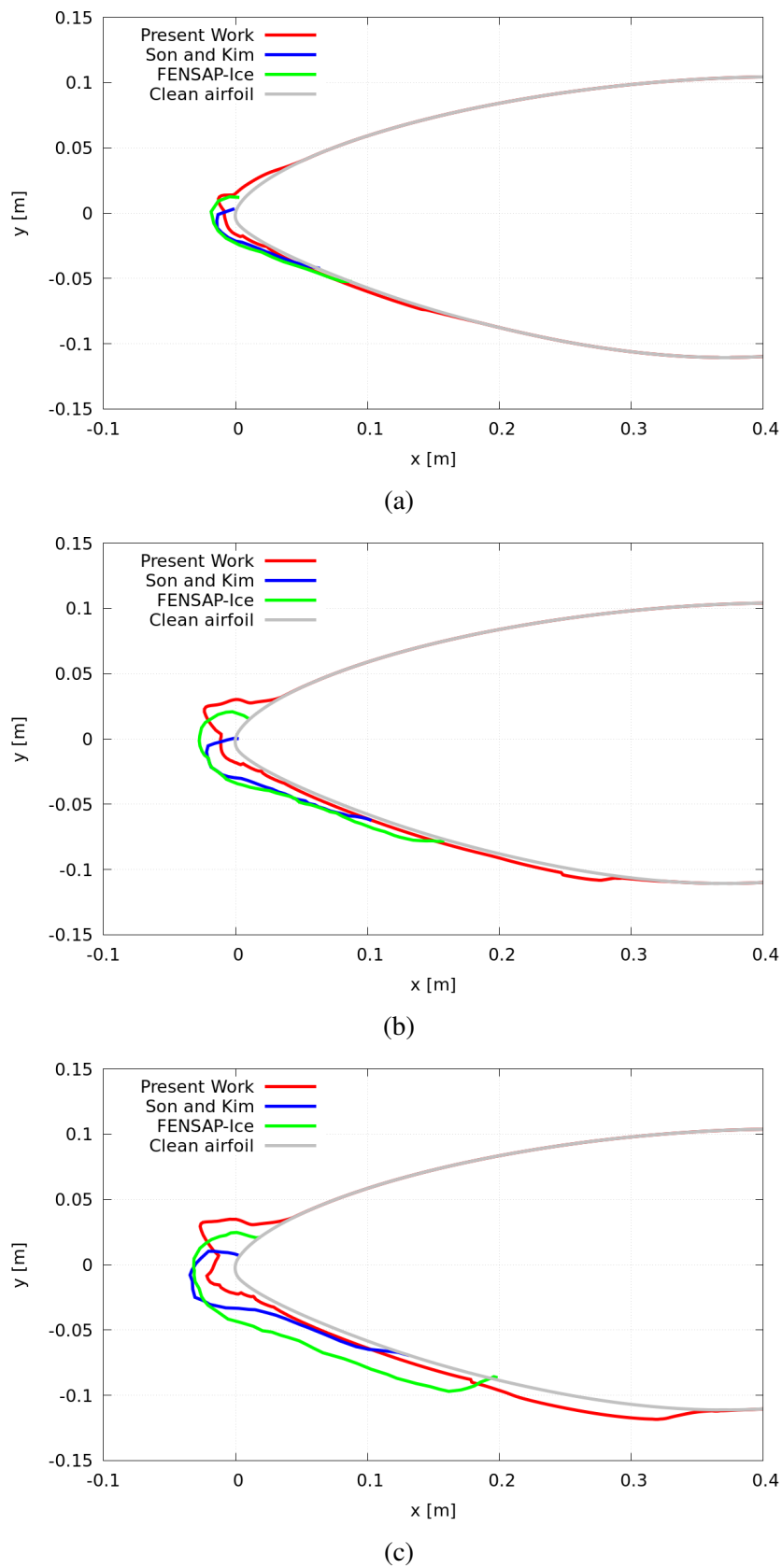


Figure 6.3: Comparison of glaze ice profiles of simulations of NREL Phase VI blade of present work, Son and Kim [8], and FENSAP-ICE [9] sections for $r/R =$ a) 0.467, b) 0.633, c) 0.8

6.3.1 Validation of air flow field

The C_p distribution over different NREL 5MW clean blade sections is compared with the quasi-3D simulations to check the 3D rotation effects that happen during the rotation of the blade. Fig. 6.4 shows the C_p distribution at blade sections located at $r/R = 0.4, 0.5, 0.6, 0.7, 0.8,$ and 0.95 . In this figure, it can be noticed that the C_p distribution agrees very well on the lower airfoil surface. However, this agreement decreases on the upper airfoil surface and the C_p distribution shows significant deviations as shown in Fig. 6.4f.

As mentioned in the NREL phase VI turbine case, the deviations in 6.4f can be justified by the radial location of this section, specifically 95% of the blade span. Since the section is located near the tip of the blade, tip vortices take place at this section and have a huge effect on the overall 3D airflow around this section and of course, this effect cannot be taken into consideration in quasi-3D simulations. This also can be noticed by the deviating C_p values at the leading edge of the airfoil. However, these deviations are thought to be close to the leading edge and the inertia of the water particles will dampen these effects on the droplets and make the droplets slower in their response to these rapid changes. In general, the C_p distribution can be considered matching between quasi-3D and 3D CFD simulations.

6.3.2 Simulation of collection efficiency

The Lagrangian particle tracking of the 2D section has led to the β distribution shown in Fig. 6.5. The maximum value of β at each point corresponds to the stagnation point of each section. Therefore, the maximum value moves towards the trailing edge of each section over the lower airfoil surface as the section is located closer to the root of the blade. This corresponds to the change of the actual AoA relative to the relative wind velocity.

Also, it can be noticed that the value of the maximum β is increasing as the radial position moves towards the tip. This is also can be justified by the relative wind velocity that increases as the radial position increases. The higher relative wind velocity means a higher rate of water particles hitting the surface of the blade compared to the upstream water mass flux. This increase is reflected in the mass of ice formed on the leading edge.

6.3.3 Simulation of ice profiles

In this section, both rime and glaze ice conditions are simulated on the NREL 5MW wind turbine blade to analyze and compare the resulting profiles in both cases. First, the simulation results of the rime ice case are shown in Fig. 6.6. For this case, it can be seen that the ice formation is not significant until $r/R = 0.5$. After this section, ice formation grows rapidly until it reaches almost 10% of the chord length at $r/R = 0.95$. This corresponds to the β distribution shown in Fig. 6.5 in which the maximum β value is increasing as the radial position increases due to the increase in relative wind speed.

In this simulation case, the rough ice surface can also be noticed. For example, in figures, 6.6d-6.6f, some rough ice locations can be noticed on the lower airfoil surface. This corresponds also to the results shown for case 27 simulations in Sec. 5.6. On the other hand, the glaze ice case shows smoother ice profiles since a part of the impinging mass keeps its liquid form and flows on the solid surface. In addition to having a smaller thickness at the stagnation point, the

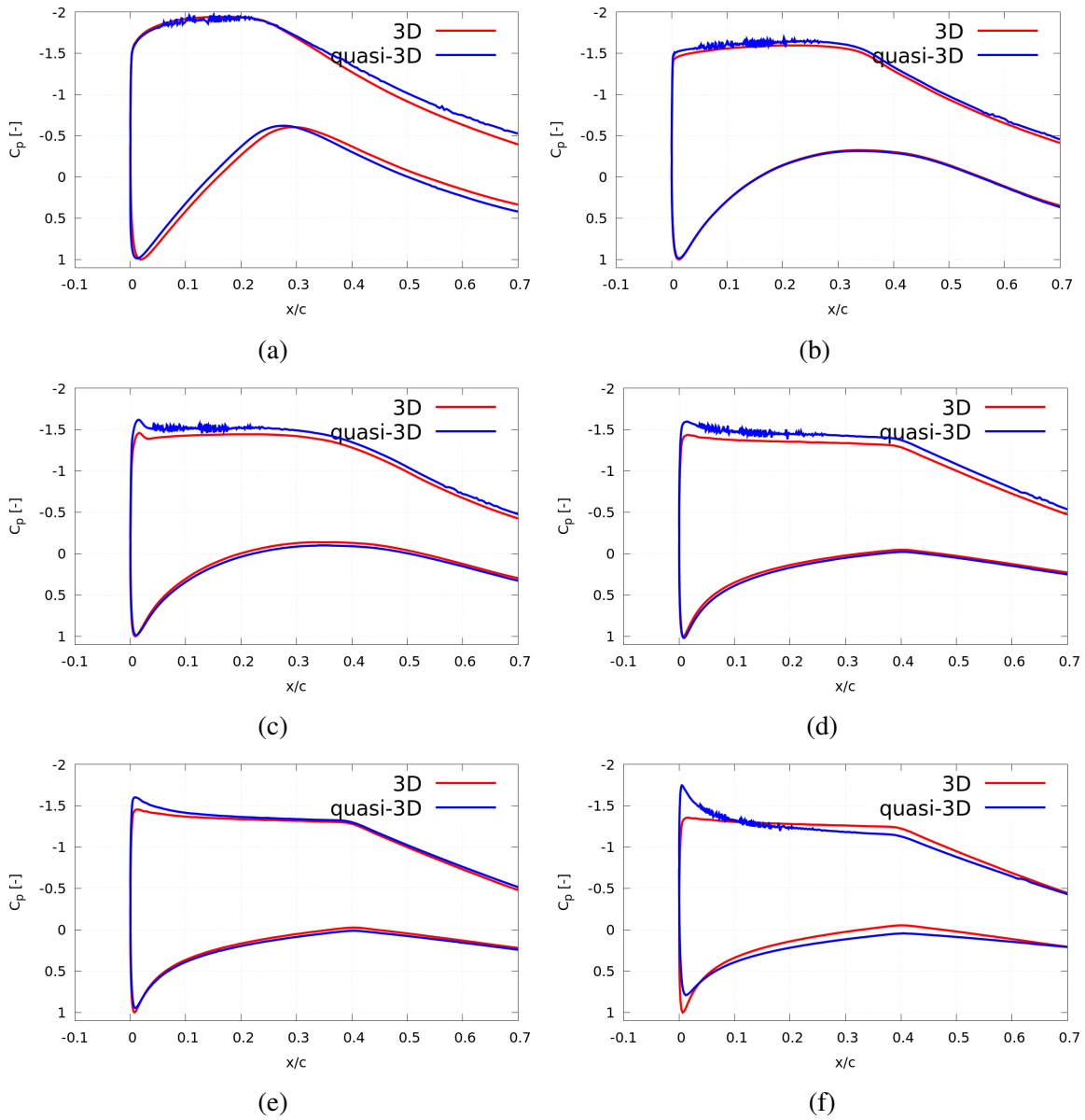


Figure 6.4: C_p distribution of 2D vs 3D CFD simulations of NREL 5MW blade sections for r/R = a) 0.4, b) 0.5, c) 0.6, d) 0.7, e) 0.8, and f) 0.95

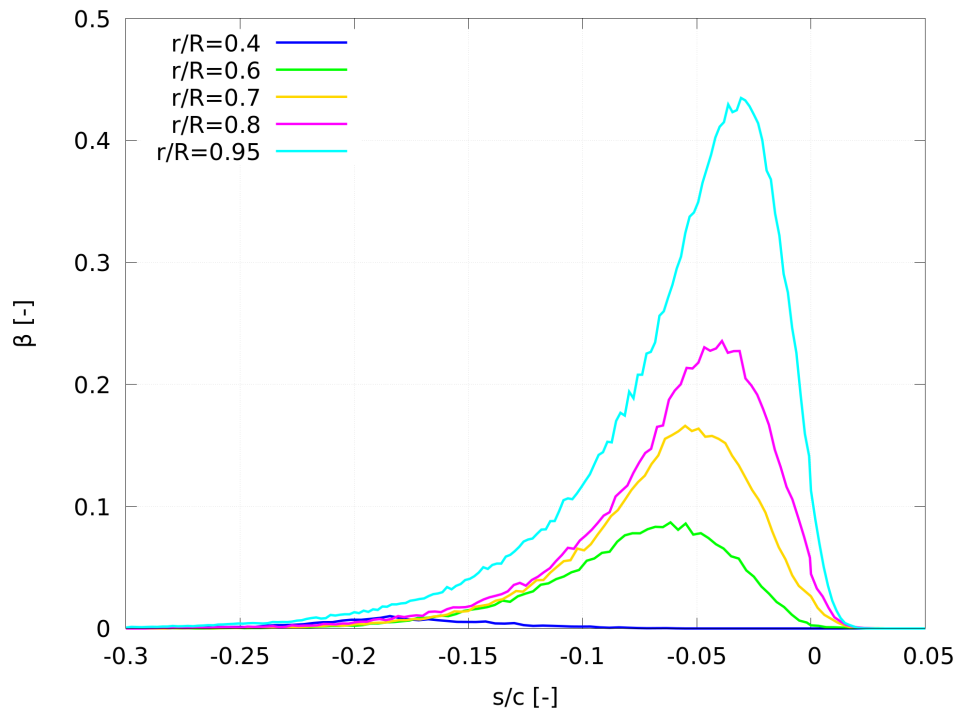


Figure 6.5: Collection efficiency distribution with the surface distance from the leading edge on different NREL 5MW blade sections

glaze ice, in this case, is swept towards the trailing edge when compared to the rime ice case. This also happens because of the water runback on the surface and the changing value of the convective heat transfer coefficient over the whole blade.

6.3.4 Simulation of anti-icing heat

The minimum required anti-icing heat, as explained in Sec. 3.7.1, is calculated for the NREL 5MW wind turbine blade. This anti-icing heat is calculated at glaze ice atmospheric conditions previously used in this section namely, $T = 270.15^{\circ}\text{K}$, $\text{LWC} = 1.864 \text{ gm}/\text{m}^3$, and $\text{MVD} = 29.46 \mu\text{m}$. The test took place for wind turbine blades exposed to icing conditions for 30 minutes at the rated wind and rotational speeds of the NREL 5MW rotor. The anti-icing heat is studied for this blade with two different surfaces:

- Ordinary surface: for which it is assumed that no water droplets will splash off the surface
- Ice-phobic coated surface: with $R_{sm} = 5.171 \times 10^{-6}$ and $R_{pk} = 1.16 \times 10^{-5}$ that represents the surface roughness properties of one of the ice-phobic coatings provided by one of the project partners.

Fig. 6.8a shows a comparison between the predicted water film mass accumulated on ordinary and ice-phobic surfaces due to the impinging water particles. This accumulated water mass is then reflected as anti-icing heat on the blade shown in Fig. 6.8b. It can be seen in Fig. 6.8

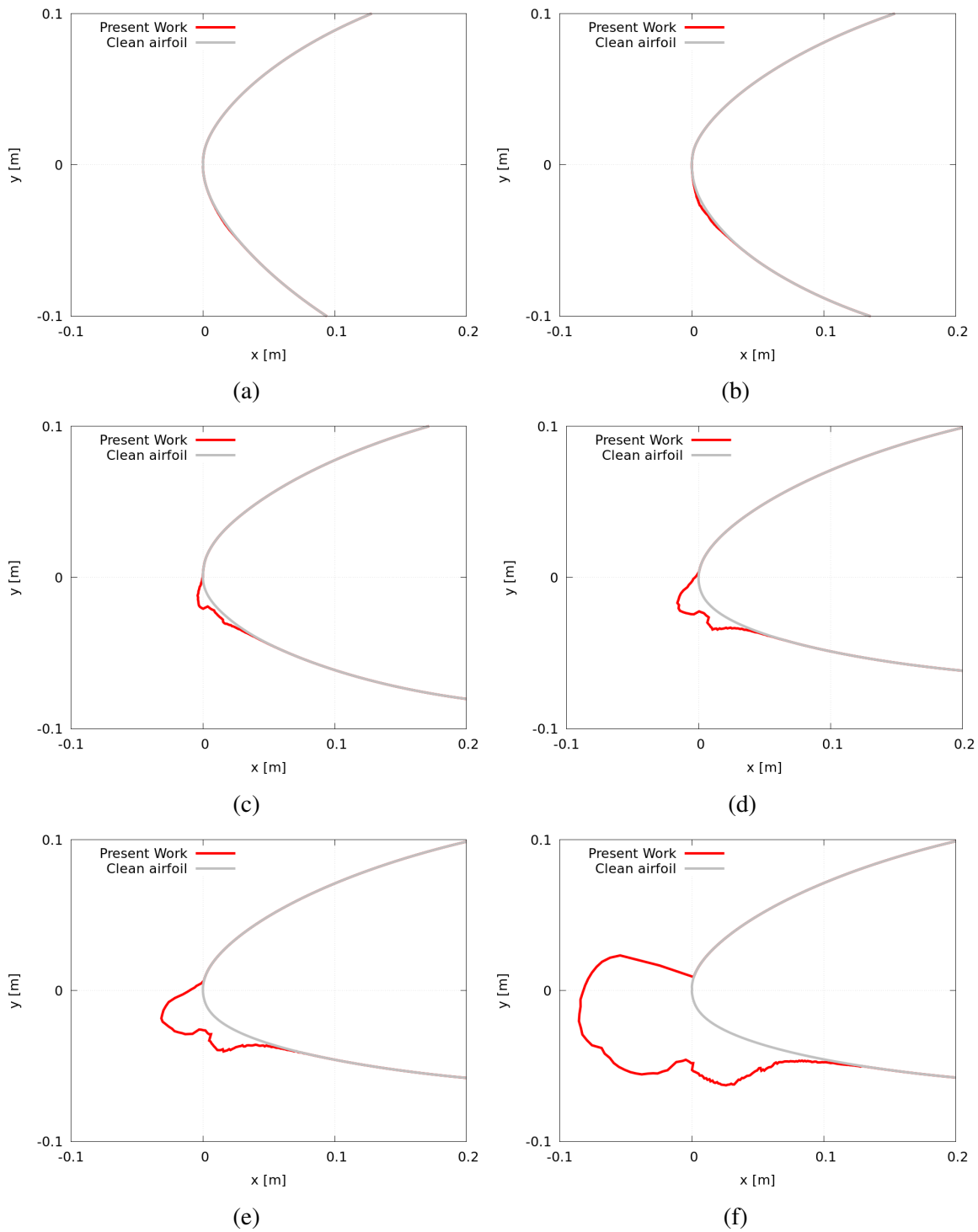


Figure 6.6: Rime ice profiles for NREL 5MW blade sections using quasi-3D approach for r/R = a) 0.4, b) 0.5, c) 0.6 , d) 0.7 , e) 0.8, and f) 0.95

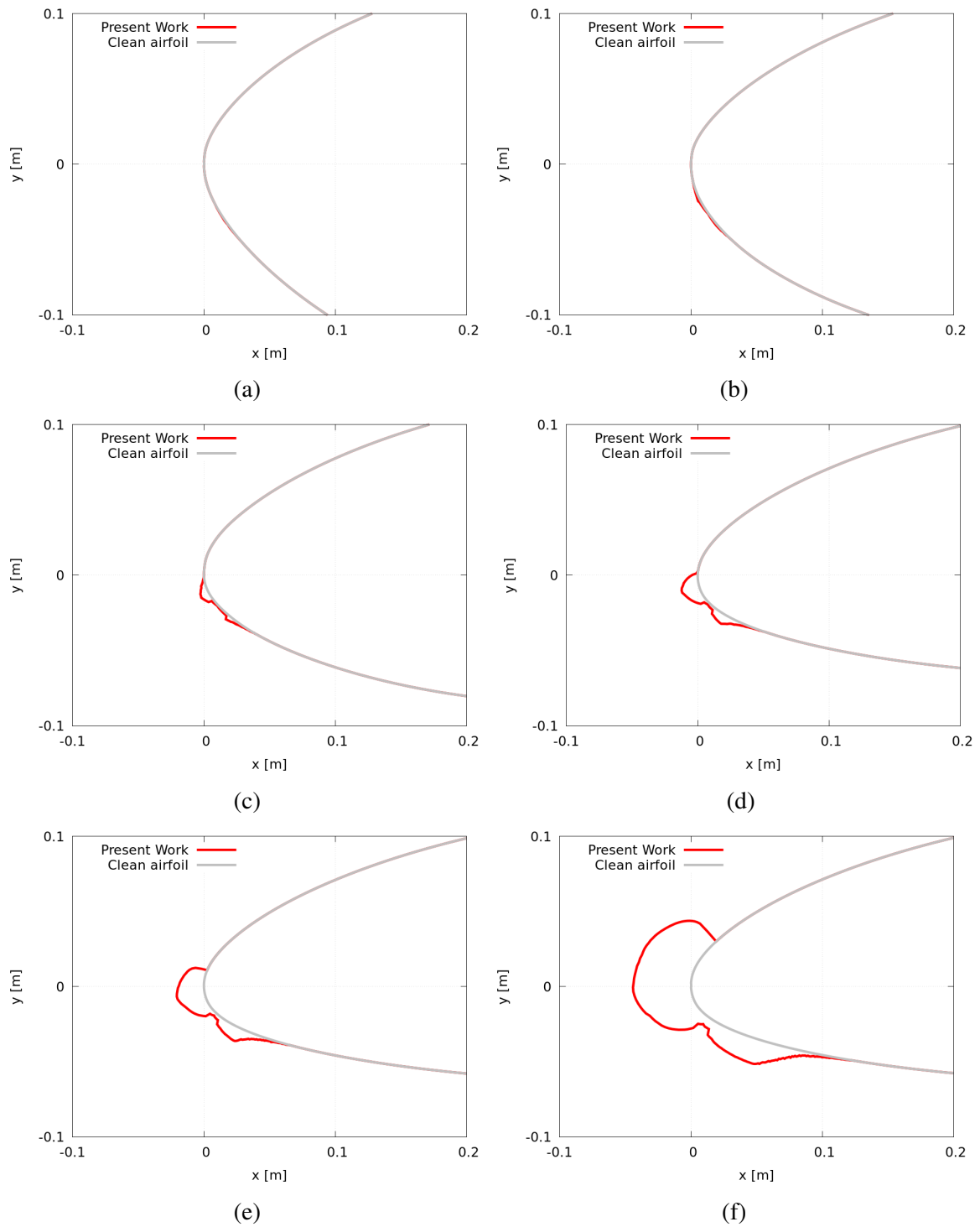


Figure 6.7: Glaze ice profiles for NREL 5MW blade sections using quasi-3D approach for r/R = a) 0.4, b) 0.5, c) 0.6 , d) 0.7 , e) 0.8, and f) 0.95

that accumulated water film on the surface of the blade is rapidly increasing for middle and tip sections (i.e., sections starting from $r/R = 0.5$). As explained in the rime and glaze ice cases, this rapid increase happens due to the increase in β . The difference between the water mass, and hence the anti-icing heat, in the case of ordinary and ice-phobic coatings is also increasing as the radial position of the section is increasing.

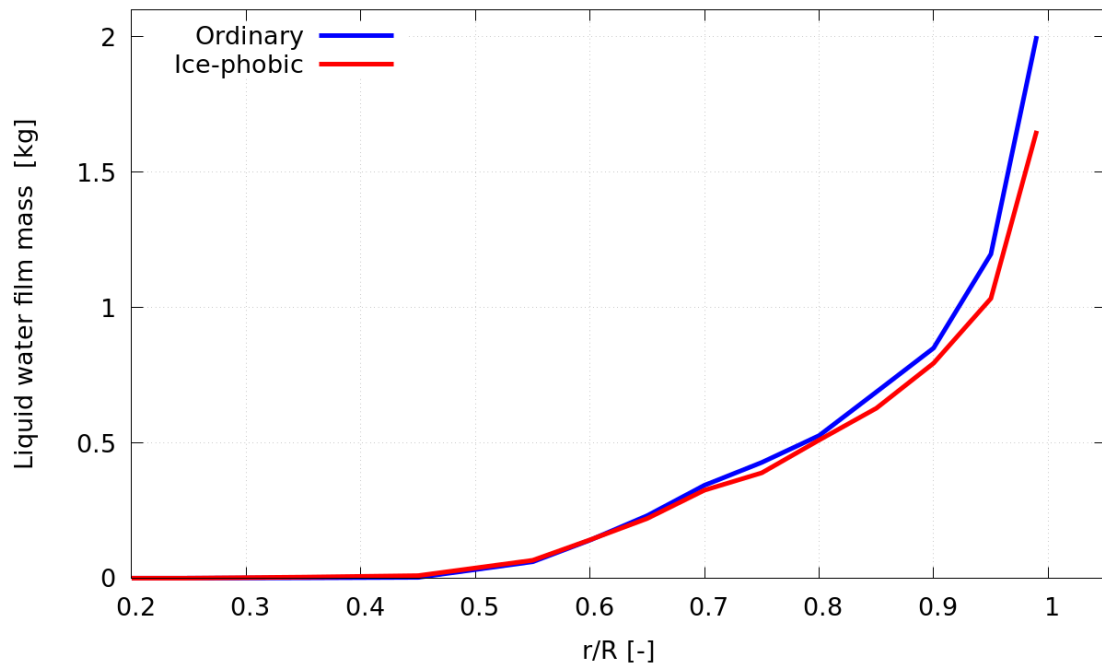
This increasing gap in anti-icing heat between the ordinary and ice-phobic coating happens due to the increase of relative velocity of the sections. As the relative wind velocity increases, water particles impinge on the surface of the blade with a higher velocity, and the particles have a higher probability to exceed the critical Weber number value (We_c) calculated from Eq. 2.21. Accordingly, more water particles will splash off the surface of ice-phobic coating as the radial position, and hence the relative wind velocity, increases.

To take a deeper look at the effects of the usage of the ice-phobic coatings, Fig. 6.9 shows the anti-icing heat distribution over the tip section of the NREL 5MW wind turbine blade located at $r/R = 0.99$. This plot shows that there is a difference of more than 25% of the peak anti-icing heat over the blade section. Also, the locations of these two peak values is located on the upper surface of the airfoil section in both cases. Regardless the ambient conditions, one should keep in mind that water film in this case should remain in the liquid state due to heating. This means that the water film is highly affected by the convective heat transfer coefficient exactly like the glaze ice case.

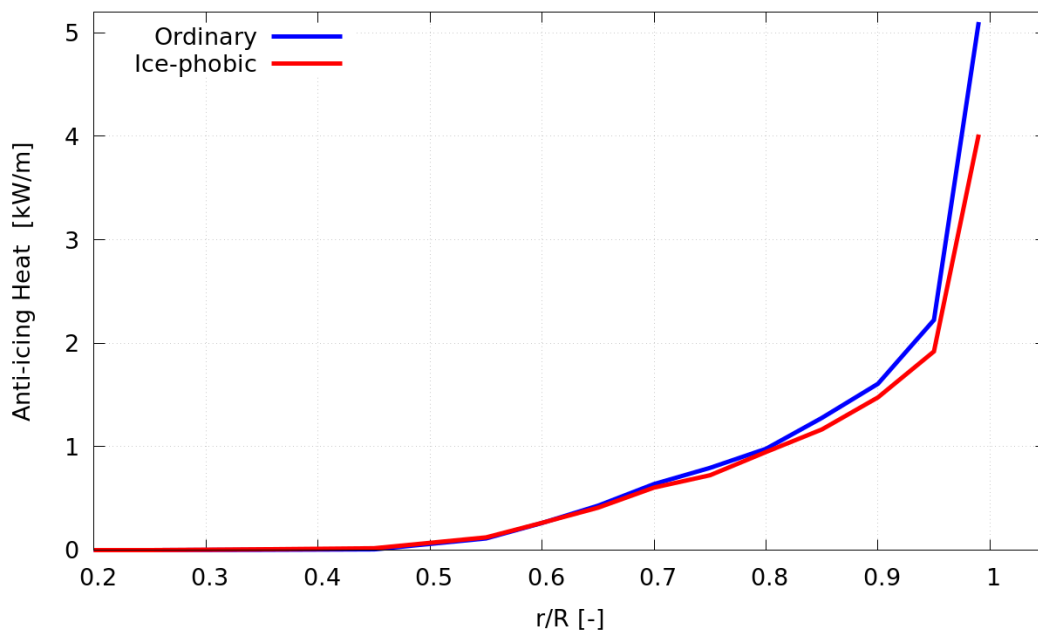
Another remark on this plot is that the location of the peak value of anti-icing heat on the section in case of using an ice-phobic coating is slightly shifted towards the trailing edge on the upper surface of the airfoil section. This slight shift downstream could be due to the decreased water film thickness and hence the decreased film velocity in the case of ice-phobic coating. The decreased film velocity causes decreased convective heat transfer rate between the water film and the solid wall, which is set to be at ambient temperature. This decrease slightly delays the peak cooling of the water film and accordingly delays the peak anti-icing heat required over this section.

From the above analysis of anti-icing heat over the NREL 5MW wind turbine blade and by knowing the width for each of the calculated sections, an estimate of the total minimum required anti-icing heat can be calculated. This estimate shows that the NREL 5MW will require about 39.13 kW for ordinary surface and 34.26 kW for the ice-phobic case for each blade. This means that using ice-phobic coating can result in about 12.8% saving in the required anti-icing heating power. Such a saving can be improved by using a more ice-phobic coating with an enhanced microscopic surface structure to be able to repel more water particles upon their impingement on the surface.

It can be concluded from this analysis that ice-phobic coatings have more effects on the anti-icing heat for the middle and tip sections of the blade. Luckily, these sections are the most affected by icing conditions and ice accumulation as was shown in the previous sections. Also, Fig. 6.9 shows obviously that the ice-phobic coating is required close to the leading edge of each section. This gives an idea about the effective way to apply such coatings on the blade and how to optimize the location of applying these coatings to decrease the cost of coatings with a maximum anti-icing heating power saving.



(a)



(b)

Figure 6.8: a) Accumulated liquid water film mass and b) the resulting anti-icing heat per meter span of the section at different radial positions for NREL 5MW wind turbine blade

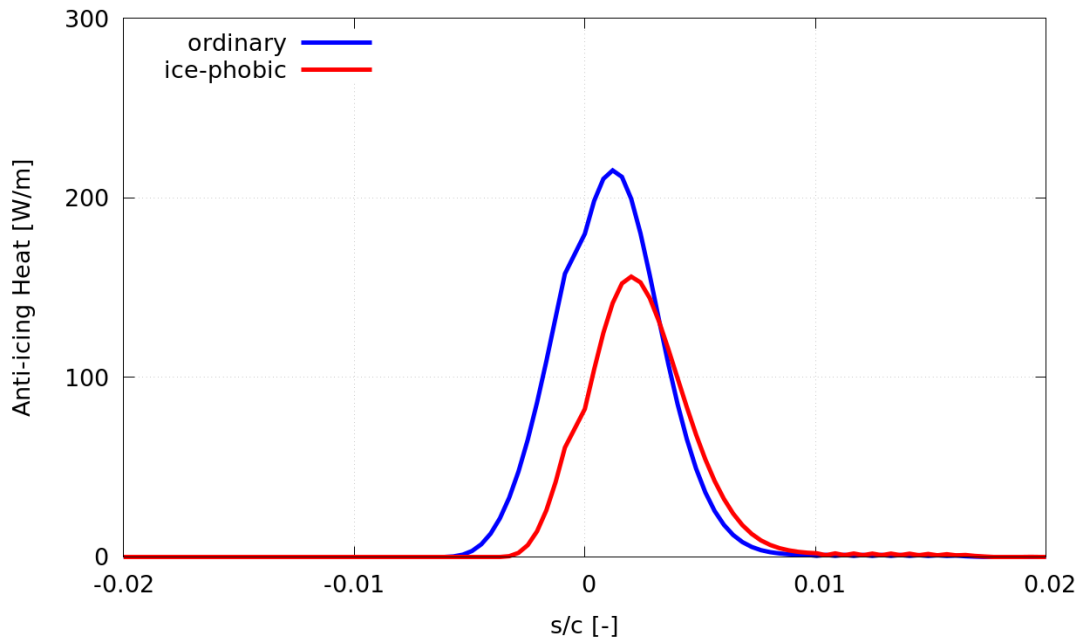


Figure 6.9: Anti-icing heat distribution over blade section at $r/R = 0.99$ for ordinary and ice-phobic coating

6.4 Conclusions and remarks

In this chapter, ice formation was simulated on the NREL PhaseVI and NREL 5MW 3D wind turbine blade. First, the quasi-3D ice accretion method was introduced and validated with results published in other literature for the NREL PhaseVI wind turbine blade. For rime ice cases, the current solver has shown a good agreement with the published results. However, in the case of glaze ice, this solver has shown a fair agreement. This could be due to the different methods of calculating the convective heat transfer coefficient for different solvers.

After that, the same method was used to simulate ice accretion on NREL 5MW wind turbine blade as an example of a multi-megawatt wind turbine. For this turbine, rime and glaze icing were simulated and the final profiles were generated. Also, anti-icing heat for different sections was calculated. The results show a considerable increase in ice masses and the required anti-icing heat as the radial position increases and also near the leading edge from each section. On the other hand, coated wind turbine blades have shown a decrease of about 12% of the total anti-icing heating power compared to ordinary surfaces.

From the simulation in this chapter, we can conclude that if ice-phobic coatings are to be considered as a solution to minimize the negative effects of ice accretion in general, then the focus of applying these coatings should be on middle and tip sections and around the leading edge of the blade to optimize the coverage of the coating to cover the most effective regions of the blade surface.

Chapter 7

Intermittent wind fields simulations

7.1 Introduction

The interest in simulating the effects of turbulent inflow on wind turbines has been growing due to the growing interest in expanding the utilization of on-shore wind farms. This growing interest has motivated many researchers to study the effects of turbulent inflow on wind turbine performance and loads. However, generating a numerical wind field that mimics the physical phenomenon of turbulence is so far impossible. In this chapter, we introduce a novel method to convert wind fields generated using the Mann model into new time-mapped Mann fields that mimic the intermittency that occurs in the real wind fields.

Despite that this topic seems to be completely different from the topics discussed in the rest of this thesis, there is a strong connection between ice formation and turbulent inflow to wind turbines. This connection lies in the fact that most of the wind farm locations that suffer from ice formation are located on-shore at high altitudes. These high-altitude locations are mostly surrounded by mountains and hills that generate such turbulence. Hence, it is equally important to study such a phenomenon with the study of ice accretion on wind turbine blades.

Applying a Random Time Mapping to Mann modelled turbulence for the generation of intermittent wind fields

Khaled Yassin¹, Arne Helms², Daniela Moreno¹, Hassan Kassem³, Leo Höning^{2,3}, and Laura J. Lukassen¹

¹ForWind, Institute of Physics, Carl von Ossietzky University Oldenburg, Küpkersweg 70, 26129 Oldenburg, Germany

²Institute of Physics, University of Oldenburg, Carl von Ossietzky University Oldenburg, Küpkersweg 70, 26129 Oldenburg, Germany

³Fraunhofer Institute for Wind Energy Systems – Fraunhofer IWES, Küpkersweg 70, 26129 Oldenburg, Germany

Correspondence: Khaled Yassin (khaled.yassin@uni-oldenburg.de), Laura J. Lukassen (laura.lukassen@uni-oldenburg.de)

Abstract. A new approach to derive a synthetic wind field model which combines spatial correlations from the Mann model and intermittency is introduced. The term intermittency describes the transition from Gaussian to non-Gaussian velocity increment statistics at small scales, where non-Gaussian velocity increment statistics imply a higher probability for extreme values than a Gaussian distribution. The presented new model is named the Time-mapped Mann model. The intermittency is introduced by applying a special random time-mapping procedure to the regular Mann model. The Time-mapping procedure is based on the so-called Continuous-time random walk model. As will be shown, the new Time-mapped Mann field reflects spatial correlations from the Mann model in the plane perpendicular to flow direction and temporal intermittency. In a first wind turbine study, the new Time-mapped Mann field and a regular Mann field are used as inflow to a wind turbine in a Blade Element Momentum simulation. It is shown that the wind field intermittency carries over to loads of the wind turbine, and, thus, shows the importance of carefully modeling synthetic wind fields.

Copyright statement. TEXT

1 Introduction

Wind energy plays a leading role in the energy transition process to renewable energy these days. In 2020, the world witnessed new wind energy installations by 93 GW to make the global installed capacity of wind energy 743 GW according to the Global Wind Energy Council (GWEC (2021)). The growing demand for wind energy resulted in growing turbine rotor diameters. This leads to an increase in loads on the different turbine components like blades and tower. Numerical simulations are now crucial to predict loads and performance parameters in the early design stages. In this context, wind fields should be accurately simulated to be able to anticipate extreme load cases and fatigue loads on different parts of the wind turbine to reach the optimum design without compromising the structural limits of these components. However, the physics of the turbulent wind fields are not yet completely understood and many models were proposed to simulate these fields as described in the following.

The IEC 61400-1 standard for wind turbines (Han (2007)) recommends using Gaussian based atmospheric turbulence models, namely Kaimal (Kaimal et al. (1972)) and Mann (Mann (1994, 1998)) models to simulate turbulent wind fields. These two turbulent wind field models imply the assumption that the velocity increments of the wind fields behave in a Gaussian manner. However, it is well documented that the velocity increments of real atmospheric wind fields show non-Gaussian behavior, which is widely called intermittency. Through the heavy tails of the distribution, this implies a larger probability for extreme values than in a Gaussian distribution. Boettcher et al. (2003) showed that wind field measurements from near the German North Sea coast line have a non-Gaussian distribution of two-point statistics of velocity increments for certain mean wind velocity intervals. Also, Vindel et al. (2008) have shown the intermittency of velocity increment statistics in data of the atmospheric boundary layer velocity measured by Cuxart et al. (2000). More recent researches like the work of Liu et al. (2010) and Mücke et al. (2011) reached the same conclusion. This means that extreme wind velocity increments happen more often than what is predicted using the turbulence models recommended by the IEC standard. Also, Morales et al. (2012) presented a statistical scheme to assess turbulent wind fields that uses both, lower and higher-order one-point and two-point statistics. They have also compared synthetic turbulent time series using the Kaimal model with atmospheric turbulent wind field measurements from the research platform FINO-1. They have shown that the synthetic fields generated with the Kaimal model failed to grasp the intermittent behavior of the wind field.

The questions that arise at this point are, how a synthetic wind field can be modeled as realistic as possible and how this is reflected on the turbine loads. In this direction, Kleinhans (2008) proposed a new approach to generate an intermittent wind field using the Continuous Time Random Walk (CTRW) theory. This approach is based on stochastic differential equations and function that maps from an intrinsic time to real time to generate such an intermittent field whereas the spatial correlations are not as realistic as in the Mann field. A brief description of the CTRW model will be introduced in Sec. 2.3. In addition to the CTRW model, there also exist other models which can be applied to generate synthetic wind fields with intermittent features, e.g. by Friedrich et al. (2021) based on multi-point statistics which are not further discussed here.

Gontier et al. (2007) compared the effect of the intermittent CTRW wind field and other standard turbulence models (Kaimal and von Kármán (1948)) on the fatigue loads of the D8 small wind turbine at different wind speeds. The authors have found that the simulated wind turbine loads in the case of using the CTRW wind model are different from the loads simulated by using the other two models. However, the authors could not give definitive conclusions regarding the peak loads from their simulations. Later, Mücke et al. (2011) compared the statistics of wind fields generated by the Kaimal model, intermittent wind fields generated using CTRW and the atmospheric wind data measured within the GROWIAN project (Körber et al. (1988)). The three cases were then used in the NREL FAST (V6.01) (Jonkman and Jonkman (2005)) Blade Element Momentum (BEM) simulator to model the resulting rotor torque of the 1.5MW WindPACT (Malcolm and Hansen (2006)) turbine. Also, the authors analyzed the stress cycles for the rotor torque time series to study the effects of the three wind fields on fatigue loads. They have concluded that the statistics of the numerical results using the Kaimal wind field qualitatively differ from the results obtained from measurements. On the other hand, they have concluded that CTRW simulated wind statistics agree quite well and also provided the intermittent rotor torque statistics very close to the resulting torque from measurements.

Gong and Chen (2014) numerically investigated the short- and long-term extreme responses of the onshore NREL 5MW tur-

bine for a Gaussian wind field using a Kaimal wind spectrum and a second non-Gaussian wind field generated by a translation process theory introduced by Gioffre et al. (2000). They showed that the non-Gaussian wind field resulted in larger extreme loads of the blade root edge-wise and tower fore-aft moments while the responses of a stand-still wind turbine case were less sensitive to the non-Gaussianity of the wind field. Schottler et al. (2017) applied an intermittent wind field on a 0.58m diameter model wind turbine in a wind tunnel to measure the effect of such a wind field on the thrust, power and torque on the rotor. The authors found out that the turbine did not smooth out the intermittency and they also concluded that assuming non-Gaussian wind fields may lead to significant differences in loads on the turbine.

Schwarz et al. (2018, 2019) isolated and investigated the effect of intermittent wind velocity on equivalent fatigue loads of the NREL 5MW wind turbine at different wind speeds using BEM simulations. To isolate the effects of intermittency, two different velocity fields were generated utilizing the CTRW model: a Gaussian and a non-Gaussian wind field. Both of them have the same features except for the intermittency that was introduced in the non-Gaussian field utilizing the time mapping, which was simply omitted in the Gaussian case. For the two wind cases, three different spatial correlations were investigated: fully correlated fields, delta-correlated fields, and 3×3 sub-divided fully correlated fields. After analyzing the results of the different cases, the authors noticed that the highest effect of intermittency of the wind fields on the loads can be observed in the fully correlated case with 5% to 10% increase in fatigue loads while it completely disappears in the delta-correlated field. For the 3×3 sub-divided fully correlated field, intermittent loads were ranged between the other two cases. The authors concluded that intermittency in the wind field had a significant effect on loads.

Berg et al. (2016) also compared Gaussian and non-Gaussian wind fields using Large Eddy Simulations (LES) in the HAWC2 Computational Fluid Dynamics (CFD) software (Larsen and Hansen (2007)). They studied the effect of the intermittency on the different blade, tower, and shaft loads and deflections of the NREL 5MW wind turbine. In contrast with the aforementioned studies, they concluded that intermittency has no significant effect on the studied parameters. This shows that even though many studies reveal the influence of intermittency, the effect needs further investigation. Recently, Bangsa and Lutz (2021) simulated the DANAERO 2MW wind turbine under turbulent inflow using CFD and BEM simulations. In their work, they have compared tip deflections, flap-wise and edge-wise loads on the blade root, and the damage equivalent load (DEL) of the DANAERO wind turbine affected by a synthetic turbulent Mann field. The results of the simulated loads and deflections in their research have shown good agreement with measured data from the turbine operating under the same conditions. Specifically, the authors compared the flapwise, edgewise, and torsional deflections' spectra of the turbine under laminar and turbulent inflows. The presented analysis of the spectra is very detailed. However, the spectra of the deflections are not enough to study all aspects of the effects of turbulence.

In the present paper, a novel method to numerically generate a synthetic, intermittent turbulent wind field is introduced. Within this new method, the time-mapping technique introduced by Kleinhans (2008) is applied on a turbulent wind field generated by the Mann model. A detailed comparison between our new wind field using this time-mapping technique referred to as the Time-mapped Mann field in the following, and a standard Mann modeled wind field is carried out. As will be shown, the advantage of the new Time-mapped Mann field is that it combines spatial correlations from the Mann wind field and intermittent behavior. Also, a first insightful comparison between selected mechanical loads on a 1.5MW wind turbine resulting from both,

the Time-mapped Mann field and the standard Mann field is illustrated. The analysis of these turbine loads reveals the effect of intermittency on wind turbine loads.

2 Scientific background on synthetic wind fields

95 Before illustrating the derivation of the new Time-mapped Mann field, general wind field statistics that will be used to analyze the generated wind fields are introduced in Sec. 2.1. After that, in 2.2 and 2.3 the Mann and CTRW turbulent wind field models are introduced. The main purpose of this section is to provide the theoretical background for the derivation of the new model and its analysis. This chapter is also intended to be self-contained and provide all the necessary equations for the introduction of the proposed new Time-mapped Mann model.

100 2.1 Statistics of wind fields

For any turbulent wind field, the wind velocity time series U_i can be expressed as a function of mean velocity $\langle U_i \rangle$ and velocity fluctuation u_i , with $i = 1, 2, 3$ in three-dimensional space:

$$U_i = \langle U_i \rangle + u_i, \quad (1)$$

where the angular brackets $\langle \cdot \rangle$ denote an ensemble average. Throughout this paper, the ensemble average is partly replaced
 105 by spatial or temporal averages for practical purposes which will be indicated in the respective cases below. In our case, we assume only a mean velocity in x_1 -direction, i.e. $\langle \mathbf{U} \rangle = (\langle U_1 \rangle, 0, 0)$ which is the inflow direction in the following. From this decomposition, the turbulence intensity (TI) can be calculated as follows:

$$TI_i = \frac{\sigma_i}{\langle U_1 \rangle} = \frac{\sqrt{\langle u_i^2 \rangle}}{\langle U_1 \rangle}, \quad (2)$$

where i indicates the direction in which the turbulence intensity is calculated with respect to the mean velocity in the inflow
 110 direction $\langle U_1 \rangle$, and σ_i as the variance of u_i . The turbulence intensity is a one-point statistics in space and time of wind fields. However, for information on the spatial structures, one-point statistics are not sufficient and two-point statistics should be used for more information about the wind fields. As an example, the co-variance tensor contains two-point statistics:

$$R_{ij}(\mathbf{r}, \mathbf{x}, t) = \langle u_i(\mathbf{x}, t) u_j(\mathbf{x} + \mathbf{r}, t) \rangle \quad (3)$$

where R_{ij} is the two-point correlation which is independent from the position \mathbf{x} in case of homogeneous turbulence and \mathbf{r}
 115 is the displacement vector between the two points. Since Eq. 3 is a theoretical equation, there are no restrictions on selecting the two points for the two-point statistics. However, in practice, it is limited to the size of the data set of the wind fields. The spectral velocity tensor for homogeneous turbulence resulting from a Fourier transform of Eq. (3) gives (Pope (2001)):

$$\Phi_{ij}(\boldsymbol{\kappa}, t) = \frac{1}{(2\pi)^3} \int_{-\infty}^{\infty} \int_{-\infty}^{\infty} \int_{-\infty}^{\infty} R_{ij}(\mathbf{r}, t) \exp(-i\boldsymbol{\kappa} \cdot \mathbf{r}) d\mathbf{r}. \quad (4)$$

In this equation, $\boldsymbol{\kappa} = (\kappa_1, \kappa_2, \kappa_3)$ represents a three-dimensional wavenumber vector for the three directions. The one-dimensional spectrum is following from Eq. (4) by integration:

$$F_i(\kappa_1, t) = \int_{-\infty}^{\infty} \int_{-\infty}^{\infty} \Phi_{ii}(\boldsymbol{\kappa}, t) d\kappa_2 d\kappa_3 = \frac{1}{2\pi} \int_{-\infty}^{\infty} R_{ii}(r_1, 0, 0, t) \exp(-i\kappa_1 r_1) dr_1 \quad (5)$$

where the ii -index refers to the respective diagonal element of the tensor. The one-dimensional spectra with respect to κ_2 and κ_3 are computed accordingly. The spectral coherence for the wavenumber κ_1 with respect to two separate points in the $x_2 - x_3$ plane reads (Mann (1994)):

$$coh_{ij}(\kappa_1, \Delta x_2, \Delta x_3, t) \equiv \frac{|\chi_{ij}(\kappa_1, \Delta x_2, \Delta x_3, t)|^2}{F_i(\kappa_1, t) F_j(\kappa_1, t)} \quad (6)$$

with $F_i(\kappa_1, t)$ from equation (5) and the cross spectra χ_{ij} as defined below:

$$\chi_{ij}(\kappa_1, \Delta x_2, \Delta x_3, t) = \frac{1}{2\pi} \int_{-\infty}^{\infty} R_{ij}(r_1, \Delta x_2, \Delta x_3) \exp(-i\kappa_1 r_1) dr_1 \quad (7)$$

$$= \int_{-\infty}^{\infty} \int_{-\infty}^{\infty} \Phi_{ij}(\boldsymbol{\kappa}, t) \exp(i(\kappa_2 \Delta x_2 + \kappa_3 \Delta x_3)) d\kappa_2 d\kappa_3. \quad (8)$$

where $\Delta \mathbf{x}$ indicates the spatial step in three-dimensional space with its components Δx_1 , Δx_2 , and Δx_3 in x_1 -, x_2 -, and x_3 -directions, respectively. Another example for two-point statistics are the increment statistics in space described by:

$$\tilde{v}_i(\mathbf{x}, \Delta \mathbf{x}, t) = u_i(\mathbf{x} + \Delta \mathbf{x}, t) - u_i(\mathbf{x}, t). \quad (9)$$

Instead of spatial increments, one can also consider temporal increments as

$$v_i(\mathbf{x}, t, \tau) = u_i(\mathbf{x}, t + \tau) - u_i(\mathbf{x}, t) \quad (10)$$

where τ indicates the time lag. The probability density functions (PDFs) of the introduced temporal increments v_i have been investigated (Vindel et al. (2008), Liu et al. (2010), Mücke et al. (2011), Böttcher et al. (2007), Muzy et al. (2010)) as part of a more detailed characterization of wind turbulence beyond the standard guidelines. The Gaussian distribution is completely described by the mean and the variance. Further statistical information is required for characterizing a non-Gaussian distribution. The so-called kurtosis of a distribution allows a quantification of its deviation from a Gaussian distribution. For the temporal increments v_i , the kurtosis is defined as:

$$Kurt(v_i)(\mathbf{x}, t, \tau) = \frac{\langle v_i(\mathbf{x}, t, \tau)^4 \rangle}{\langle v_i(\mathbf{x}, t, \tau)^2 \rangle^2}. \quad (11)$$

For a Gaussian distribution, the kurtosis equals 3. Higher values indicate a heavy-tailed distribution in which extreme velocity increment values have a higher probability than predicted by a Gaussian distribution. We assume statistically stationary turbulence and, hence, omit the time t in the equations in the following.

Fig. 1 shows characteristics of temporal velocity increment statistics of atmospheric wind speed measurements. The data were collected at the site of a Nordex wind turbine with a hub height of 125m, located in Northern Germany. Around 500 time series of 10 minutes length were considered for the analysis. These time series correspond to the horizontal magnitude (U_1, U_2) of the wind speed measured at the hub height with a sampling rate of 50Hz; the vertical component (U_3) was neglected here. The mean wind speed and turbulence intensity of the individual measured time series range between 5m/s to 15m/s and 5% to 25% respectively. All the mean values of the wind direction, calculated over each of the 10 minutes periods, are distributed within a range of 165° . The selection and preparation of the data set were performed by Nordex according to internal objectives from the analysis. Here, we used the wind data set for illustration purposes rather than for a rigorous investigation on its characterization. The increments for the atmospheric measured data $v_{meas} = \sqrt{u_1^2(\mathbf{x}, t + \tau) + u_2^2(\mathbf{x}, t + \tau)} - \sqrt{u_1^2(\mathbf{x}, t) + u_2^2(\mathbf{x}, t)}$ were calculated similar to Eq. (10). Then, the statistics are computed for the whole data set which includes the increments v_{meas} for all the available time series. Fig. 1(a) presents the PDFs of v_{meas} for different time lags τ from 1sec to 60sec. For clarity of presentation, individual distributions are depicted with different markers and shifted vertically. For comparison, all the PDFs are normalized to a standard deviation equal to 1 and the corresponding Gaussian distributions are shown by a solid line. As can be observed, the PDFs of v_{meas} deviate from the respective Gaussian distributions. Specifically, the distributions of v_{meas} show heavy tails which represent the high probability of extreme events, which is higher than for the Gaussian PDFs. This effect, which is called intermittency, is a well-known feature of atmospheric wind as Vindel et al. (2008), Liu et al. (2010), Mücke et al. (2011), Böttcher et al. (2007) and many others have found. Similar to the results from the investigations mentioned earlier, Fig. 1(a) shows that the temporal increments v_{meas} are intermittent over a broad range of time lags τ . The evolution of the intermittency with τ can be quantified from the kurtosis. Fig. 1(b) shows the calculated kurtosis of the PDFs according to Eq. (11) of the atmospheric increments v_{meas} as function of τ . The values of $\text{Kurt}(v_{meas})$ higher than 3 reveal the intermittent behavior of the atmospheric data over a wide range of τ . Furthermore, this deviation is increasing with decreasing time lag τ . For large values of τ , the value of the kurtosis saturates at $\text{Kurt} \approx 5$. This robust intermittency on large scales of atmospheric increments could be explained by Böttcher et al. (2007) as a result of mixing of isotropic turbulent subsets which do not belong to the inertial range anymore. This explanation also justifies the fact that in Fig. 1(a), the deviation from Gaussianity for large τ (e.g. 30sec, 60sec) is still very pronounced. As consequence, differences between the distributions when increasing τ are hardly observable in Fig. 1(a) but more visible in Fig. 1(b).

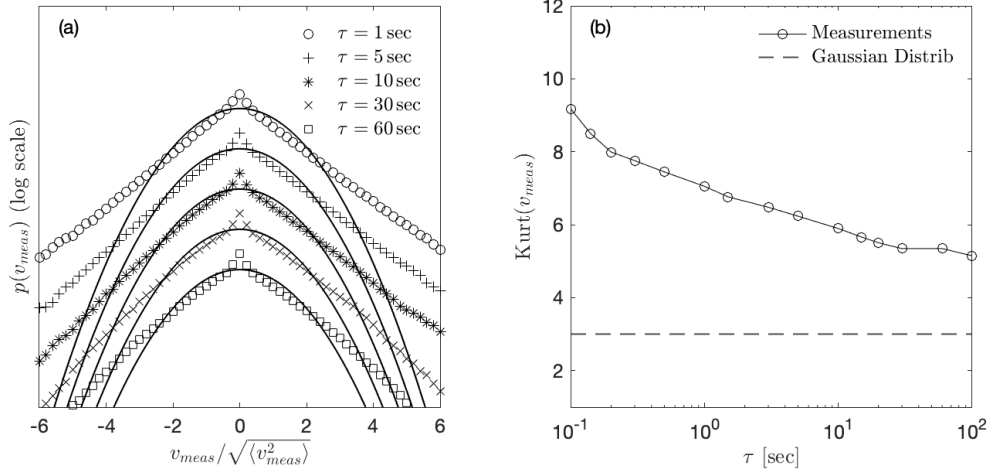


Figure 1. Statistical description of turbulent wind measurements from a Nordex wind turbine located in Northern Germany. (a) Normalized PDFs of velocity increments v_{meas} for different values of τ . The distributions for different values of τ , increasing from top to bottom, are depicted by different markers. In addition, solid lines correspond to Gaussian distributions with identical mean and standard deviation. In principle, the curves would all lie on top of each other but here, the curves are shifted vertically for a better visualization. (b) Kurtosis of velocity increments v_{meas} as function of τ . The angular brackets denote moving averages within the individual 600 s-time series and then over all data sets.

170 2.2 Mann Model

The basis of the Mann model (Mann (1994, 1998)) is a properly modeled spectral tensor according to Eq. (4). In this model, the turbulent velocity field is assumed to be incompressible and the velocity fluctuations are assumed to be homogeneous in space. The resulting velocity field depends on only three parameters, namely a length-scale L , a non-dimensional parameter Γ which is related to the eddy lifetime and, hence, to the shear gradient, and a parameter $c_K \epsilon^{2/3}$ with c_K as a constant and ϵ as the turbulent dissipation rate per unit mass. Within these assumptions, the second-order statistics such as variances and cross-spectra of real wind can be met. In case of isotropic turbulence (where assuming no shear) the spectral tensor takes the form (Pope (2001)):

$$\Phi_{ij}^{iso}(\boldsymbol{\kappa}) = \frac{E(\kappa)}{4\pi\kappa^4} (\delta_{ij}\kappa^2 - \kappa_i\kappa_j) \quad (12)$$

with κ as the magnitude of $\boldsymbol{\kappa}$ and $E(\kappa)$ as the energy spectrum. $E(\kappa)$ can be expressed with $c_K \epsilon^{2/3}$ and L that leads to (von Kármán (1948), Pope (2001)):

$$\Phi_{ij}^{iso}(\boldsymbol{\kappa}) = \frac{c_K \epsilon^{2/3} L^{17/3}}{4\pi} \frac{\delta_{ij}\kappa - \kappa_i\kappa_j}{[1 + (L\kappa)^2]^{17/6}}. \quad (13)$$

The corresponding one-dimensional spectra result in (Mann (1994)):

$$F_i(\kappa_1) = \begin{cases} \frac{9}{55} c_K \epsilon^{2/3} \frac{1}{(L^{-2} + \kappa_1^2)^{5/6}} & \text{for } i = 1 \\ \frac{3}{110} c_K \epsilon^{2/3} \frac{3L^{-2} + 8\kappa_1^2}{(L^{-2} + \kappa_1^2)^{11/6}} & \text{for } i \in \{2, 3\}, \end{cases} \quad (14)$$

accordingly, the variance becomes:

$$185 \quad \sigma_{iso}^2 = \sigma_1^2 = \sigma_2^2 = \sigma_3^2 = \frac{9}{55} \frac{\sqrt{\pi} \Gamma(\frac{1}{3})}{\Gamma(\frac{5}{6})} c_K \epsilon^{2/3} L^{2/3} \approx 0.688 c_K \epsilon^{2/3} L^{2/3} \quad (15)$$

where in this equation the Γ denotes the mathematical Gamma function. The value of the $c_K \epsilon^{2/3}$ parameter can be found by fitting the model to specific site data assuming isotropic turbulence and an infinitely large domain. Another possible way to avoid such assumptions was suggested by Larsen and Hansen (2007) who suggest choosing the value of $c_K \epsilon^{2/3}$ arbitrarily and then re-scaling the velocity field with a scaling factor. In this work, the fields used in the simulations were not re-scaled. However, the value of $c_K \epsilon^{2/3}$ was taken according to the Engineering Sciences Data Unit (ESDU (1982)) spectral model to achieve $TI_1 \approx 10\%$ as will be explained later in detail.

190 The Mann model provides a spatially correlated synthetic turbulent wind field where spatial homogeneity is one of the basic assumptions in deriving this model. However, since this model is based on the spectra but not on increment statistics of the atmospheric wind fields, it fails to display intermittency which should have effects on several turbine loads as shown in different former researches, cf. Sec. 1.

2.3 Continuous time random walk (CTRW) model

Kleinhans (2008) introduced the idea of generating a synthetic velocity time series $\mathbf{u}(s)$, on an intrinsic time scale s , based on a coupled Ornstein-Uhlenbeck process (Uhlenbeck and Ornstein (1930)) for $\mathbf{u}(s)$ and a reference wind speed $\mathbf{u}_r(s)$. Instead of a mean velocity, this reference wind speed $\mathbf{u}_r(s)$ is used in the modeling process which influences the whole velocity field (Kleinhans (2008)).

After generating the velocity time series $\mathbf{u}(s)$ for all grid points in a plane perpendicular to the flow velocity, a stochastic process is applied to map the field from the intrinsic time s to the physical time domain t . This mapping process is the crucial feature of the model for generating intermittent characteristics in the wind field. The mapping process is defined as (Fogedby (1994)):

$$205 \quad \frac{dt(s)}{ds} = \tau_\alpha(s) \quad (16)$$

where τ_α follows an α -stable Lévy distribution with characteristic exponent α (Kleinhans and Friedrich (2007)):

$$\tau_\alpha = \frac{1}{\pi} \operatorname{Re} \left\{ \int_0^\infty dz \exp \left[-iz\tau_\alpha - z^\alpha \exp \left(-i\frac{\pi\alpha}{2} \right) \right] \right\}. \quad (17)$$

Kleinhans (2008) generated the random variable τ_α according to the implementation introduced by Weron (2001):

$$\tau_\alpha = \frac{\sin(\alpha(V + \frac{\pi}{2}))}{\cos(V)^{\frac{1}{\alpha}}} \left(\frac{\cos(V - \alpha(V + \frac{\pi}{2}))}{W} \right)^{\frac{1-\alpha}{\alpha}} \quad (18)$$

210 where V is a uniformly distributed random variable that takes a value in the range between $]-\frac{\pi}{2}, \frac{\pi}{2}[$ and W is an exponentially distributed variable with a mean value = 1. The Lévy distribution is truncated for $0 < \tau_\alpha < c$ if $0 < \alpha < 1$, where c is a cutoff. Kleinhans (2008) showed that when continuous stable Lévy processes are used for the transformation from the intrinsic time s to the physical time t , the process is dominated by "waiting" regions. In this context, these regions are periods during which the wind speed is constant, a feature that is not observed in the atmospheric wind. In order to limit those periods to a realistic
 215 length, the Lévy distribution is truncated at the cutoff c . When $\alpha = 1$, $p(\tau_\alpha)$ is not a Lévy distribution anymore. It becomes a δ -correlated distribution with $\tau_1 = 1$. In that case, the mapping process from s to t is linear which makes $\mathbf{u}(s) = \mathbf{u}(t)$ and no intermittent behavior is introduced to the field.

As mentioned before, the main advantage of the CTRW model is that it manages to generate an intermittent wind field. However, the original CTRW model proposed by Kleinhans (2008) assumes that the spatial correlations of the velocity fluctuations
 220 between different points of the grid decay exponentially with the distance between them. This assumption must be understood as a simplification of atmospheric turbulence. A modified version of the original CTRW model was implemented by Schwarz et al. (2019) as introduced in Sec. 1. They generated individual CTRW time series and arranged them to generate three different spatial correlations in the wind field. Firstly, they set up fully correlated wind fields by repeating the same velocity time series in the whole x_2 - x_3 plane (perpendicular to the inflow direction). For the second arrangement, they generated delta-correlated
 225 wind fields by setting up an independent Ornstein-Uhlenbeck process in each point of the grid in the x_2 - x_3 plane. Finally, they considered an intermediate version of a 3×3 sub-divided fully correlated wind field. In this third scenario, the rotor plane was divided in a 3×3 grid in which each cell corresponds to a fully correlated area, but the nine areas are uncorrelated between them. They found different effects of the wind fields on the turbine loads depending on the resolution (i.e. fully correlated, delta-correlated, or partially correlated). However, no conclusive recommendation was provided on which resolution is most
 230 realistic.

3 The new Time-mapped Mann model

The new proposed Time-mapped Mann model aims at maintaining the spatial correlation provided by the Mann model explained in Sec. 2.2 while introducing the intermittency employing the time-mapping process of the CTRW model explained in Sec. 2.3. Accordingly, in our new Time-mapped Mann model, the Ornstein-Uhlenbeck process used to generate the wind field
 235 in the original CTRW model is replaced with a Gaussian wind field using Mann's model. The longitudinal spatial dimension in the Mann model is converted into the intrinsic time according to the Taylor hypothesis (Taylor (1938)). After that, the time mapping from intrinsic time s to physical time t is applied to each step n using the discretized form of Eq. (16) (Kleinhans (2008)):

$$t(s_{n+1}) = t(s_n) + C_{\alpha,c,\Delta s_t} \tau_\alpha(s_n) \quad (19)$$

240 where $C_{\alpha,c,\Delta s_t}$ is a normalization factor that has the dimension of a time and depends on the Lévy exponent α , the cutoff c and the discretization parameter $\Delta s_t = s_{n+1} - s_n$. The intrinsic time step Δs_t is equidistant while the physical time step Δt_n

is non-equidistant. The factor $C_{\alpha,c,\Delta s_t}$ is introduced so that the mean slope of $t(s)$ is one, which means that the development of the physical time and the intrinsic time occurs statistically at the same speed.

As shown in Fig. 2, the Time-mapped Mann model generates a turbulent wind field which is spatially correlated in the two transversal directions (x_2 and x_3) since it is not changed from the original Mann model besides an interpolation procedure explained below. On the other hand, the conversion between the intrinsic and physical time scales using the random τ_α leads to intermittent behavior in the longitudinal direction x_1 (or in other words in the temporal behavior since the longitudinal direction x_1 is converted to time with Taylor's hypothesis), as will be shown in Sec. 4. Accordingly, it presents a compromise between Gaussian, non-intermittent fields generated using the Mann model and the intermittent CTRW model.

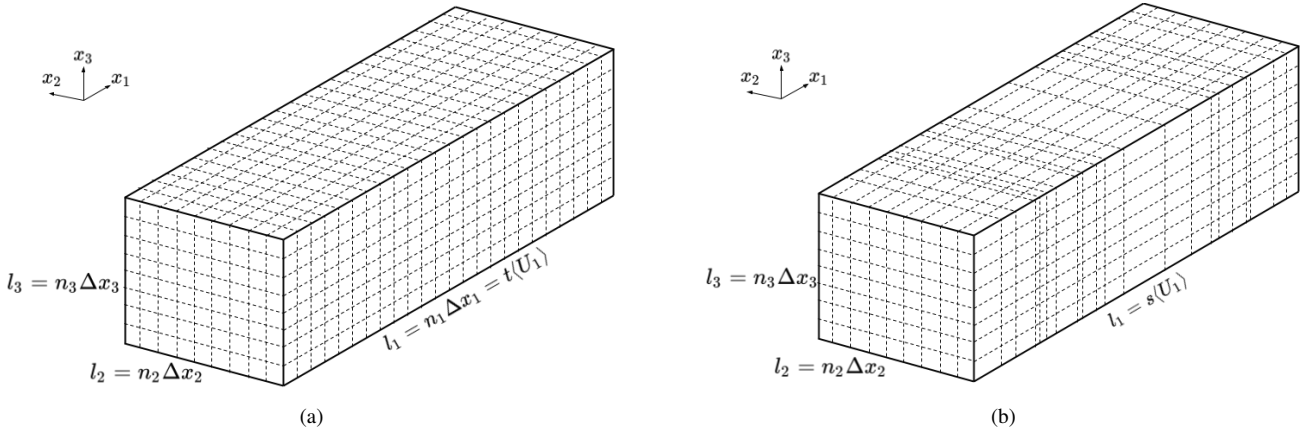


Figure 2. Schematic illustration of turbulence boxes generated by the (a) Mann model with equidistant steps and (b) Time-mapped Mann model after applying the time mapping process resulting in non-equidistant steps.

The effect of the generated intermittent wind field on loads of a wind turbine is analyzed using a numerical BEM simulation (described in Sec. 4.2). This numerical model requires that the size of the time step Δt of the incoming wind field is equidistant during the simulation. However, as schematically shown in Fig. 2, the time mapping process described by Eq. (19) generates non-equidistant time steps Δt_n , proportional to τ_α calculated with Eq. (18). Therefore, the wind speed U_i has to be linearly interpolated between the discrete points obtained with the random numbers τ_α to the required discrete points distanced by a fixed time increment Δt_{BEM} . An example of this interpolation is graphically illustrated in Fig. 3. The dashed vertical red lines correspond to the discrete times from the mapping process separated by $\Delta t_n \propto \tau_\alpha$. The red dots show the process U_i at those discrete times. Similarly, the continuous vertical black lines depict the times equally distanced by $\Delta t = \Delta t_{BEM}$. Then, the linear interpolation takes place between the red dots to obtain the values of U_i at the times depicted by the black lines. The resulting equally distanced discrete points are shown by the black squares. For clarification purposes, the schematic illustrations shown in Fig. 2 and Fig. 3 do not correspond to the same time-mapping process but should just demonstrate the mathematical process.

To generate a Mann box, the HAWC2 Mann turbulence generator tool (Larsen and Hansen (2007)) is used. After that, an

in-house Matlab (MATLAB (2019)) code is used to create the Lévy distribution for τ_α to apply the Time-mapping and interpolation processes.

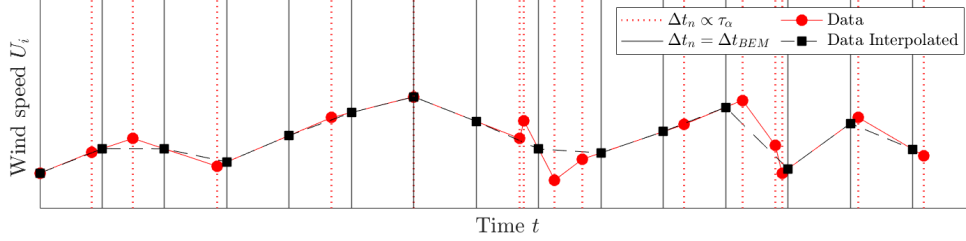


Figure 3. Schematic illustration of the interpolation from non-equally distributed time increments $\Delta t_n \propto \tau_\alpha$ to equally distributed time increments Δt_{BEM} for the BEM simulations.

265 4 Results and Discussion

In this section, the analysis of the new Time-mapped Mann wind field and exemplary resulting loads from this time mapping will be shown. To clarify the impact of intermittency on the wind fields and loads in this work, all cases will be compared to the original Mann wind field generated with the same parameters to provide a fair comparison between the two models.

4.1 Characteristics of the Time-mapped Mann model

270 This section provides a thorough comparison of statistical quantities such as the spectral tensors, the coherence, and the velocity increment distribution of both fields, the regular Mann and the new Time-mapped Mann wind field. The dimensions of the grid for the generation of the wind fields are selected according to Table 1, such that they can be used for the BEM simulations in Sec. 4.2. In this case, the defined grid has 32×32 nodes with $\Delta x_{2,m} = \Delta x_{3,m} = 2.6m$ covering an $80.6m \times 80.6m$ area. The original Mann field is generated using the Mann model at mean wind speed $\langle U_1 \rangle = 20m/s$, turbulence intensity in the flow direction, which is x_1 -direction in this case, $TI_1 = 10\%$, $\Gamma = 0$, and $c_K \epsilon^{2/3} = 0.62 m^4/3/s^2$ according to the parameters of the Mann model as introduced in the ESDU spectral model. The value of $TI_1 = 10\%$ was used in this work to keep the same standard deviation value as used for the class B turbine (average class) in the IEC 61400-1 standard (Han (2007)) at $20m/s$ mean wind speed. Corresponding to $\Gamma = 0$, we assume homogeneous turbulence, and wind shear is not taken into consideration in this work. Also, based on this assumption, the velocity components can be averaged over each slice to calculate the wind field statistics. According to Kelly (2018), the L parameter can be calculated by:

$$L = z \frac{TI_1}{a} \quad (20)$$

where z is the height of the calculation point (which is the turbine hub height in this work) and a is a shear exponent. Eq. 20 is used to calculate the length scale for multi-megawatt wind turbines (Hannesdóttir et al. (2019)). However, this equation is also used in the present work for a 1.5MW wind turbine in order to enable a generalization for larger wind turbines. Even though

285 we assume no shear in this work, the shear exponent value a is only used to calculate the value of L with no effect on the wind velocities. According to the hub height of the studied 1.5MW turbine with $z = 84m$, and for neutral conditions with a shear exponent of $a = 1/7$ (Schlichting and Gersten (2016)), Eq. (20) results in $L = 58.8m$.

Table 1. Mann box and time-mapping parameters for the generated wind fields.

n_{x_1} [-]	$n_{x_2} = n_{x_3}$ [-]	$\Delta x_{1,m}$ [m]	$\Delta x_{2,m} = \Delta x_{3,m}$ [m]	Γ [-]	L [m]	$c_K \epsilon^{2/3}$ [$m^{4/3}/s^2$]	TI_1 [%]	$\langle U_1 \rangle$ [m/s]	α [-]
1.31072×10^5	32	2	2.6	0	58.8	0.62	10	20	0.6

For the Time-mapped Mann wind field, the three components of the velocity fluctuations of each transverse plane (x_2 - x_3 in this case) are shifted according to the resulting $t(s)$. When applying the time mapping process to the wind field, the same stochastic process ($C_{\alpha,c,\Delta s_t} \tau_\alpha(s_n)$) is applied to each point of the x_2 - x_3 -plane and it is not a function of the location of different points in the x_2 - x_3 -plane. Fig. 4 shows the resulting relationship between intrinsic time scale (s) and real time scale (t) used in the time mapping process of the original Mann field to the new Time-mapped Mann field according to Eq. (19) for different values of α (in the Lévy distribution). As noticed from this figure, the relationship between s and t is not an exact straight line, which means that the resulting field will be different from the original field as explained in Sec. 3. The values of τ_α in Eq. (19) follow a Lévy's distribution with the corresponding PDFs presented in Fig. 5 at different values of α . In the following analysis and simulations, we will only consider $\alpha = 0.6$, which is highlighted with red lines in Fig. 4 and 5. Additionally, values of $c = 20$ and $\Delta s_t = 8$ sec were considered for the calculation of the scaling factor $C_{\alpha,c,\Delta s_t}$ in Eq. (19). These parameters were selected to achieve intermittency in a comparable range to the data shown in Fig.1 and to other literature values like Schwarz (2020).

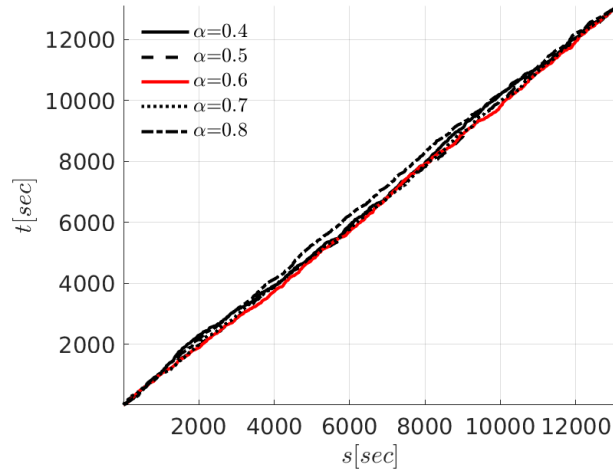


Figure 4. Relationship between intrinsic time scale (s) to physical time scale (t) (resulted from τ_α in Eq. (19)) at different values of α .

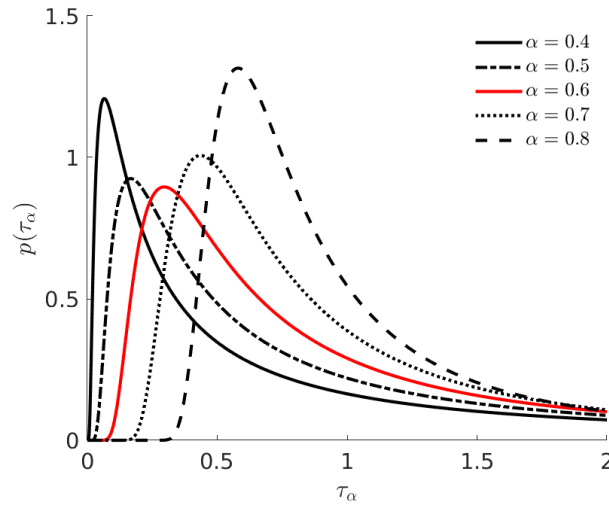


Figure 5. Lévy probability distribution of τ_α as in Eq. (17) at different values of α .

300 The comparison between the Mann and the new Time-mapped Mann wind fields regarding statistical properties is performed in terms of one-point and two-point statistics from Sec. 2.1. Starting with one-point statistics, the values of the mean wind speed in the longitudinal direction U_1 and the corresponding standard deviation $\sqrt{\langle u_1^2 \rangle}$ are presented in Table 2. These values are calculated from the time series at the hub-point (location of the hub of the turbine in the BEM simulations, see Sec. 4.2). For better comparison, the relative differences (Rel.Diff) calculated as the difference between both results over the result from

305 Mann field (i.e. (Time-map. – Mann)/Mann), are also presented in the table.

The values of the relative differences for $\langle U_1 \rangle$ and $\sqrt{\langle u_1^2 \rangle}$ are lower than 2%. This means, in terms of one-point statistics

Table 2. Values of the mean wind speed and standard deviation at the hub-point in the longitudinal direction ($\langle U_1 \rangle$ and $\sqrt{\langle u_1^2 \rangle}$) for the Mann (Mann) and Time-mapped Mann (Time-map.) wind fields.

mean $\langle U_1 \rangle$ (hub)			standard deviation $\sqrt{\langle u_1^2 \rangle}$ (hub)		
Mann	Time-map.	Rel.Diff	Mann	Time-map.	Rel.Diff
20.02 m/s	19.98 m/s	-0.20%	1.99 m/s	1.96 m/s	-1.51%

at hub-point, the two generated wind fields are comparable. The slight differences between the two fields are caused by the interpolation procedure explained in Fig. 3. However, one-point statistics are not enough to show the effects of intermittency.

To show the effect of the time mapping on the spectral properties of the new field, Fig. 6 shows a comparison between the spectra $\langle F_i(\kappa_i) \rangle_{\mathcal{I}}$ of three components of the original Mann field and the new Time-mapped Mann field. In these figures, $\langle \cdot \rangle_{\mathcal{I}}$ denotes spatial averaging over the plane $\mathcal{I} = \{(x_2, x_3) | 0 \leq x_2 \leq l_2, 0 \leq x_3 \leq l_3\}$. Fig. 6(a) shows the wavenumber spectrum of the u_1 -velocity component in the longitudinal (x_1) direction, while Fig. 6(b) and 6(c) show the same comparison but for u_2 component in the x_2 - and u_3 component in the x_3 -directions, respectively. The theoretical spectra of the Mann field from Eq. (14) are plotted in the same figures to show how the spectra should be distributed over the different wavenumbers. Further to that, an uncorrelated, intermittent wind field was also added for the comparison. This uncorrelated wind field is generated by arbitrarily shuffling the grid points of the intermittent Time-mapped Mann field in the transverse directions (x_2 - and x_3 -directions). This uncorrelated field is generated to show the difference between a correlated field in the transverse directions (which is the Time-mapped Mann field) and a completely uncorrelated turbulent field in the transverse direction.

Fig. 6 shows that the Mann and Time-mapped Mann fields are behaving almost in the same manner. Discrepancies arise through the time-mapping procedure and the interpolation procedure that is needed as described in Sec. 3. As indicated in Sec. 2.1, the velocity spectrum is not sufficient to show intermittency. Therefore, increment statistics should be used in this case to show the effects of the intermittency. Fig. 6(a) shows that both, the Time-mapped Mann field and the Mann field slightly differ in the lower and higher wavenumbers whereas both are still close to the theoretical curve. Fig. 6(b) and (c) show that both, the Mann and Time-mapped Mann have the same behavior for wavenumbers starting from $\kappa_2 = \kappa_3 \approx 8 \cdot 10^{-2}$. Velocity spectra in x_2 - and x_3 -directions at wavenumbers $\kappa_2, \kappa_3 \lesssim 8 \cdot 10^{-2}$ are not plotted since the low number of grid points in x_2 - and x_3 -directions are too low to enable capturing spectra at such low wavenumbers using Fourier transform. The deviation between the two fields at high wavenumbers happens due to the interpolation illustrated in Sec. 3 and in this case due to the low number of grid points in the transverse directions ($n_{x_2} = n_{x_3} = 32$). It should be noticed that the velocity spectrum in Fig. 6(a) shows a noisy spectrum while the spectrum in figures 6(b) and (c) are smoothed. This happens due to the difference in the number of grid points in x_1 -, x_2 -, and x_3 -directions. As indicated in Tab. 1, $n_{x_1} = 131072$ while $n_{x_2} = n_{x_3} = 32$. This means that the number of points in x_1 -direction for which the spectrum was obtained via Fourier transform is 4 orders of magnitude higher compared to the number of points in x_2 - and x_3 -directions.

For further investigation of these deviations between Mann and Time-mapped Mann fields, appendix A1 shows the same spectra as shown in Fig. 6 but with an equal number of grid points in all directions (in this case, $n_{x_1} = n_{x_2} = n_{x_3} = 512$). This case will be referred to as the "cubic case". The spectra of these fields in Fig. A1 show that for a finer discretization in x_2 - and x_3 -directions, the discrepancies between the curves almost vanish, while the most obvious deviation between the two cases can be seen in Fig. A1(a). This case can show the effect of the number of grid points and the direction on the spectra of the Mann and Time-mapped Mann field since it has more grid points in x_2 - and x_3 -directions than the former case shown in Fig. 6. For the uncorrelated intermittent field, a good agreement between this field and the Time-mapped Mann field in the longitudinal direction x_1 can be seen since the arbitrary shuffling was only applied in the transverse directions. For the spectra in the transverse directions, the spectra are around unity regardless of the wavenumber, which proves the destruction of the correlation in the transverse directions due to this shuffling.

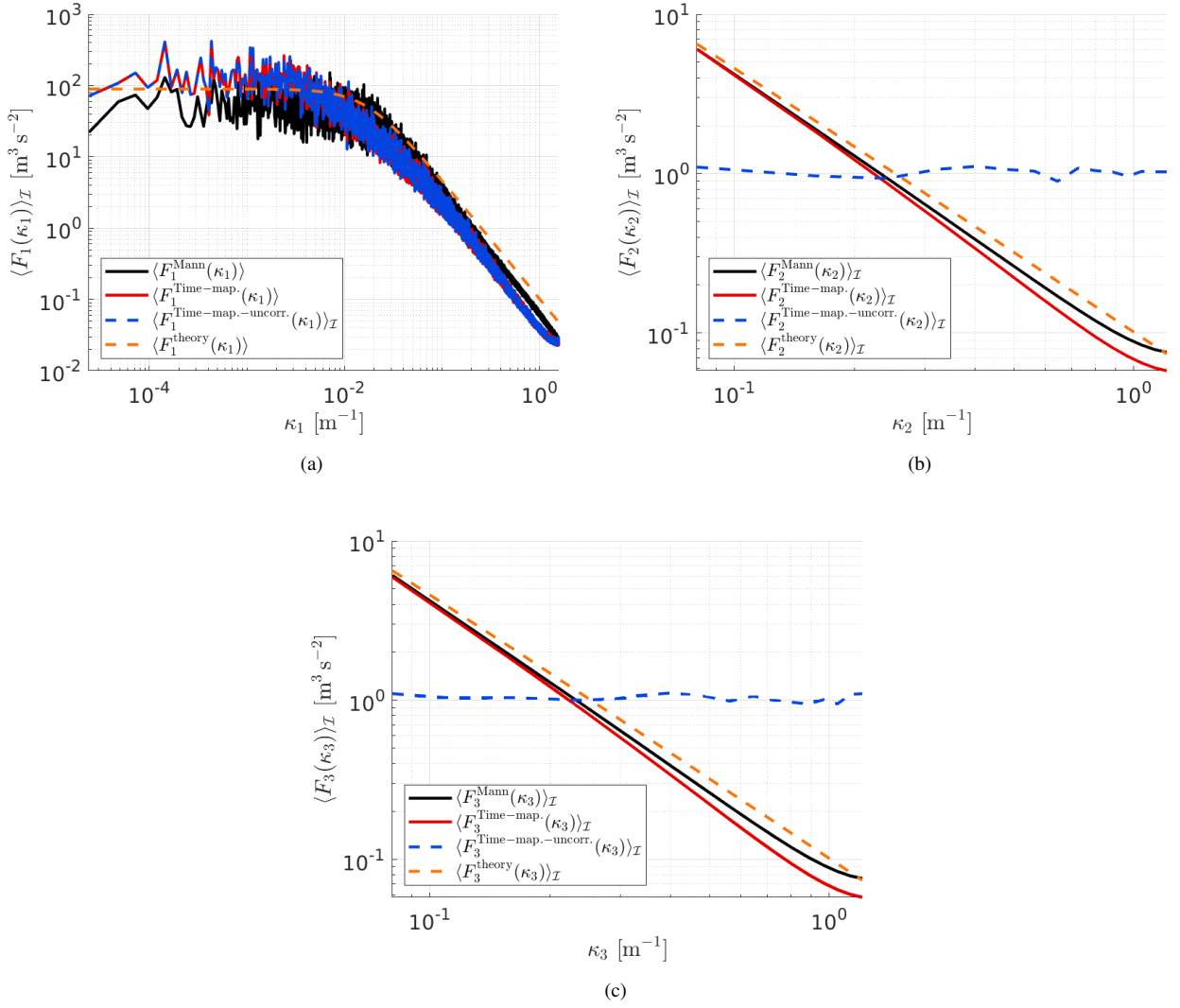
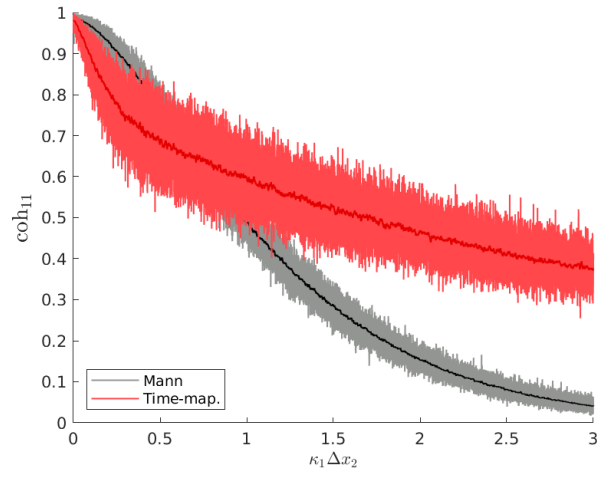


Figure 6. Comparison of averaged spectra in (a) x_1 -, (b) x_2 -, and (c) x_3 -directions for the Mann field ($F_i^{\text{Mann}}(\kappa_i)$), the Time-mapped Mann field ($F_i^{\text{Time-map.}}(\kappa_i)$), an uncorrelated Time-mapped Mann field e.g.: ($F_i^{\text{Time-map.-uncorr.}}(\kappa_i)$) and the theoretical spectra ($F_i^{\text{theory}}(\kappa_i)$) calculated from Eq. (14)

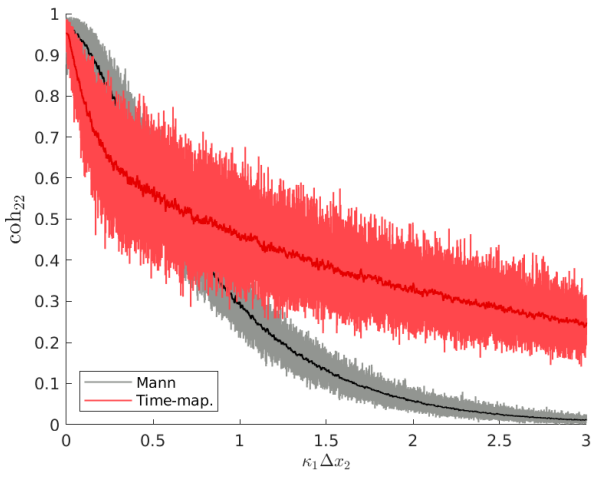
In the comparison between Mann and Time-mapped Mann fields, the velocity spectra are expected to be the same since the one-point spectra are not able to show the effect of the time mapping. Therefore, to see the differences between the Mann and the Time-mapped Mann field, the coherence of velocity components (Eq. (6)) of the two wind fields in the three spatial directions is plotted versus $\kappa_1 \Delta x_2$ in Fig. 7 with $\Delta x_2 = 2.6m$. In this figure, the difference in the coherence of the two fields as we move in x_2 -direction are obvious due to the time mapping in the longitudinal direction. On the other hand, a comparison between the coherence of the two wind fields versus $\kappa_2 \Delta x_3$ for the cubic case is shown in Fig. A2 in the appendix. In the

latter case, the differences in coherence between the two fields are small. This is due to the unchanged x_2 - x_3 planes during the
350 time mapping process. This shows that the coherence with respect to the longitudinal direction is highly influenced by the time
mapping whereas it is not with respect to the transverse direction. By comparing Fig. 7 and Fig. A2, it can be noticed that the
plots in Fig. A2 look smoother. This is also due to the difference in the number of grid points in the x_1 -direction between the
two cases.

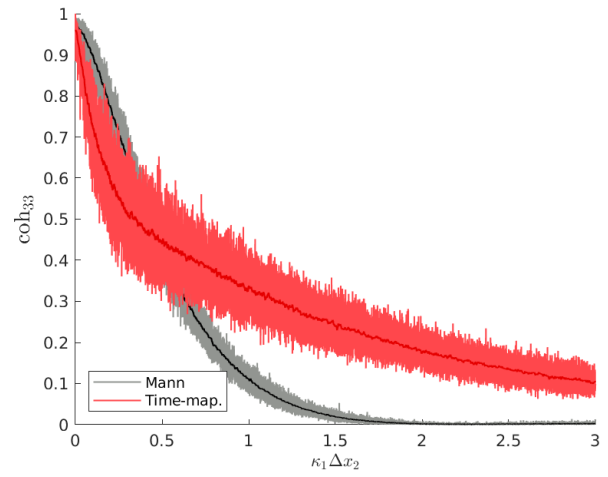
Following on from the two-point statistics analysis, the velocity increments v_1 defined in Eq. (10) and the degree of intermit-
355 tency of the wind fields are analyzed. Fig. 8 shows the comparison between the PDFs of the velocity increment of both, the
Mann and the new Time-mapped Mann wind fields. It is obvious in this figure how extreme events in the case of the Time-
mapped wind field (the red markers) have a higher probability than the corresponding events in the case of the Gaussian Mann
field (the black markers). Also, it can be noticed that the intermittency increases with the decrease of τ . Note that this τ refers
to the temporal increment in Eq. (10) and not to the τ_α introduced in the context of the Lévy distribution. Another important
360 measure of the increment statistics is the kurtosis calculated from Eq. (11). In the case of the kurtosis of the wind fields, the
angular brackets denote averaging over time and kurtosis, in this case, is only a function of τ Fig. 9 shows a comparison be-
tween the kurtosis of the velocity increment from the Mann field and the Time-mapped Mann fields at different τ values. As
explained earlier, higher values of τ show a Gaussian distribution with kurtosis of 3 and lower values of τ show more deviation
from the Gaussian PDF of the Mann field.



(a)



(b)



(c)

Figure 7. Comparison of the coherence of velocity components in (a) x_1 -, (b) x_2 -, and (c) x_3 -directions for both Mann and Time-mapped Mann fields over wavenumber $\kappa_1 \Delta x_2$ with $\Delta x_2 = 2.6\text{m}$ and $\Delta x_3 = 0$. Dark lines represent smoothed coherence values of the light lines using a moving average method.

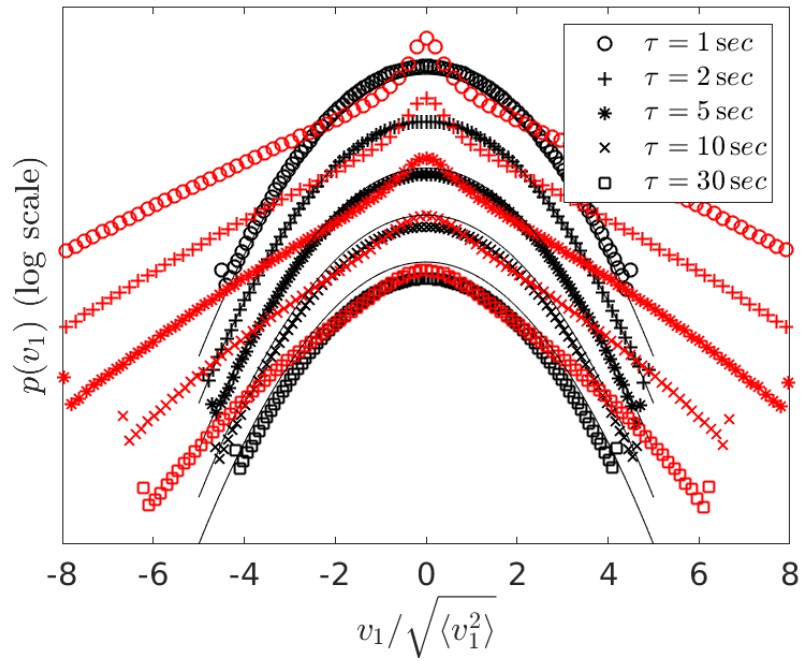


Figure 8. Spatially averaged PDF over transverse planes of velocity increments of the Mann wind field (black) and the Time-mapped Mann wind field (red) at different temporal increments τ . The black thin lines are Gaussian distributions as a reference. In principle, the curves would all lie on top of each other but here, the curves are shifted vertically for a better visualization.

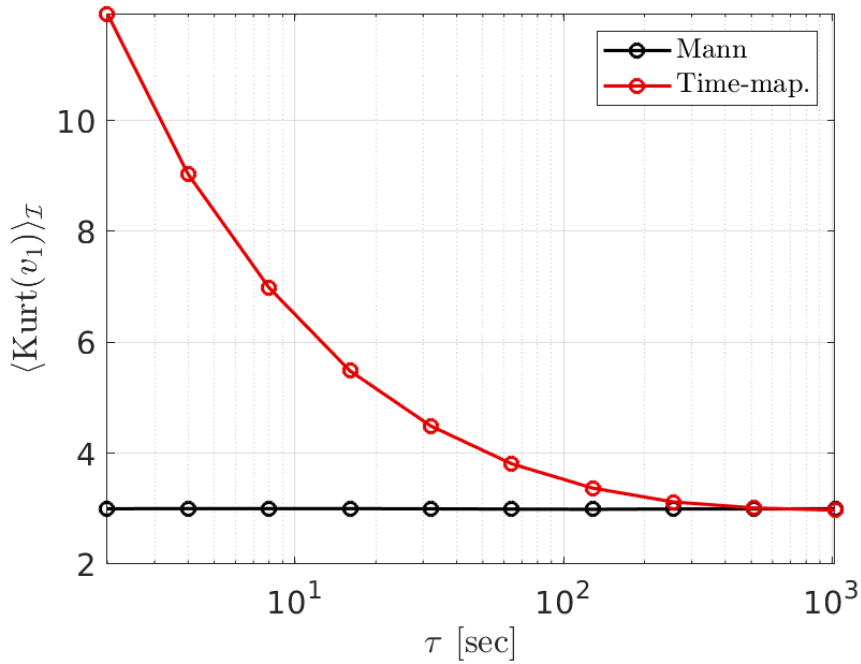


Figure 9. Kurtosis of Mann (black) and Time-mapped Mann (red) fields (Eq. (11)) at different temporal increments τ . For a Gaussian distribution the kurtosis is 3.

365 4.2 Analysis of the resulting wind turbine loads

After analyzing the effect of the time mapping on the different statistics of the wind fields in the previous section, here, the effect on exemplary turbine loads is studied. The main point of this section is to see whether the intermittency from the wind field is carried to the turbine structure. If the turbine loads are proved to reflect intermittency, this might have a significant effect on the dynamic loads acting on the wind turbine. For example, the damage equivalent loads (DEL) calculated from fatigue analysis might be affected due to intermittency because the probability for extreme values in the load increments is larger than for a Gaussian distribution.

In this work, BEM simulations of the NREL WindPACT 1.5MW (Malcolm and Hansen (2006)) virtual wind turbine are performed using the aero-elastic simulator NREL FAST (v8.16) (Jonkman and Jonkman (2016)). The main characteristics of the turbine and input parameters for the simulations are summarized in Table 3. The wind fields used in these simulations are the same Mann and Time-mapped Mann fields analyzed and compared in Sec. 4.1.

Parameter	Value/Description
Mean wind speed $\langle U_1 \rangle$	20 m/s
Mean wind speed $\langle U_2 \rangle$ and $\langle U_3 \rangle$ (averaged over transverse plane)	0 m/s
Turbulence Intensity ($TI_1 = TI_2 = TI_3$) at hub (Eq. (2))	0.10
Wind shear	No
Rotor diameter	70 m
Hub height	84 m
Control	Fixed pitch - Fixed speed
Rotor speed	20 rpm
Pitch angle	20°
Simulation time	13100 sec
Sampling frequency	20 Hz
Airfoil aerodynamics	Unsteady - (Leishman and Beddoes (1989))
Tip and hub-loss	Prandtl
Rotor tilt	5°
Structural degrees of freedom (DOF)	Turned off
Tower passage	Turned off
Wake model	Induction-BEM Model

Table 3. Main parameters of the turbine and numerical simulations. A description of the listed set-ups for the BEM simulation can be found in Jonkman et al. (2016) and Jonkman and Jonkman (2016).

Four different load sensors were selected for analyzing the effect of the intermittent wind: the bending moment at the root of the blade in the flapwise direction (`RootFlap`), the rotor torque (`Torque`), the rotor thrust (`Thrust`) and the bending moment at the base of the tower in the fore-aft direction (`TwrForeAft`). According to Schwarz (2020), these four sensors are expected to be highly sensitive and mainly dominated by aerodynamic forces in the direction of the flow and not by other sources of load such as gravitational forces.

Firstly, the mean values and standard deviations calculated over the length of the simulation are presented in Table 4. Here, the results for the four load sensors of both, the Time-mapped Mann (Time-map.) and the Mann (Mann) wind field are shown. Moreover, the relative differences (Rel.Diff) were also calculated (i.e. (Time-map. – Mann)/Mann). In Table 4, the relative differences of the mean values and standard deviations of the analyzed sensors are less than $\pm 1\%$ between the Mann and the Time-mapped Mann wind field. It can be seen that this difference is in the same order as the differences in the mean wind speed $\langle U_1 \rangle$ and standard deviation $\sqrt{\langle u_1^2 \rangle}$ at the hub point presented in Table 2. To investigate whether the intermittency in the wind field carries over to the turbine loads, the incremental statistics of the loads are evaluated. The load increments M_τ are defined similarly to velocity increments in Eq. (10):

Sensor/Load	Mean Value			Standard Deviation		
	Mann	Time-map.	Rel.Diff	Mann	Time-map.	Rel.Diff
RootFlap	861 kN.m	868 kN.m	0.81%	253 kN.m	251 kN.m	-0.79%
Torque	1126 kN.m	1136 kN.m	0.89%	269 kN.m	267 kN.m	-0.74%
Thrust	157.76 kN	158.77 kN	0.64%	24.16 kN	24.09 kN	-0.29%
TwrForeAft	10317 kN.m	10406 kN.m	0.86%	2017 kN.m	2017 kN.m	0%

Table 4. Mean values and standard deviations of time series from BEM simulations for the Mann (Mann) and the Time-mapped Mann (Time-map.) wind fields. The relative differences (Rel.Diff) between the two cases are calculated for better interpretation.

390

$$M_\tau(t, \tau) = M(t + \tau) - M(t) \quad (21)$$

where M is the time series of the load sensor and τ corresponds to the time lag. Fig. 10 shows the PDFs of M_τ for the four selected load sensors, for $\tau = 1$ s (top) up to $\tau = 30$ s (bottom). For a direct comparison to the PDFs of the velocity increments v_1 , the values of τ are selected analogously to Fig. 8. Similar to Fig. 1 and 8, all the individual PDFs are normalized to standard deviation $\sqrt{\langle M_\tau^2 \rangle} = 1$. Here, the angular brackets denote moving averages over the time series.

395

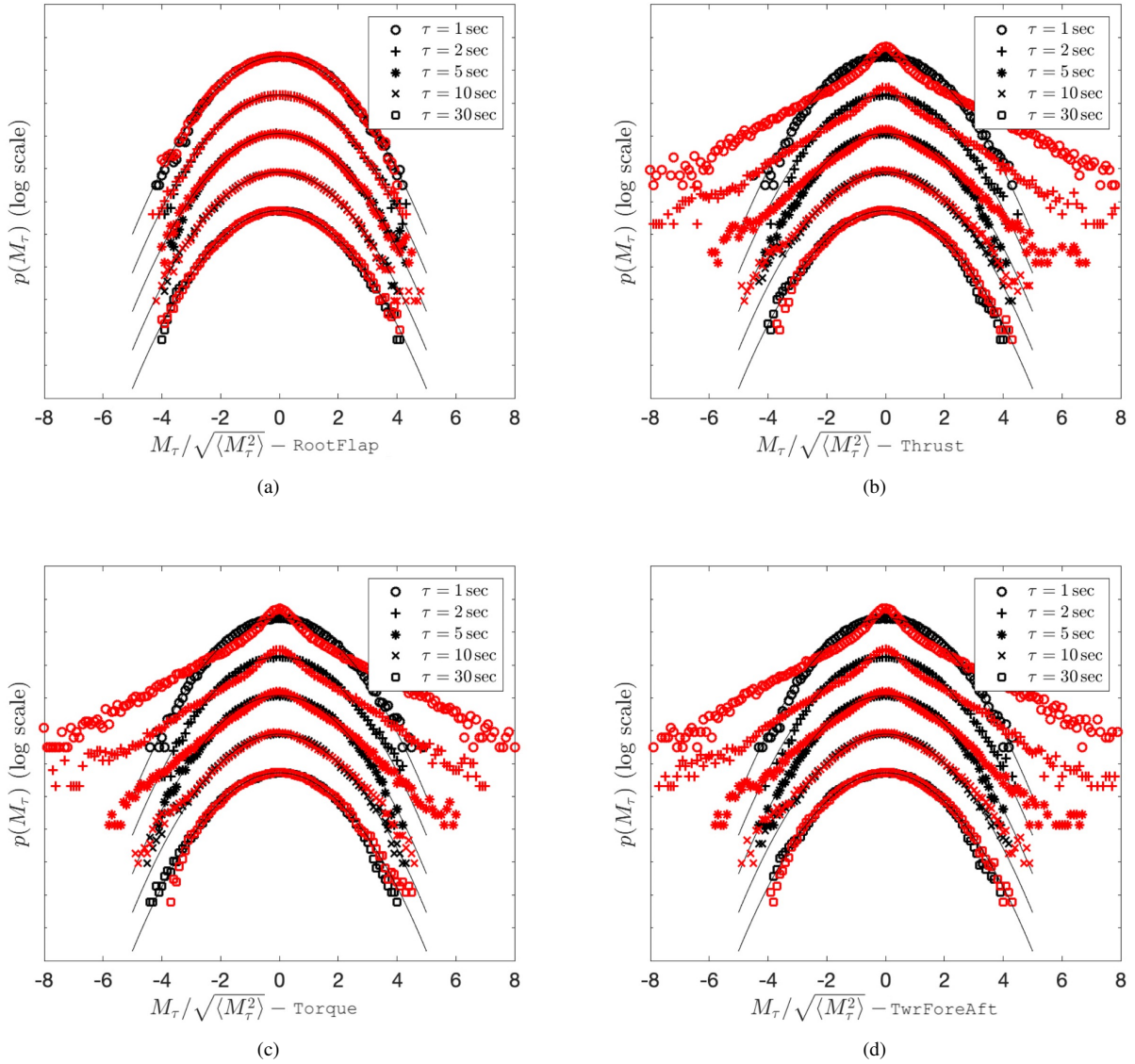


Figure 10. PDFs of load increments M_τ for (a) blade root flapwise bending moment (RootFlap) (b) rotor thrust (Thrust) (c) rotor torque (Torque) (d) tower fore-aft bending moment (TwrForeAft) of the 1.5MW turbine with Mann and Time-mapped Mann inflow wind fields at different temporal increments τ . The red markers correspond to the Time-mapped Mann field cases while black markers present the results for the Mann field cases. The black thin lines are Gaussian distributions as reference. The curves are shifted vertically for visualization.

The resulting load increments M_τ , except for the RootFlap, follow the characteristics of the wind velocity increments shown in Fig. 8. The PDFs of the Mann load increments are very well described by the Gaussian distribution. On the contrary, the PDFs of the load increments resulting from the Time-mapped Mann field deviate significantly from the Gaussian distribu-

tion for a range of scales. The observed heavy tails shown by the Time-mapped PDFs reflect, as mentioned earlier, a higher
400 probability of extreme load fluctuations than the probability of a Gaussian distribution.

Fig.10(a) shows a special case for the `RootFlap` load. In this figure, the `RootFlap` increment PDF seems to be non-intermittent at all. However, this load also exhibits oscillations but with much lower amplitude and at a different frequency which is not captured by the specific selected time step sizes in Fig. 10(a).

A more detailed description of the evolution of the intermittency of M_τ with τ is presented in Fig. 11. Here, the results of
405 $\text{Kurt}(M_\tau)$ from Eq. (11) are calculated exemplarily for the `Thrust` signal. It is visible that the values of the kurtosis for the load case with the Time-mapped Mann wind field are higher than three (value of three indicates a Gaussian distribution) for all the values of τ up to around 20 seconds. This proves the intermittent characteristics of the loading. In contrast, the corresponding values for the Mann case fluctuate around three for all the considered time scales, agreeing with the Gaussian statistics. Additionally, for time scales below one second, a decreasing intermittent behavior of the load is visible in the Time-mapped
410 case when decreasing τ . The kurtosis of the thrust in Fig 11 is overall lower than of the corresponding wind field as shown in Fig 8. This has been also shown by Mücke et al. (2011) who have used an atmospheric wind measurement as input to calculate the torque.

Further investigations should be done to explain the potential sources of the observable bumps in the kurtosis of the Time-mapped Mann case. A strong dependence of the peaks on the rotational frequency of the rotor has been recognized by the
415 authors. However, this first turbine study aimed at investigating whether the intermittency which was introduced to the wind field by deriving the Time-mapped Mann field carries over to turbine loads in general. This has clearly been shown here.

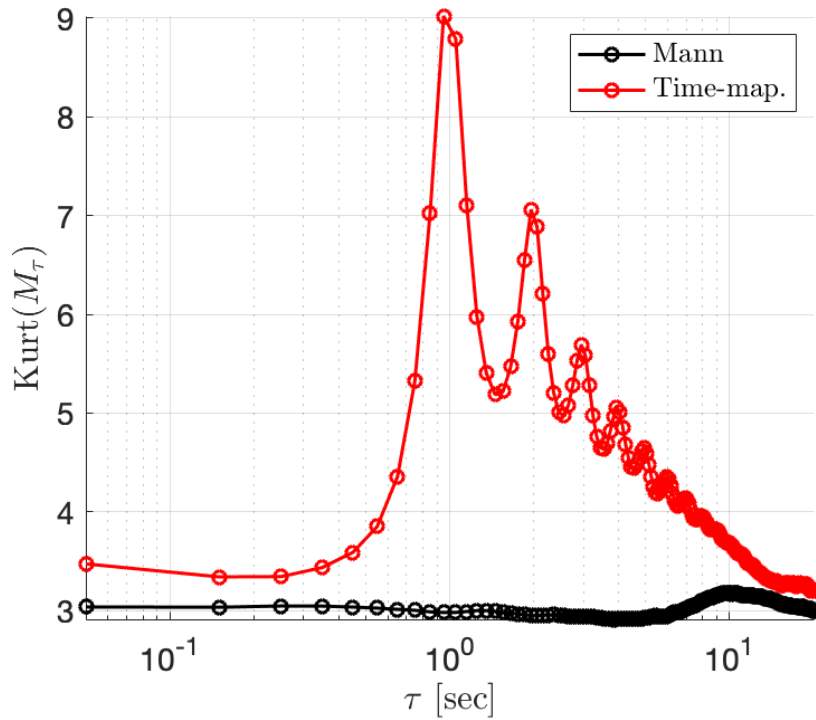


Figure 11. Kurtosis of the PDF of M_τ calculated for the Thrust according to Eq. (11) at different temporal increments τ . The red markers correspond to the Time-mapped Mann field while black markers present the results for the Mann field. A value of three corresponds to a Gaussian distribution.

5 Conclusions

In this work, a new synthetic wind field model has been introduced which combines spatial correlations from the well-known Mann model and the effect of intermittency. During the derivation, the time-mapping procedure from the so-called CTRW model has been applied to a Mann wind field to generate intermittency. This new model is called the Time-mapped Mann model. The CTRW model relies on stochastic differential equations for the velocity and assumes exponentially decaying velocity correlations. On the other hand, the Mann model is based on a proper modeling of the spectrum according to atmospheric conditions which is also recommended by the standard IEC 61400-1. With our procedure, we obtain a model which aims at keeping the spatial correlations in the transverse directions from the Mann model, and thus, following the IEC 61400-1 standard in this respect, and on the other hand adding intermittency which has also been reported as a feature inherent in the wind (Mücke et al. (2011)).

A comparison between Mann and the corresponding Time-mapped Mann fields was shown in detail in this work. The analysis of the velocity spectra, as well as the PDF and kurtosis of velocity increments, showed that this method managed to generate

an intermittent wind field in the longitudinal direction. On the other hand, this method keeps the spatial correlation almost
430 exactly as in the Mann field in the other two directions. This is due to the way the time mapping is applied where the velocity
field "slices" (x_2 - x_3 planes) of the Mann field are shifted by random time shifts. Small differences in the compared statistics
in transverse directions are due to the interpolation between the generated time-shifted slices and the new, uniformly separated
velocity field slices.

Furthermore, a first analysis and comparison of loads with respect to intermittency between Mann and Time-mapped wind
435 fields on a 1.5MW wind turbine was done. The analysis of the loads showed that the intermittency is transported from the wind
field to the structure of the wind turbine. However, these loads are different in their response to the wind field intermittency.
The increment statistics showed that in the analyzed case, rotor thrust, rotor torque, and tower fore-aft bending moment are
strongly affected by the intermittency in the wind field, whereas the blade root bending moment shows less intermittency. The
resulting non-Gaussian load increment distributions suggest that simulating wind turbines under Gaussian wind fields such as
440 Mann wind fields could potentially lead to an underestimation of the probability of extreme loads.

An important future extension of the Time-mapped Mann model would be an incorporation of shear in the Mann model. The
Mann model has the option of imposing eddy stretching to account for shear. However, it is not a straight-forward process to
add this eddy stretching to the Time-mapped Mann field. This poses a challenge to the time-mapping process since the slices
could potentially not be simply shifted as it is done now without again influencing the eddy stretching. Also, in future research
445 based on this work the different turbine loads and their response to turbulent inflow with intermittency could be investigated
with more details. This investigation should involve also different sizes of wind turbines which cover a larger area of the wind
fields, as well as variable speed, variable pitch wind turbines at a variety of wind conditions. For example, such wind conditions
could be measured from wind sites to have a better anticipation of the turbine loads in the presence of intermittency. Another
possible future work would be to compare the impact of intermittency on different wind turbine loads at different wind speeds
450 to investigate whether there are effects of wind speeds on the loads' intermittency. Additionally, fatigue load could be a subject
of further investigation which requires further discussion since the rainflow cycle counting method may not detect intermittency
properly as discussed by Mücke et al. (2011).

Appendix A: Analysis of a cubic field

For a further investigation of the effect of the time mapping of wind fields on the spectra, a Mann box with $n_{x_1} = n_{x_2} = n_{x_3} =$
455 512 and $\Delta x_{1,m} = \Delta x_{2,m} = \Delta x_{3,m} = 1m$ is studied in this appendix. The same comparison of spectra as described in Sec. 4.1
is studied here for this cubic field. As introduced in the previous sections, there are three different parameters used to generate
the box: the overall box size, the grid cell size, and the number of cells. Since it is not possible to change the value of one of
these parameters alone without changing at least one of the other two parameters to generate a grid with comparable results,
a new grid with cubic cells was generated to have independence of the direction since all directions have the same grid points
460 and cell sizes.

In Fig. A1 (a), (b), and (c) it can be seen that the spectra show generally good agreement between the Mann and the Time-

mapped Mann field. The spectra in the longitudinal direction x_1 in A1(a) show a discrepancy due to the time-mapping procedure which is applied to this direction. Further, all plots show increasing discrepancies for larger wavenumbers which should be resulting from the interpolation procedure. Note that in Fig. 6(b) and (c) where the resolution in x_2 - and x_3 -direction was much coarser, the deviations already start at smaller wavenumbers. The comparison of coherence of the same two fields in Fig. A2 shows good agreement between the two fields in the x_2 - and x_3 -directions. The small deviations result from the interpolation routine.

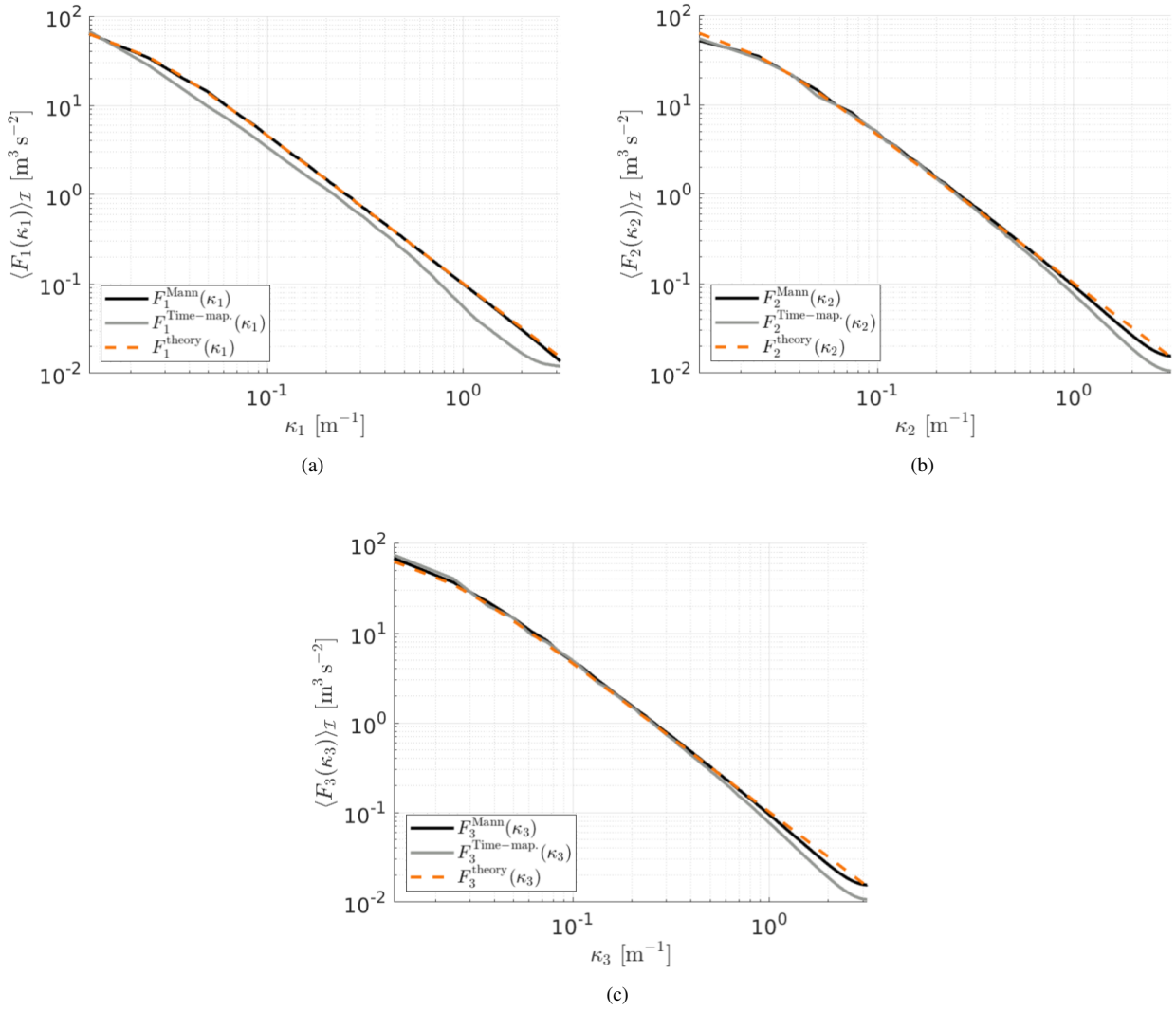


Figure A1. Comparison of averaged spectra in (a) x_1 -, (b) x_2 -, and (c) x_3 -directions respectively for the Mann field, the Time-mapped Mann field and the theoretical results calculated from Eq. (14)

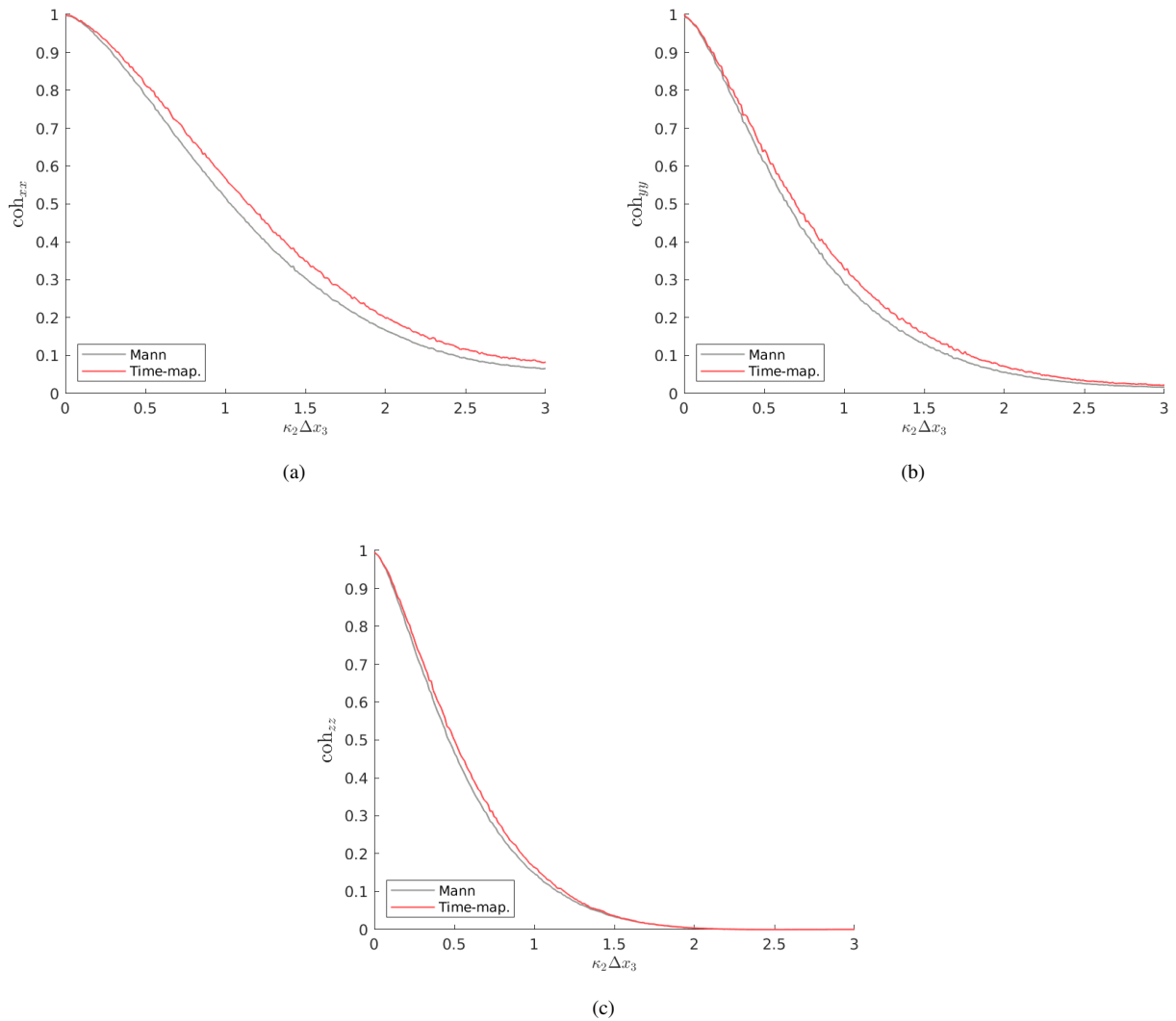


Figure A2. Comparison of the coherence of velocity components in (a) x_1 -, (b) x_2 -, and (c) x_3 -directions for the Mann field and the Time-mapped Mann field over wavenumber $\kappa_2\Delta x_3$ with $\Delta x_3 = 2.6\text{m}$ and $\Delta x_1 = 0$.

Author contributions.

KY performed the wind field simulations and the wind field analyses and wrote the paper (with contributions from the other authors). Preliminary evaluations were performed in the scope of the Master Thesis of AH at the Carl von Ossietzky University Oldenburg supervised by LJL and LH. All authors contributed to the generation of the method. DM performed the BEM simulations and the load analysis. HK and LH provided intensive reviews on the generation of the codes and the analyses. LJL

initiated the research, provided extensive consultation on the development of the method and the scientific analyses, and had a supervising function.

475 *Competing interests.* The authors declare no conflict of interest.

Disclaimer. TEXT

Acknowledgements. The authors would like to acknowledge Mr. Jörg Schwarte, Nordex Energy SE & Co.KG for providing measured wind data. Parts of this work have been performed in the scope of the project EMUwind (03EE2031A/C), PASTA (03EE2024A/B), and SFB1463 (434502799). The EMUwind and PASTA projects are funded by the German Federal Ministry for Economic Affairs and Energy
480 (Bundesministeriums für Wirtschaft und Energie-BMWi) due to a decision of the German Bundestag and the SFB1463 is funded by the German Research Foundation (Deutsche Forschungsgemeinschaft, DFG).

References

- Bangga, G. and Lutz, T.: Aerodynamic modeling of wind turbine loads exposed to turbulent inflow and validation with experimental data, *Energy*, 223, 120 076, 2021.
- 485 Berg, J., Natarajan, A., Mann, J., and Patton, E. G.: Gaussian vs non-Gaussian turbulence: impact on wind turbine loads, *Wind Energy*, 19, 1975–1989, 2016.
- Boettcher, F., Renner, C., Waldl, H.-P., and Peinke, J.: On the statistics of wind gusts, *Boundary-Layer Meteorology*, 108, 163–173, 2003.
- Böttcher, F., Barth, S., and Peinke, J.: Small and large scale fluctuations in atmospheric wind speeds, *Stochastic Environmental Research and Risk Assessment*, 21, 299–308, 2007.
- 490 Cuxart, J., Yagüe, C., Morales, G., Terradellas, E., Orbe, J., Calvo, J., Fernández, A., Soler, M., Infante, C., Buenestado, P., Espinalt, A., Joergensen, HE and Rees, J., Vilá, J., Redondo, J., Cantalapiedra, I., and Conangla, L.: Stable atmospheric boundary-layer experiment in Spain (SABLES 98): a report, *Boundary-layer meteorology*, 96, 337–370, 2000.
- ESDU: Characteristics of wind speed in the lower layers of the atmosphere near the ground: Strong winds (neutral atmosphere), The Unit, 1982.
- 495 Fogedby, H. C.: Langevin equations for continuous time Lévy flights, *Physical Review E*, 50, 1657, 1994.
- Friedrich, J., Peinke, J., Pumir, A., and Grauer, R.: Explicit construction of joint multipoint statistics in complex systems, *Journal of Physics: Complexity*, 2021.
- Gioffre, M., Gusella, V., and Grigoriu, M.: Simulation of non-Gaussian field applied to wind pressure fluctuations, *Probabilistic Engineering Mechanics*, 15, 339–345, 2000.
- 500 Gong, K. and Chen, X.: Influence of non-Gaussian wind characteristics on wind turbine extreme response, *Engineering structures*, 59, 727–744, 2014.
- Gontier, H., Schaffarczyk, A., Kleinhans, D., and Friedrich, R.: A comparison of fatigue loads of wind turbine resulting from a non-Gaussian turbulence model vs. standard ones, in: *Journal of physics: conference series*, vol. 75, p. 012070, IOP Publishing, 2007.
- GWEC: GWEC Global Wind Energy Report 2021, Global Wind Energy Council, 2021.
- 505 Han, C.-H.: International Electrotechnical Commission, *Electric Engineers Magazine*, pp. 29–34, 2007.
- Hannesdóttir, Á., Kelly, M., and Dimitrov, N.: Extreme wind fluctuations: joint statistics, extreme turbulence, and impact on wind turbine loads, *Wind Energy Science*, 4, 325–342, 2019.
- Jonkman, B. and Jonkman, J.: NWTC Design Code FAST v6.01., Tech. rep., National Renewable Energy Laboratory, 2005.
- Jonkman, B. and Jonkman, J.: NWTC Design Code FAST v8.16.00a-bjj, Tech. rep., National Renewable Energy Laboratory, 2016.
- 510 Jonkman, J., Hayman, G., Jonkman, B., Damian, R., and Murray, R.: AeroDyn v15 User’s Guide and Theory Manual (draft version), Tech. rep., National Renewable Energy Laboratory, 2016.
- Kaimal, J. C., Wyngaard, J., Izumi, Y., and Coté, O.: Spectral characteristics of surface-layer turbulence, *Quarterly Journal of the Royal Meteorological Society*, 98, 563–589, 1972.
- Kelly, M.: From standard wind measurements to spectral characterization: turbulence length scale and distribution, *Wind Energy Science*, 3, 515 533–543, 2018.
- Kleinhans, D.: Stochastische Modellierung komplexer Systeme—Von den theoretischen Grundlagen zur Simulation atmosphärischer Windfelder, Ph.D. thesis, Westfälischen Wilhelms-Universität Münster, 2008.

- Kleinhans, D. and Friedrich, R.: Continuous-time random walks: Simulation of continuous trajectories, *Physical Review E*, 76, 061 102, 2007.
- 520 Körber, F., Besel, G., and Reinhold, H.: Messprogramm an der 3 MW Windkraftanlage GROWIAN: Förderkennzeichen: 03E-4512-A, Tech. rep., 1988.
- Larsen, T. J. and Hansen, A. M.: How 2 HAWC2, the user's manual, 2007.
- Leishman, J. G. and Beddoes, T.: A Semi-Empirical model for dynamic stall, *Journal of the American Helicopter society*, 34, 3–17, 1989.
- Liu, L., Hu, F., Cheng, X.-L., and Song, L.-L.: Probability density functions of velocity increments in the atmospheric boundary layer, 525 *Boundary-layer meteorology*, 134, 243–255, 2010.
- Malcolm, D. and Hansen, A.: WindPACT Turbine Rotor Design Study: June 2000–June 2002 (Revised), Tech. rep., National Renewable Energy Lab.(NREL), Golden, CO (United States), 2006.
- Mann, J.: The spatial structure of neutral atmospheric surface-layer turbulence, *Journal of fluid mechanics*, 273, 141–168, 1994.
- Mann, J.: Wind field simulation, *Probabilistic engineering mechanics*, 13, 269–282, 1998.
- 530 MATLAB: version 9.7.0.1586710 (R2019b), Natick, Massachusetts, 2019.
- Morales, A., Wächter, M., and Peinke, J.: Characterization of wind turbulence by higher-order statistics, *Wind Energy*, 15, 391–406, 2012.
- Mücke, T., Kleinhans, D., and Peinke, J.: Atmospheric turbulence and its influence on the alternating loads on wind turbines, *Wind Energy*, 14, 301–316, 2011.
- Muzy, J.-F., Baïle, R., and Poggi, P.: Intermittency of surface-layer wind velocity series in the mesoscale range, *Phys. Rev. E*, 81, 2010.
- 535 Pope, S. B.: *Turbulent flows*, IOP Publishing, 2001.
- Schlichting, H. and Gersten, K.: *Boundary-layer theory*, Springer, 2016.
- Schottler, J., Reinke, N., Hölling, A., Whale, J., Peinke, J., and Hölling, M.: On the impact of non-Gaussian wind statistics on wind turbines—an experimental approach, *Wind Energy Science*, 2, 1–13, 2017.
- Schwarz, C. M.: Wind turbine load dynamics in the context of intermittent atmospheric turbulence, Ph.D. thesis, Carl von Ossietzky Universität Oldenburg, 2020.
- 540 Schwarz, C. M., Ehrich, S., Martín, R., and Peinke, J.: Fatigue load estimations of intermittent wind dynamics based on a Blade Element Momentum method, in: *Journal of Physics: Conference Series*, vol. 1037, p. 072040, IOP Publishing, 2018.
- Schwarz, C. M., Ehrich, S., and Peinke, J.: Wind turbine load dynamics in the context of turbulence intermittency, *Wind Energy Science*, 4, 581–594, 2019.
- 545 Taylor, G. I.: The spectrum of turbulence, *Proceedings of the Royal Society of London. Series A-Mathematical and Physical Sciences*, 164, 476–490, 1938.
- Uhlenbeck, G. E. and Ornstein, L. S.: On the theory of the Brownian motion, *Physical review*, 36, 823, 1930.
- Vindel, J., Yagüe, C., and Redondo, J.: Structure function analysis and intermittency in the atmospheric boundary layer, *Nonlinear Processes in Geophysics*, 15, 915–929, 2008.
- 550 von Kármán, T.: Progress in the statistical theory of turbulence, *Proceedings of the National Academy of Sciences of the United States of America*, 34, 530, 1948.
- Weron, R.: Levy-stable distributions revisited: tail index > 2 does not exclude the Levy-stable regime, *International Journal of Modern Physics C*, 12, 209–223, 2001.

Chapter 8

Conclusions and Outlook

8.1 Conclusions

After presenting the work done to simulate ice accretion on both 2D airfoils and Wind turbine blades, some conclusions can be drawn from this work. First, general conclusions about state of the art work can be found:

- Regarding the experimental work, there are quite a plenty of ice accretion wind tunnel tests for 2D airfoils. However, wind tunnel tests for rotating machines (wind turbine for instance) are not exact so far. The ice accretion experiments resented so far are made in closed chambers to avoid any ice throw that can damage the equipment present around the test rig. There should be a test configuration that mimics the real ice formation process on rotating blades to be able to simulate the ice accretion profiles correctly
- In general, ice accretion simulation is computationally expensive. In addition, it implies some stochasticity due to random droplet diameters and flow simulations which already suffer from accuracy problems. Accordingly, the numerical simulation of ice accretion is not yet mature enough to be accurate.
- Simulation of air flow field around rough surfaces is still not accurate compared to experiments. Laminar-turbulent transition models, rough wall functions, convective heat transfer calculations, and many other aspects are still not accurate to be used simultaneously to simulate the whole icing process.
- Performance change due to ice accretion is still not clear because of the fact that ice accretion profiles are mostly rough and non-aerodynamic. This means, doing a wind tunnel test for such profiles is not an easy task.
- Most of ice accretion experiments are done for thin airfoils used in aviation. However, there is a few number of experiments that studied ice accretion on relatively thick airfoils like the ones used in wind turbines.
- For ice-phobic coatings, splashing models are still empirical and limited to special conditions. This makes the state-of-the-art models not reliable to be used in the simulation of ice accretion on airfoils.

- The presented experiments of ice accretion on coated airfoils done by the DLR in TU-Braunschweig is one of the few experiments that were done with these conditions. Also, to the time of writing this work, it is the only experiment that analyzed the resulting ice profile instead of only generally studying the ice accretion phenomenon.
- More wind tunnel experiments should be done to correlate the coating structures and properties with the ice profile and its development with time at different icing conditions.
- Ice-phobic coatings on wind turbine blades should be optimized to cover the leading edge surface of the middle and tip sections of the blade (starting from $r/R = 0.5$) to minimize the coatings area and cost and maximize the effect of such coatings on the overall performance of wind turbine blades in cold climates.

From this work also some conclusions can be found:

- In general, it is harder to simulate glaze than rime ice accretion. That is due to the presence of many physical parameters that controls the accretion process in case of glaze ice, such as: convective heat transfer coefficient, wind shear on the surface of the airfoil (which is dependent on the state of the flow over the surface of being either laminar or turbulent), and also convection between liquid film and the solid surface.
- A rough estimation of icing conditions at any location in Europe can be estimated using the methodology explained in Sec. 3.8. This provides a simple method to extract the data necessary to perform the simulations
- The Quasi-3D ice accretion method can be useful to simulate ice accretion on wind turbine blades in case they are operating around the rated operation wind and rotational speeds. If the operation conditions varies from the rated ones, radial effects of the rotation on the air flow field will be stronger and accordingly the deviations from the quasi-3D assumptions will be more obvious.
- The provided approach for calculating the required anti-icing heat presents only the exact amount of heat required at each location just to keep water film in a liquid state. However, to calculate the actual required anti-icing heating power, other factors should be taken into consideration like the used anti-icing method and consequently the proper heat transfer mode through the blade walls. This entails Conjugate Heat transfer (CHT) simulations which are out of the scope of this thesis.

8.2 Outlook

In the future, there are many ideas that can be applied, like:

- For a better study of the performance of ice-phobic coatings, more accurate of wind tunnel experiments of ice accretion on coated airfoils should be studied. These experiments should include also different AoA values, airflow velocity, ambient temperatures, and droplet sizes to have a more general validation cases of ice accretion cases. The resulting ice accretion should be scanned with some advanced 3D scanning method to get an exact ice accretion profile to be compared with experiments.

- More experiments on the water droplets splash on inclined coated surfaces should be conducted. From these experiments, a better droplet splashing model should be derived and hence a better simulation should be achieved.
- Optimization of airfoil profile for minimum ice accretion should be studied. Such a study should give an idea about the changes in design of wind turbine blades located in cold climates that should be applied to contribute in the mitigation of ice accretion.
- Ice accretion experiments of a rotating small scaled wind turbine should be conducted. This should be very helpful for the validation of ice accretion solvers.
- The effect of the ice profile on the turbine performance should be studied experimentally. This can be done by 3D printing small scale wind turbine blades with the new iced profiles. This will also enable better validation of air flow simulations around rough surfaces.
- The effect of ice profiles on the decrease of wind turbine performance should be studied. This could be either studied by the means of BEM simulations or by CFD simulations. For BEM simulations, the effect of ice profiles on each section can be studied by simulating the effects on sectional polars. The values of the new polars can be then fed to BEM simulations. However, to do study the effect of ice formation in CFD, this requires an advanced meshing tool to be able to mesh the complex shape of ice profile and applying the suitable y^+ value to apply rwf's as studied in Chapter 4.
- Numerical simulation of the operation of wind turbines after ice formation should be conducted. The challenge in such a study will be generating the computational mesh around such complicated profiles.

Bibliography

- [1] S. Elghobashi, “On predicting particle-laden turbulent flows,” *Applied Scientific Research*, vol. 52, pp. 309–329, 06 1994.
- [2] W. B. Wright, R. Gent, and D. Guffond, “DRA/NASA/ONERA collaboration on icing research. part 2; prediction of airfoil ice accretion,” 1997.
- [3] C.-H. Choi and C.-J. Kim, “Large slip of aqueous liquid flow over a nanoengineered superhydrophobic surface,” *Physical review letters*, vol. 96, no. 6, p. 066001, 2006.
- [4] C. Ybert, C. Barentin, C. Cottin-Bizonne, P. Joseph, and L. Bocquet, “Achieving large slip with superhydrophobic surfaces: Scaling laws for generic geometries,” *Physics of fluids*, vol. 19, no. 12, p. 123601, 2007.
- [5] “Surface Roughness Measurement–Parameters.” <https://www.olympus-ims.com/en/metrology/surface-roughness-measurement-portal/parameters/>, 2021.
- [6] M. Dörenkämper, B. T. Olsen, B. Witha, A. N. Hahmann, N. N. Davis, J. Barcons, Y. Ezber, E. García-Bustamante, J. F. González-Rouco, J. Navarro, M. Sastre-Marugán, T. Šfíle, W. Trei, M. Žagar, J. Badger, J. Gottschall, J. Sanz Rodrigo, and J. Mann, “The making of the new european wind atlas – part 2: Production and evaluation,” *Geoscientific Model Development*, vol. 13, no. 10, pp. 5079–5102, 2020.
- [7] N. N. Sørensen, J. Michelsen, and S. Schreck, “Navier–stokes predictions of the nrel phase vi rotor in the nasa ames 80 ft× 120 ft wind tunnel,” *Wind Energy: An International Journal for Progress and Applications in Wind Power Conversion Technology*, vol. 5, no. 2-3, pp. 151–169, 2002.
- [8] C. Son and T. Kim, “Development of an icing simulation code for rotating wind turbines,” *Journal of Wind Engineering and Industrial Aerodynamics*, vol. 203, p. 104239, 2020.
- [9] T. Reid, G. Baruzzi, I. Ozcer, D. Switchenko, and W. Habashi, “FENSAP-ICE simulation of icing on wind turbine blades, part 1: performance degradation,” in *51st AIAA aerospace sciences meeting including the new horizons forum and aerospace exposition*, p. 750, 2013.
- [10] P. Z. A. P. S. C. C. P. S. B. N. C. Y. C. L. G. M. G. M. H. K. L. E. L. J. M. T. M. T. W. O. Y. R. Y. Masson-Delmotte, V. and B. Zhou, “Climate change 2021: The physical science basis. contribution of working group i to the sixth assessment report of the intergovernmental panel on climate change,” 2021.

- [11] GWEC, *GWEC Global Wind Energy Report 2021*. Global Wind Energy Council, 2021.
- [12] V. Lehtomäki and I. W. Task, “Wind energy in cold climates available technologies-report,” tech. rep., Tech. rep., IEA Wind, 2016.
- [13] G. Fortin, “Thermodynamique de la glace atmosphérique,” p. 9, 2009.
- [14] O. Parent and A. Ilinca, “Anti-icing and de-icing techniques for wind turbines: Critical review,” *Cold regions science and technology*, vol. 65, no. 1, pp. 88–96, 2011.
- [15] F. Lamraoui, G. Fortin, R. Benoit, J. Perron, and C. Masson, “Atmospheric icing impact on wind turbine production,” *Cold Regions Science and Technology*, vol. 100, pp. 36–49, 2014.
- [16] W. J. Jasinski, S. C. Noe, M. S. Selig, and M. B. Bragg, “Wind turbine performance under icing conditions,” 1998.
- [17] H. Seifert, “Technical requirements for rotor blades operating in cold climate,” *DEWI-Magazin*, 2005.
- [18] B. Tammelin and H. Seifert, “Wind energy production in cold climate,” 2000.
- [19] T. Laakso and E. Peltola, “Review on blade heating technology and future prospects,” 2005. Project code: C4SU00647; BOREAS VII : Impact of icing on wind energy production and other field of activities, BOREAS VII ; Conference date: 07-03-2005 Through 08-03-2005.
- [20] L. Battisti and R. Fedrizzi, “2d numerical simulation of a wind turbine de-icing system, using cycled heating,” *Wind Engineering*, vol. 31, no. 1, pp. 33–42, 2007.
- [21] J. F. Maissan, “Wind power development in sub-arctic conditions with severe rime icing,” *Northern Review*, no. 24, 2001.
- [22] L. Makkonen, T. Laakso, M. Marjaniemi, and K. J. Finstad, “Modelling and prevention of ice accretion on wind turbines,” *Wind engineering*, vol. 25, no. 1, pp. 3–21, 2001.
- [23] M. Marjaniemi, “Blade heating element design and practical experiences,” *BOREAS*, pp. 197–209, 1998.
- [24] R. Horbaty, “Wind energy in cold climates,Äthe swiss experience,” *Proceedings of the 2005 BOREAS VII, Saariselkä, Finland*, 2005.
- [25] C. Mayer, “Système électrothermique de dégivrage pour une pale d’éolienne,” *Master Thesis*, p. 193, 2007.
- [26] N. Dalili, A. Edrisy, and R. Carriveau, “A review of surface engineering issues critical to wind turbine performance,” *Renewable and Sustainable energy reviews*, vol. 13, no. 2, pp. 428–438, 2009.

- [27] C. Antonini, M. Innocenti, T. Horn, M. Marengo, and A. Amirfazli, "Understanding the effect of superhydrophobic coatings on energy reduction in anti-icing systems," *Cold Regions Science and Technology*, vol. 67, no. 1-2, pp. 58–67, 2011.
- [28] V. Patreau, F. Morency, and I. Paraschivoiu, "Analysis of thermal de-icing system for horizontal axis wind turbine blade," *BOREAS IV. FMI, Hetta, Finland*, pp. 222–235, 1998.
- [29] Y. Yuan and T. R. Lee, "Contact angle and wetting properties," in *Surface science techniques*, pp. 3–34, Springer, 2013.
- [30] T. Young, "An essay on the cohesion of fluids," *Philosophical transactions of the royal society of London*, no. 95, pp. 65–87, 1805.
- [31] E. Pierce, F. Carmona, and A. Amirfazli, "Understanding of sliding and contact angle results in tilted plate experiments," *Colloids and Surfaces A: Physicochemical and Engineering Aspects*, vol. 323, no. 1-3, pp. 73–82, 2008.
- [32] A. Cassie and S. Baxter, "Wettability of porous surfaces," *Transactions of the Faraday society*, vol. 40, pp. 546–551, 1944.
- [33] R. N. Wenzel, "Resistance of solid surfaces to wetting by water," *Industrial & Engineering Chemistry*, vol. 28, no. 8, pp. 988–994, 1936.
- [34] D. Richard and D. Quéré, "Bouncing water drops," *EPL (Europhysics Letters)*, vol. 50, no. 6, p. 769, 2000.
- [35] A. Alizadeh, M. Yamada, R. Li, W. Shang, S. Otta, S. Zhong, L. Ge, A. Dhinojwala, K. R. Conway, V. Bahadur, *et al.*, "Dynamics of ice nucleation on water repellent surfaces," *Langmuir*, vol. 28, no. 6, pp. 3180–3186, 2012.
- [36] K. A. Emelyanenko, A. M. Emelyanenko, and L. B. Boinovich, "Water and ice adhesion to solid surfaces: Common and specific, the impact of temperature and surface wettability," *Coatings*, vol. 10, p. 648, Jul 2020.
- [37] C. J. Greenshields, "OpenFOAM user guide. version 6," *OpenFOAM Foundation Ltd July*, 2017.
- [38] T. Shih, "Overset grids: Fundamental and practical issues," p. 3259, 2002.
- [39] B. Zhu, K. Chi, T. Shih, and J. Slater, "Computing aerodynamic performance of 2d iced airfoils: blocking strategy and convergence rate," in *20th AIAA Applied Aerodynamics Conference*, p. 3049, 2002.
- [40] X. Chi, B. Zhu, T. Shih, H. Addy, and Y. Choo, "CFD analysis of the aerodynamics of a business-jet airfoil with leading-edge ice accretion," p. 560, 2004.
- [41] X. Chi, Y. Li, H. Addy, G. Addy, Y. Choo, T. Shih, and H. Chen, "A comparative study using CFD to predict iced airfoil aerodynamics," in *43rd AIAA Aerospace Sciences Meeting and Exhibit*, p. 1371, 2005.

- [42] X. Chi, B. Williams, N. Crist, R. Kreeger, R. Hindman, and T. Shih, "2-D and 3-D CFD simulations of a clean and an iced wing," p. 1267, 2006.
- [43] K. Chi, B. Williams, R. Kreeger, R. Hindman, and T. Shih, "Simulations of finite wings with 2-d and 3-d ice shapes: Modern lifting-line theory versus 3-d CFD," p. 504, 2007.
- [44] Y. Li, R. Shock, R. Zhang, H. Chen, and T. I. Shih, "Simulation of flow over an iced airfoil by using a lattice-boltzmann method," in *43rd AIAA aerospace sciences meeting and exhibit*, p. 1103, 2005.
- [45] Y. Cao, K. Chen, and J. Sheridan, "Flowfield simulation and aerodynamic performance analysis of complex iced aerofoils with hybrid multi-block grid," *Proceedings of the Institution of Mechanical Engineers, Part G: Journal of Aerospace Engineering*, vol. 222, no. 3, pp. 417–422, 2008.
- [46] J. Shim, J. Chung, and K. Le, "A computational investigation of ice geometry effects on airfoil performances," in *39th Aerospace Sciences Meeting and Exhibit*, p. 540, 2001.
- [47] C. M. Marongiu, P. L. Vitagliano, G. Zanazzi, and R. Narducci, "Rans analysis of an iced airfoil at medium/high reynolds number," p. 4283, 2007.
- [48] G. Jun, D. Olliden, M. G. Potapczuk, and J.-C. Tsao, "Computational aerodynamic analysis of three-dimensional ice shapes on a naca 23012 airfoil," p. 2202, 2014.
- [49] A. Pendenza, W. G. Habashi, and M. Fossati, "A 3d mesh deformation technique for irregular in-flight ice accretion," *International Journal for Numerical Methods in Fluids*, vol. 79, no. 5, pp. 215–242, 2015.
- [50] J. Nikuradse, "Strömungsgesetze in rauhen rohren vdi-forschungsheft, bd. 361," 1933.
- [51] H. Schlichting, "Experimental investigation of the problem of surface roughness," 1937.
- [52] H. Chen and V. Patel, "Near-wall turbulence models for complex flows including separation," *AIAA journal*, vol. 26, no. 6, pp. 641–648, 1988.
- [53] A. Hellsten and S. Laine, "Extension of the k-omega-sst turbulence model for flows over rough surfaces," in *22nd Atmospheric Flight Mechanics Conference*, p. 3577, 1997.
- [54] D. C. Wilcox, "Reassessment of the scale-determining equation for advanced turbulence models," *AIAA journal*, vol. 26, no. 11, pp. 1299–1310, 1988.
- [55] J. George, A. Simone, G. Iaccarino, and J. Jiménez, "Modeling roughness effects in turbulent boundary layers by elliptic relaxation," in *Proceedings of the Summer Program*, p. 119, 2010.
- [56] B. Aupoix and P. Spalart, "Extensions of the spalart–allmaras turbulence model to account for wall roughness," *International Journal of Heat and Fluid Flow*, vol. 24, no. 4, pp. 454–462, 2003.

- [57] P. Spalart, "Trends in turbulence treatments," in *Fluids 2000 conference and exhibit*, p. 2306, 2000.
- [58] A. Blanchard, "Analyse expérimentale et théorique de la structure de la turbulence d'une couche limite sur paroi rugueuse," 1977.
- [59] M. Acharya, J. Bornstein, and M. Escudier, "Turbulent boundary layers on rough surfaces," *Experiments in Fluids*, vol. 4, no. 1, pp. 33–47, 1986.
- [60] M. Hosni, H. W. Coleman, and R. P. Taylor, "Measurements and calculations of rough-wall heat transfer in the turbulent boundary layer," *International Journal of Heat and Mass Transfer*, vol. 34, no. 4-5, pp. 1067–1082, 1991.
- [61] M. Hosni, H. W. Coleman, J. W. Garner, and R. P. Taylor, "Roughness element shape effects on heat transfer and skin friction in rough-wall turbulent boundary layers," *International Journal of Heat and Mass Transfer*, vol. 36, no. 1, pp. 147–153, 1993.
- [62] T. Knopp, B. Eisfeld, and J. B. Calvo, "A new extension for k - ω turbulence models to account for wall roughness," *International Journal of Heat and Fluid Flow*, vol. 30, no. 1, pp. 54–65, 2009.
- [63] P. M. Ligrani and R. J. Moffat, "Structure of transitionally rough and fully rough turbulent boundary layers," *Journal of Fluid Mechanics*, vol. 162, pp. 69–98, 1986.
- [64] I. H. Abbott and A. E. Von Doenhoff, *Theory of wing sections: including a summary of airfoil data*. Courier Corporation, 2012.
- [65] B. L. Ljungstroem, "Wind tunnel investigation of simulated hoar frost on a 2-dimensional wing section with and without high lift devices," tech. rep., Report FFA-AU-902, Stockholm, Sweden, 1972.
- [66] C.-H. Lee, "Rough boundary treatment method for the shear-stress transport k - ω model," *Engineering Applications of Computational Fluid Mechanics*, vol. 12, no. 1, pp. 261–269, 2018.
- [67] F. Chedevigne and B. Aupoix, "Accounting for wall roughness effects in turbulence models: a wall function approach," in *7th EUCASS conference*, 2017.
- [68] K. Suga, T. Craft, and H. Iacovides, "An analytical wall-function for turbulent flows and heat transfer over rough walls," *International Journal of Heat and Fluid Flow*, vol. 27, no. 5, pp. 852–866, 2006.
- [69] G. A. L. Da Silva, M. N. Arima, N. N. Branco, and M. de Mattos Pimenta, "Proposed wall function models for heat transfer around a cylinder with rough surface in cross flow," tech. rep., SAE Technical Paper, 2011.
- [70] G. A. Ruff and B. M. Berkowitz, "Users manual for the NASA lewis ice accretion prediction code (lewice)," 1990.

- [71] W. B. Wright, "User manual for the NASA glenn ice accretion code LEWICE. version 2.2. 2," 2002.
- [72] M. Bragg, A. Broeren, H. Addy, M. Potapczuk, D. Guffond, and E. Montreuil, "Airfoil ice-accretion aerodynamic simulation," p. 85, 2007.
- [73] G. E. Fujiwara and M. B. Bragg, "3d computational icing method for aircraft conceptual design," in *9th AIAA Atmospheric and Space Environments Conference*, p. 4375, 2017.
- [74] J. Vassberg, M. Dehaan, M. Rivers, and R. Wahls, "Development of a common research model for applied CFD validation studies," in *26th AIAA Applied Aerodynamics Conference*, p. 6919, 2008.
- [75] G. E. Fujiwara, B. Woodard, B. Wiberg, A. J. Mortonson, and M. Bragg, "A hybrid airfoil design method for icing wind tunnel tests," in *5th AIAA Atmospheric and Space Environments Conference*, p. 2826, 2013.
- [76] G. E. Fujiwara, M. B. Bragg, and A. P. Broeren, "Comparison of computational and experimental ice accretions of large swept wings," *Journal of Aircraft*, vol. 57, no. 2, pp. 342–359, 2020.
- [77] P. Verdin and C. Thompson, "Automatic multi-stepping approach for ice predictions," *IASME Transactions, Issue 1*, vol. 2, 2005.
- [78] S. Özgen and M. Canıbek, "Ice accretion simulation on multi-element airfoils using extended messinger model," *Heat and Mass Transfer*, vol. 45, no. 3, pp. 305–322, 2009.
- [79] O. Yirtici, I. H. Tuncer, and S. Ozgen, "Ice accretion prediction on wind turbines and consequent power losses," vol. 753, p. 022022, 2016.
- [80] O. Yirtici, K. Cengiz, S. Ozgen, and I. H. Tuncer, "Aerodynamic validation studies on the performance analysis of iced wind turbine blades," *Computers & Fluids*, vol. 192, p. 104271, 2019.
- [81] Z. Wang and C. Zhu, "Numerical simulation for in-cloud icing of three-dimensional wind turbine blades," *Simulation*, vol. 94, no. 1, pp. 31–41, 2018.
- [82] J. Sznajder, "Implementation of an eulerian method of determination of surface water collection efficiency for atmospheric icing problems," *Prace Instytutu Lotnictwa*, no. 1 (238), pp. 91–105, 2015.
- [83] J. Hospers and H. Hoeijmakers, "Eulerian method for ice accretion on multiple-element airfoil sections," p. 1236, 2010.
- [84] J. Kim, P. G. Dennis, L. Sankar, and R. Kreeger, "Ice accretion modeling using an eulerian approach for droplet impingement," p. 246, 2013.
- [85] D. R. Bilodeau, W. G. Habashi, M. Fossati, and G. S. Baruzzi, "Eulerian modeling of supercooled large droplet splashing and bouncing," *Journal of Aircraft*, vol. 52, no. 5, pp. 1611–1624, 2015.

- [86] R. A. Da Silveira, C. R. Maliska, D. A. Estivam, and R. Mendes, "Evaluation of collection efficiency methods for icing analysis," 2003.
- [87] S. Chang, H. Tang, H. Wu, X. Su, A. Lewis, and C. Ji, "Three-dimensional modelling and simulation of the ice accretion process on aircraft wings," *International Journal of Astronautics and Aeronautical Engineering*, 2018.
- [88] P. Fu and M. Farzaneh, "A CFD approach for modeling the rime-ice accretion process on a horizontal-axis wind turbine," *Journal of Wind Engineering and Industrial Aerodynamics*, vol. 98, no. 4-5, pp. 181–188, 2010.
- [89] L. Hu, X. Zhu, J. Chen, X. Shen, and Z. Du, "Numerical simulation of rime ice on NREL Phase VI blade," *Journal of Wind Engineering and Industrial Aerodynamics*, vol. 178, pp. 57–68, 2018.
- [90] B. L. Messinger, "Equilibrium temperature of an unheated icing surface as a function of air speed," *Journal of the aeronautical sciences*, vol. 20, no. 1, pp. 29–42, 1953.
- [91] T. G. Myers, "Extension to the messinger model for aircraft icing," *AIAA journal*, vol. 39, no. 2, pp. 211–218, 2001.
- [92] T. Myers, J. Charpin, and C. Thompson, "Slowly accreting ice due to supercooled water impacting on a cold surface," *Physics of Fluids*, vol. 14, no. 1, pp. 240–256, 2002.
- [93] T. G. Myers, J. P. Charpin, and S. J. Chapman, "The flow and solidification of a thin fluid film on an arbitrary three-dimensional surface," *Physics of Fluids*, vol. 14, no. 8, pp. 2788–2803, 2002.
- [94] L. N. Sankar and M. Ali, "In-cloud ice accretion modeling on wind turbine blades using an extended messinger model," p. 3715, 2015.
- [95] Y. Bourgault, H. Beaugendre, and W. Habashi, "Development of a shallow-water icing model in FENSAP-ICE," *Journal of Aircraft*, vol. 37, no. 4, pp. 640–646, 2000.
- [96] P. Lavoie, D. Pena, Y. Hoarau, and E. Laurendeau, "Comparison of thermodynamic models for ice accretion on airfoils," *International Journal of Numerical Methods for Heat & Fluid Flow*, 2018.
- [97] M. Pourbagian and W. Habashi, "CFD-based optimization of electro-thermal wing ice protection systems in de-icing mode," in *51st Aiaa Aerospace Sciences Meeting Including the New Horizons Forum and Aerospace Exposition*, p. 654, 2013.
- [98] D. Kelly, W. G. Habashi, G. Quaranta, P. Masarati, and M. Fossati, "Ice accretion effects on helicopter rotor performance, via multibody and CFD approaches," *Journal of Aircraft*, vol. 55, no. 3, pp. 1165–1176, 2018.
- [99] D. Switchenko, W. Habashi, T. Reid, I. Ozcer, and G. Baruzzi, "FENSAP-ICE simulation of complex wind turbine icing events, and comparison to observed performance data," p. 1399, 2014.

- [100] M. Yassin, M. Nathoo, Z. Zhan, W. G. Habashi, and M. Fossati, "Modeling of iced rotor dynamics via CFD-CSD coupling," in *2018 Applied Aerodynamics Conference*, p. 3483, 2018.
- [101] L. Makkonen, "Models for the growth of rime, glaze, icicles and wet snow on structures," *Philosophical Transactions of the Royal Society of London. Series A: Mathematical, Physical and Engineering Sciences*, vol. 358, no. 1776, pp. 2913–2939, 2000.
- [102] M. Marjaniemi, L. Makkonen, and T. Laakso, "TURBICE - the wind turbine blade icing model," 2000.
- [103] A. Hudecz, H. Koss, and M. O. L. Hansen, "Ice accretion on wind turbine blades," 2013.
- [104] M. C. Homola, M. S. Virk, T. Wallenius, P. J. Nicklasson, and P. A. Sundsbø, "Effect of atmospheric temperature and droplet size variation on ice accretion of wind turbine blades," *Journal of wind engineering and industrial aerodynamics*, vol. 98, no. 12, pp. 724–729, 2010.
- [105] M. S. Virk, M. C. Homola, and P. J. Nicklasson, "Effect of rime ice accretion on aerodynamic characteristics of wind turbine blade profiles," *Wind Engineering*, vol. 34, no. 2, pp. 207–218, 2010.
- [106] M. S. Virk, M. C. Homola, P. J. Nicklasson, *et al.*, "Atmospheric icing on large wind turbine blades," *Int. J. Energy Environ*, vol. 3, no. 1, pp. 1–8, 2012.
- [107] Z. Li and X. Jiang, "Simulation of rime ice accretion on wind turbine blade," in *2020 IEEE International Conference on High Voltage Engineering and Application (ICHVE)*, pp. 1–4, IEEE, 2020.
- [108] H. Addy, A. Broeren, J. Zoeckler, and S. Lee, "A wind tunnel study of icing effects on a business jet airfoil," p. 727, 2003.
- [109] J. Krøgenes, L. Brandrud, R. Hann, J. Bartl, T. Bracchi, and L. Sætran, "Aerodynamic performance of the NREL S826 airfoil in icing conditions," *Wind Energy Science Discussions*, vol. 2017, pp. 1–17, 2017.
- [110] Y. Han, J. Palacios, and S. Schmitz, "Scaled ice accretion experiments on a rotating wind turbine blade," *Journal of Wind Engineering and Industrial Aerodynamics*, vol. 109, pp. 55–67, 2012.
- [111] L. Gao, Y. Liu, W. Zhou, and H. Hu, "An experimental study on the aerodynamic performance degradation of a wind turbine blade model induced by ice accretion process," *Renewable Energy*, vol. 133, pp. 663–675, 2019.
- [112] X. Huang, N. Tepylo, V. Pommier-Budinger, M. Budinger, E. Bonaccorso, P. Villedieu, and L. Bennani, "A survey of icephobic coatings and their potential use in a hybrid coating/active ice protection system for aerospace applications," *Progress in Aerospace Sciences*, vol. 105, pp. 74–97, 2019.

- [113] C. Tropea, M. Schremb, and I. V. Roisman, "Physics of sld impact and solidification," in *Proceedings of the 7th European Conference for Aeronautics and Space Sciences, Milan, Italy. EUCASS*, 2017.
- [114] J.-L. Barrat and L. Bocquet, "Large slip effect at a nonwetting fluid-solid interface," *Physical review letters*, vol. 82, no. 23, p. 4671, 1999.
- [115] S. Douezan and F. Brochard-Wyart, "Decorating a liquid interface promotes splashing," *Langmuir*, vol. 27, no. 16, pp. 9955–9960, 2011.
- [116] M. McCarthy, K. Gerasopoulos, R. Enright, J. N. Culver, R. Ghodssi, and E. N. Wang, "Biotemplated hierarchical surfaces and the role of dual length scales on the repellency of impacting droplets," *Applied Physics Letters*, vol. 100, no. 26, p. 263701, 2012.
- [117] D. G. Aboud and A.-M. Kietzig, "On the oblique impact dynamics of drops on superhydrophobic surfaces. part ii: Restitution coefficient and contact time," *Langmuir*, vol. 34, no. 34, pp. 9889–9896, 2018.
- [118] H. Wang, C. Liu, H. Zhan, and Y. Liu, "Droplet asymmetric bouncing on inclined superhydrophobic surfaces," *ACS omega*, vol. 4, no. 7, pp. 12238–12243, 2019.
- [119] H. Almohammadi and A. Amirfazli, "Droplet impact: Viscosity and wettability effects on splashing," *Journal of colloid and interface science*, vol. 553, pp. 22–30, 2019.
- [120] A. M. Moqaddam, S. S. Chikatamarla, and I. V. Karlin, "Drops bouncing off macrotextured superhydrophobic surfaces," *Journal of Fluid Mechanics*, vol. 824, pp. 866–885, 2017.
- [121] C. Yin, T. Wang, Z. Che, M. Jia, and K. Sun, "Oblique impact of droplets on microstructured superhydrophobic surfaces," *International Journal of Heat and Mass Transfer*, vol. 123, pp. 693–704, 2018.
- [122] M. A. Delele, D. Nuyttens, A. Duga, A. Ambaw, F. Lebeau, B. Nicolai, and P. Verboven, "Predicting the dynamic impact behaviour of spray droplets on flat plant surfaces," *Soft Matter*, vol. 12, no. 34, pp. 7195–7211, 2016.
- [123] I. V. Roisman, A. Lembach, and C. Tropea, "Drop splashing induced by target roughness and porosity: The size plays no role," *Advances in colloid and interface science*, vol. 222, pp. 615–621, 2015.
- [124] M. A. Quetzeri-Santiago, A. A. Castrejón-Pita, and J. R. Castrejón-Pita, "The effect of surface roughness on the contact line and splashing dynamics of impacting droplets," *Scientific reports*, vol. 9, no. 1, pp. 1–10, 2019.
- [125] M. A. Quetzeri-Santiago, K. Yokoi, A. A. Castrejón-Pita, and J. R. Castrejón-Pita, "Role of the dynamic contact angle on splashing," *Physical review letters*, vol. 122, no. 22, p. 228001, 2019.
- [126] C. Josserand and S. T. Thoroddsen, "Drop impact on a solid surface," *Annual review of fluid mechanics*, vol. 48, pp. 365–391, 2016.

- [127] D. Khojasteh, M. Kazerooni, S. Salarian, and R. Kamali, “Droplet impact on superhydrophobic surfaces: A review of recent developments,” *Journal of Industrial and Engineering Chemistry*, vol. 42, pp. 1–14, 2016.
- [128] L. K. Malla, N. D. Patil, R. Bhardwaj, and A. Neild, “Droplet bouncing and breakup during impact on a microgrooved surface,” *Langmuir*, vol. 33, no. 38, pp. 9620–9631, 2017.
- [129] J. Breitenbach, I. V. Roisman, and C. Tropea, “From drop impact physics to spray cooling models: a critical review,” *Experiments in Fluids*, vol. 59, no. 3, pp. 1–21, 2018.
- [130] D. De Pauw and A. Dolatabadi, “Effect of superhydrophobic coating on the anti-icing and deicing of an airfoil,” *Journal of Aircraft*, vol. 54, no. 2, pp. 490–499, 2017.
- [131] L. Gao, Y. Liu, L. Ma, and H. Hu, “A hybrid strategy combining minimized leading-edge electric-heating and superhydro-/ice-phobic surface coating for wind turbine icing mitigation,” *Renewable Energy*, vol. 140, pp. 943–956, 2019.
- [132] K. Morita, S. Kimura, and H. Sakaue, “Hybrid system combining ice-phobic coating and electrothermal heating for wing ice protection,” *Aerospace*, vol. 7, no. 8, p. 102, 2020.
- [133] P. Spalart and S. Allmaras, “A one-equation turbulence model for aerodynamic flows,” p. 439, 1992.
- [134] F. Menter, “Two-equation eddy-viscosity turbulence models for engineering applications,” *AIAA journal*, vol. 32, no. 8, pp. 1598–1605, 1994.
- [135] R. Dirling, JR, “A method for computing rough wall heat transfer rates on reentry nose tips,” in *8th Thermophysics Conference*, p. 763, 1973.
- [136] T. Cebeci, *Analysis of Turbulent Flows with Computer Programs*. Elsevier, 2004.
- [137] A. Putnam, “Integratable form of droplet drag coefficient,” 1961.
- [138] L. Schiller and A. Naumann, “A drag coefficient correlation,” *Zeitschrift des Vereins Deutscher Ingenieure*, vol. 77, pp. 318–320, 1935.
- [139] I. Langmuir and K. Blodgett, *A mathematical investigation of water droplet trajectories*. No. 5418, Army Air Forces Headquarters, Air Technical Service Command, 1946.
- [140] J. RILEY and D. JECK, “Volume spectra in supercooled clouds for several research flights,” in *30th Aerospace Sciences Meeting and Exhibit*, p. 167, 1992.
- [141] S. Yoon, J. Hewson, P. DesJardin, D. Glaze, A. Black, and R. Skaggs, “Numerical modeling and experimental measurements of a high speed solid-cone water spray for use in fire suppression applications,” *International Journal of Multiphase Flow*, vol. 30, no. 11, pp. 1369–1388, 2004.
- [142] K. Meredith, Y. Xin, and J. de Vries, “A numerical model for simulation of thin-film water transport over solid fuel surfaces,” *Fire Safety Science*, vol. 10, pp. 415–428, 2011.

- [143] T. L. Bergman, F. P. Incropera, D. P. DeWitt, and A. S. Lavine, *Fundamentals of heat and mass transfer*. John Wiley & Sons, 2011.
- [144] C. Geuzaine and J.-F. Remacle, “GMSH: A 3-D finite element mesh generator with built-in pre-and post-processing facilities,” *International journal for numerical methods in engineering*, vol. 79, no. 11, pp. 1309–1331, 2009.
- [145] C. Bai and A. Gosman, “Mathematical modelling of wall films formed by impinging sprays,” *SAE transactions*, pp. 782–796, 1996.
- [146] C. Bai, H. Rusche, and A. Gosman, “Modeling of gasoline spray impingement,” *Atomization and Sprays*, vol. 12, no. 1-3, 2002.
- [147] DIN, “4287: Geometrische produktspezifikation (gps)–oberflächenbeschaffenheit: Tastschnittverfahren–benennungen, definitionen und kenngößen der oberflächenbeschaffenheit,” *Beuth-Verlag, Berlin*, 2010.
- [148] M. C. Salcedo, I. B. Coral, and G. V. Ochoa, “Characterization of surface topography with abbot firestone curve,” *Contemporary Engineering Sciences*, vol. 11, no. 68, pp. 3397–3407, 2018.
- [149] B. E. K. Nygaard, J. E. Kristjánsson, and L. Makkonen, “Prediction of in-cloud icing conditions at ground level using the wrf model,” *Journal of Applied Meteorology and Climatology*, vol. 50, no. 12, pp. 2445–2459, 2011.
- [150] E. Achenbach, “The effect of surface roughness on the heat transfer from a circular cylinder to the cross flow of air,” *International Journal of Heat and Mass Transfer*, vol. 20, no. 4, pp. 359–369, 1977.
- [151] G. dutch wind tunnels, “German–dutch wind tunnels.”
- [152] M. Papadakis, K. E. Hung, G. T. Vu, H. W. Yeong, C. S. Bidwell, M. D. Breer, and T. J. Bencic, “Experimental investigation of water droplet impingement on airfoils, finite wings, and an s-duct engine inlet,” 2002.
- [153] L. Ma, Z. Zhang, L. Gao, Y. Liu, and H. Hu, “Bio-inspired icephobic coatings for aircraft icing mitigation: A critical review,” *Progress in Adhesion and Adhesives*, vol. 6, pp. 171–201, 2021.

List of Publications

Peer reviewed papers:

- Yassin, K., Helms, A., Moreno, D., Kassem, H., Höning, L., & Lukassen, L. J. (2021). Applying a Random Time Mapping to Mann modelled turbulence for the generation of intermittent wind fields. *Wind Energy Science Discussions*, 1-29. (under review)
- Yassin, K., Kassem, H., Stoevesandt, B., Klemme, T., & Peinke, J. (2021). Numerical Simulation of Roughness Effects of Ice Accretion on Wind Turbine Airfoils. *Energies*, 2022. (under review)
- Yassin, K., Stoevesandt, B., and Peinke, J. (2020, September). Numerical Estimation of Anti-icing Heating Power for NREL 5MW Wind Turbine Blades in Cold Climate. In *Journal of Physics: Conference Series* (Vol. 1618, No. 5, p. 052075). IOP Publishing.

Conference contributions:

- Yassin, K., Stoevesandt, B., Peinke, J.: Numerical Simulation of the effects of Ice-phobic Coatings on Wind Turbine Blade Performance in Cold Climate, *Wind Energy Science Conference 2021, Hannover (virtual)*, 25.-28. May 2021
- Helms, A., Moreno, D., Yassin, K., Kassem, H., Höning, L., Lukassen, L. J.: Applying the CTRW time-mapping to Mann modeled turbulence for the generation of intermittent wind fields, *Wind Energy Science Conference 2021, Hannover (virtual)*, 25.-28. May 2021
- Yassin, K., Stoevesandt, B., Peinke, J.: Icing on Wind Turbine Profiles, *OpenFOAM-Workshop, Bremen, Germany*, 21. Februar 2019
- Yassin, K., Kassem, H., Stoevesandt, B., Klemme, T., Peinke, J.: Numerical Investigation of Aerodynamic Performance of Wind Turbine Airfoils with Ice Accretion, *Wind Energy Science Conference 2019, Cork, Ireland*, 17. – 20. June 2019
- Yassin, K., Stoevesandt, B., Peinke, J.: Numerical Simulation of Ice Accretion on Coated Wind Turbine Blades, *14th EAWC PhD Seminar on Wind Energy, Brussel*, 18.09.2018 – 20.09.2018

Acknowledgement

First of all, I would like to thank my supervisors: Prof.Dr. Joachim Peinke and Dr.rer.nat. Bernhard Stoevesandt for their contentious scientific and professional support and their dedication to helping me whenever I needed their help. Also, I would like to thank my current and former colleagues at ForWind and Fraunhofer IWES for their help during this research work and the interesting discussions. I would like to especially thank Dr. Hassan Kassem, Dr. Johannes Nicolaas Theron, Mohamed Cherif Mihoubi, and Leo Höning from Fraunhofer IWES for their huge support with OpenFOAM issues. Without them, this work would have taken a few more years. Also, I would like to thank Mrs. Agnes Seeger for her efforts with official documents and communication with the university officials. Finally, I would like to thank Prof.Dr. Peter Wulf from HAW Hamburg, Prof.Dr. Holger Marschall and Prof. Dr. Ilia Roisman from TU Darmstadt, and Prof Taeseong Kim and Dr. Chankyu Son from DTU for their help.

During the journey of this Ph.D. and even before it, I faced a lot of hard times and disappointments. But I couldn't get out of these hardships without the support of my family and friends. I would like to dedicate this effort and success to my father Associate Prof. Osama Yassin who provided amazing academic and personal advice during the years of this journey. Also, I would like to thank my mother for her love and prayers that always lighten my road and make me always feel loved and appreciated. I would like to thank my brothers and sisters for their unconditional love and support. Also, I would like to thank my wife, Mariam, and her family for their love and encouragement. I feel blessed to have such a family around me, even when we live on three different continents.

Finally, I want to dedicate this work and all my efforts in the past, the present, and the future to my wife, Mariam, and our future family to whom this work truly belongs and for whom I am, and will be, always motivated to keep moving forward in this life.

Curriculum Vitae

Personal data

Name Khaled Osama Mohammed Yassin
Date of birth 16th of June, 1988
Place of birth Bangor/United Kingdom
Citizenship Egyptian

Education

10/2017 – Present Doctoral student of Prof. Dr. Joachim Peinke,
AG TWiSt (Turbulence, Wind energy, Stochastics),
C.v.O. University of Oldenburg
09/2012 – 02/2016 M.Sc. of Mechanical Power Engineering,
Ain-Shams University, Cairo, Egypt
09/2005 – 04/2010 B.Sc. of Mechanical Power Engineering,
Ain-Shams University, Cairo, Egypt

Professional experience

since 03/2018 Research fellow
ForWind, Institute of Physics, C.v.O. University of Oldenburg
07/2012 - 10/2017 Mechanical Design Engineer
Dar Al-Handasah Consulting, Cairo, Egypt
11/2010 - 07/2012 Mechanical Design Engineer
Al Bee'ah Consulting, Cairo, Egypt

Erklärung

Ich erkläre hiermit, dass:

- eine Promotion zum Dr.-Ing. angestrebt wird,
- ich diese Arbeit selbständig verfasst und nur die angegebenen Hilfsmittel benutzt habe, und dass die Arbeit in Teilen bereits veröffentlicht bzw. zur Veröffentlichung eingereicht wurde,
- diese Dissertation weder in ihrer Gesamtheit noch in Teilen einer anderen Hochschule zur Begutachtung in einem Promotionsverfahren vorgelegen hat.

Oldenburg, den 18. März 2022

.....
(Khaled Yassin)